



*Vibrational spectroscopy of linear and branched long alkanes.*

WICKRAMARACHCHI, P.A.S.R.

Available from the Sheffield Hallam University Research Archive (SHURA) at:

<http://shura.shu.ac.uk/20531/>

## A Sheffield Hallam University thesis

This thesis is protected by copyright which belongs to the author.

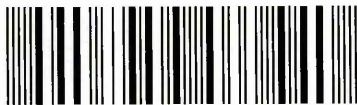
The content must not be changed in any way or sold commercially in any format or medium without the formal permission of the author.

When referring to this work, full bibliographic details including the author, title, awarding institution and date of the thesis must be given.

Please visit <http://shura.shu.ac.uk/20531/> and <http://shura.shu.ac.uk/information.html> for further details about copyright and re-use permissions.

Sheffield S1 1WB

101 826 208 3



**Fines are charged at 50p per hour**

**REFERENCE**

ProQuest Number: 10701178

All rights reserved

INFORMATION TO ALL USERS

The quality of this reproduction is dependent upon the quality of the copy submitted.

In the unlikely event that the author did not send a complete manuscript and there are missing pages, these will be noted. Also, if material had to be removed, a note will indicate the deletion.



ProQuest 10701178

Published by ProQuest LLC (2017). Copyright of the Dissertation is held by the Author.

All rights reserved.

This work is protected against unauthorized copying under Title 17, United States Code  
Microform Edition © ProQuest LLC.

ProQuest LLC.  
789 East Eisenhower Parkway  
P.O. Box 1346  
Ann Arbor, MI 48106 – 1346

# **Vibrational Spectroscopy of Linear and Branched Long Alkanes**

By

**P.A.S.R. Wickramarachchi**

A thesis submitted in part fulfilment of the requirements of  
Sheffield Hallam University for the degree of  
Doctor of Philosophy

February 2006

## **Declaration**

The work described in this thesis was carried out by the author in the Materials and Engineering Research Institute, Sheffield Hallam University, between January 2001 and July 2005. The author declares that this work has not been submitted for any other degree. The work is original except where acknowledged by reference.

Author:

( P.A.S.R. Wickramarachchi)

Supervisor:

(Dr. S.J. Spells)

## **Acknowledgements**

First of all I would like to thank my supervisor Dr. S.J. Spells for his support, guidance and advice throughout this project and for giving me this opportunity. I am very much grateful to Prof. G. Ungar and Dr. X.B. Zeng of the University of Sheffield for providing me samples and X-ray facility, for their support and helpful discussions.

I also thank the staff and my colleagues at MERI, Sheffield Hallam University for their co-operation during this project. I am very grateful to the Sheffield Hallam University for providing me financial support.

My special thanks to my family: my husband, Ruwan for his understanding, support and sacrifices and for encouraging me throughout my studies, my mum, dad and my sister for their support in various ways, and my mother-in-law who came to UK to help out during difficult situations, and my father-in-law and sister-in-law for their understanding and support. Finally a big Thank You to Sahan, our son, who has not got a clue what I have been doing or why I have been doing it, for his understanding and all his sacrifices throughout my studies.

## Abstract

In this work we studied monodisperse long chain alkanes as model compounds for semi crystalline polymers, using vibrational spectroscopy. The interest in vibrational spectroscopy is due to its sensitivity to both the crystalline structure and conformational disorder. We used the following vibrational techniques: Fourier transform infrared transmission, Fourier transform infrared – attenuated total reflection (FTIR-ATR), Raman spectroscopy and Inelastic neutron scattering (INS) spectroscopy. In addition, small angle X-ray scattering (SAXS) was used where necessary. In this study FTIR-ATR and INS techniques were not successful in the characterisation of long chain alkanes.

A Raman spectroscopic method, based on conformationally sensitive vibrations, was established using a short chain n-alkane to identify solid-solid phase transitions and was applied to long chain alkanes. Using this method a transition to a non-integer form (NIF) form was identified in two 'Y-shaped' long chain alkane samples at similar temperatures as SAXS. One of these samples is partially deuterated (with deuterium end caps) while the other one is its hydrogenated analogue. However, the end-deuterated sample is not 100% end-deuterated due to a fault in the synthesis. Therefore, here we developed a FTIR-transmission method to determine the isotopic ratio in these partially deuterated alkane samples. Our calculations based on this method showed that the end deuterated 'Y-shaped' alkane only consists of 79.9% of the expected deuterium(D)/hydrogen(H) ratio.

A SAXS study on a linear end-deuterated alkane showed that the chains achieve a maximum tilt of  $35^\circ$ , which is the most common tilt angle also for polyethylene. Combining these results with those from previous studies on the same sample, a relationship between chain perfecting and the chain tilt was established. It was found that the ordering of the crystal structure induces chain tilting in order to accommodate the incoming chain ends to the crystalline layer. The increase in the domain size during this process was found to be from 16 to more than 50 chains per domain. The attempt to explain the observed shift of the SAXS spacings in the tilting experiment, away from the positions predicted by Bragg's equation by using a paracrystalline model failed. Hence, we suggest a model with an asymmetric thickness distribution will be more appropriate in this regard. The simulated  $\text{CD}_2$  bending vibration mode splitting of the infrared spectrum of the random fold model of this end-deuterated alkane is  $9.0 \text{ cm}^{-1}$  whereas a maximum splitting of  $9.1 \text{ cm}^{-1}$  is expected for this mode for a regular fold model of the same alkane. Therefore a vibrational spectroscopic differentiation between these two models based on the experimental  $\text{CD}_2$  bending splitting is highly unlikely.

# Contents

<b>Chapter 1</b>	<b>Introduction</b>	
1.1	Polymers	1
1.1.1	Introduction to polymers	1
1.1.1.1	What is a polymer?	1
1.1.1.2	The structure of polymers	1
1.1.1.3	Skeletal structure	2
1.1.1.4	Classification of polymers	2
1.1.1.4A	Thermoplastics (plastics)	3
1.1.1.4B	Elastomers	4
1.1.1.4C	Thermosets	4
1.1.1.5	Characteristics of polymers	4
1.1.1.6	History of polymer industry	5
1.1.2	Structure and morphology of polymers	6
1.1.2.1	Structure of crystalline polymers	6
1.1.2.1.1	Configurations and conformations of polymer chains	6
1.1.2.1.1 A	Polymer configurations	7
1.1.2.1.1 B	Polymer conformations	8
1.1.2.1.2	Crystal structures of polymers	10
1.1.2.1.2 A	Factors determining crystal structure	11
1.1.2.1.2 B	Crystalline structures	11
1.1.2.2	Morphology of crystalline polymers	13
1.1.2.2.1	Polymer single crystals	13
1.1.2.2.2	Melt crystallisation	15
1.1.2.2.2A	Spherulites	15
1.1.2.2.2B	Extended-chain crystals	16
1.1.2.2.3	The defect structure of crystalline polymers	17
1.1.2.2.4	Nature of the chain fold	18
1.1.2.2.5	Chain tilt	19
1.1.3	Polymer crystallisation and melting	20
1.1.3.1	Crystallisation	20
1.1.3.1.1	General considerations	20
1.1.3.1.2	Growth theories	22
1.1.3.1.2A	Surface nucleation models	22
1.1.3.1.2B	Rough surface growth models	25
1.1.3.2	Melting	26
1.1.4	Structure and physical properties	27
1.1.4.1	Properties involving large deformations	27
1.1.4.1.1	Melt properties	27
1.1.4.1.2	Tensile strength and related properties	28
1.1.4.2	Properties involving small deformations	28
1.1.4.2.1	Effect of crystallinity	28
1.1.4.2.2	Effect of molecular weight	29
1.1.4.2.3	Effect of polar groups	29
1.2	Short chain n-alkanes	29
	References	35



<b>Chapter 2</b>	<b>Long Chain n-Alkanes: Model compounds for polymer semi-crystallinity</b>	
2.1	Introduction	37
2.2	Synthesis	39
2.3	Crystallisation of long chain alkanes	40
2.3.1	Crystalline structures	41
2.3.1.1	Integer folded forms (IF)	41
2.3.1.2	Non-integer folded forms (NIF)	42
2.3.1.3	Superlattice structures	45
2.3.1.4	Structures in branched alkanes	47
2.3.2	Crystallisation rate minima and 'self-poisoning'	50
2.4	Other monodisperse oligomers	51
2.5	Aims and objectives	52
	References	54

<b>Chapter 3</b>	<b>Techniques</b>	
3.1	Infrared Techniques	56
3.1.1	Infrared spectroscopy	56
3.1.1.1	Principles	56
3.1.1.2	Instrumentation	60
3.1.1.2.1	Dispersive spectrometers	60
3.1.1.2.2	FTIR spectrometers	61
3.1.1.2.2A	Principles	61
3.1.1.2.2B	FTIR-ATR spectrometer	64
3.1.1.3	The infrared spectra of polymers	66
3.1.2	Mixed crystal infrared spectroscopy	67
3.1.3	Wagging modes	74
3.2	Raman Spectroscopy	78
3.2.1	Introduction	78
3.2.2	Principles	80
3.3	Neutron Scattering	81
3.3.1	Principles	81
3.3.2	Inelastic neutron scattering (INS)	83
3.4	X-ray Techniques	84
3.4.1	Principles	84
3.4.2	Small angle X-ray scattering (SAXS) on polymers	85
	References	87
	Appendix	89

<b>Chapter 4</b>	<b>Vibrational Spectrum of the Short Chain Alkanes, C<sub>34</sub>H<sub>70</sub> and the mixture, C<sub>34</sub>H<sub>70</sub>/C<sub>36</sub>D<sub>74</sub></b>	
4.1	Identification of phase transition in C <sub>34</sub> H <sub>70</sub> by vibrational spectroscopy	92
4.1.1	Introduction	92
4.1.2	ATR Measurements on C <sub>34</sub> H <sub>70</sub>	95
4.1.2.1	Experimental	95
4.1.2.2	Results and discussion	95
4.1.3	Raman measurements on C <sub>34</sub> H <sub>70</sub>	98
4.1.3.1	Experimental	98
4.1.3.2	Results and discussion	98
4.1.4	Conclusion	109

4.2	Analysis of progression bands in the infrared spectrum of $C_{34}H_{70}$ and a mixture of $C_{34}H_{70}/C_{36}D_{74}$	110
4.2.1	Introduction	110
4.2.2	Calculation of the all- <i>trans</i> chain length	113
4.2.3	Results and discussion	113
4.2.4	Conclusion	120
	References	122

## **Chapter 5      Establishment of an Infrared Method to Determine the Isotopic Ratio in End-Deuterated Long Chain Alkanes**

5.1	Introduction	124
5.2	Experimental	125
5.2.1	Sample preparation	125
5.2.2	Recording the infrared spectrum	126
5.3	Calculation	126
5.3.1	Calculation of weight fraction	126
5.3.2	Calculation of intensity ratio : $I [CH_2]/[CD_2]$	127
5.3.3	Simulation of the doublet to singlet ratio of the $CD_2$ bending mode of $C_{34}H_{70}/C_{36}D_{74}$ mixture	127
5.4	Results and Discussion	129
5.5	Conclusion	141
	References	142

## **Chapter 6      Partially (End) Deuterated Long Chain Alkanes**

6.1	Introduction	143
6.2	Experimental	148
6.2.1	FTIR Studies on deuterated Tridecane	148
6.2.2	SAXS on $C_{12}D_{25}C_{192}H_{384}C_{12}HD_{24}$	148
6.3	Results and Discussion	149
6.3.1	Infrared work on deuterated alkanes	149
6.3.1.1	FTIR studies on deuterated Tridecane	149
6.3.1.2	Calculation of the domain sizes of deuterated end caps before and after annealing of $C_{12}D_{25}C_{192}H_{384}C_{12}HD_{24}$	151
6.3.2	X-ray work on deuterated alkanes	153
6.3.2.1	Determination of the tilt angle of $C_{12}D_{25}C_{192}H_{384}C_{12}HD_{24}$ with increasing annealing temperature	153
6.3.2.2	Evaluation of SAXS of $C_{12}D_{25}C_{192}H_{384}C_{12}HD_{24}$ using a paracrystalline model	158
6.3.3	Simulation of the fold arrangement and resulting $CD_2$ bending vibration in the once – folded form of $C_{12}D_{25}C_{192}H_{384}C_{12}HD_{24}$	167
6.4	Conclusion	171
	References	174

## **Chapter 7      Characterisation of Branched Alkanes**

7.1	Introduction	175
7.2	Experimental	178
7.2.1	C168D	178
7.2.2	End-deuterated branched alkane, A	179

7.2.3	Branched alkane, B	179
7.3	Results and Discussion	179
7.3.1	C168D	179
7.3.2	Branched alkanes: A and B	185
7.4	Conclusion	200
	References	202
 <b>Chapter 8 Inelastic Neutron Scattering (INS) on Long Chain Alkanes</b>		
8.1	Introduction	203
8.2	Experimental	204
8.3	Results and Discussion	204
8.4	Conclusion	207
	References	208
 <b>Chapter 9 Conclusions and Future work</b>		
9.1	Conclusions	209
9.2	Future Work	216
	References	219

# Chapter 1

---

## Introduction

### 1.1 Polymers

#### 1.1.1 Introduction to polymers

##### 1.1.1.1 What is a polymer?

Simply, a polymer is a molecule made of many units. Many 'monomers' combined together to make a polymer.

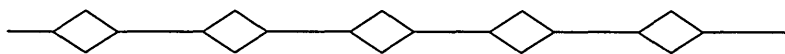


*Fig 1.1: Simple diagram of a polymer.*

Usually a single polymer molecule consists of thousands of repeat units. Sometimes polymers are called 'macromolecules' as polymers are very large molecules.

##### 1.1.1.2 The structure of polymers

Many polymers are made of hydrocarbons. Carbon makes up the backbone of the polymer chain while hydrogen atoms are bonded along the backbone. For example look at polyethylene, the simplest of polymer structures.



*Fig 1.2: The structure of polyethylene.*

However, the other elements such as O, Cl, F, N, Si, P and S can also be found in the molecular make-up of polymers. For example Polyvinyl chloride (PVC) contains Cl, Nylon contains N, Poly tetra fluoro ethylene (PTFE) contains F and Polyester and Polycarbonates contain O. Although the backbone of many polymers is made of C, there are some polymers with a Si or P backbone. They are considered as inorganic polymers.

#### 1.1.1.3 Skeletal structure

Polymers can have linear, branched or network structure.

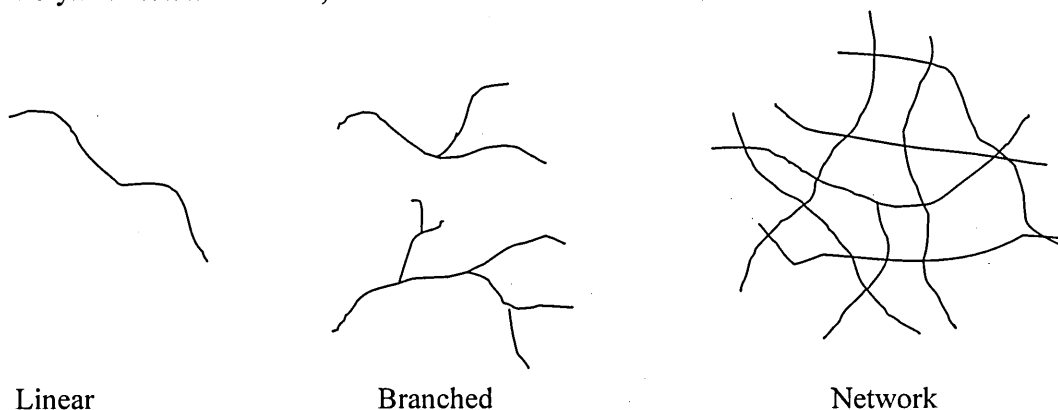


*Fig 1.3: Skeletal structures of polymers.*

A linear polymer is made up of one repeat unit after another, hooked together in a long chain. A branched polymer has short side chains attached to the backbone. In network polymers the main chains are interconnected by crosslinks to form a network structure.

#### 1.1.1.4 Classification of polymers

Given below is the most common way of classifying polymers. It is essentially based upon the underlying molecular structure of the polymers.

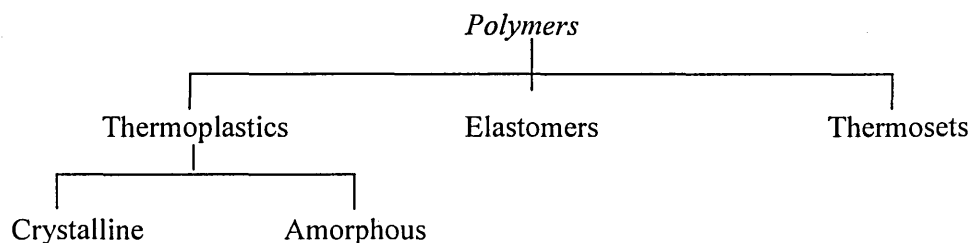


Fig 1.4: Classification of polymers.

#### 1.1.1.4A Thermoplastics (plastics)

Thermoplastics are linear or branched polymers which can be melted upon the application of heat. This property allows for easy processing and facilitates recycling. The majority of polymers are thermoplastic. Thermoplastics are further divided into two groups: amorphous and crystalline thermoplastics. Most thermoplastics are amorphous. The most notable parameter of an amorphous polymer is the glass transition temperature ( $T_g$ ). This is defined as the temperature below which the polymer segments do not have sufficient energy to move past one another. At that point the polymer undergoes marked changes in its properties associated with the cessation of molecular motion. Below the glass transition temperature, materials are a glass. Below  $T_g$ , many amorphous polymers possess the properties of inorganic glasses such as hardness, stiffness, brittleness and transparency. These properties of amorphous polymers are utilised in applications such as food wrap, plastic windows, headlights and contact lenses.

Some thermoplastics are capable of crystallising upon cooling to the solid state. However, they are not 100% crystalline. They only form a 'semi-crystalline' structure with both crystalline and amorphous regions. It is very difficult to form a fully crystalline structure as it requires ordering of the highly coiled and entangled macromolecules present in the liquid state. The polymers with highly regular geometrical structure or small substituents atoms or groups on the backbone chain can achieve a higher crystallinity. The crystalline phases of such polymers are characterised by their 'melting temperature',  $T_m$ . Crystalline polymers have remarkable properties. They are strong, tough, stiff and resistant to chemicals. These properties can be further improved by mechanical processing or adding various fillers and additives into the base polymer.

#### 1.1.1.4B Elastomers

Elastomers are crosslinked rubbery polymers that can be stretched easily to high extensions and which rapidly recover their original dimensions when applied stress is released.

#### 1.1.1.4C Thermosets

Thermosets are rigid materials and are network polymers in which chain motion is greatly restricted by a high degree of crosslinking. They are stable to heat and cannot be made to flow or melt.

#### 1.1.1.5 Characteristics of polymers

Every polymer has very distinct characteristics but most polymers possess the following general attributes. These characteristics of polymers make them useful in various applications. The general characteristics of polymers and relevant applications are given below.

- ◆ Polymers are low density materials with varying degrees of strength. Therefore they are used in a diversity of applications: from toys to the frame structure of space stations or from delicate nylon fibre in pantyhose or kevlar in bullet-proof jackets.
- ◆ Polymers are resistant to most chemicals. It makes them suitable as a packaging material for chemicals. Most of the cleaning fluids are packaged with plastics.
- ◆ Polymers are both thermal and electrical insulators. All the electrical appliances are covered with polymeric material. Thermal resistance is evident in kitchen appliances. Pot and pan handles, the coffee pot handles, the foam core of refrigerators and freezers, insulated cups, coolers and microwaves are some examples. Fibrefill in winter jackets is acrylic and underwear that many skiers wear is made of polypropylene.
- ◆ Polymers can be easily formed into shapes. For example plastics can be moulded into bottles or the body of a car or be mixed with solvents to become an adhesive or a

paint. Elastomers and some plastics stretch and are very flexible. Some polymers like polystyrene and urethane can be foamed.

- ◆ Polymers are recyclable. Consumption of recycled plastics is increasing every day. They can be blended with unprocessed plastics without sacrificing properties in many applications. Picnic tables made of polymeric timbers, fences and outdoor toys, fibre made from plastic water bottles are a few examples of applications of recycled plastics.
- ◆ Polymers are cheaper than metals.
- ◆ Polymers are non-corrosive.
- ◆ Most polymers are safe and non-toxic. However, the monomers that are used to make polymers are often toxic. Therefore special attention should be paid to the removal of residual monomers.

The above characteristics of polymers make them dominant in a wide variety of applications. Polymers are substituting metals from simple household items to the aerospace industry.

#### 1.1.1.6 History of polymer industry

Natural polymers such as polysaccharides, DNA, RNA and proteins were available since life began. They play a crucial role in plant and animal life. From the earliest time man has exploited naturally-occurring polymers for his clothing, decoration, shelter, tools, weapons, writing material etc.

The origin of today's polymer industry is believed to be in the nineteenth century. Modifying natural polymers led to important discoveries. In 1820 Thomas Hancock discovered that by mastication, natural rubber becomes more fluid, making it easier to blend with additives and to mould. Some years later, Charles Goodyear invented the process of "vulcanisation" of natural rubber. By vulcanisation the elastic properties of natural rubber can be improved and its tackiness is eliminated. He obtained the patents for this invention. The polymer industry rose up further after Christian Schonbein prepared nitro-cellulose (gun cotton). In 1892 Charles Cross, Edward Bevan and Clayton



Beadle patented the 'viscose process' for dissolving and then regenerating cellulose. This process was first used to produce textile fibres, and subsequently for production of Cellophane film.

The synthetic polymer industry began in 1910. Phenol-formaldehyde resin (Bakelite) synthesised by Leo Baekland has the distinction of being the first fully synthetic polymer to be commercialised. Then during the World War I the first synthetic rubber was manufactured from 2,3-dimethylbutadiene. Today there are a large number of synthetic polymers in commercial production, a few of them being polystyrene (PS), polyethylene (PE), nylon 6.6, polyvinylchloride (PVC), polymethyl methacrylate (PMMA).

Although the polymer industry was firmly established, the growth of it was restricted by the lack of understanding of the nature of the polymers. Until 1920 the common belief was that they consisted of physically associated aggregates of small molecules. In 1920 Herman Staudinger came up with a new hypothesis that polymers were composed of very large molecules containing long sequences of simple chemical units linked together by covalent bonds. He introduced the word 'macromolecules' to describe polymers. By early 1930s most scientists were convinced of the macromolecular structure of polymers.

### 1.1.2 Structure and morphology of polymers

#### 1.1.2.1 Structure of crystalline polymers

##### 1.1.2.1.1 Configurations and conformations of polymer chains

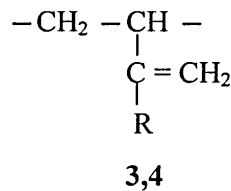
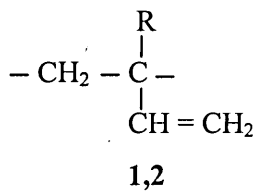
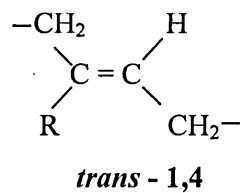
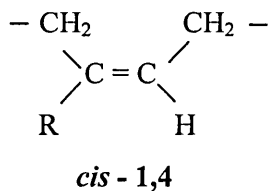
In polymers, the atoms are joined together by covalent bonds along the macromolecular chains. The geometrical arrangement of the atoms in a polymer chain can be divided into two categories:

- Arrangements of atoms that are fixed by the primary chemical bonds. These arrangements can only be altered by breaking and reforming primary bonds. They are called 'configurations'.
- Arrangements arising from rotation about single bonds. These arrangements are described as 'conformations'.

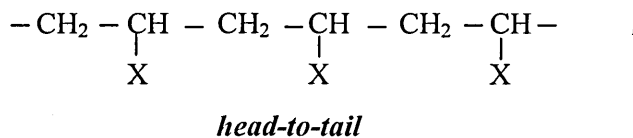
## 1.1.2.1.1A Polymer configurations

Some common examples involving configurations are head-to-head/head-to-tail/tail-to-tail arrangements in vinyl polymers, isotactic/syndiotactic/atactic polymers, cis/ trans isomers, 1,2/1,4 addition etc. Some of these are depicted below.

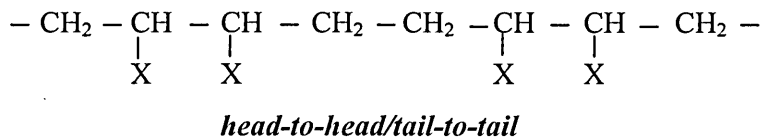
(a)



(b)



(c)



(d)

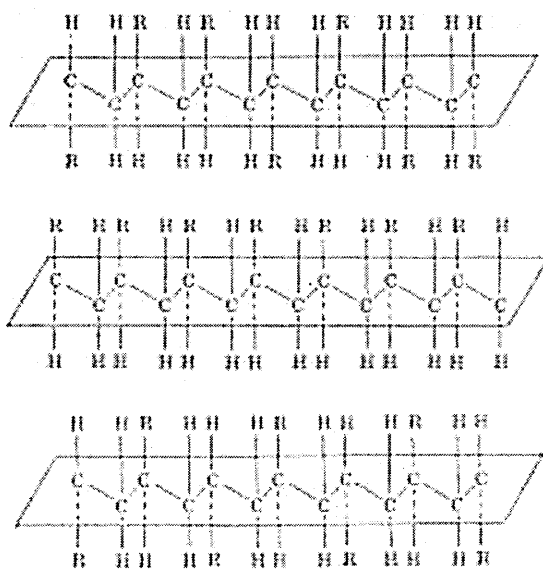


Fig.1.5: Common examples of polymer configurations (a) cis/trans and 1,2/3,4 addition (b) head-to-tail configuration (c) head-to-head/tail-to-tail configuration (d) atactic (top), isotactic (centre), syndiotactic (bottom) configurations<sup>1</sup>.

#### 1.1.2.1.1B Polymer conformations

It is well accepted that the fully extended planar *zigzag* form is the lowest energy conformation for an isolated section of a hydrocarbon chain with all bonds in the trans state as in figure 1.6.

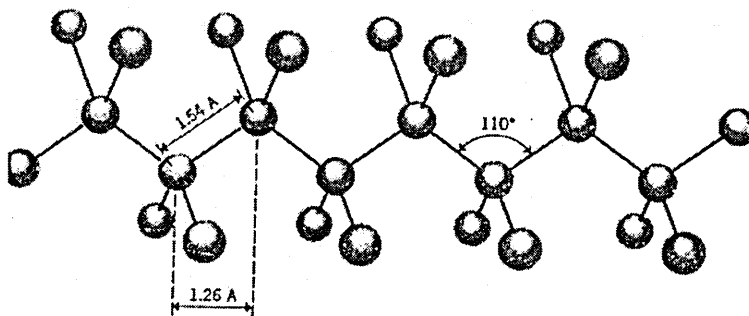


Fig 1.6: The fully extended all-trans conformation of the carbon-carbon chain<sup>1</sup>.

However, at high temperatures and in solutions and melts they can adopt somewhat higher energy conformations involving *gauche* bonds of which the definition is given below. The structural differences between these forms are demonstrated below using n-butane.

Each C atom of n-butane is  $sp^3$  hybridised so it assumes a tetrahedral structure in space. The rotation about the  $C_2-C_3$  bond of the butane molecule is illustrated in figure 1.7. This will result in several conformations. The Newman projections of these conformations and the potential energy associated with each of these forms are illustrated in figures 1.8 and 1.9 respectively. The potential energy of the each form is determined by the steric interactions between substituent atoms and groups on each C atom.

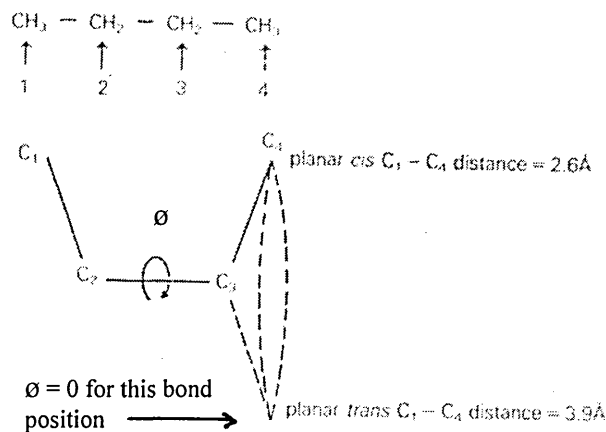


Fig 1.7: Effects of bond rotation upon the conformation of a n-butane molecule<sup>2</sup>.

This is clearly evident from the minima in the potential energy diagram which correspond to the staggered conformations and maxima which correspond to the eclipsed conformations. In the planar-*trans* conformation the two methyl groups; the largest substituent in butane, are far apart from each other while in the planar-*cis* conformation the distance between these two groups achieves a minimum. The relevant energies of these two forms are represented by the lowest minimum at  $\phi = 0$  and the two maxima at  $\phi = \pm 180^\circ$  respectively. The other two minima correspond to the *gauche* conformations of staggered forms in which the methyl groups and hydrogen atoms are at  $60^\circ$  to each other.

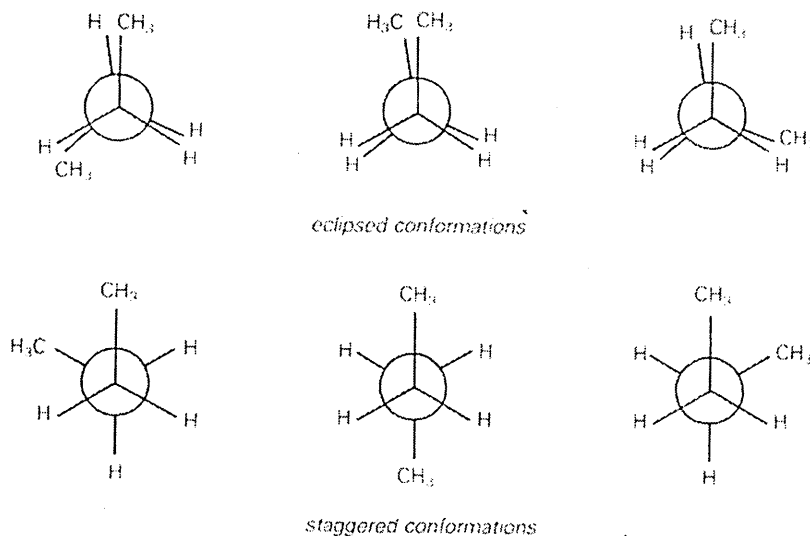


Fig 1.8: Newman projections of the eclipsed and staggered conformations of a *n*-butane molecule<sup>2</sup>.

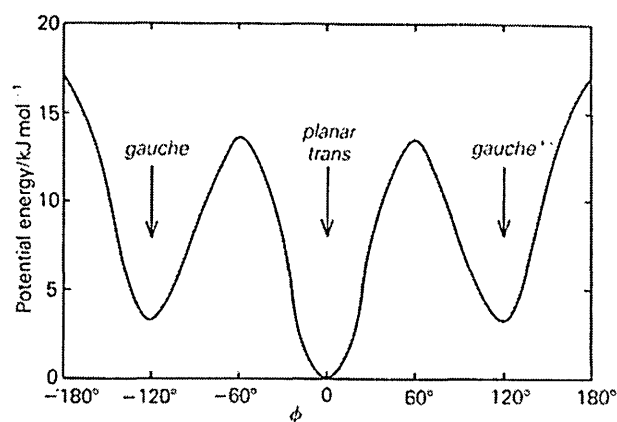


Fig 1.9: Potential energy of a *n*-butane molecule as a function of the angle  $\Phi$  of bond rotation<sup>2</sup>.

#### 1.1.2.1.2 Crystal structures of polymers

Many polymer molecules possess the ability to crystallise. The main characteristic of crystalline polymers that distinguishes them from most other crystals is that they are only 'semi-crystalline'. This is evident from X-ray studies and their densities. The importance of polymer crystallinity is due to its effect upon polymer properties.

#### 1.1.2.1.2A Factors determining crystal structure

Certain structural requirements are necessary for a polymer molecule to crystallise.

- ♦ Linearity of the chains – the crystallisability of a polymer is closely related to the regularity of the molecular structure. Typical crystalline polymers have a highly regular chemical and geometrical structure. Occasional irregularities such as branching limit the extent of crystallinity, but do not prevent its occurrence.
- ♦ Tacticity – in general isotactic and syndiotactic polymers are crystalline whereas atactic polymers are non - crystalline.
- ♦ Copolymerisation – although it affects the perfection of a polymer chain, it can be tolerated to a limited extent. For example copolymers of ethylene and vinyl alcohol; ethylene and tetrafluoroethylene and ethylene and carbon monoxide are crystalline. All these polymers have very similar structures and  $\text{CH}_2$ ,  $\text{CHOH}$ ,  $\text{CF}_2$  and  $\text{C=O}$  groups are approximately similar in size. Therefore they can fit into the similar crystal lattices despite the stereochemical irregularity of the polymers.

#### 1.1.2.1.2B Crystalline structures

- ♦ Structures based on extended chains - In most polymer crystals fully extended planar zigzag chains are favoured as it is the minimum energy conformation. Fully extended chains are found in the crystal structures of polyethylene, poly vinyl alcohol, syndiotactic polymers, most polyamides and cellulose.

The structure of any crystalline solid can be described by defining a regular pattern of atoms, which is repeated in the structure. This repeating unit is known as the 'unit cell' and the crystals are made up of stacks of the cells. In polymers, unit cells are made up of the repeating segments of the polymer chains packed together, often with several segments in each unit cell. The three dimensional structures of several hundred polymer molecules have been determined using X-ray Diffractometry. The structures of a few common polymers are given in the Table 1.1.

Table 1.1: Crystal structures of some common polymers<sup>2</sup>.

Macromolecule	Crystal system
Polyethylene I $-\text{CH}_2-$	Orthorhombic
Polyethylene II $-\text{CH}_2-$	Monoclinic
Polytetrafluoroethylene I $-\text{CF}_2-$	Triclinic
Polytetrafluoroethylene I $-\text{CF}_2-$	Trigonal
Polypropylene (iso) $-\text{CH}_2-\text{CHCH}_3-$	Monoclinic
Polystyrene (iso) $-\text{CH}_2-\text{CHC}_6\text{H}_5-$	Trigonal
Polypropylene (syndio) $-\text{CH}_2-\text{CHCH}_3-$	Orthorhombic
Poly(vinyl chloride) (syndio) $-\text{CH}_2-\text{CHCl}-$	Orthorhombic
1,4-polyisoprene (cis) $-\text{CH}_2-\text{CCH}_3=\text{CH}-\text{CH}_2$	Orthorhombic
1,4-Polyisoprene (trans) $-\text{CH}_2-\text{CCH}_3=\text{CH}-\text{CH}_2$	Orthorhombic

- ♦ Helical structures – polymers with bulky substituents closely spaced along the chain often prefer a helical structure. This allows the substituents to pack closely without appreciable distortion of chain bonds. Most isotactic polymers fall in this class: isotactic polypropylene, one form of poly(1-butene) and polystyrene are some of them. Polytetrafluoroethylene exists in two helical conformations as two twisted ribbons. Helical structures are very common among biological polymers. For example DNA, RNA and the  $\alpha$ -keratin structure assumed by many polypeptides are helices.

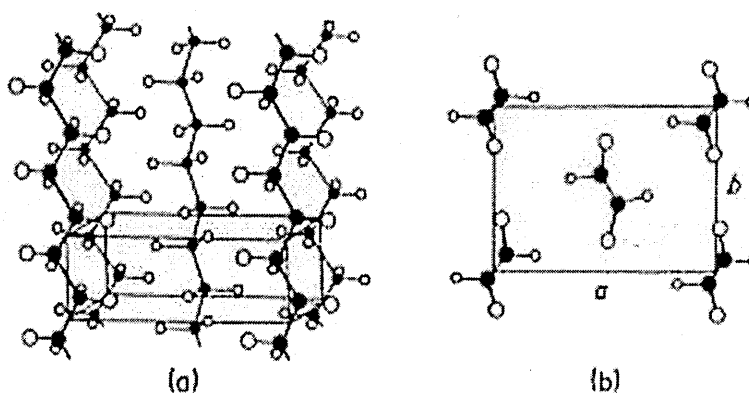


Fig 1.10: Crystal structure of orthorhombic polyethylene (a) General view of unit cell (b) Projection of unit cell parallel to the chain direction. (Carbon atoms ● Hydrogen atoms ○)<sup>2</sup>.

#### 1.1.2.2 Morphology of crystalline polymers

##### 1.1.2.2.1 Polymer single crystals

Isolated single crystals can be prepared by precipitation from dilute solution. They have been observed in many polymers including polyethylene, polypropylene, polyoxomethylene, polyamides and cellulose and its derivatives.

The polymer single crystals are thin and plate-like (lamellar). The thickness of a lamella is around 10 nm and they are many microns in lateral dimensions. According to electron diffraction measurements, polymer chains are oriented normal or very nearly normal to the lamellar plane. This was somewhat surprising since polymer chains are several hundred nanometers in length. Therefore it is evident that polymer molecules fold 'back and forth' between the top and bottom surfaces of the lamellae.

The size, shape and regularity of the crystals depend on their growth conditions such as solvent, temperature and growth rate. For example, at the lowest crystallisation temperatures, the crystals are lozenge-shaped and bounded by {110} faces (figure 1.11a). As the crystallisation temperature is increased the lozenges become truncated with {100} faces (figure 1.11b – e). Eventually, these {100} faces become curved and the curvature is prominent at higher temperatures.



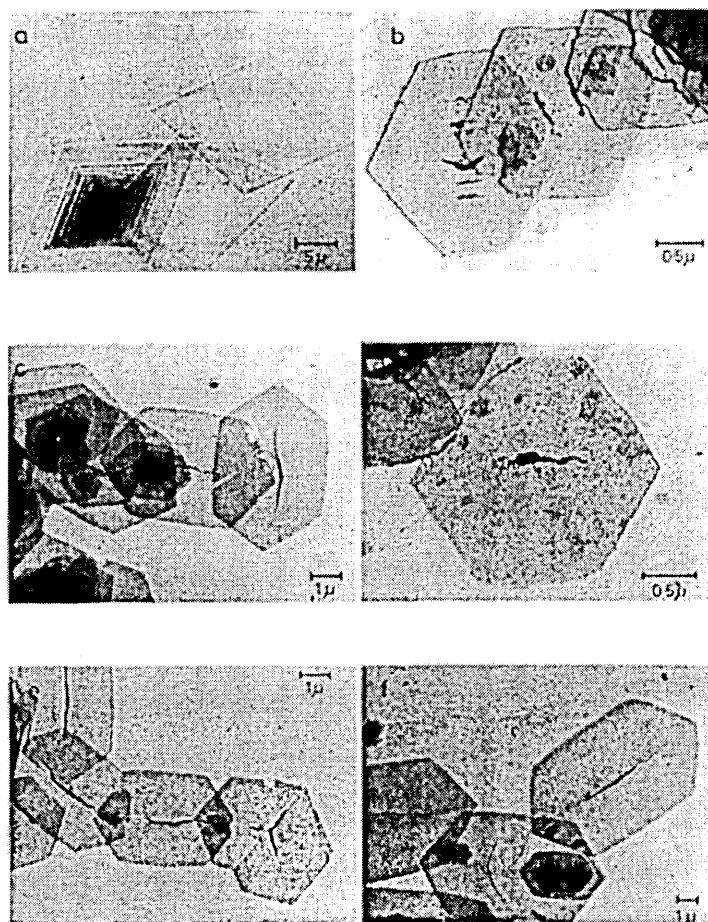


*Fig 1.11: Some forms of lamellar crystals<sup>3</sup>.*

Many single crystals of polyethylene show secondary structural features such as corrugations and pleats. It was found by optical microscopy that both these features are due to a hollow pyramidal structure (figure 1.12). Many crystals of polyethylene grow in the form of hollow pyramids. The fold surface of pyramidal polyethylene single crystals is close to the  $\{312\}$  plane of the polyethylene unit cell.

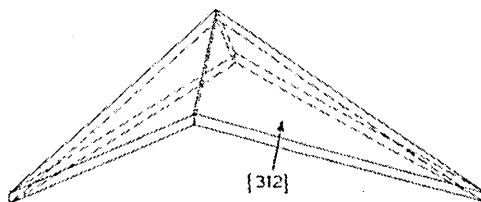


*Fig 1.12: Schematic representation of a pyramidal polyethylene single crystals<sup>2</sup>.*

Solution-grown samples of polyethylene are about 80% crystalline. It is generally thought the non-crystalline component resides mainly in the fold surfaces of the crystals. Several models have been proposed for the fold surface as shown in figure 1.13. The isolated chain-folded lamellar single crystals are only obtained by crystallisation from dilute solutions. As the solution becomes more concentrated the molecules become entangled. This results in more complex crystal forms. These entangled chains have the probability of being incorporated in more than one crystal during crystallisation giving rise to inter-crystalline links. The crystals obtained by crystallisation from concentrated solutions are often found either as lamellae with spiral overgrowths or aggregates of lamellar crystals. Even more complex features such as twinned crystals, dendritic growths, steps, dislocation networks, moiré patterns and epitaxial growths have been identified in solution crystallisation.

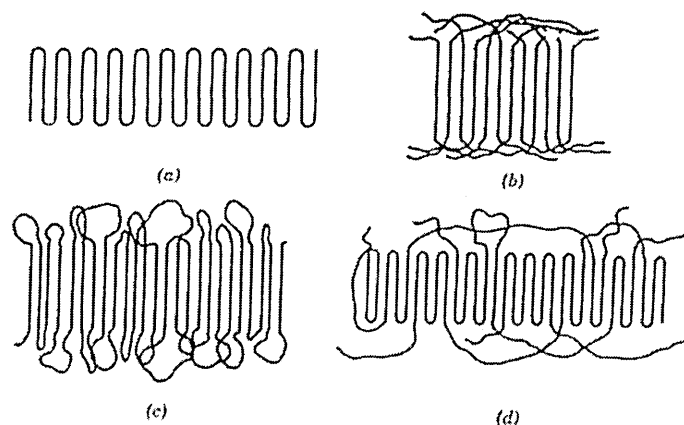


*Fig 1.13: Schematic two-dimensional representations of models of the fold surface in polymer lamellae (a) sharp folds (b) 'switchboard model' (c) loose loops with adjacent re-entry (d) a combination of several features<sup>1</sup>.*

#### 1.1.2.2.2 Melt crystallisation

##### 1.1.2.2.2A Spherulites

Melt crystallisation is not fundamentally different from solution crystallisation especially when the solutions are concentrated. In the melt, chain entanglements are more prominent which results in more irregularly shaped crystals than in solution crystallisation.

The main characteristic of melt crystallisation is the 'spherulitic' structure. These structures form by nucleation at different points in the sample and grow as spherical entities. The growth of the spherulites stops when impingement of adjacent spherulites occurs.

The detailed structure of polymer spherulities can best be studied by electron microscopy. It was observed that a polymeric spherulite consists of numerous crystals radiating from a central nucleus and terminating at the spherulite boundaries. Close examination of the micrograph shows that the crystals are lamellar. The dimensions of these crystal lamellae are similar to those of solution-grown lamellar single crystals. It further reveals that these crystals are twisted in the spherulites. A possible structure of the twisted lamellae in polyethylene spherulites is illustrated schematically in figure 1.14.

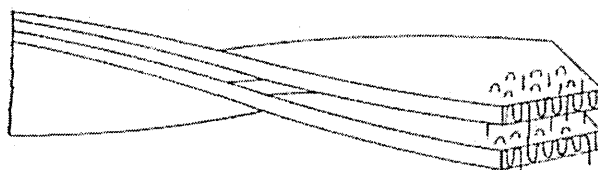


*Fig 1.14: Schematic representation of a possible model for twisted lamellae in spherulitic form<sup>2</sup>.*

The nature of the conformation of the molecules within the twisted crystals is a subject of great interest. It is thought, in these crystals there are small proportions of fairly sharp chain folding and a large number of inter-crystalline links with a given molecule shared between at least two crystals.

#### 1.1.2.2.2 B Extended-chain crystals

In addition to folded-chain crystallisation, during melt crystallisation polymers can also crystallise in the extended form. However, this depends on crystallisation conditions including applied pressure and supercooling. Extended morphology is easily accessible in low-molecular-weight polymers. The crystal thickness of the extended chain crystals is equal to the extended chain length.

### 1.1.2.2.3 The defect structure of crystalline polymers

Crystalline polymers are not entirely perfect. They have amorphous regions and also crystalline areas, which are partially disordered. Crystals of any material contain imperfections such as dislocations or point-defects. The most predominant types of defects in polymer crystals are chain end disorder, short branches, folds and copolymer units. It has been observed that the majority of this chain disorder is excluded from the crystalline regions and incorporated in the amorphous regions.

- ◆ Point defects - point defects such as vacancies and interstitial atoms or ions are very common in atomic and ionic crystals. In the case of polymer crystals, it is relatively restricted by the long-chain nature of the polymer molecules. The most remarkable example of a point defect which occurs in crystalline regions of the polymer crystals is the molecular 'kink'. A kink can occur in a planar zig-zag chain consisting of all *trans* bonds by making two of the bonds gauche. The sequence of the bonds would be  $tg^+tg^-t$  instead of the  $tttt$  sequence of the all-*trans* chain. One important aspect of such a kink is it enables an extra  $-CH_2-$  group to be incorporated in the crystal. The motion of the defect along the chain allows the transport of material across the crystal.
- ◆ Dislocations - dislocations are fairly common in polymers. The types of dislocations are screw dislocation, edge dislocation and mixed screw and edge dislocation. Screw dislocations are frequent in polyethylene and the most obvious example for this type of defect is crystals containing growth spirals.
- ◆ Two-dimensional imperfections – the fold surface is the most interesting in this type (figure 1.13).
- ◆ Amorphous defects – this is defined as disorders large enough to disrupt the lattice surrounding their own immediate area by forcing other atoms out of their normal positions

The net effect of all the many types of defects discussed above, in particular the fold surfaces and surrounding regions, is to provide localised amorphous regions and deformed or distorted lattices. Amorphous regions contribute to diffuse X-ray scattering.

The deformed or distorted lattices, termed 'paracrystallinity' (Hosemann 1962), produce broadening of the X-ray diffraction maxima.

#### 1.1.2.2.4 Nature of the chain fold

One of the remarkable characteristics of polymers is their crystallisation by chain folding. At what chain length chain folding starts and the nature of this fold have been central questions in polymer science. Several models ranging from the highly ordered, tight adjacent folds to the random re-entry 'switch board' model with loose loops have been proposed<sup>4</sup>. One of the reasons for the controversy is the lack of evidence of the polymer surface. In polydisperse (chains with different lengths) polymers the chain ends remain on the surface as 'cilia' masking the surface from surface analysis particularly in view of the small depth (<1nm) of the fold itself. Recently synthesised model alkanes are an immense help in order to mimic the chain folding behaviour of polymers. Monodisperse (uniform chain lengths) long chain alkane crystals (Chapter 2) which are capable of integer folding have the advantage of not containing cilia and thus having the fold surface uncovered. However, still the surface analysis techniques are not very useful due to small depth and the mobility of the fold. Therefore, vibrational spectroscopy plays a major role here.

The studies of polyethylene single crystals consisting of folded chains started almost 5 decades ago<sup>4</sup>. Tasumi and Krimm tried to answer the questions; A) in which crystallographic plane does the fold propagate? B) How many ethylene groups does a fold contain? They were successful in answering the first question. They have identified two morphologies: a) chain folding in the (110) plane for crystals grown from dilute solutions b) folding parallel to the (100) plane for crystals obtained from other conditions but the latter possibility was later shown to be wrong. There was no definite answer for the second question. Estimates of the number of methylene groups in a fold had been made only from model building and from simple potential energy calculations. Tasumi and Krimm were the first to propose a spectroscopic study of the fold geometry<sup>4</sup>. Their basis for a vibrational analysis was the effect of interchain interactions, mainly the nearest neighbour H...H interactions. By considering structures in which neighbouring methylene units are selectively deuterated, they have shown the effect of interchain

interactions on the spectrum is specifically dependant on the pattern of deuteration. They were able to predict the nature of the fold based on calculated frequencies for certain groups of labelled stems. Since then several computer modelling and vibrational studies have been done on the geometry of the chain<sup>5,6,7,8</sup>. Computer model studies by Chum et al have shown that more than one fold type may be present in polyethylene crystals. They have found that the energy difference between the global minimum and other conformations ranged from 4.5 to 6.2 kcal mol<sup>-1</sup>. This small energy difference enables us to anticipate the existence of other fold geometries as well<sup>9</sup>.

#### 1.1.2.2.5 Chain tilt

In many crystalline polymers chains are often tilted relative to the layer normal. In polyethylene this leads to the 'hollow pyramid' shape of solution grown single crystals<sup>10</sup>. Further chain tilt is believed to be responsible for lamellar twist in melt-crystallised spherulites<sup>11,12</sup>. In some polymers chain tilt is found in all circumstances, while in others it develops only on high temperature crystallisation. Crystal lamellae with tilted chains are obtained at high crystallisation temperature ( $T_c$ ) from the melt<sup>13</sup>. X-ray diffraction results on polyethylene single crystals suggest that in some cases, an initially small tilt increases upon annealing<sup>14</sup>. Bassett and Hodge<sup>15-18</sup> studied polyethylene spherulites using electron microscopy and found lamellae having crystal stems inclined at angles: 19°, 35° and 41° corresponding to the basal planes of {101}, {201} and {502} respectively, with 35° being the most common. Voigt-Martin<sup>19</sup> also concluded from electron microscopy data that most of the polyethylene lamellae exhibit basal planes of the type  $\{h01\}$ . Tilt angles higher than 45° have also been reported under special conditions of sample preparations<sup>20</sup>. In the case of perpendicular chains the basal plane is {001}. The {201} tilt arises when each consecutive chain is shifted by one lattice period along the chain direction. Such a tilt allows chain ends and folds an increased surface area.

In solution-grown crystals of long chain alkanes both folded and extended chain crystals are perpendicular to the lamellar normal while the melt grown crystals are tilted<sup>21</sup>. As in polyethylene, the difference has been associated with  $T_c$  being lower in the former case. In long chain alkanes tilt is also usually 35° corresponding to a {201} basal plane and perpendicular chains form a {001} basal plane.

In apparent agreement with the behaviour of polyethylene, shorter n-alkanes crystallise with perpendicular chains as long as  $T_c$  is below 60-70° C<sup>22</sup>. This is true for odd numbered alkanes. However, even numbered alkanes display a more complex behaviour due to molecular symmetry<sup>23</sup>. In C<sub>33</sub>H<sub>68</sub> a {101} tilted form has been observed at higher temperatures after two discrete first order transitions<sup>24</sup>. In short chain alkanes, the tilt at high temperature is attributed to the surface disorder and the absence of tilt at low temperature is attributed to high end group order<sup>25</sup>. When perpendicular chain solution crystallised alkanes with more than 50 carbons are heated, chain tilt is introduced gradually. However, crystals of alkanes up to C<sub>94</sub>H<sub>190</sub> melt before 35° tilt is reached<sup>26</sup>.

Although it is agreed that the chain tilts at higher temperature to accommodate conformationally disordered chain ends and/or chain folds, the reason for the lack of tilt at low temperature is still in controversy. In short chain alkanes this is attributed to high surface order while in polyethylene this is attributed to kinetically introduced surface roughness<sup>12,27</sup>. This will be discussed in detail in Chapter 4. The relation between chain tilt and chain end disorder has been studied using the recently synthesised long chain alkanes<sup>28</sup>. This study takes advantage of recently synthesised end-deuterated long chain alkanes to probe the chain end region separately from the chain interior to further investigate the relationship of chain tilt and chain disorder. Based on these observations the coincidence of onset of chain tilt and the perfecting of chain ends will be discussed in Chapter 6.

### 1.1.3 Polymer crystallisation and melting

#### 1.1.3.1 Crystallisation

##### 1.1.3.1.1 General considerations

Crystallisation takes place mainly by two distinct steps: nucleation and growth. When the temperature of a polymer melt is reduced to the melting temperature there is a tendency for the random tangled molecules in the melt to become aligned and form small ordered regions. They are called 'nuclei' and the process of making nuclei is called 'nucleation'. The second step is the 'growth' whereby crystal nuclei grow by the addition of further chains.

Nucleation can be either homogeneous or heterogeneous. Polymer crystallisation usually occurs heterogeneously on foreign bodies such as dust particles or the walls of the container. The growth of a crystal nucleus can take place either one, two or three dimensionally. The growth of polymer crystals occurs by incorporation of the macromolecular chains to a lamellar crystal.

It has been observed experimentally that the linear dimension ( $r$ ) of the growing entities at a given crystallisation temperature is usually linear with time ( $t$ ) thus giving the relationship;

$$r = vt \quad \dots\dots\dots (1.1)$$

where  $v$  is the growth rate. The growth rate is strongly dependent on the crystallisation temperature,  $T_c$  (figure 1.15). The growth rate is relatively low at crystallisation temperatures just below the melting temperature of the polymer. As supercooling is increased,  $v$  increases rapidly until a maximum is obtained. Further increase in  $T_c$  reduces  $v$ . The maximum in the  $v$  is due to two competing effects.

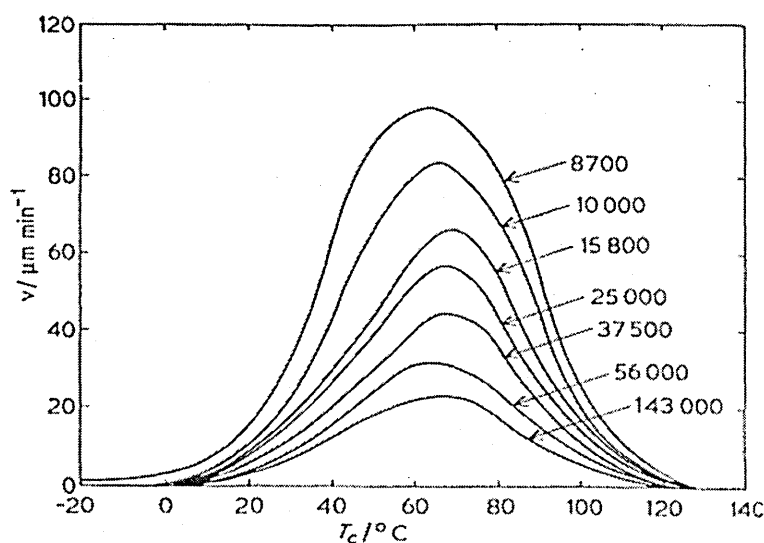


Fig 1.15: Dependence of crystal growth rate upon crystallisation temperature,  $T_c$ .

The thermodynamic driving force for crystallisation will increase as the  $T_c$  is lowered thus enhancing the  $v$ . However, the reduction in temperature results in increased viscosity so that the transport of material to the growth point will be more difficult. This



causes a reduction in  $v$  as the temperature is reduced although the driving force continues to increase.

#### 1.1.3.1.2 Growth theories

There have been many attempts to develop theories to explain the important aspects of crystallisation. However, any theory on crystallisation of polymers must account for the following main experimental observations;

- ◆ Both solution and melt crystallised crystals are usually thin and lamellar
- ◆ Lamellar thickness,  $l$ , is inversely proportional to supercooling,  $\Delta T$ ;

$$l \propto \frac{1}{\Delta T} \quad \dots\dots\dots (1.2)$$

- ◆ Polymer chains are folded within the lamellar crystals obtained from solution crystallisation and in melt crystallised lamellae they are folded to a certain extent
- ◆ At low supercoolings ( $\Delta T$ ), curved crystals develop while at high  $\Delta T$ , faceted crystals occur.

Two main theories have been developed:

- ◆ Surface nucleation models – Lauritzen and Hoffman<sup>29</sup>, 1960
- ◆ Continuous growth models – Sadler and Gilmer<sup>30</sup>, 1984

#### 1.1.3.1.2A Surface nucleation models

This is a kinetic description used by Lauritzen and Hoffman<sup>29</sup> to explain the effects observed during polymer crystallisation. This is an extension of the kinetic approach used to explain the crystallisation of small molecules. This is also divided into two steps; initial nucleation followed by crystal growth. The main parameter used here is the Gibbs free energy,  $G$ . The change in free energy,  $\Delta G$ , on crystallisation at a constant temperature,  $T$  is given by;

$$\Delta G = \Delta H - T\Delta S \quad \dots\dots\dots (1.3)$$

where  $\Delta H$  is the enthalpy change and  $\Delta S$  is the change in entropy. During primary nucleation a few molecules pack side-by-side to form a small cylindrical crystalline embryo. This will create a new surface which has a surface energy. This tends to increase  $G$  whereas the incorporation of molecules in the crystal causes a reduction in  $G$  which also depends upon the crystal volume. These two effects result in a change in free energy. The change in  $\Delta G$  during the nucleation process is shown in figure 1.16.

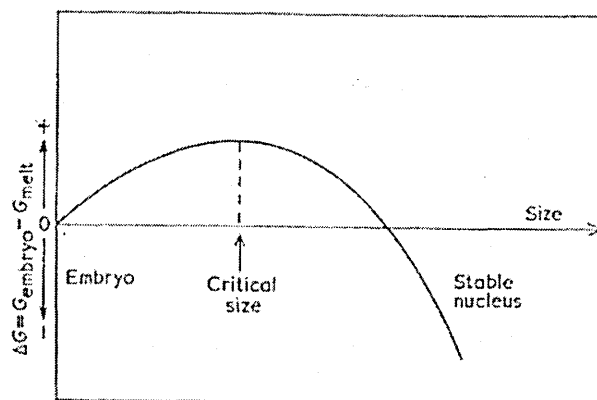


*Fig 1.16: Schematic representation of change in free energy for the nucleation process during polymer crystallisation<sup>2</sup>.*

At the beginning, the embryo is small, the surface to volume ratio is high so that the  $G$  increases because of the rapid increase in surface energy. As the embryo becomes larger surface to volume ratio decreases, and there will be a critical size above which  $G$  starts to decrease and eventually the free energy will be less than that of the original melt. Once the nucleus is greater than the critical size it will grow spontaneously. The peak in the curve is an energy barrier. It is envisaged that at the crystallisation temperature there will be sufficient thermal fluctuations to allow it to be overcome.

It is accepted that the growth of the polymer crystals occurs through secondary nucleation on a pre-existing crystal surface. In this process new molecules are added to a molecularly smooth crystal surface (figure 1.17). The first step is the laying down of a molecular strand on an otherwise smooth crystal surface. This is followed by the subsequent addition of further segments through a chain folding process. However, chain

folding only occurs in flexible molecules whereas more rigid molecules crystallise in extended form.

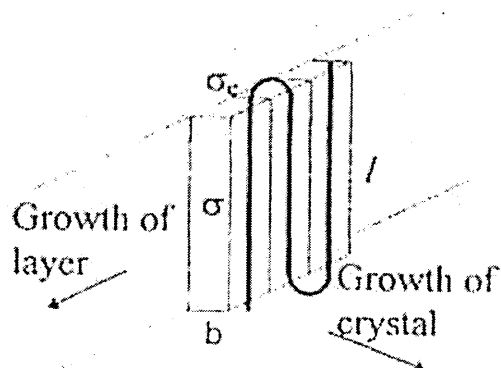


Fig 1.17: Chain deposition on the side surface of a polymer crystal<sup>29</sup>.

An approximate equation relating  $l$  to  $\Delta T$  has been obtained.

$$l = \frac{2\gamma_e T_m^0}{\Delta H_v \Delta T} \dots\dots\dots(1.4)$$

- Where  $l$  = crystal thickness  
 $\gamma_e$  = fold surface energy  
 $T_m^0$  = equilibrium melting temperature  
 $\Delta H_v$  = enthalpy of fusion per unit volume  
 $\Delta T$  = supercooling

The equation 1.4 proves that  $l \propto 1/\Delta T$  in agreement with experimental observations. But this model is unable to predict the curved faces at low  $\Delta T$ .

### 1.1.3.1.2B Rough surface growth model

This model was proposed by Sadler and Gilmer<sup>30</sup>. This theory opposes the previous ideas that the nucleation is always the rate controlling factor. Instead, this basically considers an 'entropic barrier' for initiating a new layer of crystal.

Figure 1.18 shows three different types of roughness which commonly occur on the lamella surface. In figure 1.18a all growth units are complete stems of same length. In figure 1.18b all the stems are laid down as complete stems which are of the differing lengths. In figure 1.18c growth units are only parts of complete stems. These small segments of stems can add to anywhere on the surface. If the polymer units are complete (fig 1.18a & b), then the free energy involved in creating a step is high compared with  $kT$ , thus the surface can never reach equilibrium roughness. If the units are only part of a stem (figure 1.18c) their energy of interaction may be comparable to  $kT$  thus enabling roughness to occur.

A growth face in contact with fluids will constantly have units attaching and detaching from it. The growth of a crystal occurs by the net accumulation of material. A low molecular material can add anywhere on to the surface. However, the addition of a long chain molecule onto the growth surface is restricted by its long chain nature. A polymer chain segments can attach itself in different ways to the crystal face, but not all of these configurations will favour further crystal growth: a stem which has folded over will be unable to lengthen by the addition of new units onto the fold surface and if the length of that stem is less than that required for thermodynamic stability then the fold must 'undo' in order to increase the stem length. The growth is also impeded if a chain forms stems at two well separated surface sites so that either of the stems cannot lengthen without the removal of the other. This creates a barrier to growth which is termed as 'configurational entropy barrier'. This theory is capable of explaining why some polymer crystals show no evidence of faceting. Burton et al<sup>31</sup> have shown that the equilibrium structure of the surface could be either molecularly smooth or rough. There should be a transition between two structures. At higher temperatures crystal surfaces are rough. Changes in surface roughness affect the lamellar habit. For example polyethylene shows a range of lamellar habits depending on the crystallisation temperature.

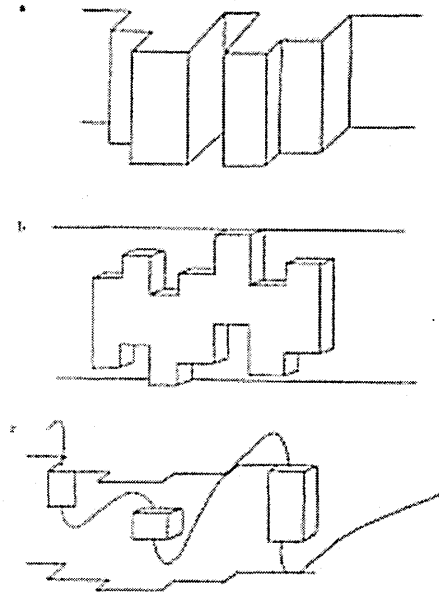


*Fig 1.18: Various types of roughness which may occur on the growth face of a lamellae (a) all growth units are complete stems which are of the same length (b) stems of differing length (c) growth units are only parts of complete stems<sup>30</sup>.*

For crystallisation below  $70^{\circ}$  -  $75^{\circ}$  C, the characteristic crystals have four  $\{110\}$  facets. As the temperature of crystallisation is raised near  $110^{\circ}$  C, the roughness become sufficient for there to be no free energy penalty for arbitrary crystal shapes. Above this temperature, the apices in the direction of ' $a$ ' (see figure 1.10) become truncated by  $(100)$  facets of increasing length until the crystal obtains a 'leaf' shape with no more  $\{110\}$  faces. These changes are attributed to the increase in roughness with temperature on the  $\{110\}$  faces.

At present, rough growth models appear to predict experimental observations better. However, debate is still in progress, and various modifications to both theories have been suggested.

### 1.1.3.2 Melting

This is the exact reverse of crystallisation. There are several characteristics associated with melting behaviour of polymers;

- ◆ Melting takes place over a temperature range
- ◆ Melting behaviour is dependent on the rate of heating
- ◆ Specimen history and the crystallisation temperature have a strong impact on melting behaviour

The disappearance of the crystalline phase at the melting point is associated with various changes in physical properties: The polymer becomes a (viscous) liquid and there is a discontinuous change in density, refractive index, heat capacity, transparency and other properties. Measurement of any of these changes can be used to detect the crystalline melting point.  $T_m$ .  $T_m$  is always higher than the crystallisation temperature,  $T_c$ .

There are several factors which affect  $T_m$ : molar mass and degree of branching, stiffness of the main polymer chain, presence of polar groups, type and size of side groups can increase or decrease  $T_m$ .

#### 1.1.4 Structure and physical properties

The structure of a polymer is generally responsible for determining its properties. The unique properties of polymers such as elasticity and abrasion resistance of rubbers, strength and toughness of fibres, flexibility and clarity of films are attributed to their long-chain nature. In the study of structure-property relationship it is convenient to classify the properties as those involving large and small deformations. Large deformations include tensile strength and phenomena observed in melt. The properties involving small deformations include electrical and optical behaviour, mechanical properties such as stiffness and yield point.

##### 1.1.4.1 Properties involving large deformations

###### 1.1.4.1.1 Melt properties

Melt viscosity - The viscosity of a polymer melt is strongly dependent on weight-average molecular weight. Melt viscosity is also influenced by chain branching. It was

found in polyethylene and in silicone polymers melt viscosity decreases with increasing degree of long chain branching. Crosslinking also has a pronounced effect on melt viscosity. The addition of a low-molecular-weight species reduces melt viscosity by lowering average molecular weight. Bulky side groups, too, reduce the melt viscosity.

#### 1.1.4.1.2 Tensile strength and related properties

Tensile strength varies significantly with molecular weight in the range of interest for polymers. Morphology is very important in determining the mechanical properties of crystalline polymers. Both tensile strength and the mechanism of failure are influenced by spherulite size and structure. Crystals with smaller, finer-textured spherulites tend to fail at higher elongations after drawing whereas large, coarse spherulites often fail by brittle fracture between spherulites at low elongations.

#### 1.1.4.2 Properties involving small deformations

The properties which fall into this category are mechanical properties such as stiffness, yield stress, elongation etc., solubility and related phenomena, optical properties such as refractive index and transparency and electrical properties such as dielectric constant, dielectric length etc.

##### 1.1.4.2.1 Effect of crystallinity

- ♦ Mechanical properties – the degree of crystallinity determines the stiffness and yield point for most crystalline plastics. As the crystallinity decreases both stiffness and yield stress decrease.
- ♦ Solubility and related properties – Crystallinity decreases the solubility of polymers. The solubility of liquids and gases in polymers is also strongly dependent on crystallinity. Permeability is also a function of crystallinity.
- ♦ Electrical and optical properties – Crystallinity affects the dielectric constant and the refractive index of a polymer. This is due to the changes in density between the crystalline and amorphous regions. This difference leads to scattering of visible

light. Thus crystalline plastics are usually translucent or opaque except in thin films. Their transparency increases with decreasing spherulite size.

#### 1.1.4.2.2 Effect of molecular weight

Solubility – When there is no crystalline phase, molecular weight becomes the determining factor of solubility and related properties. They are inversely related to the molecular weight.

However, some properties are a function of combined effect of crystallinity and molecular weight. A number of mechanical properties such as hardness, softening temperature, elongation at tensile break etc. fall into this category. For example softening temperature of branched polyethylene increases with increasing molecular weight and increasing crystallinity.

#### 1.1.4.2.3 Effect of polar groups

- ◆ Solubility and related properties – Introduction of polar groups leads to strong polymer-polymer bonds thus reducing the solubility of the polymer. The permeability of polymers to gases and liquids also decreases with increasing polarity.
- ◆ Electrical properties – They are mainly dependent on the asymmetry of dipoles arising from the presence of polar groups. Polyethylene and polytetrafluoroethylene have a low dielectric constant. But polymers containing both hydrogen and fluorine or chlorine have a much larger dielectric constant.

### 1.2 Short chain n-alkanes

Hydrocarbon chains are a basic component in a number of systems as diverse as polymers, biological membranes, fuels and lipids. Most of the physical properties of these materials depend on the crystalline structure. A better understanding of these properties provides a better understanding of these more complex systems. Crystalline n-alkanes have been studied for many years as model systems to these complex systems.



Crystal structure, crystal growth and morphology, melting temperature, chain mobility and conformational structure of n-alkanes have been extensively studied.

Short chain n-alkanes crystallise as does polyethylene in the form of thin lozenges and show a diversity of crystal structures. Four distinct crystal structures - rotator, triclinic, monoclinic and orthorhombic - describe the solid phases of all odd n-paraffins with more than nine carbon atoms in the chain and all even n-paraffins above four carbons<sup>32</sup>. The latter two structures become equivalent at longer chain lengths. The stable form at low temperature involves an orthorhombic phase for odd paraffins between C<sub>9</sub> and C<sub>40</sub> while monoclinic and triclinic forms exist for even n-paraffins. The triclinic structure is most favourable for even paraffins below 26 Carbon atoms, whereas for molecules above 26 carbon atoms the monoclinic form with an orthorhombic subcell is the most favourable.

However, this odd-even difference only applies when there is a tilted phase involved. The structures are determined largely by the differences in end group packing. When the paraffin chains are packed vertically there is no difference of the packing of either end groups or chain groups between odd and even numbered chains. But when tilted only the even paraffins have the symmetry required for equivalent (apparently low energy) packing of both end groups. If an odd numbered chain is tilted, one end assumes an advantageous low energy position, but the other end is forced into a high energy position. Hence only the even paraffins can have tilted modifications of low energy. For the non tilted modifications (hexagonal and orthorhombic), both even and odd paraffins are equivalent and indistinguishable.

An orientationally disordered (plastic) crystalline state has been observed just below the melting point in the odd paraffins from C<sub>9</sub> to C<sub>43</sub> and in the even paraffins from C<sub>22</sub> to C<sub>44</sub><sup>32</sup>. Müller<sup>33</sup> first observed that the orthorhombic paraffins tend towards or reach hexagonal symmetry on approaching melting temperature. In this form the chains are arranged perpendicularly to the plane formed by the methyl end groups. He also proposed that the molecules in the hexagonal phase rotate as rigid rods around their long axes and hence the name 'rotator' phase was given for the disordered crystal form. This disordered phase has ever since been studied both experimentally and theoretically.

The work of Strobl et al on polymorphic transitions on  $C_{33}H_{68}$  resulted in some remarkable revelations<sup>34</sup>. Four crystal modifications were found including a monoclinic phase for the highest temperature modification<sup>35</sup>. Also it was found to contain a considerable proportion of non-planar molecules with one or two gauche bonds. Already in 1948 Mazee observed that the rotator phase in  $n-C_{21}H_{44}$  and  $n-C_{23}H_{48}$ <sup>35</sup> has an orthorhombic unit cell. Subsequent studies on  $C_{19}H_{40}$ <sup>36</sup> and the studies of Doucet et al on  $C_{17}H_{36}$ ,  $C_{19}H_{40}$ ,  $C_{21}H_{44}$ <sup>37</sup>, further support the polymorphic behaviour observed by Strobl<sup>35</sup>. Ungar further studied this polymorphic behaviour of crystalline odd-numbered alkanes from  $C_{11}H_{24}$  to  $C_{25}H_{52}$  and of binary mixtures<sup>38</sup>. He observed, with increasing temperature alkanes up to  $C_{21}H_{44}$  undergo one first-order transition into an orthorhombic phase.  $C_{23}H_{48}$  to  $C_{25}H_{52}$  undergo a further weak transition into a rhombohedral modification with a hexagonal subcell, 3-5 K below the melting point<sup>38</sup>.

Ungar and Masic have studied the order in the rotator phase with increasing temperature by monitoring the correlation splitting of the IR active  $CH_2$  rocking vibration and the Raman active  $CH_2$  bending mode in the infrared and Raman spectra of a  $C_{21}H_{44}/C_{23}H_{48}$  mixture<sup>39</sup>. Two rotator modifications appear: an orthorhombic phase at lower temperature and a rhombohedral (hexagonal) modification at higher temperature. Doubling of the strong methylene rocking and bending absorptions was previously observed for paraffins having the orthorhombic and monoclinic structures<sup>40</sup>. The  $CH_2$  rocking and bending modes of triclinic crystal forms are singlets<sup>40</sup>. The doubling of absorption bands was attributed to crystal field splitting. There are two non-equivalent molecules in the subcell of orthorhombic and monoclinic forms. In-phase and out-of-phase vibrations of these two molecules results in two different vibrational frequencies which are observed as a doublet splitting in the infrared spectrum. The subcell of triclinic form contains only one molecule hence only a singlet is observed for the  $CH_2$  bending and rocking modes. Earlier studies reported the disappearance of  $CH_2$  band splittings in the rotator phase of  $n$ -alkanes<sup>41,42</sup>. Recently, however weak band splitting has been detected in the disordered phase of some  $n$ -alkanes<sup>38,43,44</sup>. Ungar and Masic observed that the splitting of  $CH_2$  rocking and bending modes gradually disappears with increasing temperature. The observed decrease may arise due to two reasons: decreased molecular interaction due to lattice expansion and break-up of long-range orientational correlation (uncoupling of oscillators) with increasing temperature. The calculations on reduction of splitting due to lattice expansion and reduction in size of ordered domains show that the

disappearance of vibrational band splitting in this region is primarily caused by the latter phenomenon<sup>39</sup>. The observed splitting for the CH<sub>2</sub> rocking mode at the lowest temperature phase is 8.5 cm<sup>-1</sup>. It was calculated that the average correlated domain of this phase consists of 20-30 molecules while the size of domain decreases as hexagonal symmetry is approached.

In general, the stability of a particular phase is closely related to the packing of methyl end groups at the crystal surfaces. Infrared spectroscopy is sensitive to the different environments of the CH<sub>3</sub> end groups. Gorce et al used the infrared active methyl group vibration as a probe for chain end organisation and crystal structure<sup>45</sup>. They identified infrared bands at 1371 cm<sup>-1</sup> for (011) monoclinic, 1378 cm<sup>-1</sup> for (101) monoclinic, 1384/5 cm<sup>-1</sup> for orthorhombic II and 1377 cm<sup>-1</sup> for triclinic crystal forms with the help of parallel XRD measurements on these crystal phases of C<sub>44</sub>H<sub>90</sub><sup>45</sup>.

A band at around 890 cm<sup>-1</sup> ascribed to the methyl rocking mode also shows conformational sensitivity. Snyder reported low temperature measurements showing a single band near 893 cm<sup>-1</sup> for a triclinic, a doublet at 889 and 893 cm<sup>-1</sup> for a monoclinic and a doublet at 891 and 894 cm<sup>-1</sup> for an orthorhombic I structures respectively<sup>41</sup>.

The structure and phase behaviour of hydrocarbon chain systems are of interest in areas as diverse as the thermal processing of synthetic polymers and the biological activity of lipid bio-membranes. A high pressure solid-solid transition has been identified in polyethylene<sup>46</sup>. Model bio-membrane systems are known to undergo two<sup>48</sup> and possibly three phase transitions<sup>48</sup> in which the hydrocarbon chains play an important role. The crystalline n-alkanes also undergo solid-solid phase transitions as discussed above, which is one reason they are used as an attractive model systems for polymers.

These solid-solid transitions are accompanied by a change in the degree of chain disorder. Certain kinds of non-planar molecules exist in crystals of n-alkanes. It has been observed that there is a discontinuous jump in the concentration of such non-planar molecules at each solid-solid phase transition as temperature is increased. Infrared spectroscopy is sensitive to these conformational changes. Hence, the solid-solid phase transition of n-alkanes has thoroughly been studied using infrared spectroscopy. Snyder et al studied the phase transition in n-alkanes using the constant and variable frequency

bands of the infrared spectrum<sup>49</sup>. Constant frequency bands are associated with the localised conformational structure and variable-frequency bands with molecules that have a high degree of conformational order. Most constant-frequency bands that are observed in the high-temperature phases are associated with molecules having an end-*gauche* (*gt*) conformation. The other constant-frequency bands that can be observed at higher temperatures are attributed to double-*gauche* (*gg*) and *gtg* conformations. Variable frequency bands are associated with non-localised vibrations and involve the entire chain. These non-localised modes give rise to band progressions and are confined mainly to 700 – 1400  $\text{cm}^{-1}$  region of the infrared spectrum. Three series of band progressions arising from all-*trans* chains have been identified in this area. They are the methylene rocking-twisting ( $P_k$ ), wagging ( $W_k$ ) and C-C stretching progressions ( $R_k$ ). The subscript  $k$  is an integer which is used to denote the each mode in a progression. It is related to the relative phase difference between the motions of adjacent methylene groups along the chain<sup>50</sup>. The number, the frequencies and the intensities of the progression bands are dependent on both chain length and chain conformation. For the isolated all-*trans* conformer, only the  $k$ -odd members of the rocking progression are infrared active, and indeed only odd members appear in the low-temperature spectrum.

Maroncelli et al have studied solid-solid phase transitions of the odd n-alkanes  $\text{C}_{17}\text{H}_{36}$  through  $\text{C}_{29}\text{H}_{60}$  using differential scanning calorimetry and infrared spectroscopy<sup>51</sup>. They observed discontinuous changes in the infrared spectra that occur exactly at the DSC transition temperatures. The low temperature spectrum of phase I, shows three, well defined series of progression bands in the conformationally sensitive region between 1400 and 700  $\text{cm}^{-1}$  corresponding to a crystal structure having all-*trans* chains. It was observed that some of the bands, especially the rocking-mode bands are split into two. This doubling arises from the factor group splitting of modes in the orthorhombic unit cell. As the temperature increases, these bands become broader and their intensity greatly reduces. Factor group splitting is absent or much diminished in phase II. Most significantly, a new series of another progression becomes visible in between the previous progression bands. These are not attributable to vibrations of all-*trans* conformers. They were identified as even bands due to deviations from all-*trans* conformation. Thus, while the all-*trans* molecules are still a major component of phase II, non-planar molecules are clearly in evidence. In the liquid, all these odd and even bands due to nonlocalised rocking and wagging progressions tend to overlap to form a

continuous background. For this reason localised modes account for most of the bands observed in the liquid. These localised bands include new bands which are associated with CH<sub>2</sub> wagging modes localised at specific nonplanar conformational sequences. Three types of non-planar defects were identified in the higher temperature phases: *gt*, *gtg* and *gg*. The *gt* defect was observed in the lower temperature phases as well. *gtg* was observed only in the highest temperature phase while the *gg* conformation was observable only within a few degrees of the melting point. It was noticed that there is a discontinuous jump of the concentration of the defects at each phase transition.

Although short chain alkanes were studied as model compounds for polymers, the vast difference between chain lengths of short chain alkanes and those of polymers, prevents the maximum use of short chain alkanes in this aspect. Also some polymer properties and behaviour are associated with the long chain nature of the polymer. This gap in chain length between polymers and short alkanes was filled by recently synthesised long chain n-alkanes which are capable of crystallisation by chain folding. In this sense, alkanes can be regarded as 'polymers'. Ever since, these long chain n-alkanes have been the most attractive model compounds for semi-crystalline polymers.

## References

1. Billmeyer FW, 'Text Book of Polymer Science', 3<sup>rd</sup> ed., John Wiley & Sons, New York (1984)
2. Young RJ, Lovell PA, 'Introduction to Polymers', 2<sup>nd</sup> ed., Chapman and Hall, London (1996)
3. Spells SJ in 'Characterisation of Solid polymers', ed. Spells SJ, Chapman & Hall, London (1994)
4. Tasumi M, Krimm S, J. Polym. Sci., part A2, **6**, 995 (1968)
5. Spells SJ, Organ SJ, Keller A, Zerbi G, Polymer, **28**, 697 (1987)
6. Ungar G, Organ SJ, Polym. Commun., **28**, 232 (1987)
7. Tasumi M, Krimm S, J. Polym. Sci. part A2, **6**, 995 (1968)
8. Painter PC, Havens J, Hart WW, Koenig JL, J. Polym. Sci. Polym. Phys. Ed., **15**, 1237 (1977)
9. Chum SP, Knight GW, Ruiz JM, Philips PJ, Macromolecules, **27**, 656 (1994)
10. Wunderlich B, Macromolecular Physics, Vol. 1: Crystal structure, morphology, defects, Academic Press, New York (1973)
11. Keith HD, Padden FJ, Macromolecules, **24**, 7776 (1996)
12. Abo el Maaty MI, Bassett DC, Polymer, **42**, 4957 (2001)
13. Bassett DC, Hodge AM, Proc. R. Soc. London A, **25**, 377 (1981)
14. Balta Calleja FJ, Bassett DC, Keller A, Polymer, **4**, 269 (1963)
15. Bassett DC, Hodge AM, Proc. R. Soc. London, **A359**, 121 (1978)
16. Bassett DC, Hodge AM, Proc. R. Soc. London, **A377**, 25 (1981)
17. Bassett DC, Hodge AM, Holley RH, Proc. R. Soc. London, **A377**, 39 (1981)
18. Bassett DC, Hodge AM, Proc. R. Soc. London, **A359**, 61 (1981)
19. Voigt-Martin IG, J. Polym. Phys. **19**, 1769 (1981)
20. Varnell WD, Ryba E, Harrison JR, J. Macromol. Sci., Phys. B, **26**, 135 (1987)
21. Ungar G, Stejny J, Keller A, Bidd I, Whiting MC, Science, **229**, 386 (1985)
22. Smith AE, J. Chem. Phys., **21**, 2229 (1953)
23. Broadhurst MG, J. Res. Natl. Bur. Stand. Sect. A, **66**, 241 (1962)
24. Piesczek W, Strobl GR, Malzahn K, Acta Cryst., B, **30**, 1278 (1974)
25. Zerbi G, Magni R, Gussoni M, Holland-Moritz K, Bigotto A, Dirlikov S, J. Chem. Phys., **75**, 3175 (1981)
26. Takamizawa K, Ogawa Y, Oyama T, Polym. J., **14**, 441 (1982)
27. Bassett DC, Frank FC, Keller A, Phil. Mag. **8**, 1753 (1963)

28. De Silva DSM, Zeng XB, Ungar G, Spells SJ, *Macromolecules*, **35**, 7730 (2002)
29. Lauritzen JI Jr, Hoffman JD, *J. Res. Nat. Bur. Stds.*, **64A**, 73 (1960)
30. Sadler DM, Gilmer GH, *Polymer*, **25**, 1446 (1984)
31. Burton WK, Cabrera N, Frank FD, *Phil. Trans. Roy. Soc., London*, **243A**, 299 (1951)
32. Broadhurst MG, *J. Res. Natl. Bur. Stand.*, **66A**, 241 (1962)
33. Müller A, *Proc. Roy. Soc. (London) [A]*, **127**, 417 (1930)
34. Ewen B, Strobl GR, Richter D, *Faraday discuss. Chem. Soc.*, **69**, 19 (1980)
35. Mazee WM, *Recl. Trav. Chim. Pays-Bas*, **67**, 197 (1948)
36. Larsson K, *Nature (London)*, **13**, 383 (1967)
37. Doucet J, Denicolo I, Craievich A, *J. Chem. Phys.*, **75**, 1523 (1981)
38. Ungar G, *J. Phys. Chem.* **87**, 689 (1983)
39. Ungar G, Masic N, *J. Phys. Chem.*, **89**, 1036 (1985)
40. Snyder RG, *J. Mol. Spectroscopy*, **7**, 116 (1961)
41. Snyder RG, *J. Mol. Spectros.*, **4**, 411 (1960)
42. Kobayashi M, Kobayashi T, Itoh Y, Chatani Y, Tadokoro H, *J. Chem. Phys.*, **72**, 224 (1980)
43. Zerbi G, Magni M, Gussoni K, Moritz H, Bigotto A, Dirlikov S, *J. Chem. Phys.*, **75**, 3175 (1981)
44. Maroncelli M, Qi SP, Strauss HL, Snyder RG, *J. Am. Chem. Soc.*, **104**, 6237 (1982)
45. Gorce J-P, Spells SJ, Zeng XB, Ungar G, *J. Phys. Chem. B*, **108**, 3130 (2004)
46. Bassett DC, Turner B, *Nature (London) Phys. Sci.*, **240**, 146 (1972)
47. Nagle JF, *Annu. Rev. Phys. Chem.*, **31**, 157 (1980)
48. Chen SC, Sturtevant JM, Gaff BJ, *Proc. Natl. Acad. Sci., U.S.A.*, **77**, 5060 (1980)
49. Snyder RG, Maroncelli M, Qi SP, Strauss HL, *Science*, **214**, 188 (1981)
50. Snyder RG, Schachtschneider JH, *Spectrochim. Acta*, **19**, 85 (1963)
51. Maroncelli M, Song PQ, Strauss HL, Snyder RG, *J. Am. Chem. Soc.*, **104**, 6237 (1982)

## ***Chapter 2***

---

### **Long Chain n-Alkanes: Model Compounds for Polymer Semi-crystallinity**

#### **2.1 Introduction**

Polymerisation always produces polymer molecules of variable length. They have a distribution of molecular weight. These polymers are said to be polydisperse. In order to study the fundamentals of polymer behaviour we need monodisperse systems i.e. systems with uniform chain length. These monodisperse systems act as model compounds for polymers in terms of their crystalline structure and crystallisation kinetics.

These polymers can only be synthesised by a series of carefully controlled reactions, which involves end-group protection and deprotection and careful purification of intermediate products. Very long chain monodisperse alkanes have been successfully synthesised in this way<sup>1</sup>. The longest one so far is n- C<sub>390</sub>H<sub>782</sub>.

It has been recognised for many years that many polymer molecules possess the ability to crystallise. It is now universally accepted that polymers with reasonably flexible chains crystallise as thin lamellae with chain folding (see figure 2.1). The main interest of the synthesis of monodisperse n-alkanes was to study their crystallisation behaviour. Monodisperse long chain alkanes synthesised at the University of Durham, are providing ideal models for semicrystalline polymers. It has been found that these materials and their binary mixtures can make different crystal structures such as extended chain crystals, integer-folded chain crystals, non-integer form (NIF) and layer structures.



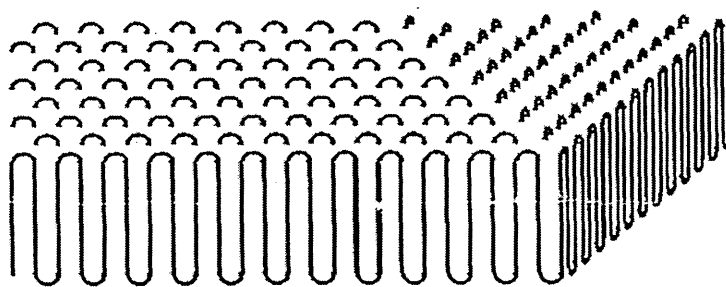


Fig 2.1: An idealised arrangement of a polymer molecule in a lamella. (Folding is not so regular in reality).

Chains larger than 150 C atoms were found to be capable of crystallising in chain folded forms. Depending on crystallisation temperature,  $n\text{-C}_{390}\text{H}_{782}$  can adopt any conformation from fully extended to folded in five.

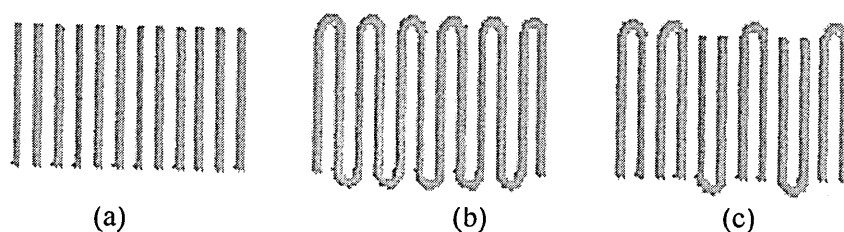


Fig 2.2: Different crystalline arrangements (a) extended form (b) folded form (c) once-folded form.

Long alkanes generally fold in such a way so as to leave the chain ends at the lamellar surface. This means that a chain makes an integer number of complete traverses through the crystal i.e. one: for extended form, two: for once-folded form etc. This “integer” folding enables the long alkanes to achieve a high degree of crystallinity. Polydisperse polymers are always incompletely crystalline (semicrystalline).

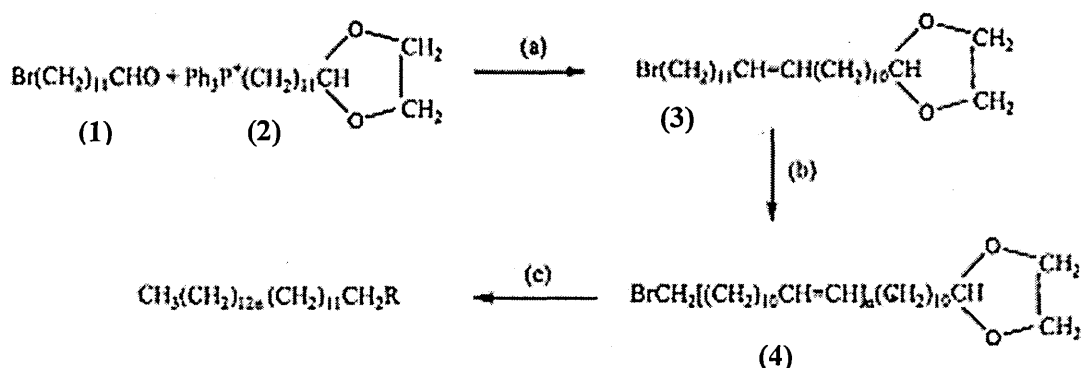
Long chain alkane derivatives such as branched, star-shaped long alkanes, carboxylic acids, as well as labelled compounds have also been synthesised recently. The crystallisation behaviour of these compounds has not been investigated so far and is of great interest, in terms of both crystallisation kinetics and the structures formed. Both of

these can help in the understanding of polymer behaviour, particularly in the context of polymer processing.

## 2.2 Synthesis

Two methods of synthesis of n-alkanes have been presented independently by Wegner<sup>2</sup> and Bidd et al<sup>1</sup>. Wegner used the C<sub>24</sub> diyne, HC≡C(CH<sub>2</sub>)<sub>20</sub>C≡CH which was oxidatively coupled with copper (II) acetate to give a mixture of oligomers, HC≡C(CH<sub>2</sub>)<sub>20</sub>C≡C[C≡C(CH<sub>2</sub>)<sub>20</sub>C≡C]<sub>n</sub>H (n = 1-16). It was carefully separated by chromatography. As the chain length increased the separation of higher homologues became more difficult. The main disadvantages of the Wegner's method are; chain lengths are limited to multiplets of C<sub>24</sub> and only hydrocarbons could be synthesised.

The basis of Bidd et al procedure for the synthesis of long chain alkanes is shown in figure 2.3.



(a) K<sub>2</sub>CO<sub>3</sub>, 18-crown-6, THF

(b) Hydrolysis (half material); Ph<sub>3</sub>P (half material); repetition

(c) Hydrolysis; RCH=PPh<sub>3</sub>; LiBHET<sub>3</sub>; hydrogenation

Fig 2.3: Chemical path used by Bidd et al in the synthesis of monodisperse alkanes<sup>1</sup>.

The starting material was 12-bromodecanal ethylene acetal which on deprotection gave the aldehyde (1) while reaction with triphenylphosphine gave the phosphonium bromide (2). The reaction of (1) and (2) and K<sub>2</sub>CO<sub>3</sub> in the presence of 18-crown-6 to generate the ylide *in situ* in tetrahydrofuran (THF) gave the chain doubled C<sub>24</sub> bromo acetal (3). Repetition of the above reaction sequence with (3) gave the second chain doubled

product,  $C_{48}$  bromoacetal, which in turn was converted into the  $C_{96}$  product, and then into the  $C_{192}$  bromoacetal; the  $C_{192}$  acetal was chain doubled to the  $C_{384}$  acetal. Deprotection of acetals (4) and capping the resulting aldehyde using a Wittig reagent of any desired length, followed by replacement of Br by H using lithium triethyl borohydride and finally hydrogenation of the polyalkene, gave the alkane with desired chain length.

In this way the following linear long chain monodisperse n-alkanes have been synthesised:  $C_{98}H_{198}$ ,  $C_{122}H_{246}$ ,  $C_{162}H_{326}$ ,  $C_{194}H_{390}$ ,  $C_{198}H_{398}$ ,  $C_{210}H_{422}$ ,  $C_{242}H_{486}$ ,  $C_{258}H_{518}$ ,  $C_{294}H_{590}$ ,  $C_{390}H_{782}$  and  $C_{434}H_{870}$ <sup>3</sup>. The self condensation reaction of one of the intermediate aldehydes has given two chain-branched hydrocarbons:  $C_{96}H_{193}CHRC_{94}H_{189}$  where  $R = CH_3$  and  $CH_3(CH_2)_3$ <sup>3</sup>. In the same way, two Y-shaped alkanes  $CH_3(CH_2)_{119}CHR(CH_2)_{117}CH_3$  [ $R = -(CH_2)_{194}CH_3$  and  $-(CH_2)_{60}CH_3$ ] have also been synthesised<sup>4</sup>. Brooke et al were also successful in synthesising two end-deuterated straight chain alkanes:  $C_{12}D_{25}-(CH_2)_{144}-CHDC_{11}H_{23}$  and  $C_{12}D_{25}-(CH_2)_{192}-CHDC_{11}H_{23}$  using the bromoacetals of newly synthesised long chain alkanes  $C_{144}$  and  $C_{192}$ <sup>4</sup>. In addition, three long-chain compounds containing carboxylic acid groups have been prepared<sup>3</sup>. They are  $CH_3(CH_2)_{190}CO_2H$ ,  $HO_2C(CH_2)_{48}CO_2H$  and  $HO_2C(CH_2)_{192}CO_2H$ .

### 2.3 Crystallisation of long chain alkanes

One of the most remarkable characteristics of flexible polymers is that they crystallise by chain folding<sup>5</sup>. However, the nature of folding and the exact length at which the folding occurs have been a central question in polymer science until the recent synthesis of normal alkanes with strictly uniform chain lengths. Ungar et al were successful in finding the answers for the above questions with the help of these monodisperse n-alkanes. They found that chain folding in all these alkanes occurs for  $C_{150}H_{302}$  and above<sup>6</sup>. As with polyethylenes obtained by conventional polymerisation, the fold length in the normal alkane varies with crystallisation temperature and it was found that these folds in n-alkanes are sharp and adjacently re-entrant<sup>6</sup>.

## 2.3.1 Crystalline Structures

Monodisperse *n*-alkanes are capable of forming a wide range of crystal structures including extended chains, folded chains, integer and non-integer forms and different layer structures. Each of these structures is described below.

## 2.3.1.1 Integer folded forms (IF)

Crystallisation experiments on long chain alkanes have been performed both from solution and from melt<sup>6</sup>. It has been shown that chain lengths below  $C_{150}$  can crystallise only in extended form while  $C_{150}H_{302}$  and other higher alkanes are capable of chain folding. The number of folds per chain is dependent on the chain length and the crystallisation temperature.  $C_{150}H_{302}$  can crystallise only in once folded form while the longest alkane  $C_{390}H_{782}$  can be obtained with up to four folds. The tendency towards chain folding increases with increasing chain length. Folded chain crystals of  $C_{150}H_{302}$  could be grown only at high supercoolings. Even then they were mixed with the extended chain form. In contrast, the longest *n*-alkane  $C_{390}H_{782}$  folded so readily, extra measures were needed to obtain the extended form. SAXS and Raman LAM (see Chapter 3.2.1) measurements have shown the lamellar periodicity of these crystalline structures is exactly an integer fraction of their chain length; hence the name given 'integer' folded forms.






Chain conform. Paraffin	E	F2	F3	F4	F5
					
$C_{102}$	+				
$C_{150}$	+	+			
$C_{198}$	+	+	+		
$C_{246}$	+	+	+	+	
$C_{294}$	+	+	+	+	
$C_{390}$	+	+	+	+	+

Fig 2.4: Integer folded forms observed in long *n*-alkanes  $C_{102}H_{206}$  through  $C_{390}H_{782}$ , F2-once folded, F3-twice folded etc<sup>7</sup>.

In solution-grown crystals this relationship between the lamellar periodicity and the chain length is strictly observed by both SAXS and Raman LAM measurements. However, for melt-crystallised alkanes, the lamellar periodicity from SAXS measurements has to be corrected for the  $35^\circ$  chain tilt in order to ascertain the above relationship. Different integer folded forms achieved by these alkanes are shown in figure 2.4. From these results, the strong preference for integer folding in mature crystals was indeed confirmed. The tendency in pure alkanes for integer folding indicates their preference to exclude the chain ends from the crystal interior. In this way any defects in the crystal interior are largely minimised.

#### 2.3.1.2 Non-integer folded forms (NIF)

Despite the fact that mature crystals have a strong preference for integer folding, real-time small angle X-ray scattering (SAXS) experiments on melt crystallisation have shown that initially the stacks do not have integer periodicities<sup>7</sup>. Initial melt-grown crystals usually have a fold length intermediate between those of the integer forms. This is called the non-integer form (NIF). This transient non-integer form (NIF) soon transforms into an integer form (figure 2.5).

Small angle X-ray studies (SAXS) on NIF showed some molecules crystallise fully and fold exactly into two within the crystalline layer, while others traverse the crystal layer only once leaving the two long ends (cilia) in the amorphous phase<sup>7</sup>. It is assumed that these cilia are generally too short to be incorporated into the crystal. The NIF  $\rightarrow$  F2 transformation involves post crystallisation of the cilia as they reach a length of  $l/2$  through chain translation. The NIF form is up to one-third amorphous. The transformation of NIF  $\rightarrow$  F2 occurs through a process called 'lamellar thinning'. This has been further investigated using real-time Raman longitudinal acoustic mode (LAM) spectroscopy and SAXS<sup>8</sup>. It was found that the overall long period,  $l$ , is gradually reduced.

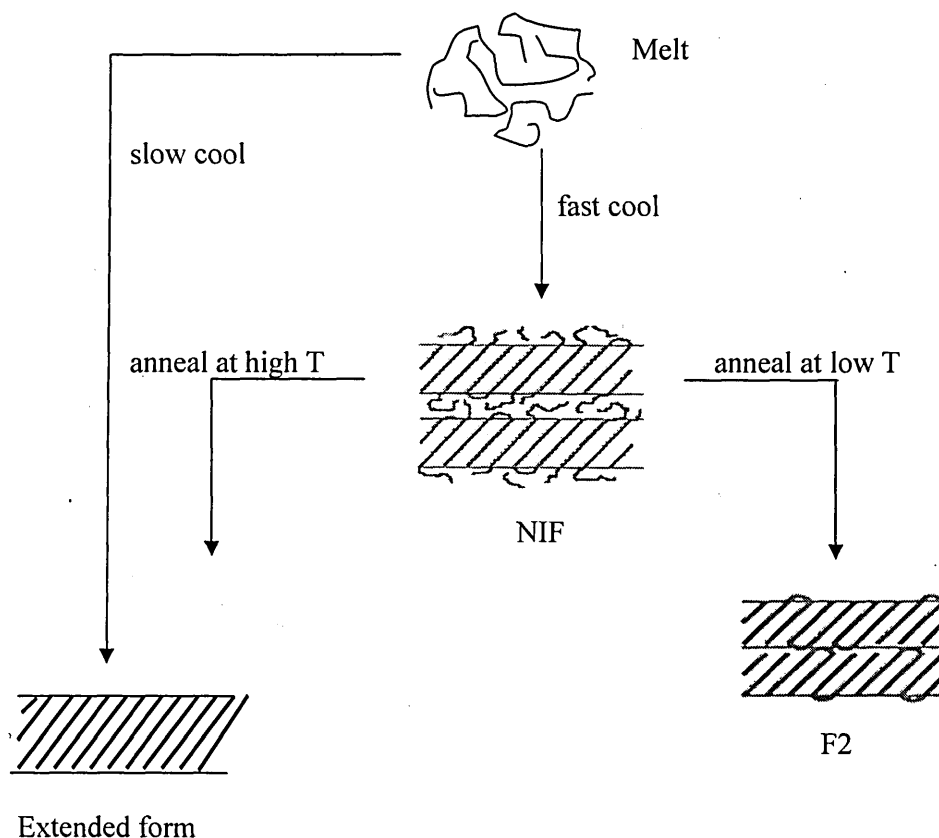


Fig 2.5: Formation of NIF form and its subsequent transformation into either extended or once folded form.

Electron density profiles reconstructed from successive small angle diffractograms\* indicate that subsequent reduction in lamellar spacing,  $l = l_c + l_a$ , proceeds through a reduction in the amorphous thickness  $l_a$ , with the crystalline thickness,  $l_c$ , remaining unchanged<sup>8</sup>. This implies that the NIF  $\rightarrow$  F2 transformation consists of the cilia gradually finding their way into the crystal. The Raman studies fully confirm the NIF structure and its subsequent transformation into F2. Also it proves the previous conclusion that the chains are tilted within the crystalline layers of the NIF.

\* This is done by the inverse Fourier transformation using discrete diffraction profiles. It needs several orders: at least four. Normally a large number of small-angle diffraction orders are observed for the highly periodic lamellar stacks of *n*-alkanes. Electron density profile is constructed by the Fourier transformation of the Lorenz-corrected intensities of successive small angle diffractograms<sup>10</sup>.

The studies using  $C_{246}H_{494}$  and a long alkane with a methyl branch in the centre of the chain ( $C_{96}H_{193}CH(CH_3)C_{94}H_{189}$ ) have shown that this transformation is rapid in the branched alkane while it is considerably slower in the linear alkane<sup>9</sup>. This is believed to be due to the initial preference for 'correct' chain attachment, with the branch at the lamellar surface, thus leaving the cilia of length  $l/2$  suitable for incorporation into the  $F_2$  crystals. It was found that the life time of NIF stage of  $C_{96}H_{193}CH(CH_3)C_{94}H_{189}$  is very short<sup>7</sup>.

However, recently, these authors have found that shorter alkanes  $C_{210}H_{422}$  and  $C_{198}H_{398}$  have a different mechanism of transforming the NIF compared with the longer ones<sup>8</sup>. It has been seen from synchrotron SAXS data and the Raman LAM spectrum that these shorter alkanes pass through the preliminary NIF stage, but turn into a new more complex layered structure instead of transforming into  $F_2$  (figure 2.6). This is a mixed-integer 'folded-extended' (FE) layer structure. In the  $NIF \rightarrow FE$  transformation, the cilia form a new crystalline layer of the same or similar thickness as the existing crystalline layers of the NIF. The new crystalline layer is 'shared' between the cilia emanating from the original crystal layers on either side.

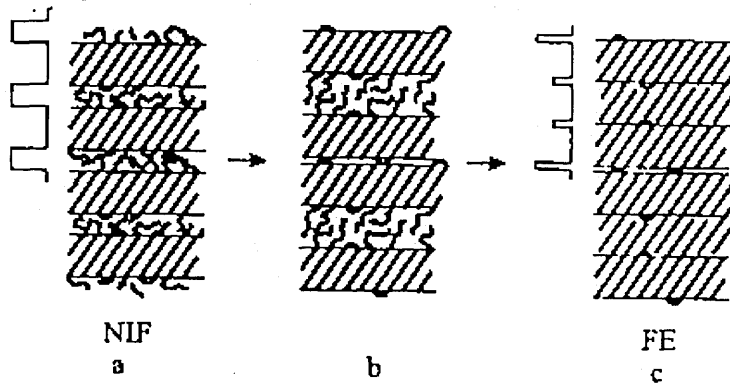


Fig 2.6: Schematic representation of transformation of the NIF form of  $C_{210}H_{422}$  and  $C_{198}H_{398}$ , a, to the FE form, c with their electron density profiles<sup>8</sup>.

This results in a triple layer crystalline superlattice in which once-folded and extended chains are mixed in the outer two sub layers, while the middle layer contains only interdigitated portions of unfolded chains (figure 2.6c). Similar behaviour of cooperative lamellar transformations and complex superlattice formation have recently been found in Y-shaped branched alkanes<sup>7</sup> and long chain alkane mixtures<sup>11</sup>.

The reason for the strong preference for the NIF to IF, at the initial stages of crystal growth is entirely kinetic. The NIF allows crystals to grow faster than the IF since not all chains are needed to attach 'correctly' in the crystal. However, if the lamella is to grow, nearly half the chains needed to be placed 'correctly' and crystallise fully with a fold in the middle in order to prevent overcrowding at the surface<sup>7</sup>.

### 2.3.1.3 Superlattice structures

The lamellar structure formed by melt crystallisation of binary mixtures of monodisperse long *n*-alkanes has been extensively studied using SAXS, thermal analysis (DSC) and Raman LAM spectroscopy by Zeng et al<sup>7,11</sup>. Two new types of layered structures have been found in binary mixtures of *n*-alkanes ranging from  $C_{122}H_{246}$  to  $C_{294}H_{590}$ . At high temperatures a semicrystalline form (SCF) is the stable phase, having a regular structure of alternating crystalline and amorphous layers. The shorter chains are fully crystalline and confined to the crystal layer. The longer molecules traverse the crystal layer and are only partially crystalline. The amorphous layer consists of the surplus length of the longer chains (figure 2.7a).

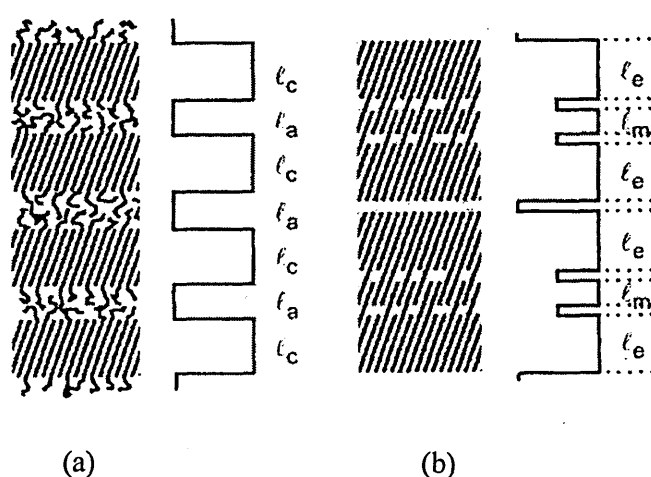


Fig 2.7: Schematic structures (a) of the high temperature semi crystalline phase and (b) of the lower temperature triple layer superlattice. Model electron density profiles are shown on the right<sup>7</sup>.

The thickness of the crystalline layer is defined by the extended chain length of the shorter alkane tilted at  $35^\circ$  to the layer normal. This structure is similar to the transient non-integer folded (NIF) form in pure long *n*-alkanes. At lower temperatures a reversible



transition occurs to a triple layer superlattice structure with a periodicity up to 50 nm (Fig. 2.7b). The superlattice structure was preliminarily proposed on the basis of SAXS data and is supported by the results from thermal analysis. Additional confirmation of this structure is provided by the Raman LAM region. The two outer layers,  $l_e$  contain extended chains of the shorter alkane as well as the major portion of the longer alkane. The middle layer,  $l_m$  contains only the surplus length of the longer molecules protruding from the two end layers. All three layers are crystalline, although there is evidence for poor crystallinity for the middle layer from WAXS and calorimetry. The SCF  $\rightarrow$  superlattice transition occurs through pairs of SCF layers acting in tandem. Stable SCF solid solutions have been found for long alkanes with length ratios up to 1.7:1 and a chain length difference up to 100 carbons although the large discrepancies in chain lengths are not tolerated by crystals of shorter alkanes<sup>12</sup>.

The above superlattice structures in binary long chain alkane mixtures have been confirmed using recently synthesised end deuterated alkanes<sup>13</sup>.  $C_{12}D_{25}C_{144}H_{288}CHDC_{11}D_{23}$  and  $C_{12}D_{25}C_{192}H_{384}CHDC_{11}D_{23}$  were used as the end deuterated alkanes.

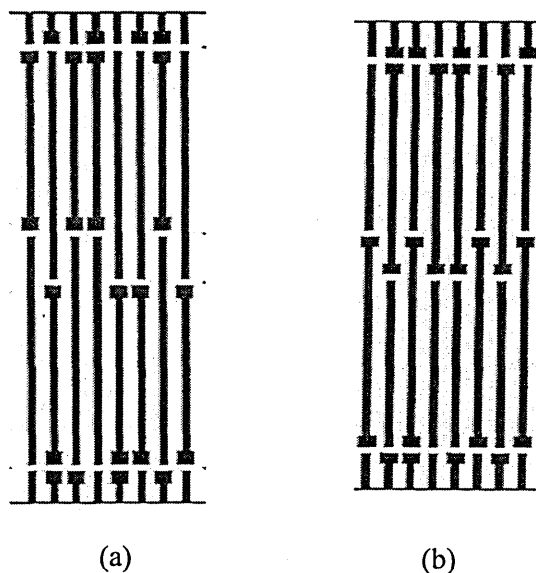


Fig 2.8: Schematic diagram of the triple-layer superlattice model for the binary mixtures  $C_{168}D + C_{242}H$  (a) and  $C_{162}H + C_{216}D$  (b)<sup>13</sup>.

Hereafter they will be referred as  $C_{168}D$  and  $C_{216}D$  respectively. Two 50:50 mixtures were prepared:  $C_{168}D + C_{242}H$  and  $C_{162}H + C_{216}D$ , where  $C_{242}H$  and  $C_{162}H$  stands

for alkanes  $C_{242}H_{486}$  and  $C_{162}H_{326}$ . Small angle neutron scattering (SANS) and small angle X-ray scattering (SAXS) studies were carried out on these samples. The resulting Fourier reconstruction profiles from SAXS and SANS proposed a similar triple layer superlattice structure to that of undeuterated binary mixtures. The proposed structures for the above two mixtures are shown in figure 2.8 (a) and (b).

However, the lamellar thicknesses obtained for these mixtures deviate slightly from the ideal model. This deviation aroused suspicion for a chain tilt in the middle layer which may occur to avoid material deficiency in the middle layer. Note that the molar fraction of the longer component in both these mixtures is less than 0.5. However, in the case of C168D + C242H mixture this would imply an increase of the tilt angle in the middle layer from  $35^{\circ}$  to  $48^{\circ}$ . Raman LAM experiments on the triple layer form of several non-deuterated binary mixtures showed that the chains in the middle layer are indeed straight and not folded<sup>11</sup>. The overall measured spacing of the second mixture, C162H + C216D, matches closely the ideal model but is 12 Å longer than that expected from the model with extra tilt in the middle layer. A similar situation has been obtained in the undeuterated mixture,  $C_{162}H_{326} + C_{210}H_{422}$ <sup>11</sup>. All the other binary long chain alkane mixtures with superlattice structure support the model with an extra chain tilt in the middle layer<sup>11,14</sup>. Further experiments are in progress regarding a possible effect of composition on chain tilt in the middle layer.

#### 2.3.1.4 Structures in branched alkanes

Studies on  $C_{96}H_{193}CH(CH_3)C_{94}H_{189}$  and  $C_{96}H_{193}CH(C_4H_9)C_{94}H_{189}$ , which contains a short branch in the centre of an otherwise linear chain, always produced the once folded conformation. The structure of asymmetrically methyl-branched alkane  $C_{191}H_{383}CH(CH_3)C_{99}H_{199}$ , synthesised recently, has been studied by-real time SAXS<sup>7</sup>. It crystallises in two different semicrystalline forms depending on the crystallisation temperature,  $T_c$ . As evidenced from electron density profiles, in each case the structure consists of alternating crystalline and amorphous layers with respective thicknesses,  $l_c$  and  $l_a$ . In the first form, which is obtainable only at high  $T_c$ , the longer arm of the alkane crystallises as an extended chain, while the shorter arm remains as a cilium, contributing to the amorphous layer (Fig. 2.9b). At low  $T_c$ , another semicrystalline structure is formed with the short arm of the alkane deciding the crystalline layer thickness. Here, the

extended shorter arm and a part of the longer arm contribute to the crystalline layer while the rest of the longer arm forms the amorphous layer (Fig. 2.9d). When cooled further, the first semicrystalline form transforms into a double-layer superlattice structure (Fig. 2.9c) and the latter forms a triple-layer crystalline structure (Fig. 2.9e).

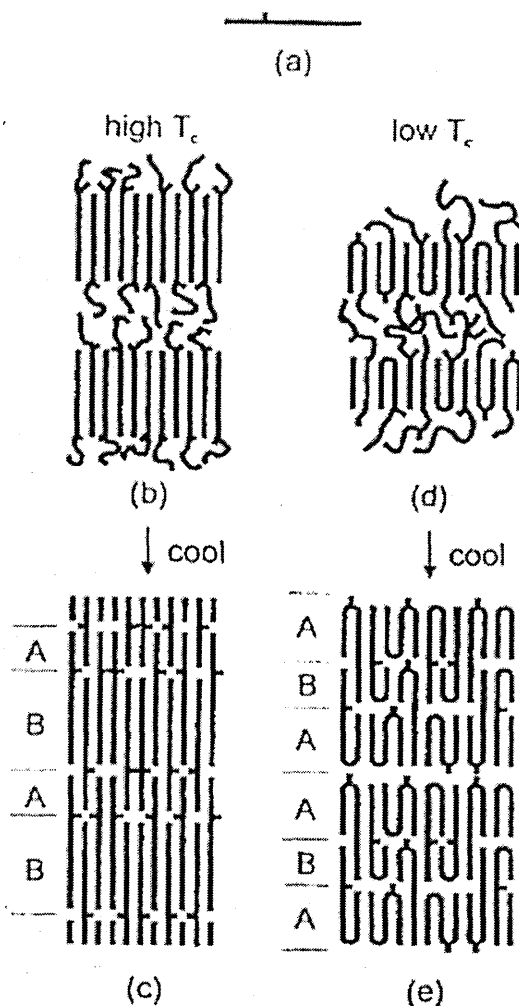


Fig. 2.9: Schematic drawing of different lamellar structures observed in asymmetric methyl-branched alkane  $C_{191}H_{383}CH(CH_3)C_{99}H_{199}$ <sup>7</sup>.

Another type of branched chain alkane, possessing a 'Y' shaped structure has been investigated for the crystalline structure (Fig. 2.10a). A semicrystalline form was found again for the 'Y' shaped alkane,  $C_{120}H_{241}CH(C_{61}H_{123})C_{119}H_{239}$  at high  $T_c$ . The crystalline layer is formed by the longer arms and the shorter arm remains as a cilium in the amorphous layer. However, some molecules have both their long arms crystallised, while

others have only one long arm crystallised and the other two remaining in the amorphous layer (Fig. 2.10b). This will subsequently transform into a double layer superlattice structure on further cooling. Here, one layer consists only of the long arms of the molecules and the other layer consists of both the extended short arms and folded long arms (see fig. 2.10c).

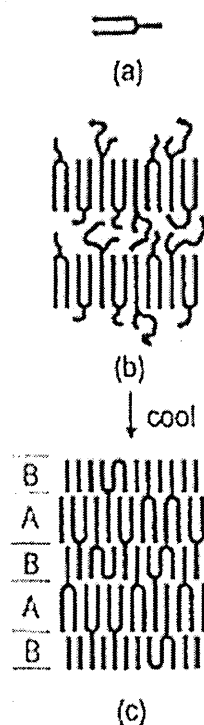


Fig. 2.10: Schematic drawing of different lamellar structures observed in Y-shaped alkane  $C_{120}H_{241}CH(C_6H_{123})C_{119}H_{239}$ <sup>7</sup>.

A study by Ikedou et al on crystal structures of branched alkanes makes an interesting comparison to the above results<sup>15</sup>. The crystal structure of four branched chain alkanes having 35 carbon in the main chain to which a methyl ( $CH_3$ ), butyl ( $C_4H_9$ ), hexyl ( $C_6H_{13}$ ) and butyl phenyl groups were attached at the middle have been studied by DSC, IR and Raman spectroscopy, X-ray diffraction and computer simulation. They have found the branches too, aligned inside the crystal in the extended form along with the main chain extended crystals. This totally contradicts to the structures suggested by Ungar et al where the branch is always excluded to the lamellar surface.

### 2.3.2 Crystallisation rate minima and ‘self-poisoning’

Crystallisation rate experiments on model alkanes have shown a rather different picture. This was observed for the first time in a rate experiment on uniform alkanes  $C_{246}H_{494}$  and  $C_{198}H_{398}$  using DSC and in situ X-ray diffraction<sup>16</sup>. It showed that the growth rate passes through a minimum with increasing supercooling. This was found to occur both in crystallisation from melt<sup>16</sup> and from solution<sup>17</sup> and it applies to both primary nucleation and growth. This is shown in figure 2.11.

A decrease in crystallisation rate at significantly larger supercoolings, arising from decreased mobility is quite common in polymers but is irrelevant in this case as this was observed at supercoolings which were well above temperatures where the transport term dominates. A discontinuity in the growth rate had been observed previously in studies on polyethyleneoxides<sup>18</sup> and polyethylene<sup>19</sup>. These discontinuities correspond to changes from extended to once-folded, from once folded to twice-folded etc. crystallisation. Nevertheless, there the growth rate still increases throughout all the supercoolings.

The anomalous behaviour in growth rate observed in monodisperse alkanes was attributed to an effect termed ‘self-poisoning’. This supports the roughness-pinning crystallisation theory of Sadler<sup>20</sup>. According to the Sadler’s theory, the chains that are wrongly attached to the crystal surface may hinder further growth. This blocking may be not very significant in polymers, but it becomes very pronounced in monodisperse alkanes. At higher  $T_c$ , only the extended chain depositions are stable. Close to the melting temperature of folded chains the life time of folded chain depositions becomes significant. As extended chains cannot grow on a folded chain substrate, growth is temporarily blocked until the folded-chain overgrowth detaches. At  $T_m^F$  itself the detachment rate of folded chains drops to the level of the attachment rate and the entire surface is blocked for extended chains. The growth rate minima observed in *n*-alkanes cannot be explained by the secondary nucleation theory in its present form as the competing attachments to the growth face are ignored. The ‘self-poisoning’ mechanism is supported by rate equation treatment based on a simple ‘fine grain’ model and Monte Carlo simulation<sup>21</sup>.

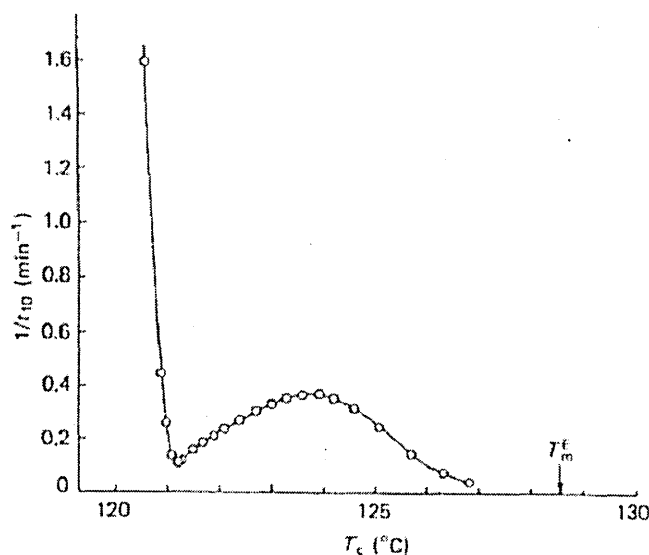


Fig 2.11: Relationship between the rate of crystallisation and the  $T_c$  <sup>15</sup>.

#### 2.4 Other monodisperse oligomers

The on-going studies on hydroxy butyrate oligomers (HB), short chain analogues of polyhydroxy butyrate (PHB), provide an interesting comparison to those of long chain *n*-alkanes. PHB is used as an energy storage medium by many bacteria<sup>22,23</sup>. Furthermore, HB oligomers occur naturally in cell walls. It is believed that HB is involved in ion transport across the lipid membrane<sup>24</sup>. Monodisperse HB oligomers containing 24 and 32 repeat units have been synthesised<sup>25</sup> and their crystallisation behaviour and the crystal morphology have been in interest. A range of morphologies has been observed also in HB oligomers<sup>25</sup>. They have shown extended and once folded crystals, in common with *n*-alkanes. In addition, a stable NIF form too, has been observed in HB. This is somewhat surprising. Although NIF state is common in *n*-alkanes it is a transient form and ultimately transforms into an integer folded form (see section 2.3.1.2). The length of this HB NIF form is 2/3 of the of the extended chain length. A structure in which some of the chain ends folds into the crystalline core has been proposed for this NIF form<sup>25</sup>. Cheng et al have reported a more stable NIF form than the IF form in polyethyleneoxide (PEO)<sup>26</sup>. They too, have proposed a similar structure to that of HB NIF form for this state. HB oligomers also show a similar growth rate to that of *n*-alkanes. A discontinuity in rate

has been observed where crystallisation changes from folded to extended chains<sup>27</sup>. However, this is much less pronounced here than in n-alkanes.

Another interesting area of research is, on-going studies on monodisperse nylon oligomers. Pure monodisperse nylon 6<sup>28</sup> and nylon 6,6<sup>29</sup> oligomers have been successfully synthesised with sufficient length to form chain folded crystals. The most notable difference between alkanes and nylons is alkane chains are flexible whereas nylons are rigid due to H bonding. Once folded crystals of nylon 6 nonamer and decamer<sup>30,31</sup> and twice folded crystals of nylon 6 17-mer<sup>32</sup> have been obtained. Nylon 6 oligomers were found to be capable of forming alkane or amide folds. The folds are in the plane of the sheets. In 12-amide and 16-amide nylon 6,6 only once folded crystals have been obtained<sup>33</sup>. Temperature induced structural changes in crystals of monodisperse nylon 6 and nylon 6,6 such as unfolding, intersheet shear, and orthorhombic-pseudo-hexagonal transition etc. have also been studied<sup>33</sup>. In Nylons the stability of all these structural forms depends on their ability to form Hydrogen bonds between planar zig-zag chains whereas in n-alkanes the chains can move freely.

## 2.5 Aims and objectives

Synthesis of monodisperse long chain alkanes paved the way for a new area of research. They were successful in bridging the gap between short chain alkanes and polymers and serve as ideal models for polymers in terms of structure, crystallisation behaviour and refolding. Many aspects of structure and crystallisation can usefully be studied without the 'smearing' effects inherent with a distribution of chain lengths. A diversity of crystal structures have been identified for these materials. These structures show a wide variation in the proportion of disordered material, as indeed do polymers themselves. Previous research work made substantial progress in developing a FTIR technique to study the extent of disorder in n-alkanes<sup>34</sup>. In that study the disorder was studied mainly using the CH<sub>2</sub> wagging region of the infra-red spectrum. This was followed by SAXS and infrared work on end-deuterated alkanes<sup>35</sup> and both these areas are further investigated here. In the case of deuterium-labelled molecules, the extent of disorder in the chain end regions was characterised using CD<sub>2</sub> bending mode since mode coupling prohibits using CD<sub>2</sub> wagging modes<sup>36</sup>.

This project aims to investigate the extent of disorder, as well as isotopic regularity in 3-arm star alkanes as models for branched polymers. X-ray diffraction work at the University of Sheffield has proved that these alkanes also show polymorphism<sup>7</sup>. The proportion and type of disorder involved is therefore likely to be variable. This will be studied using infrared and Raman spectroscopy. Where necessary small angle X-ray scattering (SAXS) and inelastic neutron scattering (INS) will also be used for characterisation. All the monodisperse long chain alkanes studied in this work were synthesised at the University of Durham and were kindly provided by the University of Sheffield. In addition, short chain alkanes and mixtures of short alkanes will be used mainly for feasibility studies or for calibration purposes.



## References

1. Bidd I, Holdup DW and Whiting MC, *J.Chem. Soc., Perkin Trans.*, **1**, 2455 (1985)
2. Lee KS, Wegner G, *Makromol. Chem., Rapid Commun.*, **6**, 203 (1985)
3. Brooke GM, Burnett S, Mohammed S, Proctor D, Whiting MC, *J. Chem. Soc., Perkin Trans.*, **1**, 1635 (1996)
4. Brooke GM, Farren C, Harden A, Whiting MC, *Polymer*, **42**, 2777 (2001)
5. Keller A, *Rep. Progress Phys.* **31**, 623 (1968)
6. Ungar G, Stejny J, Keller A, Bidd I and Whiting MC, **229**,386 (1985)
7. Ungar G, Zeng XB, *Chem. Rev.*, **101**, 4157 (2001)
8. Ungar G, Zeng XB, Spells SJ, *Polymer*, **41**, 8775 (2000)
9. Ungar G, Zeng XB, Brooke GM, Mohammed S, *Macromol.*, **31**, 1875, (1998)
10. Zeng XB, Ungar G, *Polymer*, **39**, 4523 (1998)
11. Zeng XB, Ungar G, *Polymer*, **43**, 1657 (2002)
12. Dorset DL, *Macromolecules*, **18**, 2158 (1985); **19**, 2965 (1986); **20**, 2782 (1987); **23**, 623 (1990)
13. Zeng XB, Ungar G, *Macromolecules*, **36**, 4686 (2003).
14. Zeng XB, Ungar G, *J. Macromol. Sci., Phys.*, **B41**, 1305 (2002)
15. Ikedou K, Yamamoto H, Nagashima H, Nemoto N, Tashiro K, *J. Phys. Chem. B*, **109**, 10668 (2005)
16. Ungar G, Keller A, *Polymer*, **28**, 1899 (1987)
17. Organ SJ, Ungar G, Keller A, *Macromolecules*, **22**, 1995 (1989)
18. Buckley CP, Kovacs AJ, 'Structure of crystalline Polymers', Ed. I. H. Hall, Elsevier-Applied Science, London, p. 261 (1984)
19. Leung WM, Manley RJ, Panaras AR, *Macromolecules*, **18**, 760 (1985)
20. Sadler DM, Gilmer GH, *Polymer*, **25**, 1446 (1984)
21. Higgs PG, Ungar G, *J. Chem. Phys.*, **114**, 6958 (2001)
22. Lemoigne M, *Ann. Inst. Pasteur.* **39**, 144 (1925)
23. Merrick J, *J. Photosynth. Bact.*, **199**, 219 (1978)
24. Reusch RN, Huang R, Bramble LL, *Biophys J*, **69**, 754 (1995)
25. Li J, Organ SJ, Hobbs JK, Terry AE, Baraham, Seebach D, *Polymer*, **45**, 8913 (2004)
26. Cheng SZD, Zhang A, Chen J, Heberer DP, *J. Poly. Sci., Polym. Phys. Ed.* **29**, 287 (1991)
27. Organ SJ, Li J, Terry AE, Hobbs JK, Barham PJ, *Polymer*, **45**, 8925 (2004)

28. Brooke GM, Mohammed S, Whiting MC, J. Chem. Soc., Perkin Trans., **1**, 22, 3371 (1997)
29. Brooke GM, Mohammed S, Whiting MC, Polymer, **49**, 773 (1999)
30. Atkins EDT, Hill MJ, Jones NA, Sikorski P, J. Mater. Sci., **35**, 5179 (2000)
31. Jones NA, Sikorski P, Atkins EDT, Hill MJ, Macromolecules, **3**, 4146 (2000)
32. Cooper SJ, Atkins EDT, Hill MJ, Macromolecules, **31**, 5032 (1998)
33. Cooper SJ, Atkins EDT, Hill MJ, Macromolecules, **31**, 1, 8947 (1998)
34. Gorce J-P, PhD Thesis, Sheffield Hallam University, June (2000)
35. De Silva DSM, PhD Thesis, University of Sheffield, February (2002)
36. Hirata S, Iwata S, J. Chem. Phys., **108**, 7901 (1998)

## Chapter 3

---

### Techniques

#### 3.1 Infrared techniques

##### 3.1.1 Infrared spectroscopy

##### 3.1.1.1 Principles

The vibrational energy of atoms in a molecule is quantised. Absorption of electromagnetic radiation in the infrared region ( $400 - 4000 \text{ cm}^{-1}$ ) gives rise to transitions between different vibrational states. Absorption results from coupling of a vibration with the oscillating electric field of the infrared radiation. This interaction can only occur when the vibration produces an oscillating dipole moment.

The vibrating atoms are linked together by chemical bonds. Therefore vibrations are usually referred to as bond deformations. In a simple diatomic molecule the only vibration which can occur is a periodic extension and compression. The compression and extension of a bond may be likened to the behaviour of a spring. Therefore we assume the bond, like a spring, obeys Hooke's law given by

$$f = -k (r - r_{eq}) \dots\dots\dots (3.1)$$

where  $f$  = restoring force  
 $k$  = force constant  
 $r$  = inter nuclear distance  
 $r_{eq}$  = equilibrium distance

In this case the energy curve is parabolic and has the form

$$E = \frac{1}{2} k (r - r_{eq})^2 \dots\dots\dots (3.2)$$

This model of a vibrating diatomic molecule is called the simple harmonic oscillator model. An elastic bond, like a spring, has a certain vibration frequency dependent

upon the mass of the system and the force constant, but independent of the amount of distortion. The oscillation frequency,  $\nu$ , is given by

$$\nu = \frac{1}{2\pi} \sqrt{\frac{k}{\mu}} \quad \dots\dots\dots(3.3)$$

where  $\mu$  is the reduced mass.

The vibrational energies for any particular system can be calculated from the Schrödinger equation. For the simple harmonic oscillator these turn out to be:

$$E_v = (v + \frac{1}{2}) h\nu \quad (v = 0, 1, 2, \dots) \quad \dots\dots\dots(3.4)$$

Where  $v$  is the vibrational quantum number and  $h$  is the Plank constant.

Converting equation (3.4) to the spectroscopic units,  $\text{cm}^{-1}$ ,

$$\epsilon_v = E_v/hc = (v + \frac{1}{2}) \bar{\nu} \quad \dots\dots\dots(3.5)$$

are the only energies allowed to a simple harmonic vibrator. Further use of the Schrödinger equation leads to the selection rule for the harmonic oscillator undergoing vibrational changes:

$$\Delta v = \pm 1$$

Since the vibrational levels are equally spaced, transitions between any two neighbouring states will give rise to the same energy change. But real molecules do not obey exactly the laws of simple harmonic motion. Real bonds, although elastic, are not so homogeneous as to obey Hooke's law. The Schrödinger equation for the anharmonic oscillator is:

$$\epsilon_v = (v + \frac{1}{2}) \bar{\nu}_e - (v + \frac{1}{2})^2 \bar{\nu}_e x_e \quad \dots\dots\dots(3.6)$$

where  $x_e$  is the corresponding anharmonicity constant.

For bond stretching vibrations  $x_e$  is always small and positive ( $\sim +0.01$ ), so that vibrational levels crowd more closely together with increasing  $v$ .  $\nu_e$  is the equilibrium oscillation frequency of the anharmonic system - the frequency for infinitely small vibrations about the equilibrium point.

The selection rules for the anharmonic oscillator are found to be:

$$\Delta v = \pm 1, \pm 2, \pm 3, \pm 4$$

It has been observed, in practice, that normally only the lines of  $\Delta v = \pm 1, \pm 2$  and  $\pm 3$ , at the most, have observable intensity.

Using equation (3.6);

for  $v = 0 \longrightarrow v = 1$ :  $\Delta v = +1$ , with considerable intensity.

$$\begin{aligned}\Delta E &= E_{v=1} - E_{v=0} \\ &= \bar{\nu}_e(1 - 2x_e)\end{aligned}$$

for  $v = 0 \longrightarrow v = 2$ :  $\Delta v = +2$ , with small intensity.

$$\begin{aligned}\Delta E &= E_{v=2} - E_{v=0} \\ &= 2\bar{\nu}_e(1 - 3x_e)\end{aligned}$$

for  $v = 0 \longrightarrow v = 3$ :  $\Delta v = +3$ , with normally negligible intensity.

$$\begin{aligned}\Delta E &= E_{v=3} - E_{v=0} \\ &= 3\bar{\nu}_e(1 - 4x_e)\end{aligned}$$

Since  $x_e \sim 0.01$ , the three spectral lines lie very close to  $\bar{\nu}_e$ ,  $2\bar{\nu}_e$  and  $3\bar{\nu}_e$ . The line near  $\bar{\nu}_e$  is called the 'fundamental absorption', while those near  $2\bar{\nu}_e$  and  $3\bar{\nu}_e$  are called the first and second overtones, respectively.

The simplest types of vibrations are stretching and bending. For a particular infrared active bond deformation, absorption will occur when

$$\nu = \Delta E/h \quad \dots\dots\dots (3.7)$$

where  $\nu$  = frequency of the radiation

$\Delta E$  = energy difference between the upper and lower vibrational energy levels for the particular bond deformation

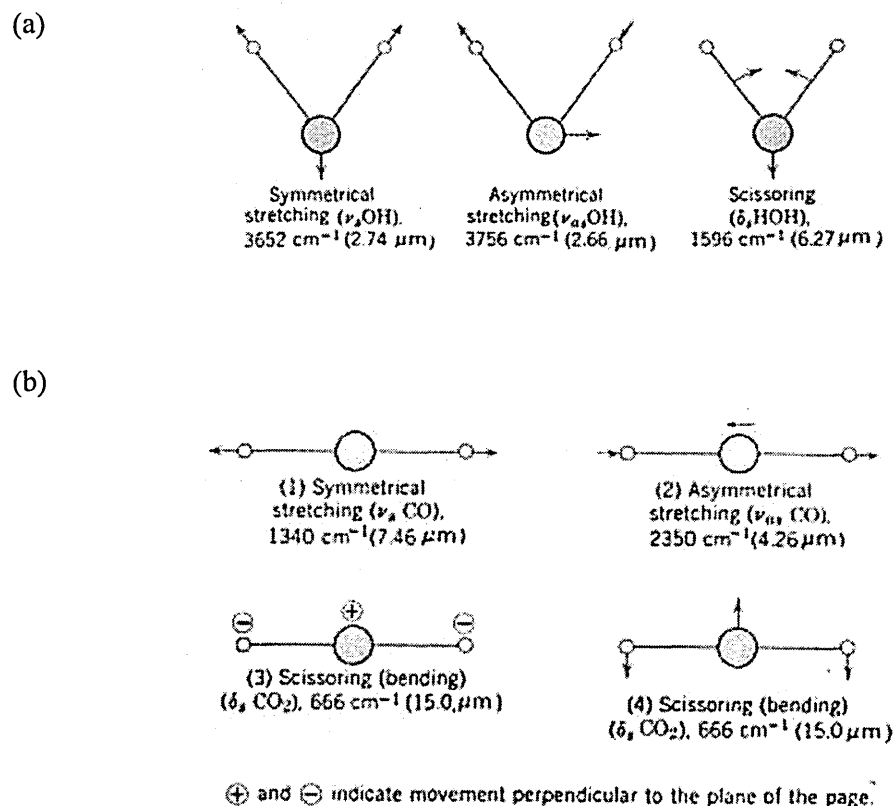
$h$  = Planck's constant.

By measuring the absorption of infrared radiation over a range of  $\nu$ , a spectrum is obtained which contains a series of absorptions at different  $\nu$ . Each absorption corresponds to a specific type of deformation of a particular bond and is characteristic of that bond deformation. The spectra are recorded as 'absorbance',  $A$ , against the

wavenumber,  $\bar{\nu}$  ( $\bar{\nu} = \nu/c = 1/\lambda$ ), where  $A = \log(I_0/I)$  in which  $I_0$  and  $I$  are the intensity of the incident radiation and the intensity of the transmitted radiation respectively.

A molecule has as many degrees of freedom as the total degrees of its individual atoms. Each atom has three degrees of freedom. Therefore a molecule of  $N$  atoms has  $3N$  degrees of freedom. For a non-linear molecule three degrees of freedom describe rotation and three describe translation; the remaining  $3N-6$  degrees of freedom are vibrational degrees of freedom. Linear molecules have  $3N-5$  vibrational degrees of freedom since only two degrees of freedom are required to describe rotation.

There are two main types of molecular vibration: stretching and bending. Bending vibrations include twisting, rocking, scissoring and wagging modes, while the stretching vibrations involve symmetric and antisymmetric stretching. The vibrational modes of some molecules are shown in figure 3.1 below.



(c)

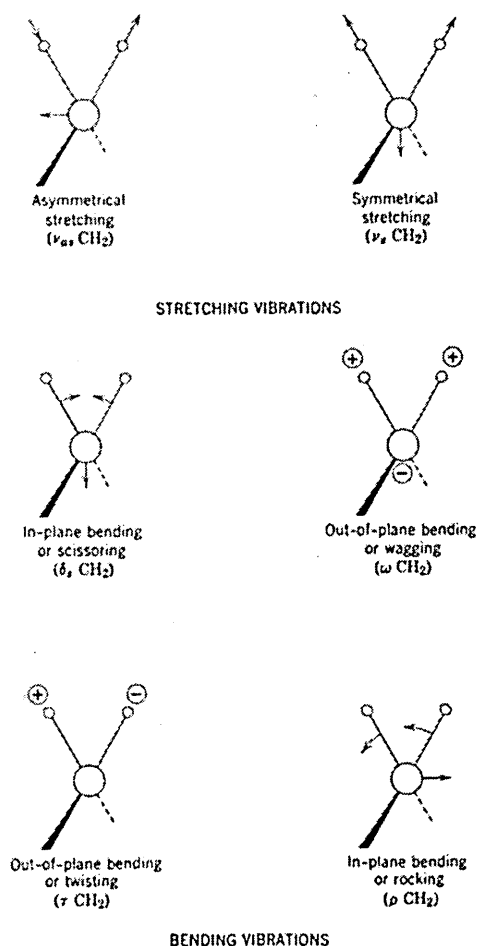


Fig 3.1: Vibrational modes for (a)  $\text{H}_2\text{O}$  molecule (b)  $\text{CO}_2$  molecule (c)  $-\text{CH}_2-$  group.

### 3.1.1.2 Instrumentation

There are two general types of instrument for recording IR spectra, namely Dispersive and Fourier transform (FTIR) spectrometers.

#### 3.1.1.2.1 Dispersive spectrometers

Historically, spectrometers were first equipped with dispersive optical elements such as prisms or gratings. There are two types of dispersive spectrometers;

##### a) Single-beam IR spectrometer

Radiation from the source passes through the sample and then through the entrance slit to the dispersion element. The desired wavelength is chosen by

rotating the dispersion element and passed through the exit slit to the detector, which measures the intensity of the remaining radiation.

b) Double-beam IR spectrometer

This instrument splits the source beam into two beams of approximately equal intensity, the reference and the sample beam. The sample is placed in the sample beam and a reference material is placed in the reference beam. The two beams are then recombined and passed along the optical path to the detector.

The main disadvantages of dispersive spectrometers are: the measurement of one resolution element at a time and limiting of the energy entering and leaving the monochromator by a narrow slit. The former leads to low speed and the latter causes a low signal to noise ratio.

3.1.1.2.2 FTIR spectrometer

3.1.1.2.2A Principles

In Fourier transform infrared spectroscopy, light covering a broad frequency range is split into two beams by a beam splitter. The beam splitter is a plate (e.g. Potassium bromide) coated with a transparent material (e.g. Germanium) so as to reflect just 50% of the radiation falling on it. Thus, half the radiation goes to the mirror  $M_1$ , and half to mirror  $M_2$ , returns from both these mirrors along the same path, and then is recombined into a single beam at the beam splitter. The recombined beam leaving B towards the detector shows either constructive or destructive interference, depending on the relative path lengths B to  $M_1$  and B to  $M_2$ . For monochromatic light if the path lengths are identical or differ by an integral number of wavelengths, constructive interference gives a bright beam leaving B. If the difference is a half-integral number of wavelengths, the beams cancel at B and no signal is detected. By systematically changing the difference in the two paths, the interference patterns change like a cosine function to produce a detected signal varying with optical path difference. This pattern is known as the 'interferogram'.



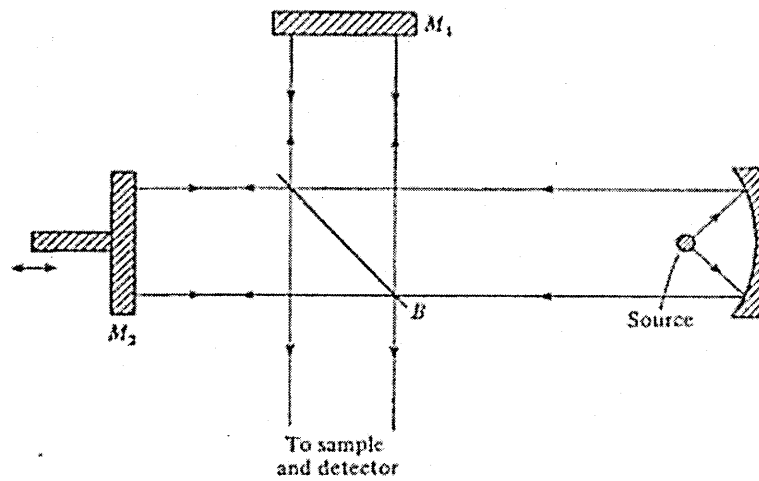


Fig 3.2: A schematic diagram of a Michelson interferometer<sup>1</sup>.

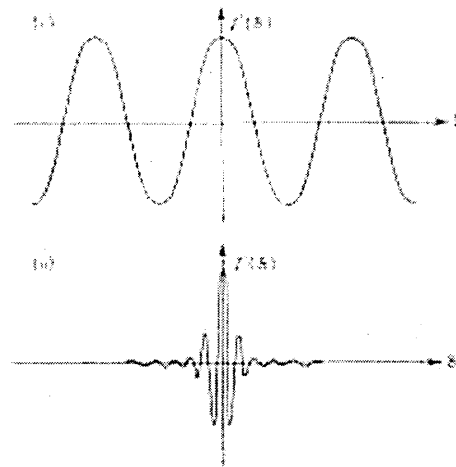


Fig 3.3: Interferograms for (i) monochromatic radiation (ii) white light<sup>2</sup>.

The development of the technique for recording an interference pattern by scanning the moving mirror through a distance of  $\delta/2$  produces a total path difference of  $\delta$ . The resultant interference pattern is shown in fig 3.3 (i) for a source of monochromatic radiation and (ii) for a source of polychromatic radiation. The former is a simple cosine function but the latter is of more complicated form. In the latter case the detector sees intensity due to many cosine waves of different wavelengths so that the corresponding detector signal, as a function of  $\delta$ , will be the result of adding together very many cosine waves of different wavelengths. The signal is large at  $\delta = 0$  since all the waves are in-

phase but elsewhere they may be out-of-phase and produce total cancellation of the signal. Fourier transformation of the interferogram, using a computer built into the machine, converts it into a plot of absorption against wave number, which resembles the usual spectrum, obtained by the traditional method.

There are several advantages to FTIR over the traditional methods:

- a) Fellgett/Multiplex advantage :- Since all the frequencies are recorded simultaneously rather than sequentially as in dispersive spectroscopy so they are said to be 'multiplexed'. The whole spectrum is measured in few seconds because it is not necessary to scan each wave number successively.
- b) Jacquinot/Throughput advantage:- In the FTIR spectrometer, the narrow entrance slit that restricts the radiation throughput in dispersive spectrometers is replaced by a circular aperture of larger area. Therefore, the cross-section of the beam of radiation in an interferometer is much larger than that of a dispersive spectrometer thus leading to considerable improvements in signal to noise.
- c) Connes advantage :- In a FT system spectral wavelength is known very accurately because sampling is controlled by a laser whose wavelength is fixed at 632.8 nm. This absolute spectral control is very important in spectral subtraction.

Most FTIR spectra are also recorded in absorption mode and good emission characteristics are needed from the source over the IR region of interest. A heated black body emits strongly in the mid and near-infrared region and a Nernst filament, consisting of a mixture of rare earth oxides, or a silicon carbide Globar emulate a black body well.

The response time of FTIR detectors has to be much more rapid than in dispersive spectroscopy because they take a large amount of energy quickly rather than a small amount of energy slowly. There are two commonly used detectors. The normal detector for routine work is a pyroelectric device incorporating deuterium triglycine sulphate in a temperature resistant alkali halide window. For extreme sensitivity, mercury cadmium telluride detectors are used but they have to be cooled to liquid nitrogen temperatures.

## 3.1.1.2.2B FTIR- ATR spectroscopy

Attenuated total reflectance (ATR) is also known as internal reflectance spectroscopy (IRS). It is the most widely used FTIR sampling tool today. ATR generally allows quantitative or qualitative analysis of samples with little or no preparation of samples.

In ATR we direct the IR beam into a crystal of relatively higher refractive index. Light propagating through a medium with higher refractive index (ATR crystal), at an angle greater than the critical angle ( $\theta_c$ ) undergoes total internal reflection at the interface with a medium of lower refractive index (sample) and creates an evanescent wave which projects orthogonally into the sample. An evanescent wave is a penetrating electromagnetic field whose intensity quickly decays as it moves away from its source. This phenomenon is shown in the following representation of a single reflection ATR:

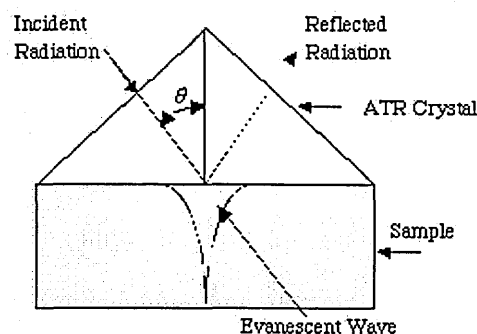


Fig 3.4: Schematic representation of path of a ray of light in ATR spectrometer with an evanescent wave escaping into the rarer medium.

An ATR accessory measures the totally reflected infrared beam when the beam comes in contact with a sample. The principle of ATR measurements is based on the expression of total absorption intensity,  $A$ , as a function of the incident angle,  $\theta$ :

$$A(\theta) = \int_0^{\infty} \alpha(z) e^{-\beta z} dz \quad \dots\dots\dots (3.8)$$

$$\beta = \frac{4\pi}{\lambda_1} \frac{\sqrt{n_1^2 \sin^2 \theta - n_2^2}}{\lambda_1} \quad \dots\dots\dots (3.9)$$

where  $n_1$  and  $n_2$  are the ATR crystal and sample refraction indices respectively.  $\lambda_1$  is the wavelength of radiation in denser medium ( $\lambda_1 = \lambda/n_1$ ),  $\alpha(z)$  is the absorption coefficient of the sample as a function of the depth  $z$ , which is determined by the concentration of the sample.

The dispersion in the refractive index affects the spectra for internal reflection. The effect of this dispersion is dependent on the angle of incidence near the critical angle for measurements on bulk materials. For measurements made at angles greater than a few degrees above the critical angle, the character of the spectra does not change much with change in angle of incidence. They are much similar to transmission spectra. On the other hand, for measurements made near the critical angle, the bands become broadened on the longer wavelength side and shifted to longer wavelengths. However, the band position and the band shape of the spectra of very thin films do not depend on the angle of incidence and they usually resemble the transmission spectra. But, those parameters for the spectra of bulk materials are dependent on two factors. They are: the penetration depth and the effect of dispersion. For bulk materials, the penetration depth, hence the effective thickness, increases with wavelength. Therefore the bands at the longer wavelengths tend to be relatively stronger and, for broad bands, there is a noticeable broadening on the long wavelength side and a shift to longer wavelengths relative to transmission measurements. The internal reflection spectra of bulk materials measured near the critical angle of incidence become distorted due to the effect of dispersion. It has been noted that the bands become distorted and shifted to longer wavelengths as the angle of incidence approaches the critical angle<sup>3</sup>.

The widely used materials for ATR crystals are ZnSe, Ge, ZnS, Si, and Diamond. The main advantages of ATR compared with transmission are;

- ◆ In ATR most samples can be run 'neat' which means in their 'natural state'
- ◆ ATR sampling is fast and easy because little or no sample preparation is required

The main disadvantage of ATR is if the sample does not have good contact with the crystal the data will not be accurate.

### 3.1.1.3 The infrared spectra of polymers

Infrared spectroscopy has been of immense help in the characterisation and identification of polymers. It is the most widely used method for characterising the molecular structures of polymers, principally because it provides a lot of information and is relatively inexpensive and easy to perform.

When the vibrations of small molecules are considered we can see that a non-linear molecule consisting of  $N$  atoms have  $3N-6$  normal modes of vibration. A polymer molecule may contain tens of thousands of atoms and may thus have tens to hundreds of thousands of normal modes. Therefore the infrared spectrum of a polymer might be expected to be impossibly complicated. But this is not so. The basic reason is that the molecule of a homopolymer consists of a large number of chemically identical units, each of which usually contains only tens of atoms or fewer. This leads to a considerable reduction in the complexity of the infrared spectrum. The repeat unit of a polymer has typical dimensions of order  $10^{-9}\text{m}$ , whereas the wavelength of infrared radiation that is absorbed by the vibrating molecules is usually greater than  $2 \times 10^{-6}\text{m}$ . There are thus many repeat units within one wavelength and the interaction of the polymer molecule with the radiation will therefore depend on the sum of the interactions over many repeat units. If the polymer chain is a perfectly regular one in a crystalline region of a polymer, only a small fraction of the possible vibrations are such that all the repeat units in the chain vibrate in phase. The other modes are essentially standing-wave modes in which the vibrations of all repeat units in the chain are similar but the phases alternate along the chain. In these modes the interactions of the individual repeat units with the radiation cancel out over the length of the chain and the modes are thus inactive in infrared spectroscopy. The infrared active modes belong to the group of modes in which all repeat units vibrate in phase. It is possible for even some of these modes to be inactive thus leading to further reduction of the complexity of the spectrum. For an irregular chain in a non-crystalline region of a polymer all normal modes are potentially infrared active because there is no molecular symmetry. We expect to see broad infrared absorption peaks due to 'group vibrations' the broadening arising because the groups of atoms of the same kind in different repeat units have slightly different frequencies of vibration as a result of the different physical environments of the units to which they belong. We see, therefore, that the infra-red spectrum of a polymer will usually contain a

number of peaks which is of order  $3n$  or less ( $n$  is the number of atoms in the repeat unit) rather than  $3N$  ( $N$  is the number of atoms in the whole molecule). Since the spectrum of a polymer is to a first approximation that of its repeat unit, i.r. spectroscopy can help to provide a qualitative analysis of the polymer, that is to find out the kinds of repeat units in a polymer or a polymer blend.

Vibrational spectroscopy can give very useful information about the physical structure, which strongly influences the physical properties of the polymer. Any two regions of the polymer which differ in the way the repeat units are arranged may show detectable differences in their spectra. Sometimes peaks are split and sometimes totally new peaks appear as a result of some treatment (for instance when a polymer is allowed to crystallise or is subjected to physical deformation). If spectra are obtained using polarised radiation, information can be obtained about the degree of molecular orientation which can provide a better understanding of the properties of the materials.

### 3.1.2 Mixed crystal infrared spectroscopy

Isotopic substitution has been very useful in determining the chain conformation where conventional characterisation techniques have been inadequate. Deuterium substitution is assumed to change the vibrational frequencies of a molecule, while leaving other physical characteristics unchanged. It has long been used in polymers, primarily as an aid to band assignments. The basis of this method is the shift in vibrational frequency which results from a change in mass of one (or more) of the vibrating atoms. The frequency is expected to change by a factor of  $\sqrt{2}$  for a simple C-X stretching vibration ( $X = \text{H}$  or  $\text{D}$ ), while the factor is observed to be similar for other vibrational modes. Therefore, the spectral bands arising from polyethylene (PEH) and perdeuterated polyethylene (PED) are clearly separated from each other.

Tasumi and Krimm have calculated the vibrational frequencies for solid solutions of PEH and PED with a variety of arrangements of 'guest' stems within a host lattice<sup>4</sup>. They have shown that differences in the calculated splittings resulting from inter-stem interactions might provide a test for various models of chain folding (and hence crystal stem arrangements) in polyethylene single crystals. Polyethylene usually crystallises

with an orthorhombic structure. The unit cell contains two chains which are not equivalent in the crystallographic sense, so that some vibrations (eg.  $CX_2$  bending and rocking) appear as doublets in the IR spectrum. Tasumi and Krimm calculated vibrational frequencies for various mixtures of PEH and PED. The most significant of the models considered are shown in figure 3.5.

Three factors were considered in calculating vibrational frequencies resulting from H ... H and D .. D interactions for a system of PEH with a small a proportion PED. They are;

- ◆ The interactions are limited to similar type of stems (i.e. no interactions between neighbouring PEH and PED stems)
- ◆ Such interactions are limited only to the nearest neighbour(s)
- ◆ And all such interactions are limited to  $\langle 110 \rangle$  crystallographic directions

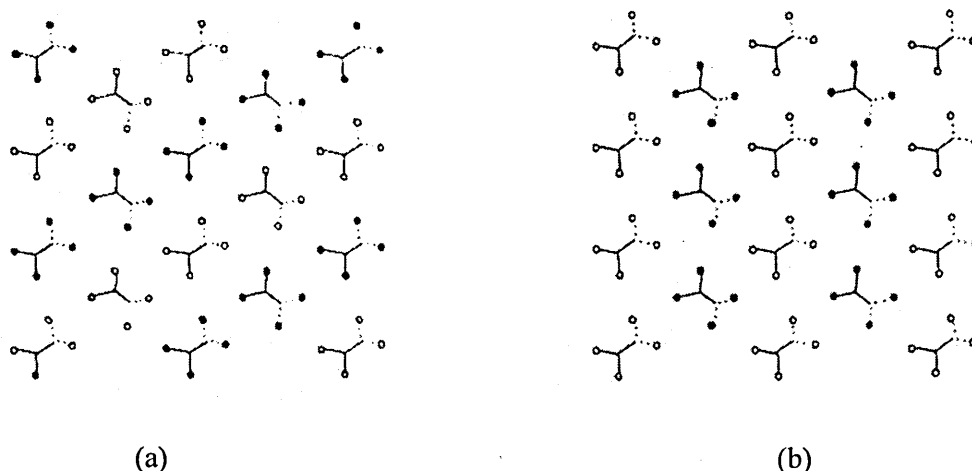


Fig. 3.5: Cross-section of the crystal lattice containing PEH stems (open circles) and PED stems (shaded circles). (a) Chain stems in (110) planes (b) chain stems in (200) planes<sup>5</sup>.

In such a mixture, there can be several possibilities of stem arrangements giving rise to different vibrational spectra in the  $CD_2$  bending and  $CD_2$  rocking regions. If PED stems are randomly distributed within the PEH lattice most PED stems will be isolated with respect to other PED stems resulting in no nearest neighbour interaction between PED stems in  $\langle 110 \rangle$  direction. Such a situation will lead to a singlet in the  $CD_2$  bending and

CD<sub>2</sub> rocking vibrational spectrum. A smaller number of PED stems with  $\langle 110 \rangle$  nearest neighbour interactions will result in smaller doublet splittings - smaller than in pure PED, due to the absence of a larger number of PED stems in the  $\langle 110 \rangle$  direction. Another possibility is the distribution of PED stems along a particular crystallographic plane e.g. (110) or (200). Such a situation is illustrated in fig. 3.5(a) and (b) respectively. The  $\nu_b$  (bending) and  $\nu_r$  (rocking) modes are expected to be doublets for the situation fig. 3.5(a). However, the splittings will be smaller than in pure PED, since each PED stem in fig 3.5(a) has two PED nearest neighbours, whereas in pure PED each PED stem has four such neighbours. For the situation in fig 3.5(b), the spectrum would be expected to show  $\nu_b$  and  $\nu_r$  singlets, because neighbouring stems in the (200) plane are equivalent.

Since the analysis described here is concerned with the arrangement of crystal stems, it is equally applicable to n-alkane mixtures. Since short chain alkanes are not capable of chain folding, a co-crystallised isotopic mixture would be expected to show a random arrangement of normal and deuterated crystal stems. Mixtures of this type provide useful 'model' systems to compare with polyethylene mixed crystals.

The general technique of isotopic isolation method was first reported by Hiebert and Hornig<sup>6</sup>. It has since been widely used to determine structure and intermolecular forces and to study molecular clustering. This has been successfully applied to polymers, especially to investigate chain folding in semicrystalline polyethylene as described below. Infra-red spectroscopy was the first technique to be used in the analysis of mixed crystal spectroscopy<sup>7</sup> and followed several years later by neutron scattering<sup>8</sup>. The early works of Krimm et al made use of the simple presence of resolved doublet splittings, in the case of solution crystallised samples, as evidence of adjacent non-equivalent guest stems<sup>9</sup>. The early studies using the mixed crystal i.r. technique have been on both PED and PEH matrix samples<sup>9</sup>. In solution crystallised materials, the guest (X) species gave rise to a doublet in the CX<sub>2</sub> bending vibration indicating the presence of neighbouring group interactions in the  $\langle 110 \rangle$  direction and hence of adjacent re-entry along a {110} fold plane. In contrast to the previous work by Krimm et al, infra-red measurements were carried out on samples with a wider range of guest molecular weights, several years later by Spells et al. Contrary to earlier results, a clearly resolved doublet was not generally



observed<sup>10</sup>. Only at sufficiently high guest molecular weight and/or concentration was a doublet resolved. This led to the development of a model with specific regular arrangements of stems. However more recent low temperature results using FTIR showed that this band profile is not just a simple doublet but a complex multiplet structure<sup>11,12,13</sup>. This is evidence for the existence of several possible environments for guest stems. The calculations were therefore extended to take account of more 'irregular groups'. The theoretical models used in each case are briefly described below.

In a two dimensional crystal of pure polymer each labelled stem has four non-equivalent neighbours in  $\langle 110 \rangle$  direction. In an infinite isolated 'sheet' of labelled stems the number of non equivalent neighbours is two; hence the observed splitting for such a sheet is half of the value for pure polymer. Similarly, an isolated pair of labelled non-equivalent stems surrounded by the host material should have a splitting of a quarter of that for pure polymer. In order to calculate the splittings for the above situations Cheam and Krimm used normal vibrational analysis together with a coupled oscillator model<sup>12</sup>. In this model, the repeating unit was considered as the two non-equivalent stems in the unit cell (i.e. a pair of oscillators) to calculate the splitting. They have obtained values of 8.76 and 4.38  $\text{cm}^{-1}$  for the  $\text{CD}_2$  bending splitting, for an infinite stack of infinite  $\{110\}$  sheet of stems ( $\Delta v_{\infty \times \infty}$ ), and for an infinite  $\{110\}$  sheet of stems ( $\Delta v_{\infty}$ ) respectively. For an isolated pair of PED stems,  $\Delta v_0 = 2.25 \text{ cm}^{-1}$  was obtained. These results approximated to the expected relationship:

$$\Delta v_{\infty \times \infty} = 2\Delta v_{\infty} = 4\Delta v_0 \quad \dots\dots\dots (3.10)$$

Cheam and Krimm developed the simple coupled oscillator theory on a model with regular groups of stems in finite sheets and the method was later extended to include multiple sheets<sup>12</sup>. A pair of non-equivalent crystal stems was the basis in their calculation. The splitting for such a pair is  $\Delta v_0$ . The IR splitting for  $N$  such pairs in a  $(110)$  row is given by the relationship:

$$\Delta v_N = \Delta v_0 + (\Delta v_{\infty} - \Delta v_0) \sin^2 \frac{(N-1)\pi}{2N} \quad \dots\dots\dots (3.11)$$

The analysis was extended for a domain of  $j$  stems in the  $(110)$  plane, and  $k$  adjacent planes each with  $j$  stems. The splitting for such an arrangement,  $\Delta v_{j \times k}$ , was obtained by

considering a single plane of  $j$  stems to be a single oscillator. This is given by the relationship;

$$\Delta\nu_{j\infty} = \Delta\nu_j + (\Delta\nu_{j\infty} - \Delta\nu_j) \sin^2 \frac{(k-1)\pi}{2k} \quad \dots\dots\dots (3.12)$$

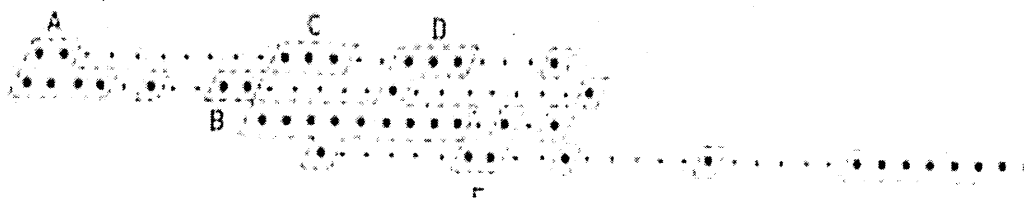
With the aid of experimental data for PED and simple symmetry relations, several terms in equation (3.12) have been determined. Pure PED showed a  $\text{CD}_2$  bending splitting of  $10.2 \text{ cm}^{-1}$ , corresponding to  $\Delta\nu_{\infty\infty}$ . Therefore, according to equation (3.10) the splitting for  $\Delta\nu_{\infty} = 5.1 \text{ cm}^{-1}$ . A series of absolute values were calculated corresponding to different  $\Delta\nu_{j\infty}$  values<sup>12</sup>. Analogous calculation for  $\text{CH}_2$  bending vibration have also been made<sup>14</sup>. Cheam and Krimm used this data on solution-crystallised PE samples. Doublet splittings obtained from curvefitting procedures were compared with the absolute values of splittings and the domain size corresponding to each doublet splitting was obtained. These results clearly supported a multiple sheet structure. However, there were ambiguities between the domain sizes assigned to the observed doublets and the expected domain size for a complete molecule.

It was found later that Krimm's model with 'regular groups' is inadequate to describe realistic chain conformations incorporating a certain amount of disorder. Therefore, Spells et al have extended Krimm's model with regular groups of adjacent stems to deal with more 'irregular groups' of adjacent stems which arise from the statistical model developed for solution-grown polyethylene crystals<sup>11</sup>. The main features of this model are;

- ◆ the stems are arranged in sheets along a (110) plane
- ◆ a labelled molecule is diluted along the fold plane by other molecule(s)
- ◆ adjacent re-entry of molecules

According to this model, the number of parallel sheets of stems ( $n$ ), increases with the molecular weight. This model was intended to provide a detailed basis for comparison with both the complex multiplet structure of the  $\text{CD}_2$  bending vibration in polyethylene single crystals and also information obtained from neutron scattering measurements. In order to consider the contribution of such irregular stems arrangements to the  $\text{CD}_2$  bending vibration, the labelled stems were sorted into 'groups' of interacting stems (fig. 3.6). Figure 3.6 shows a computer-generated molecular conformation with 50% dilution

and four parallel superfolded sheets of stems. Such groups are effectively independent of others and make separate contributions to the IR band profile. Each group is then transformed into an 'equivalent group' (see appendix) in order to simplify the geometry and hence the calculation of vibrational frequencies. It has properties identical to the original group. An equivalent group has a similar number of stems to the original group,



and a similar distribution of  $\{110\}$  interactions between them.

Fig 3.6: Division of a computer-generated model into groups of stems, which are linked by  $\{110\}$  interactions<sup>11</sup>.

The arrangement of stems in an equivalent group is simpler than in the original group. Each sheet starts in register along a  $\{110\}$  plane, which is not the principal fold plane. The sheets may have unequal numbers of labelled stems, but no unlabelled stems are allowed to interrupt these. Figure 3.7 illustrates the notation previously developed to describe two different equivalent groups of stems. Figure 3.7(b) is called a 'closed group' and is labelled  $(X \times Y)$ . This indicates  $Y$  adjacent sheets each with  $X$  adjacent stems. Figure 3.7(a) shows a group, which is not itself closed but nevertheless contains a closed component  $(3 \times 2)$ .



Fig 3.7: Illustration of the notation used to describe equivalent groups of stems: (a) an  $(8,3)$  group; (b) an  $(8 \times 3)$  group<sup>11</sup>.

An equivalent group may include several alternative closed subgroups, and the subgroup with the maximum splitting (as calculated from coupled oscillator theory<sup>12</sup>) has been used as the basis for calculating the doublet splitting for the equivalent group. Additional stems within the equivalent group, which are not included in the closed subgroup,

provide additional {110} interactions, which increase the splitting. A correction term corresponding to the splitting by additional stems has been added to the value of splitting from the main sub-group to obtain the total doublet splitting of the particular equivalent group. This model has been successfully applied to solution crystallised polyethylene with a minority of the deuterated species<sup>13</sup>. This method of calculating the i.r. band profile from molecular conformational models has also been applied on samples with a deuterated matrix and a good agreement between experimental and calculated results has been obtained<sup>13</sup>. We extensively used this statistical model in Chapter 6.3.3 to determine the CD<sub>2</sub> bending profile of the random folded model for once-folded form of C<sub>12</sub>D<sub>25</sub>C<sub>192</sub>H<sub>384</sub>C<sub>12</sub>HD<sub>24</sub>.

Snyder et al have recently calculated domain sizes of isotopic components of a mixture of n-alkanes by monitoring the splitting of the CH<sub>2</sub> bending band, considering the domains as clusters of adjacent isotopically identical stems<sup>15</sup>. In a two-dimensional crystal, a chain can interact with its four nearest neighbours provided all the neighbouring chains are isotopically identical. Although the degree of splitting mainly depends on the number of interactions between the neighbouring chains, the shape of the domain too, has a minor effect. Therefore, Snyder et al have considered both square and randomly-shaped domains. Random shaped domains were generated by adding one chain at a time to the edge of a domain consisting initially of a single chain. The probability for addition was taken to be equal for all edge sites. They derived a simple relationship between splitting and domain size. The observed splittings were converted to a normalised splitting, R, that is defined:

$$R = \Delta\nu/\Delta\nu_0 \quad \dots\dots\dots (3.13)$$

Where  $\Delta\nu$  is the splitting of the bending band of either the hydrogenated or the deuterated n-alkane component and  $\Delta\nu_0$  is the splitting for the neat n-alkane of the corresponding isotope. The normalised splitting associated with a two dimensional square domain, was found to be given by the expression:

$$R = \cos\left(\frac{\pi}{N^{1/2} + 1}\right) \quad \dots\dots\dots (3.14)$$

Where  $\pi$  = phase angle

N = number of chains in the two dimensional domain

They used this relationship to calculate the average domain sizes of the segregated components of mixtures, in which one component is hydrogenated and the other deuterated. The degree of segregation was expressed in terms of  $N$ . This method depends on the fact that the intermolecular coupling produces splitting only in the arrangements of isotopically-alike chains; if the chains are isotopically different, the coupling is negligible and the spectrum is not affected.

The main differences of this model as compared with the Krimm's model and Spells' statistical model are the absence of chain folding and the absence of a preferred plane for the adjacent molecules. Since short chain alkanes are not capable of chain folding, a co-crystallised isotopic mixture would be expected to show a random arrangement of normal and deuterated crystal stems. Isotopically labelled domains are therefore likely to be randomly shaped, so that this model will best describe the situation in short chain alkanes. This method was used to calculate the domain size of  $C_{12}D_{25}C_{192}H_{384}C_{12}HD_{24}$  as-grown crystals and annealed crystals in Chapter 6.3.1.2.

### 3.1.3 Wagging modes

In crystalline *n*-paraffins, the methylene wagging, rocking, twisting and bending vibrations are confined to well defined regions of the infrared spectrum. Out of these, the wagging region plays a major role in identifying various non-planar conformers. The infrared spectrum of even the most highly crystalline polyethylene displays absorption bands which cannot be assigned to the vibrational modes of an infinitely long and fully extended chain. The intensities of most of these bands increase greatly with increasing temperature up to the melting point of the polymer, after which the increase may continue but at a much slower rate. This behaviour strongly suggests that these bands are associated with vibrations of non-planar chains. In the case of the *n*-paraffins, the greater complexity of the vibrational spectra of the liquid relative to that of the crystalline solid is known to be the result of rotational isomerism in the liquid state<sup>15</sup>. These additional bands are mainly confined to the 1400 - 1200  $\text{cm}^{-1}$  area of the infrared spectrum.

The use of infra-red spectroscopy in the study of alkyl chain disorder was pioneered by Snyder<sup>16</sup>. He measured the infrared spectra of two samples of polyethylene, both having high crystallinity but differing in the kind of end groups. One sample with methyl end groups was denoted polyethylene II and corresponded to the limiting case of a very long n-paraffin; the other sample, polyethylene I, had vinyl end groups. In the spectrum of molten polyethylene I there were two overlapping bands at 1368 and 1352  $\text{cm}^{-1}$ . The intensity of the 1352  $\text{cm}^{-1}$  band increased with increasing temperature at a rate greater than that of its companion. On the lower frequency side of the 1352  $\text{cm}^{-1}$  band a shoulder at about 1338  $\text{cm}^{-1}$  was also observed. In addition, he observed a very asymmetric band at 1308  $\text{cm}^{-1}$  with greater absorption on the low-frequency side. Upon cooling the sample to room temperature the low-frequency tail became less intense, suggesting that this band was a composite of two bands, at 1308  $\text{cm}^{-1}$  and around 1270  $\text{cm}^{-1}$ . The spectrum of polyethylene II showed all of the above five bands plus two more. One, is the well-known methyl symmetric deformation vibration at 1375  $\text{cm}^{-1}$  and the second one appeared at 1344  $\text{cm}^{-1}$  where it overlapped the weaker band at 1338  $\text{cm}^{-1}$ .

All of the above bands of polyethylene in the region 1380 – 1340  $\text{cm}^{-1}$  have been found in the spectra of the liquid n-paraffins n-C<sub>8</sub>H<sub>18</sub> and higher. In the spectra of the shortest n-paraffins, a complex of bands near 1300  $\text{cm}^{-1}$  has been observed. In going to longer chains, this complex merged into a band which corresponds to the 1308  $\text{cm}^{-1}$  band of polyethylene. Snyder assigned all these bands, except the one at 1375  $\text{cm}^{-1}$ , to methylene wagging vibrations. Accompanying the 1375  $\text{cm}^{-1}$  band was another at 1344  $\text{cm}^{-1}$ . The ratio of the intensities of these two bands was nearly constant for all the n-paraffins at room temperature. Therefore, the 1344  $\text{cm}^{-1}$  band must also be associated with a vibration at the end of the molecule. Snyder assigned this band to a vibration of a *tg* conformation at the end of a molecule. The wagging motions of methylene groups in the *gtg* and *gtg'* conformation are largely uncoupled from other motions. Snyder assigned these motions to the well defined bands observed at 1368 and 1308  $\text{cm}^{-1}$ . However, this was presented with suspicion as the *gtg'* mode should not appear in the infrared spectrum according to symmetry rules. However, it seemed that such a band might appear if the amplitude of torsional motion about the central C-C bond of the *gtg'* sequence were sufficiently large. But recent calculations, aimed at simulating the infrared spectrum of conformationally disordered polymethylene chains, have shown that these torsions are too small to allow the *gtg'* wagging mode to appear in the infrared spectrum with any

significant intensity<sup>17</sup>. The band at  $1338\text{ cm}^{-1}$  has been assigned to the *gttg* conformation and involves wagging of the methylenes in the *trans* sequence. The temperature behaviour of the  $1352\text{ cm}^{-1}$  band suggests that it belongs to a higher energy conformation such as *gg*. For this conformation the calculated wagging frequency was  $1354\text{ cm}^{-1}$ . Therefore Snyder assigned the band at  $1352\text{ cm}^{-1}$  to this mode. Out of these the most widely used defect modes are; end-gauche (*gt*) conformation at  $1344\text{ cm}^{-1}$ , double gauche (*gg*) conformation at  $1352\text{ cm}^{-1}$  and *gtg* modes at  $1368$  and  $1308\text{ cm}^{-1}$ . These assignments have since been widely used to characterise the chain disorder in a range of systems, including n-alkanes,<sup>18</sup> polyethylene,<sup>19,20</sup> long chain n-alkanes,<sup>21,22</sup> carboxylic acids,<sup>23</sup> phospholipids,<sup>24</sup> and surfactant molecules<sup>25</sup>.

In addition, they are of great importance in identifying the solid-solid phase transitions of short chain alkanes just below the melting point. The fact that many crystalline n-alkanes undergo a solid-solid phase transition a few degrees below their melting point has been known since 1932, when Müller reported the high-temperature “hexagonal” or “rotator” phase of these systems<sup>26</sup>. However, the early evidence for premelting was largely based on calorimetric measurements. Ubbelohde suggested premelting in crystalline n-alkanes using specific heat measurements in 1938<sup>27</sup>. Infrared spectroscopy is capable of providing detailed information about conformational disorder in chain molecule assemblies irrespective of physical state. A more recent detailed analysis of conformational disorder at solid-solid phase transitions has been made by Snyder et al. They found that the disorder is greatest at the chain ends, but extends into the chain interior<sup>28</sup>. An infrared study on conformational disorder with increasing temperature of a series of short chain alkanes, from  $\text{C}_{17}$  through to  $\text{C}_{29}$ , has been reported<sup>18</sup>, in which it was observed that as the n-alkane is warmed up, abrupt changes in the concentration of non-planar conformers occur at temperatures that correspond to the solid–solid transitions. These non-planar conformers are observed in phase I (the lower temperature phase) at temperatures at least 20K below the first (lowest temperature) transition. As the temperature is increased, their concentration gradually increases; a discontinuous jump occurs at each transition.

Kim et al have observed the conformational disorder in longer chain n-alkanes prior to melting<sup>29</sup>. They observed that the onset of disorder for  $\text{C}_{50}$  and  $\text{C}_{60}$  is not associated with a solid-solid transition unlike short chain alkanes, and occurs gradually. Therefore,  $\text{C}_{50}$

and C<sub>60</sub> can be said to undergo true premelting. However, there are many close similarities between short and long chain alkanes regarding the conformational disorder. The similarities are in the width of the temperature range over which disordering occurs, in the total concentration of the disorder and its distribution. These similarities suggest a common disordering mechanism. Snyder et al suggested that the disordering mechanism involves longitudinal diffusion<sup>18</sup>.

The direct sensitivity of 'defect' CH<sub>2</sub> wagging vibrations to the chain conformation provides the possibility of studying the fold structure directly. Ungar's study on chain folding benefited from the recent synthesis of model n-alkanes. His work takes the advantage of ability of these alkanes to crystallise in both folded and extended form. These folds were found to be sharp and adjacently re-entrant<sup>30</sup>. Ungar et al studied the fold structure of C<sub>198</sub>H<sub>398</sub> by infra-red spectroscopy<sup>31</sup>. Three characteristic fold bands for folding in the (110) plane have been observed in the spectra of once folded crystals after subtracting the extended spectrum from the folded spectrum. This resulted in the first direct observation of i.r. bands due to tight, adjacently re-entrant fold in polymethylene systems. They were identified at 1345-1346 cm<sup>-1</sup>, 1369-1370 cm<sup>-1</sup> and at 1298 cm<sup>-1</sup>, which agreed well with the calculated values<sup>31</sup>. The band at 1345 cm<sup>-1</sup> has been assigned to two strained *gg* pairs. Gorce et al have done a detailed analysis of the extent of disorder in the extended and folded forms of these longer chain n-alkanes<sup>32</sup> using FTIR techniques. They exploited the CH<sub>2</sub> wagging region in the infra-red spectrum in this regard. In addition to the above fold bands they observed two new bands at 1353 and 1363 cm<sup>-1</sup> which were assigned to *gg* conformers and (tentatively) to strained *gtg/gtg* conformation<sup>32</sup>.

In our work on monodisperse long chain alkanes, the CH<sub>2</sub> wagging region is extensively used to investigate the extent of disorder, in various crystal systems, as part of their characterisation. Besides the well-known extended and folded chain crystals, a NIF form and different layer structures have been recently discovered in these n-alkanes<sup>33</sup>. These structures show a wide variation in the proportion of disordered material. However, in the case of the deuterium-labelled molecules, the extent of disorder in the chain end region could not be studied using the CD<sub>2</sub> wagging mode region as mode coupling prohibits using CD<sub>2</sub> wagging modes<sup>34</sup>. Therefore, the extent of order in these alkanes was studied using the CD<sub>2</sub> bending vibration of the infrared spectrum<sup>35</sup>. However, the CH<sub>2</sub>



wagging region was again helpful in the determination of extent of disorder in the crystal interior of the end-deuterated alkanes. Contrary to short chain alkanes, these results from end-deuterated n-alkanes showed that the chains become more ordered with increasing temperature. It was concluded that the chains become more translationally ordered. In the current work it was confirmed that this translational ordering process coincides with chain tilting.

## 3.2 Raman Spectroscopy

### 3.2.1 Introduction

Raman spectroscopy is another form of vibrational spectroscopy, which is frequently being used to characterise polymer structure. But it complements i.r. spectroscopy in that bond vibration modes which are Raman active tend to be i.r. inactive and vice-versa. Raman spectroscopy can be used to identify particular bonds and functional groups in the structure of a polymer in much the same way as i.r. spectroscopy. The low frequency longitudinal acoustic mode (LAM) is very useful to characterise polymer structure and morphology. Vibrational Raman spectroscopy is not limited to intramolecular vibrations. Crystal lattice vibrations and other motions of extended solids are Raman active. Their spectra are important in such fields as polymers and semiconductors.

We are already aware that photons interact with molecules to induce transitions between energy states in the molecules. During this interaction a small amount of photons is scattered. Most of these photons are elastically scattered i.e. the emitted photon has the same energy (frequency) and therefore, same wavelength, as the incident photons. This process is called Rayleigh scattering. However, a small fraction of light (approximately 1 in  $10^7$  photons) is scattered inelastically. This process was discovered by the Indian physicist, C.V. Raman in 1928. Hence, the process leading to this inelastic scatter is termed the Raman effect. Raman scattering can occur with a change in vibrational, rotational or electronic energy of a molecule. Here we use the term Raman effect to mean vibrational Raman effect only. In Raman scattering the energies of the incident and scattered photons are different. A simplified diagram to illustrate this concept is given in figure 3.8.

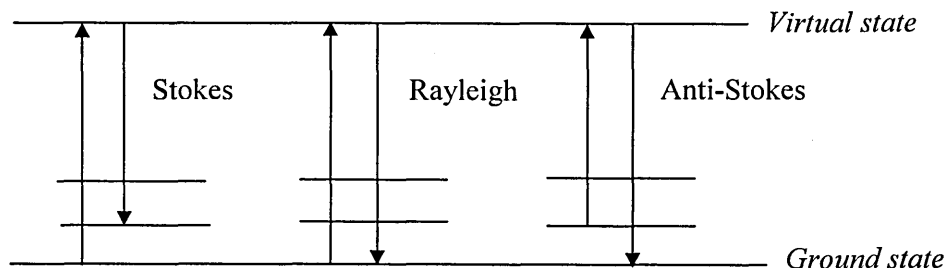


Fig 3.8: Energy level diagram showing Raman and Rayleigh scattering.

In Stokes scattering the energy of the scattered radiation is less than the incident radiation and it is more in anti-Stokes scattering. The energy difference between the incident photon and the Raman scattered photon is equal to the vibrational energy of the scattering molecule. A plot of intensity of scattered light versus energy difference (usually converted to  $\text{cm}^{-1}$ ) is the Raman spectrum. Stokes lines are more intense than the anti-Stokes lines in the spectrum. This is because the anti-Stokes lines are arising from molecules that are vibrationally excited prior to irradiation. Since the number of molecules at higher vibrational states is lower than that of the ground state at room temperature, the intensities of anti-Stokes lines are lower than the Stokes lines. Therefore, in Raman spectroscopy only the more intense Stokes line is measured. Since Raman scattering is not very efficient, high power excitation source is needed. Raman spectroscopy is conventionally performed with green, red or near infra-red lasers.

There are three main spectral regions which are sensitive to the order and disorder state of the semi-crystalline polyethylene. The internal modes ( $900 - 1500 \text{ cm}^{-1}$ ) give quantitative information with respect to the elements of phase structures. The longitudinal acoustic mode (LAM), in the range of about  $5 - 50 \text{ cm}^{-1}$  gives the ordered sequence length distribution. The disordered LAM (DLAM) is in the region of  $200 \text{ cm}^{-1}$  and gives a measure of the long - range conformational disorder. The ordered sequence length can be obtained from the relationship;

$$\bar{\Delta\nu} = m/2cL (E/\rho)^{1/2} \dots\dots\dots(3.15)$$

where  $\bar{\Delta\nu}$  = LAM mode frequency

$m$  = mode order ( $m = 1, 3, 5, \dots$ )

$c$  = velocity of light

- $\rho$  = density of the vibrating sequence  
 $E$  = Young's modulus in the chain direction

Thus, the ordered sequence length, ( $L$ ), is inversely related to the mode frequency. This length can be directly related to the lamellar thickness. The LAM has been observed in many crystalline polymers and has been widely used in studying their structure. This LAM is particularly of interest because

- tilted chains will show straight chain lengths which are greater than the crystal thickness obtained from SAXS
- it does not require a regular crystal/amorphous stack to observe LAM (unlike the SAXS long period)

### 3.2.2 Principles

The Raman effect is due to the interaction of the electromagnetic field of the incident radiation,  $E$ , with a molecule. The electric field induces an electric dipole,  $P$ , in the molecule given by ;

$$P = \alpha E \quad \dots\dots\dots(3.16)$$

Where  $\alpha$  = polarizability of the molecule

The polarizability measures the ease with which the electron cloud around a molecule can be distorted. Raman scattering occurs because a molecular vibration can change the polarizability. The change in the polarizability is described by its derivative,

$$\frac{d\alpha}{dQ} \quad \dots\dots\dots(3.17)$$

Where  $Q$  = displacement co-ordinate

In order to be Raman active, there should be a change in the polarizability during the vibration as given in equation 3.19.

$$\frac{d\alpha}{dQ} \neq 0 \quad \dots\dots\dots(3.18)$$

Scattering intensity is proportional to the square of the induced dipole moment, thus to the square of the polarizability derivative ;

$$\left( \frac{d\alpha}{dQ} \right)^2 \quad \dots\dots\dots(3.19)$$

If a vibration does not change the polarizability, then the polarizability derivative will be near zero and the intensity of the Raman band will be low. The vibrations of a high polar moiety such as a O-H bond are usually weak as the external electric field cannot induce a large change in the dipole moment of the molecule.

### 3.3 Neutron Scattering

Neutron scattering can be either elastic or inelastic. Elastic scattering leads to the small angle neutron scattering (SANS) technique and the inelastic scattering leads to inelastic neutron scattering (INS) spectroscopy both of which are widely used in the field of polymer. Neutron radiation can be produced to cover a range of wavelengths: 0.01 – 3 nm. This is comparable with that of X-rays (Cu-K $\alpha$  line is at 0.15 nm). However it is much smaller than that of visible light (400 – 700 nm). Therefore, the usefulness of neutrons and X-rays to colloid and polymer science is obvious when the length scales are considered: bond lengths are typically around 0.1 nm, the radius of gyration of a polymer in solution is  $\sim 1 - 10$  nm and a surfactant micelle  $\sim 10 - 100$  nm in diameter. The fundamental difference between neutron and electromagnetic radiation is the mechanism by which the incident radiation interacts with matter. Light and X-rays are both scattered by the electrons surrounding atomic nuclei, but neutrons are scattered by the nucleus itself. The interaction of neutrons with matter is weak and the absorption of neutrons by most materials is correspondingly small. Therefore neutron radiation is very penetrating.

There are some drawbacks with using neutron radiation. The main disadvantage is that it is not a technique for the laboratory benchtop. Neutron sources like synchrotron radiation sources are very large and costly. The other disadvantage is neutron sources are relatively weak compared to light or X-rays.

#### 3.3.1 Principles

An idealised scattering experiment is shown in figure 3.9. An incident wave with defined wavelength and direction is allowed to fall on the sample. The scattered wave is measured and the intensity is recorded as a function of its angle (and in some experiments of energy). A vector notation is used to describe this process relating the

incident wavelength  $\lambda_i$  and energy  $E_i$  to a wave vector  $\mathbf{k}_i$  (momentum  $\mathbf{p}_i$ ) with the de Broglie relationships:

$$E_i = h \nu_i, \quad \mathbf{p}_i = \hbar \mathbf{k}_i$$

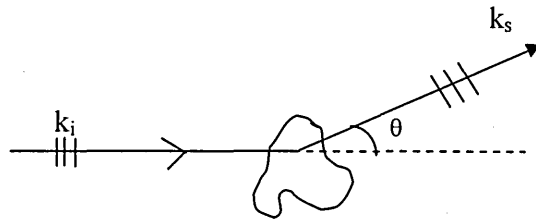
$$|\mathbf{k}_i| = 2\pi/\lambda_i$$

Where  $\nu_i$  = frequency of the wave

$h$  = Planck's constant ( $6.63 \times 10^{-34}$  J s)

$\hbar = h/2\pi$

(a)



(b)

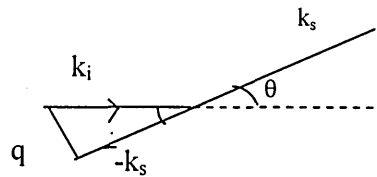


Fig 3.9: Schematic diagram (a) of a scattering experiment showing an incident wave with vector  $\mathbf{k}_i$ , scattered at an angle  $\theta$  to give a wave with vector  $\mathbf{k}_s$ . The vector diagram (b) shows the result for  $\mathbf{q} = \mathbf{k}_i - \mathbf{k}_s$ .

The usual relationship of energy to velocity  $v$  or momentum and mass  $m$  also applies:

$$E_i = \frac{1}{2} m v_i^2 = \frac{1}{2} |\mathbf{p}_i|^2 / m \quad \dots\dots\dots (3.20)$$

Similar relations can be written for the scattered wave and we note that there is in general a change of momentum  $\mathbf{q}$  which is expressed as:

$$\mathbf{q} = \mathbf{k}_s - \mathbf{k}_i \quad \dots\dots\dots (3.21)$$

In elastic scattering this can be reduced to;

$$q = |\mathbf{q}| = (4\pi/\lambda) \cdot \sin(\theta/2) \quad \dots\dots\dots (3.22)$$

Where  $\theta$  is the scattering angle.

For inelastic scattering

$$E = h(\nu_s - \nu_i) = \hbar(\omega_s - \omega_i) \quad \dots\dots\dots (3.23)$$

with  $\omega$  the angular frequency of the wave ( $2\pi\nu$ ).

The theory of scattering is devoted to the calculation of scattered intensity  $I_s$  as a function of the incident intensity  $I_i$  and the variables  $\mathbf{q}$  and  $E$  for a given sample. Within certain limits this can be written as:

$$I_s = I_i \cdot d\Sigma(\mathbf{q}, E) / d\mathbf{q} dE \quad \dots\dots\dots (3.24)$$

Where  $d\Sigma / d\mathbf{q} dE$  is the differential scattering cross-section. The scattering occurs due to a property known as neutron scattering length density difference.

### 3.3.2 Inelastic neutron scattering (INS)

Inelastic neutron scattering is the process of scattering neutrons from a sample, accompanied by a change in energy of the neutron. Neutrons scattered off a sample may either absorb or lose energy but at low temperatures neutron energy loss to the sample is much more likely. The energy imparted to the sample creates an excitation of the sample. In INS spectroscopy we are interested in those cases where the excitation of the sample is due to vibrational motions. Therefore in some respect INS is similar to infrared and Raman spectroscopy.

#### TOSCA

This is an inelastic neutron scattering (INS) spectrometer optimised for vibrational spectroscopy. This replaced the previous spectrometer TFXA and installed at the ISIS pulsed neutron spallation source at Rutherford Appleton Laboratory, UK. TOSCA measures incoherent neutron scattering at large energy transfers ( $0.5 < \omega < 1000$  meV) with a resolution of about 2 – 2.5 % of the energy transfer in the whole  $\omega$  range. TOSCA consists of two parts: the back scattering part (phase I) and the forward scattering bank (phase II). TOSCA-I replaced the TFXA. Completion of the phase II of TOSCA improved the resolution from 2-3% to 1-1.5% of the energy transfer.

The intensity of the  $i$  th molecular vibrational transition,  $I_i$ , is proportional to;

$$I_i \propto Q^2 U_i^2 \exp(-Q^2 U_{total}^2) \sigma \quad \dots\dots\dots (3.25)$$

Where  $Q$  = momentum

$U_i$  = amplitude of vibration of the atoms undergoing the particular mode

$U_{total}$  = mean square displacement of the molecule

Exponential term = Debye-Waller factor

In order to maximise the INS intensity it is necessary to reduce the Debye-Waller factor as much as possible. The magnitude of  $U_{total}$  is partly determined by the thermal motion of the molecule. This can be reduced by cooling the sample and so spectra are typically recorded below 50K.

### 3.4 X-ray Techniques

#### 3.4.1 Principles

When X-rays of a given wavelength impinge on the electrons in an atom, the electrons become secondary emitters of X-rays. Two kinds of scattering take place; coherent and incoherent. The major part of the energy of scattering goes into coherent scattering, which can be utilised for structural studies. The shape of the coherent-scattering curve as a function of scattering angle is called the 'scattering factor', ( $f$ ), of the atom. The atomic scattering factor at zero scattering angle,  $f_0$ , is equal to the number of electrons present in the atom concerned. Therefore it is evident that the X-ray scattering power of light elements, such as H, C, N and O is much smaller than that of heavy elements. This has important consequences in the study of polymers, which are composed chiefly of light elements.

The incoherent scattering, also frequently termed 'Compton' scattering, results from the encounter of an X-ray photon with a loosely bound or free electron. Incoherent scattering contributes to the diffuse background in an X-ray diffraction pattern. Depending on the angle of deviation from the direct beam, designated  $2\theta$ , X-ray diffraction effects are separated into small and wide angle regions. Small angle diffraction, or scatter, refers to effects observed at angles smaller than about  $2^\circ$  or  $3^\circ$ . Wide angle diffraction encompasses effects that are observed at all larger angles, theoretically extending up to  $180^\circ$ . For most polymers diffraction effects are observed at angles well below  $90^\circ$ .

A typical X-ray source is illustrated schematically in figure 3.10. When a cathode in the form of a metal wire is electrically heated, it gives off electrons. If a positive voltage in the form of an anode, is placed near these electrons, the electrons are accelerated toward the anode. Upon striking the anode, the electrons transfer their energy to its metallic surface, which then gives off radiation. This radiation, which has very short wavelength (0.01-10 nm) is called X-ray radiation. The anode is called the target. The most common target elements are copper, molybdenum and tungsten. A widely used X-ray source in the field of polymers is the synchrotron radiation. The core of a synchrotron facility is the storage ring around which particles circulate at a high velocity. High energy charged particles circulate within a high-vacuum tube. The path of the electrons is deflected by a magnetic field. Electromagnetic radiation (including X-rays) is emitted as the electrons are deflected.

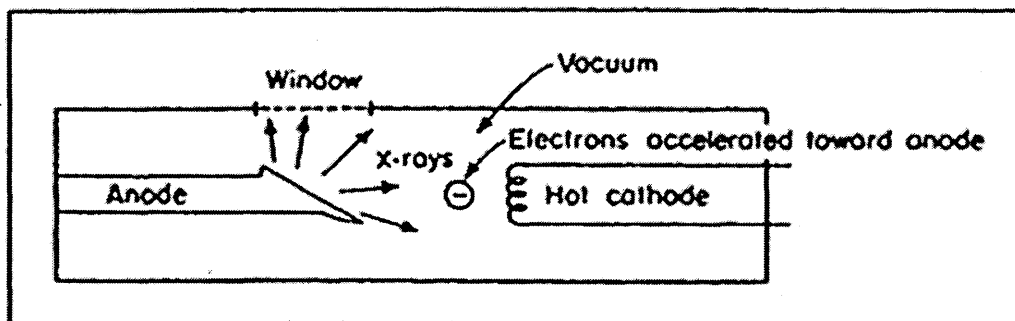


Fig 3.10: Schematic diagram of a X-ray source<sup>36</sup>.

#### 3.4.2 Small angle X-ray scattering (SAXS) on polymers

Polymer crystals consist of stacks of plate-like lamellae. The most characteristic dimension of these lamellae is their thickness. There are several methods to determine the crystal thickness. These include shadowing lamellae deposited upon a substrate and measuring the length of the shadow by electron microscopy; measuring the thickness by interference microscopy and determining it by using small angle X-ray scattering (SAXS) from a stack of deposited crystals. The stack scatters X-rays in a similar way to the atoms in a crystal lattice. Scattering of X-rays results from electron density differences of the stack (figure 3.11).



This scattering obeys Bragg's law;

$$n\lambda = 2d\sin\theta \quad \dots\dots\dots (3.26)$$

where  $n$ , the order of diffraction,  $\lambda$  is the wavelength of radiation,  $d$  is the periodicity of array,  $2\theta$  is the diffraction angle. Generally the crystal thickness of most alkanes lies between 10 – 30 nm, so that the angle  $\theta$  is less than  $2^\circ$ . Hence small angle scattering is involved.

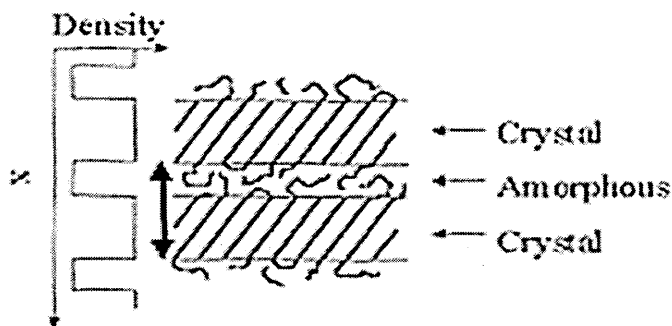


Fig 3.11: Variation of electron density across a lamellar stack.

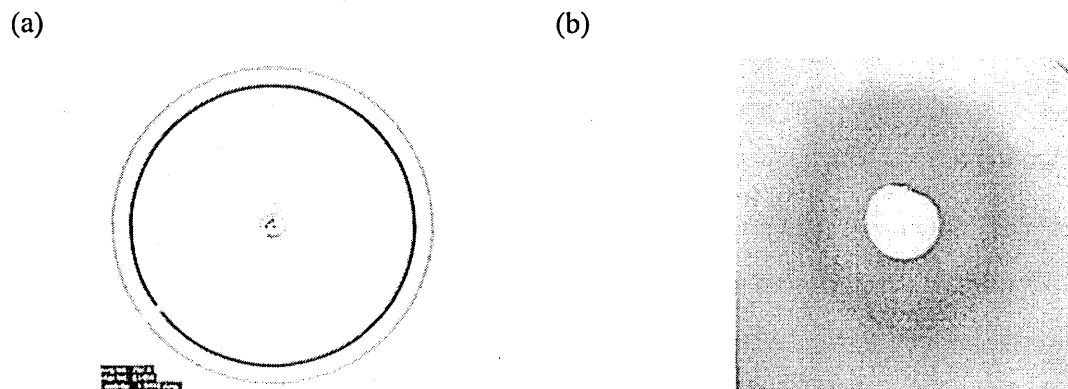


Fig 3.12: Wide angle X-ray diffraction pattern of (a) *n*-alkane<sup>37</sup> (b) atactic polystyrene<sup>38</sup>.

X-ray diffraction patterns from a polymer crystal shows dark rings superimposed on a background of diffuse X-ray scattering and an amorphous halo (fig. 3.12(b)). But in the XRD pattern of a long *n*-alkane we cannot identify this amorphous halo as there is very little amorphous material (fig. 3.12(a)).

## References

- 1 Fundamentals of Molecular Spectroscopy, Banwell CN, 2<sup>nd</sup> edition, McGraw-Hill Book Company (UK) Limited (1972)
- 2 Infrared Spectroscopy, George WO, McIntyre PS, John Wiley & Sons, Great Britain (1987)
- 3 Internal Reflection Spectroscopy, Harrick NJ, Harrick Scientific Corporation, New York (1987)
- 4 Tasumi M, Krimm S, J. Polym. Sci. A-2, **6**, 995 (1968)
- 5 Spells SJ in "Characterisation of Solid Polymers", ed. Spells SJ, Chapman and Hall, London (1994)
- 6 Hiebert GL, Hornig DF, J. Chem. Phys., **20**, 918 (1952)
- 7 Tasumi M, Krimm S, J. Chem. Phys., **46**, 755 (1967); and J. Polym. Sci., A-2, **7**, 1785 (1968)
- 8 Sadler DM, Keller A, Macromolecules, **10**, 1128 (1977)
- 9 Bank MI, Krimm S, J. Polym. Sci., A-2, **7**, 1785 (1969)
- 10 Spells SJ, Sadler DM, Keller A, Polymer, **21**, 1121 (1980)
- 11 Spells SJ, Keller A, Sadler DM, Polymer **25**, 749 (1984)
- 12 Cheam TC, Krimm S, J. Polym. Sci. Polym. Phys. Edn. **19**, 423 (1981)
- 13 Spells SJ, Polymer (commun.), **25**, 162 (1984)
- 14 Sheppard QN, Advan. Specry. **1**, 288 (1959)
- 15 Snyder RG, Goh MC, Srivatsavoy VJP, Strauss HL, Dorset DL, J. Phys. Chem., **96**, 10008 (1992)
- 16 Snyder RG, J. Chem. Phys. **47**, 1316 (1967)
- 17 Cates DA, Strauss HL, Snyder RG, J. Phys. Chem. **98**, 4483 (1994)
- 18 Maroncelli M, Qi SP, Strauss HL, Snyder RG, J. Am. Chem. Soc., **104**, 6237 (1982)
- 19 Painter PC, Havens J, Hart WW, Koenig JL, J. Polym. Sci., **15**, 1223 (1977)
- 20 Spells SJ, Organ SJ, Keller A, Zerbi G, Polymer **28**, 697 (1987)
- 21 Ungar G, Organ SJ, Polym. Commun. **28**, 232 (1987)
- 22 Gorce J-P, Spells SJ, Polymer **43**, 2581 (2002)
- 23 Zerbi G, Conti G, Minoni G, Pison S, Bigotto A, J. Phys. Chem. **91**, 2386 (1987)
- 24 Senak L, Davies MA, Mendelsohn R, J. Phys. Chem. **95**, 2565 (1991)
- 25 Barron C; Spells SJ, J. Phys. Chem. **97**, 6737 (1993)
- 26 Muller A, Proc. R. Soc. London Ser. A, **138**, 514 (1932)
- 27 Ubbelohde AR, Trans. Faraday Soc. **34**, 282 (1938)

- 28 Snyder RG, Maroncelli M, Qi SP, Strauss HL, Science, **214**, 188 (1981)
- 29 Kim Y, Strauss HL, Snyder RG, J. Phys. Chem. **93**, 7520 (1989)
- 30 Ungar G, Stejny J, Keller A, Bidd I, Whiting MC, Science, **229**, 386c (1985)
- 31 Ungar G, Organ SJ, Polym. Commun., **28**, 232 (1987)
- 32 Gorce JP, Spells SJ, Polymer, **43**, 2581 (2002)
- 33 Zeng XB, Ungar G, Phys. Rev. Letters, **86**, 4875 (2001)
- 34 Hirata S, Iwata S, J. Chem. Phys., **108**, 7901 (1998)
- 35 De Silva DSM, Gorce J-P, Wickramarachchi PASR, Spells SJ, Macromol. Symp. **184**,67 (2002)
- 36 Undergraduate Instrumental Analysis, 5<sup>th</sup> Edition, Robinson JW, Marcel Dekker, Inc., New York (1995)
- 37 This was supplied by Dr. Zeng XB, University of Sheffield, UK
- 38 Introduction to polymers, Young RJ, Lovell PJ, 2<sup>nd</sup> Edition, Chapman and Hall, UK (1991)

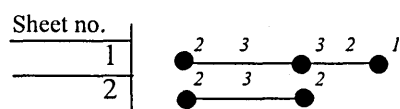
## Appendix

### Conversion of an irregular group to an equivalent group using the number of interactions of each stem in the specified group

Here we consider;

- sheets of stems
- only some stems are indicated by dark spots (●) here
- figures in italics are the number of (110) interactions experienced by each stem

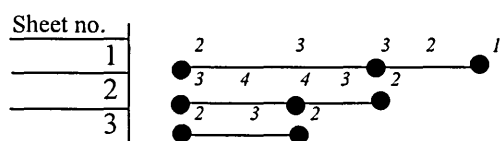
#### 1) Two sheet equivalent group model



$$\text{No. of stems in sheet 2} = \frac{\text{No. of (3) interactions} + 3}{2}$$

$$\text{No. of stems in sheet 1} = \text{No. of stems in sheet 2} + \text{No. of (2) interactions} - 2$$

#### 2) Three sheet equivalent group model

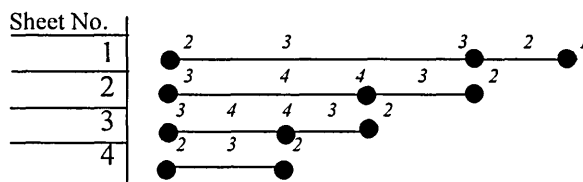


$$\text{No. of stems in sheet 2} = \frac{\text{No. of (3) interactions} + 3}{2}$$

$$\text{No. of stems in sheet 1} = \text{No. of stems in sheet 2} + \text{No. of (2) interactions} - 3$$

$$\text{No. of stems in sheet 3} = \text{No. of (4) interactions} + 1$$

## 3) Four sheet equivalent group model



$$\text{No. of stems in sheet 2} = \frac{\text{No. of (3) interactions} + 3}{2}$$

$$\text{No. of stems in sheet 1} = \text{No. of stems in sheet 2} + \text{No. of (2) interactions} - 4$$

$$\text{No. of (4) interactions} + 2 = \text{No. of stems in sheet 3} + \text{No. of stems in sheet 4}$$

**Example:- Conversion of the irregular group E in fig. 6.15 to an equivalent group**

No. of interactions with the neighbouring stems	No. of stems
4	4
3	19
2	18
1	5

Most of the stems in group E are distributed among three sheets. Therefore this was considered as a three sheet model.

$$\begin{aligned} \text{No. of stems in sheet 2} &= \frac{\text{No. of (3) interactions} + 3}{2} \\ &= (19 + 3) / 2 \\ &= 11 \end{aligned}$$

$$\begin{aligned} \text{No. of stems in sheet 1} &= \text{No. of stems in sheet 2} + \text{No. of (2) interactions} - 3 \\ &= 11 + 18 - 3 \\ &= 26 \end{aligned}$$

$$\begin{aligned} \text{No. of stems in sheet 3} &= \text{No. of (4) interactions} + 1 \\ &= 4 + 1 \\ &= 5 \end{aligned}$$

Note that as fractions of stems are not permitted, the numbers must be rounded up or down to the nearest integer. By adjusting them specially in opposite directions, any errors introduced in calculating splittings are minimized.

### Vibrational Spectrum of the Short Chain Alkane, C<sub>34</sub>H<sub>70</sub> and the mixture, C<sub>34</sub>H<sub>70</sub>/C<sub>36</sub>D<sub>74</sub>

#### 4.1 Determination of phase transitions in C<sub>34</sub>H<sub>70</sub> by vibrational spectroscopy

##### 4.1.1 Introduction

Solid n-alkanes with the general formula C<sub>n</sub>H<sub>2n+2</sub> show polymorphism<sup>1</sup>. All the odd paraffins between C<sub>9</sub> and C<sub>39</sub> possess an orthorhombic structure while a monoclinic and a triclinic form exist for even paraffins at lower temperatures. The alkanes below C<sub>26</sub> crystallise with a triclinic structure and chains with more than 26 carbon atoms adopt a monoclinic form with an orthorhombic subcell<sup>1</sup>. Polyethylene has an orthorhombic unit cell containing two molecules<sup>2</sup>. The CH<sub>2</sub> rocking and bending modes in the vibrational spectrum of alkanes with an orthorhombic and/or monoclinic crystal form and of polyethylene show crystal field splitting<sup>3</sup>. Boerio and Koenig studied the effect of crystal structure on the CH<sub>2</sub> bending mode in Raman spectrum. They monitored the crystal field splitting of several crystal forms by Raman spectroscopy and reported Raman frequencies of the methylene bending mode for crystalline polyethylene and several alkanes as given in Table 4.1<sup>4</sup>.

Kim et al have identified several conformational bands due to different CH<sub>3</sub> rocking vibrations in the frequency region 900 – 830 cm<sup>-1</sup> in the Raman spectrum of C<sub>50</sub>H<sub>102</sub> and a binary n-alkane mixture<sup>5</sup>. Separate Raman bands were observed for *tt*-, *gt*-, *gg*- and *tg*-chain ends of an otherwise all-*trans* chain. They are tabulated in Table 4.2. In addition, there are two more areas which show conformational dependence in the Raman spectrum. They are the CH<sub>2</sub> twisting mode at 1300 cm<sup>-1</sup> and the C-C stretching mode in the range 1000 – 1200 cm<sup>-1</sup>. The CH<sub>2</sub> twisting band is a combination of two vibrational modes: 1295 cm<sup>-1</sup> crystalline and 1305 cm<sup>-1</sup> *gauche* counterpart<sup>6</sup>. This Raman line is sharp and strong for solid polymethylene systems. With the incorporation of conformational disorder it slightly broadens and the melt spectrum is dominated by the 1305 cm<sup>-1</sup> band. However, Strobl and Hagedorn have experimentally verified that the

overall intensity in this spectral range for polyethylene is conformer - and thus temperature - independent<sup>7</sup>.

Table 4.1: Methylene bending frequencies in the Raman spectrum at three different temperatures<sup>4</sup>.

Sample	Unit cell	Frequency (cm <sup>-1</sup> )		
		59°C	25°C	-160°C
<i>n</i> -C <sub>20</sub> H <sub>42</sub>	Triclinic		1484 1463 1445	1484 1478 1470 1451 1447
<i>n</i> -C <sub>28</sub> H <sub>58</sub>	Hexagonal	1458 1438		
<i>n</i> -C <sub>28</sub> H <sub>58</sub>	Monoclinic		1462 1441 1418	1472 1466 1443 1414
<i>n</i> -C <sub>23</sub> H <sub>48</sub>	Orthorhombic		1470 1463  1441 1420	1470 1465 1456 1443 1416
Polyethylene	Orthorhombic		1463 1441 1418	1467 1442 1414

Table 4.2: Constant-frequency methyl rocking modes of alkanes<sup>5</sup>.

Chain-end conformation	Observed frequency (cm <sup>-1</sup> )		Calculated frequency (cm <sup>-1</sup> )
	C <sub>21</sub> H <sub>44</sub> <sup>a</sup>	C <sub>50</sub> H <sub>102</sub> <sup>b</sup>	
<i>tt</i>	891	891 <sup>c</sup>	892
<i>gt</i>	875	871	879
<i>gg</i>	862	862	862
<i>tg</i>	843	845	850

<sup>a</sup> observed for rotator phase, <sup>b</sup> observed for the C<sub>50</sub>/C<sub>46</sub> mixture at 23°C and for neat C<sub>50</sub> at 80°C,

<sup>c</sup> the observed frequency is 891 cm<sup>-1</sup> for the C<sub>50</sub>/C<sub>46</sub> mixture at 23°C and for neat C<sub>50</sub> at 80°C and 894 cm<sup>-1</sup> for neat C<sub>50</sub> at 23°C.



The C-C stretching region from 1000 to 1200  $\text{cm}^{-1}$  comprises of two strong bands at 1060 and 1130  $\text{cm}^{-1}$  arising from *trans* C-C bonds and a broad band centred around 1080  $\text{cm}^{-1}$  due to *gauche* conformers<sup>6,8</sup>. The intensity of the 1080  $\text{cm}^{-1}$  band increases with increasing temperature whereas the two strong bands become progressively weaker. The melt spectrum is dominated by a broad band centred around 1080  $\text{cm}^{-1}$ .

The presence of an intermediate phase just below the melting point in n-alkanes is now well known. Since Müller first reported about it<sup>9</sup>, its nature and structure have been studied by X-ray scattering<sup>10-14</sup>, neutron scattering<sup>15,16</sup>, infrared and Raman spectroscopy<sup>17-20</sup>, N.M.R<sup>21-24</sup> and dielectric absorption<sup>25</sup>.

The vibrational spectroscopic investigations on what is now recognised as the rotator phase have mainly focussed on the disappearance of the correlation splitting of the CH<sub>2</sub> bending and rocking modes at the phase transition<sup>26,27</sup>. The solid-solid phase transition is also accompanied by a change in the degree of chain disorder. The disorder within the rotator phase has been extensively studied by infrared spectroscopy<sup>17,28-30</sup>. CH<sub>2</sub> wagging modes are important in this regard. A detailed analysis of these modes is given in Chapter 3.1.3. In addition, CH<sub>2</sub> rocking-twisting and wagging progressions are good indicators of the different phases<sup>28,31</sup> (a detailed explanation of progression bands is given in section 4.2).

Maissara and Devauve have used the CH<sub>3</sub> rocking modes in the Raman spectrum to study crystalline n-alkanes in the rotator phase<sup>32</sup>. Kim et al also observed these conformational bands in the Raman spectrum of n-C<sub>21</sub>H<sub>44</sub> for the high-temperature disordered phase<sup>5</sup>. In addition, a second set of bands assigned to CH<sub>2</sub> rocking progressions were also observed at the rotator phase but were not observed in the ordered solid phase<sup>5</sup>. These analyses have been mainly based on short alkanes (< C<sub>34</sub>). However, a detailed Raman spectroscopic analysis of conformational changes associated with phase transitions on short chain alkanes has not been reported. Such a study was recently reported for ultrahigh-molecular-weight polyethylene (UHMW-PE)<sup>33</sup>.

Here we aim to study the phase transitions of a short chain alkane using vibrational techniques. The main objective of it is to select a suitable technique to study the phase transition of long chain branched alkanes at a later stage in our research. Firstly, we

focussed on ATR-FTIR. The main reason for using ATR instead of transmission-FTIR is the ability to set the sample horizontally on the ATR crystal. In transmission – FTIR the sample is set vertically in a cryostat so that when it has melted the sample may leak out thereby losing some of the sample thus the intensity in the infrared spectrum. The other advantage of ATR-FTIR is the ability to obtain uniform temperature control. However, in our study we failed to detect the phase transition clearly by analysing wagging modes using ATR-FTIR. In addition, we observed a broadening of some of the vibrational modes in the ATR-FTIR spectrum. Due to above reasons we shifted our analysis to Raman spectroscopy.

#### 4.1.2 ATR-FTIR measurements on $C_{34}H_{70}$

##### 4.1.2.1 Experimental

$C_{34}H_{70}$  was purchased from Sigma Chemical Company. The purity is 99%. A few milligrams of this sample was melt crystallised on to the ATR crystal. The sample was heated continuously until melting and then cooled at  $0.2^{\circ} \text{C min}^{-1}$ . The spectra were collected at  $1^{\circ} \text{C}$  interval during both runs.

##### 4.1.2.2 Results and Discussion

$\text{CH}_2$  defect modes region from  $1300 - 1400 \text{ cm}^{-1}$  in the FTIR spectrum was analysed. The wagging modes corresponding to  $gtg : 1368 \text{ cm}^{-1}$ ,  $gg : 1352 \text{ cm}^{-1}$  and  $gt : 1341 \text{ cm}^{-1}$  were identified in the FTIR spectrum of  $C_{34}H_{70}$ . This region is illustrated in figure 4.1 at three different temperatures. The above defect modes are marked with an asterisk. We can see that the intensity of the defect modes increases with increasing temperature. The area of each of these bands was determined by curve fitting. Figure 4.2 depicts the variation of the area of each band with temperature. We can see a significant increase of the area of all the bands at melting ( $\sim 74^{\circ} \text{C}$ ). From  $55^{\circ}$  to  $65^{\circ} \text{C}$  there is no noticeable change. Around  $67^{\circ} \text{C}$  a sudden increase of the area of the  $1368 \text{ cm}^{-1}$  band could be noticed. However this change is not very prominent and no upward trend could be identified in the other two bands.

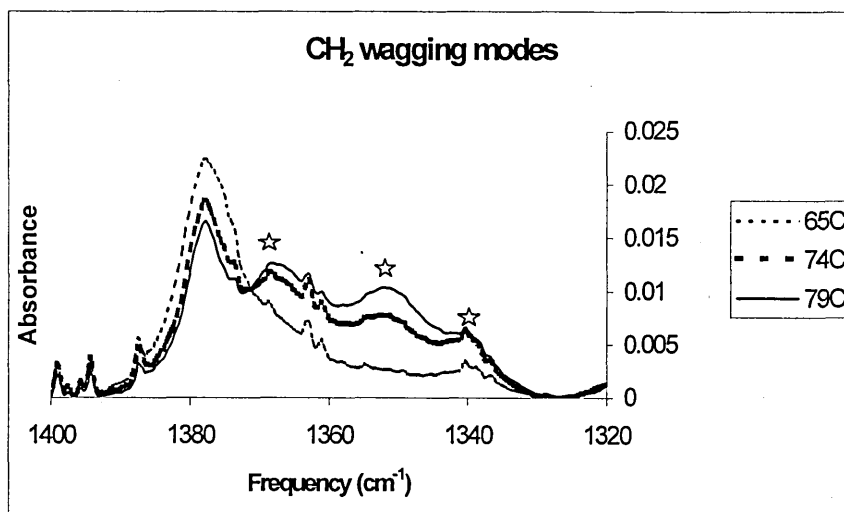


Fig 4.1: The  $\text{CH}_2$  wagging region of the FTIR spectrum of  $\text{C}_{34}\text{H}_{70}$  at  $65^\circ$ ,  $74^\circ$  and  $79^\circ$  C. Stars correspond to the defect modes.

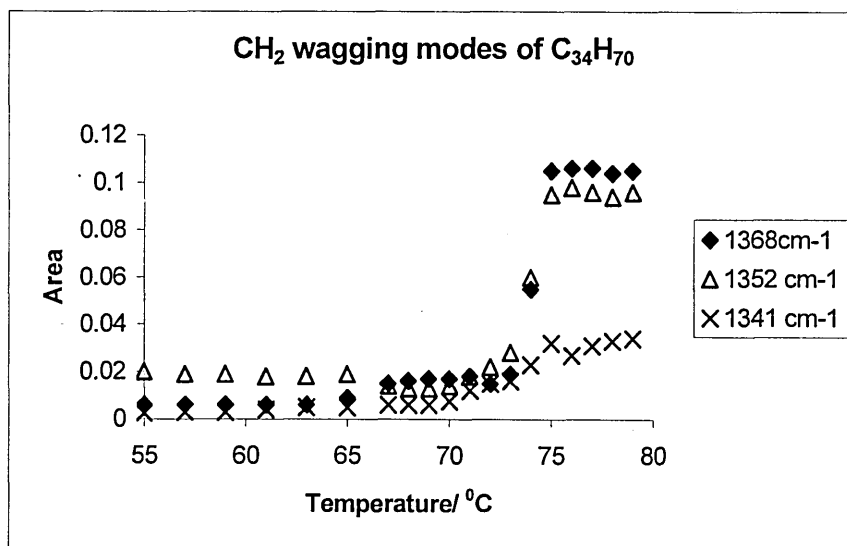


Fig 4.2: Variation of area of the  $\text{CH}_2$  wagging modes with temperature for  $\text{C}_{34}\text{H}_{70}$ .

$\text{CH}_2$  rocking doublet at  $720/730\text{ cm}^{-1}$  which is also generally sensitive to the rotator phase transition showed no indication of a rotator phase transition here to support the above observation. Snyder et al also report the difficulty of using these wagging modes, which are normally used to analyse conformational disorder in relatively short chain

alkanes<sup>31</sup>, in a mixture of rather longer alkanes<sup>34</sup>. They heavily relied on Raman spectra in this case.

In addition, we could observe some of the bands in the ATR-FTIR spectrum of  $C_{34}H_{70}$  are broadened. In order to compare it, another sample of  $C_{34}H_{70}$  prepared by melt crystallising on to a KBr disc under similar conditions, was measured using transmission-FTIR. The corresponding spectra are illustrated in figure 4.3.

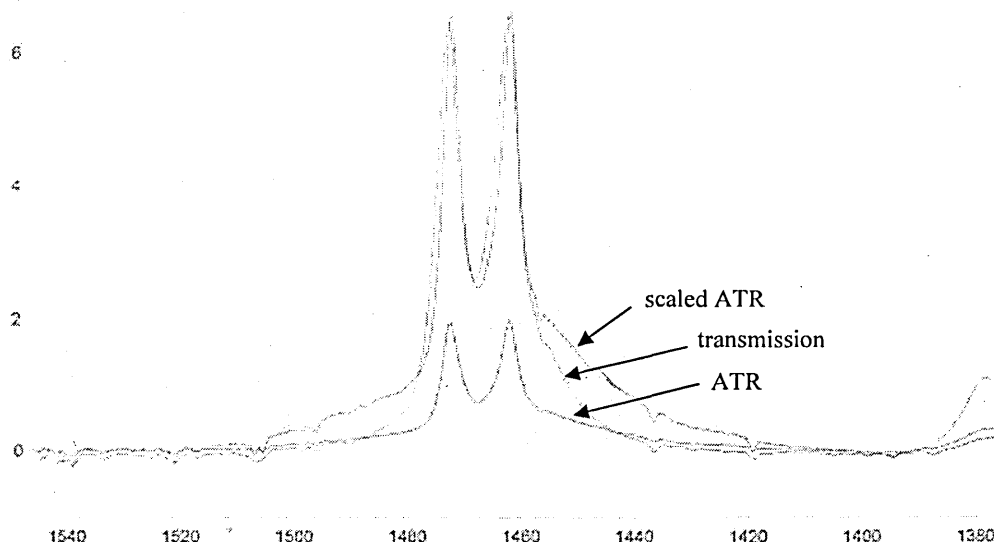


Fig 4.3: ATR-FTIR and transmission-FTIR spectra of  $C_{34}H_{70}$ .

This broadening is mainly due to the dispersion of the refractive index. The effect of dispersion on the resulting ATR spectrum has been demonstrated by Mirabella<sup>35</sup> with measurements on polypropylene near the critical angle. Any measured optical quantity such as absorption, transmittance or reflectance, is a complicated function of the refractive index ( $n$ ) and the absorption index ( $k$ ) of the material. A detailed analysis of absorption behaviour of materials in the mid-infrared region using different infrared techniques was done by Brogly et al<sup>36</sup>. They prove that these differences among spectra from different infrared techniques are entirely due to optical effects and not true sample differences. However, the influence of optical dispersion on transmission spectroscopy is typically small so that it is often ignored. Due to the fact that the phase transition of

$C_{34}H_{70}$  was not clear and in view of the band broadening effect in ATR it was decided to investigate for Raman spectroscopy for our analysis on  $C_{34}H_{70}$ .

#### 4.1.3 Raman measurements on $C_{34}H_{70}$

##### 4.1.3.1 Experimental

About 3mg of  $C_{34}H_{70}$  crystals straight from the bottle were placed on the lid of a DSC pan (Mettler design). This formed the sample holder which was used here. It was covered by a circular aluminium foil to obtain a better temperature control. The diameters of the sample holder and the aluminium foil were roughly equal. A small hole with a 2 mm diameter was made on the aluminium foil to allow the passage of light through. The spectra were collected as a function of temperature between 55<sup>o</sup> and 80<sup>o</sup> C using a Renishaw Raman Spectrometer. The sample was heated step-wise, at a rate of 5<sup>o</sup> C min<sup>-1</sup> between data collection, using a Linkam hot stage. The hot stage was fixed on to an Olympus microscope stage. The Raman spectra were recorded at every 1<sup>o</sup> C. A diode laser at 785 nm was used as the excitation source. Laser light was focussed on the sample using a 20× microscope objective. The spectra were measured between 1700 and 150 cm<sup>-1</sup> with a resolution of 2 cm<sup>-1</sup>. A cooling run was also carried out using similar experimental conditions. The analysis of the Raman spectra involved baseline correction and curve fitting procedures. The curve fitting was performed using GRAMS 32 software.

---

##### 4.1.3.2 Results and Discussion

Our first aim was to identify the spectral bands in the Raman spectrum as this is our first Raman study on an alkane. A Raman spectrum was collected at room temperature in the region 1700 to 150 cm<sup>-1</sup>. The room temperature spectrum between 1700 and 700 cm<sup>-1</sup>, the area which we are most interested in, is shown in figure 4.4. The observed bands were assigned to relevant vibrational modes as given in Table 4.3.

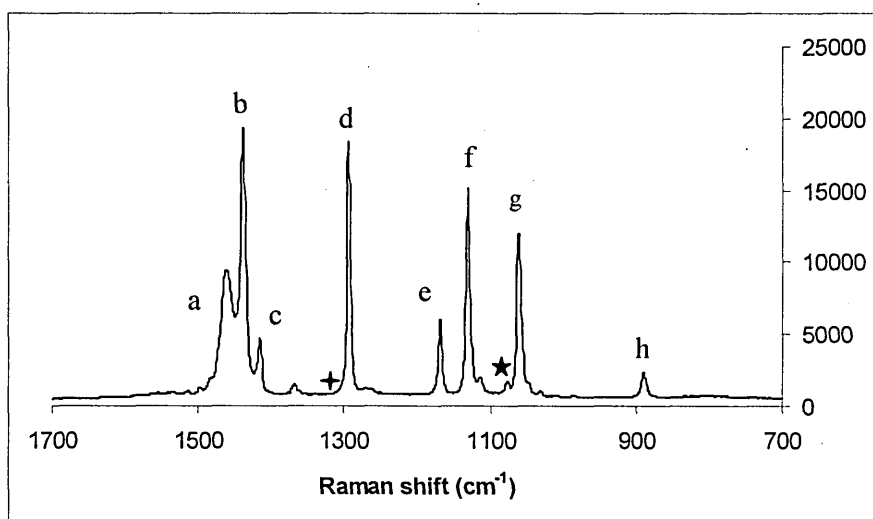


Fig 4.4: The room temperature Raman spectrum of  $C_{34}H_{70}$ .

Table 4.3: The observed frequencies and the vibrational modes of  $C_{34}H_{70}$  at room temperature.

Frequency ( $\text{cm}^{-1}$ )	Vibrational mode
1460 (a)	$\text{CH}_2$ bending <sup>4</sup>
1438 (b)	
1418 (c)	
1305 (+)	$\text{CH}_2$ twisting – amorphous counterpart
1295 (d)	$\text{CH}_2$ twisting – crystalline band <sup>37</sup>
1170 (e)	$\text{CH}_2$ rocking – crystalline <sup>37</sup>
1131 (f)	C-C stretching; symmetric- crystalline <sup>37</sup>
1080(★)	C-C stretching – conformationally disordered chains <sup>8</sup>
1062 (g)	C-C stretching;antisymmetric – crystalline <sup>37</sup>
892 (h)	$\text{CH}_3$ rocking – <i>tt</i> conformation <sup>5</sup>

The phase transition of  $C_{34}H_{70}$  at high temperature will be discussed in terms of the spectral region between 700 and 1700  $cm^{-1}$ . This area can be divided into four different regions. The first region, is the complex bending vibrational triplet which lies between 1400 and 1500  $cm^{-1}$ . The second region of interest is the  $CH_2$  twisting vibration which is observed as a strong sharp peak in the room temperature spectrum. According to the literature this region is independent of conformational changes and is thus used as an internal standard<sup>7,38</sup>. However, in this study, we observed a slight broadening of the 1295  $cm^{-1}$  band at the solid-solid phase transition and a significant change in this region in the melt. The third region mainly comprises the C-C skeletal vibration mode from 1000 to 1200  $cm^{-1}$ . It shows two strong sharp bands at 1060 and 1130  $cm^{-1}$  corresponding to in-phase and out-of-phase C-C stretching respectively. In the melt, the broad band around 1080  $cm^{-1}$  becomes prominent and the 1060 and 1130  $cm^{-1}$  bands have nearly disappeared. The last region falls around 890  $cm^{-1}$  where we can observe changes in the  $CH_3$  rocking vibration with the conformational changes at the chain end of the alkane at transition temperatures. However, this band cannot be observed in polyethylene and long chain n-alkanes.

$C_{34}H_{70}$  has a monoclinic crystal form at low temperature<sup>1</sup>. It transforms to an orthorhombic structure at 69.2<sup>0</sup> C and the orthorhombic to hexagonal transition occurs at 69.6<sup>0</sup> C. It melts at 72.9<sup>0</sup> C<sup>1</sup>. Our first task was to identify the phase transitions of  $C_{34}H_{70}$  by Raman spectroscopy. For this purpose we analysed the Raman spectrum in the above - mentioned four regions and the changes accompanying the phase transitions will be discussed below.

#### $CH_2$ bending region (1600 – 1400 $cm^{-1}$ )

This region is somewhat complicated by combination bands and overtones, in particular the presence of a Fermi resonance of the IR active  $CH_2$  rocking doublet at 720/730  $cm^{-1}$ <sup>33,26</sup>. However, a well resolved triplet can be identified at 1460, 1438 and 1418  $cm^{-1}$  in this region. There is no doubt concerning the two narrow bands at 1438 and 1418  $cm^{-1}$  as the  $CH_2$  bending doublet<sup>4,7</sup>. Boerio and Koenig reported the dependency of the 1418  $cm^{-1}$  band on the crystal structure<sup>4</sup> (see Table 4.2). The disappearance of the 1418  $cm^{-1}$  (denoted by a star in figure 4.5) at the monoclinic to hexagonal transition was the key to

the identification of the phase transformation. In the rotator phase the  $1418\text{ cm}^{-1}$  band has disappeared but the  $1460$  and  $1438\text{ cm}^{-1}$  bands are still resolved. A small shift of the  $1460\text{ cm}^{-1}$  band can be observed at the phase transition (as indicated by the dotted line in figure 4.5). In the melt the bending triplet has completely disappeared and instead a broad band can be identified centred around  $1438\text{ cm}^{-1}$ .

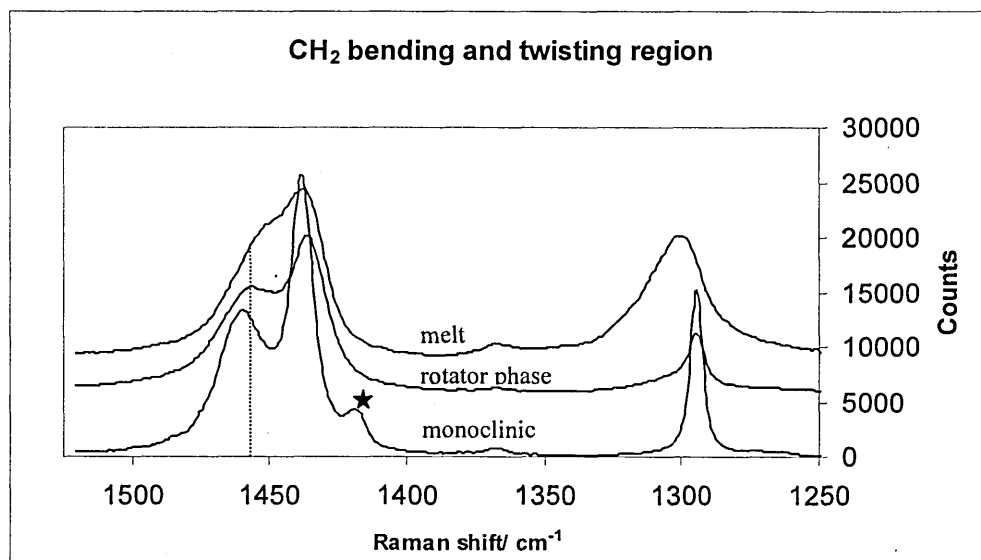


Fig 4.5: CH<sub>2</sub> bending and twisting region of the Raman spectra of C<sub>34</sub>H<sub>70</sub> in monoclinic, rotator and melt phases at 62<sup>o</sup>, 71<sup>o</sup> and 76<sup>o</sup> C respectively.

The changes in the band positions of the bending triplet with variation of temperature are graphically denoted in figure 4.6. We can see that the  $1418\text{ cm}^{-1}$  band disappears at 67<sup>o</sup> C during heating whereas in cooling it appears at 69<sup>o</sup> C. These changes indicate the onset of rotator phase. This is accompanied by shifts in the  $1460$  and  $1438\text{ cm}^{-1}$  bands. The  $1438\text{ cm}^{-1}$  band shifts to lower frequency at the phase transition and remains constant over the rest of the temperature range. The  $1460\text{ cm}^{-1}$  band shows two steps in its frequency-temperature curve. The first step denotes the monoclinic to hexagonal transition whereas the second shows the onset of melting/crystallisation. In figure 4.6 we can see frequency-temperature curves corresponding to the  $1460$  and  $1438\text{ cm}^{-1}$  bands, for the heating run shows a rather gradual change in slope at the phase transitions while the corresponding cooling curves show a sudden step.



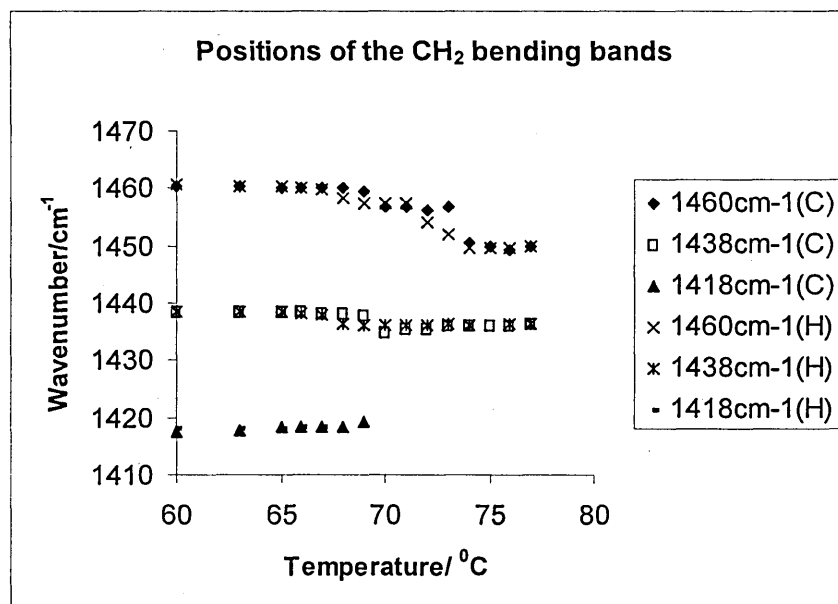


Fig 4.6: The changes in the band positions of the  $\text{CH}_2$  bending triplet with temperature. C-cooling, H-heating.

#### $\text{CH}_2$ twisting region ( $1300\text{ cm}^{-1}$ )

The monoclinic phase spectrum of  $\text{C}_{34}\text{H}_{70}$  shows only a narrow peak at  $1295\text{ cm}^{-1}$ . In the rotator phase we can see the broadening of this band indicating the appearance of a  $1305\text{ cm}^{-1}$  band resulting from conformationally disordered chains (figure 4.5). In the melt the  $1305\text{ cm}^{-1}$  band dominates. The changes of this region with increasing temperature is given in figure 4.7. According to figure 4.7 there is no sign of the  $1305\text{ cm}^{-1}$  band until  $68^\circ\text{C}$  during the heating whereas in cooling it disappears at  $68^\circ\text{C}$ . Below  $68^\circ\text{C}$  we can only see the  $1295\text{ cm}^{-1}$  band. This is not surprising at all with the high crystallinity of short chain alkanes at lower temperatures. This appearance/disappearance of the  $1305\text{ cm}^{-1}$  band coincides with the reduction/increase in the area of the  $1295\text{ cm}^{-1}$  band. This marks the phase transition to the rotator phase at  $68^\circ\text{C}$ . The area of the  $1295\text{ cm}^{-1}$  band decreases throughout the rotator phase during heating while it remains constant in cooling.

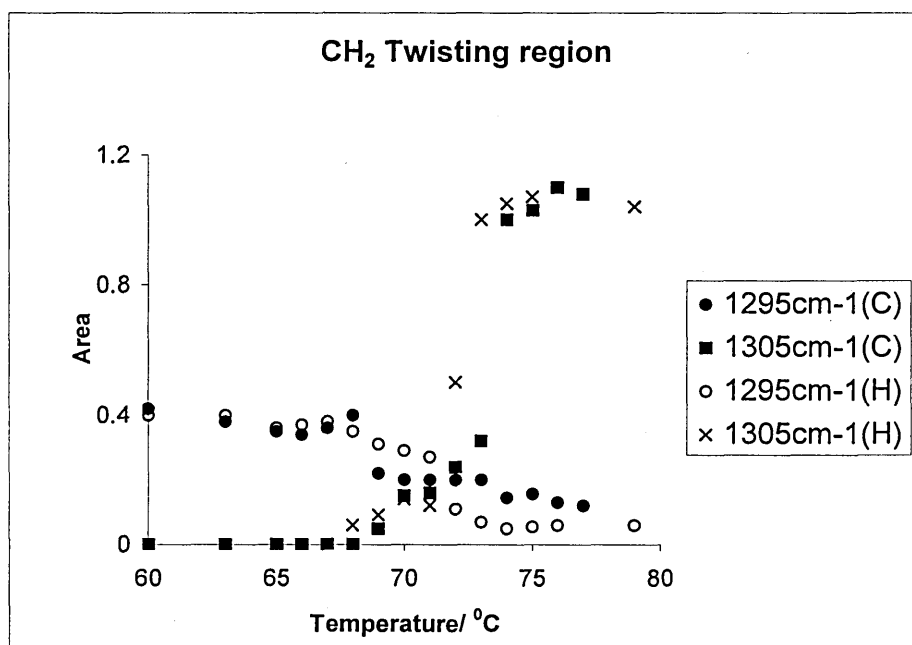


Fig 4.7: The variation of the area of 1295 and 1305  $\text{cm}^{-1}$  bands with temperature.

The area of the 1305  $\text{cm}^{-1}$  band slightly increases throughout the rotator phase in both runs and followed by a large increase. This indicates the melting of the crystals. The area of the 1295  $\text{cm}^{-1}$  band slightly decreases at melting. Within the rotator phase major portion of chains retain the all-*trans* conformation and only a small proportion deviate from planarity. This supports the observed small reduction and slight increase of the areas of the 1295 and 1305  $\text{cm}^{-1}$  bands respectively. At melting, a large proportion of chains adopts a *gauche* conformation. This causes a large increase in the area of the 1305  $\text{cm}^{-1}$  band.

In figure 4.5 we could observe this band around 1300  $\text{cm}^{-1}$  slightly broadens with the transition to the rotator phase and it is very broad in the melt spectrum. Therefore the band width was interesting with a view to identifying the phase transition. This broadening mainly occurs at the base of the band thus the width at 10% height was monitored with temperature. It is plotted in figure 4.8 below.

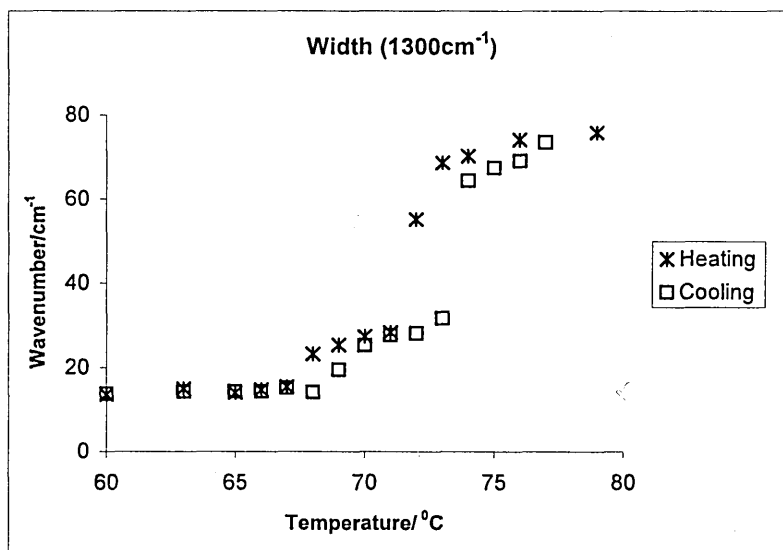


Fig 4.8: The variation of the width of the  $1300\text{ cm}^{-1}$  band at 10% of its height with temperature.

The changes of the width of the  $1300\text{ cm}^{-1}$  band are very interesting. It shows the transitions very clearly. The width remains constant until the rotator phase transition temperature and it slightly increases through the rotator phase. The melting/crystallisation is indicated by a large increase/reduction of the width. However, this is not a very good parameter as the  $\text{CH}_2$  twisting mode is a combination of two bands and the height of its gauche component ( $1305\text{ cm}^{-1}$ ) changes with temperature. Therefore these results are purely empirical.

The skeletal C-C stretching mode ( $1200 - 1000\text{ cm}^{-1}$ )

The Raman spectrum of  $\text{C}_{34}\text{H}_{70}$  in the region  $1000 - 1200\text{ cm}^{-1}$  is depicted in figure 4.9. We are mainly interested in  $1130$ ,  $1060$  and  $1080\text{ cm}^{-1}$  (marked by an asterisk) bands. The origin of these bands was discussed above. The  $1080\text{ cm}^{-1}$  band shows significant changes when going from monoclinic phase – rotator – melt. This becomes dominant in the melt spectrum while signs of  $1130$  and  $1060\text{ cm}^{-1}$  bands are still observable.

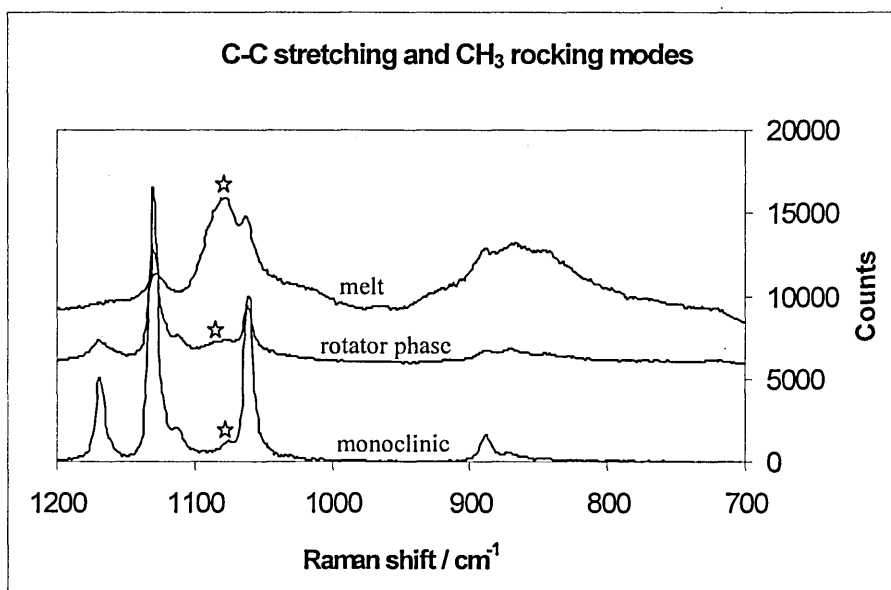


Fig 4.9: The C-C stretching and  $CH_3$  rocking modes of  $C_{34}H_{70}$  for different phases at  $62^\circ$ ,  $71^\circ$  and  $76^\circ$  C respectively.

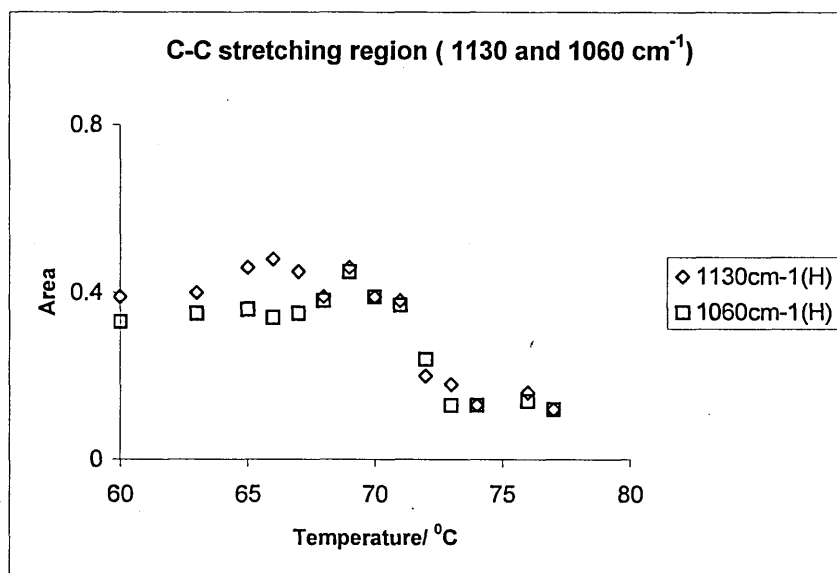


Fig 4.10: Relative area of 1130 and 1060  $cm^{-1}$  C-C skeletal modes of  $C_{34}H_{70}$  vs temperature during heating run.

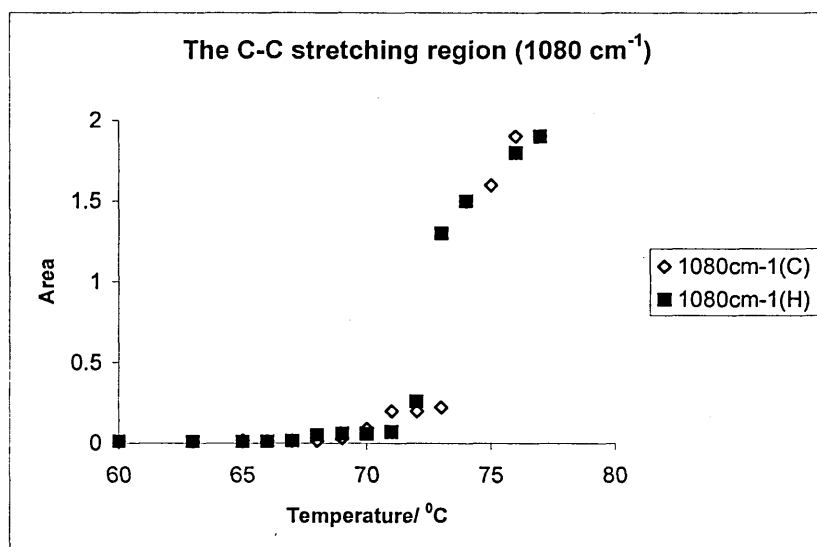


Fig 4.11: Relative area of  $1080\text{ cm}^{-1}$  C-C skeletal mode of  $\text{C}_{34}\text{H}_{70}$  vs temperature.

The relative areas of each of these bands to the total C-C stretching area with temperature are given in figures 4.10 and 4.11. According to figure 4.10 the area of the  $1130$  and  $1060\text{ cm}^{-1}$  bands decreases around  $72^{\circ} - 73^{\circ}\text{ C}$ . This indicates the melting of the crystals whereas there is no sign of phase transition in this figure. The corresponding cooling plot is very noisy so that it is not shown here. In contrast, the relative area of the  $1080\text{ cm}^{-1}$  band is very low at lower temperatures, starts increasing with the onset of the rotator phase and increases drastically on melting. It continues to increase within the melt phase, which suggests the creation of defects at the rotator transition and their increasing numbers in the melt.

The increase of defect content with the onset of the rotator phase is further supported by the behaviour of  $\text{CH}_3$  rocking conformational modes observed around  $890\text{ cm}^{-1}$  in the Raman spectrum. This area is further discussed below.

#### $\text{CH}_3$ Rocking conformations ( $890\text{ cm}^{-1}$ )

The Raman spectra of these modes for each phase is illustrated in figure 4.9. In this region we could identify the vibrational modes of *tt*, *gt*, *gg* and *tg* rocking conformers by curvefitting. They were identified using the frequencies stated in Table 4.2. The

monoclinic phase spectrum of  $C_{34}H_{70}$  (figure 4.9) shows mainly the *tt* band. The *gauche* bands are very low in intensity. The room temperature spectrum shows no sign of *gauche* conformational modes and this region is dominated by the *tt* band (figure 4.4). According to figure 4.11 there are significant numbers of *gauche* conformations in the rotator phase and the proportion further increases in the melt. The relative change (normalised to C-C stretching area) of each type of *gauche* content with temperature is given in figure 4.12.

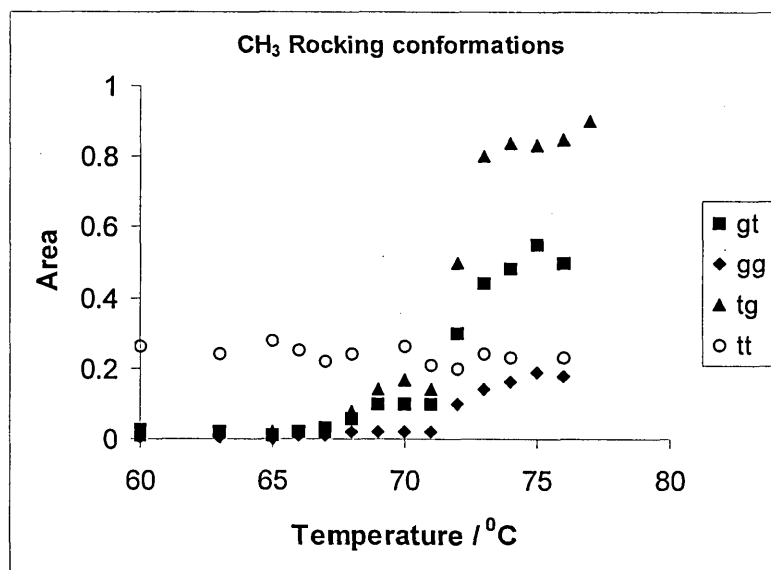


Fig 4.12: Variation of the relative areas of the  $CH_3$  rocking conformations with temperature.

All three defect modes (*gg*, *gt*, *tg*) have small areas at lower temperatures. We can see at  $68^\circ C$ , with the occurrence of the phase transition, there is a marked increase in the concentration of *gauche* forms. This increase is larger for the *gt* and *tg* conformations whereas a smaller increase is observable for the *gg* conformation. Throughout the rotator phase the defect level slowly increases. With the start of melting all these defect modes show a rapid increase with the *tg* conformation showing the largest increase in area. However, the concentration of *tt* conformers remains virtually constant throughout the temperature range. This means that even in the melt still some portions of the chains

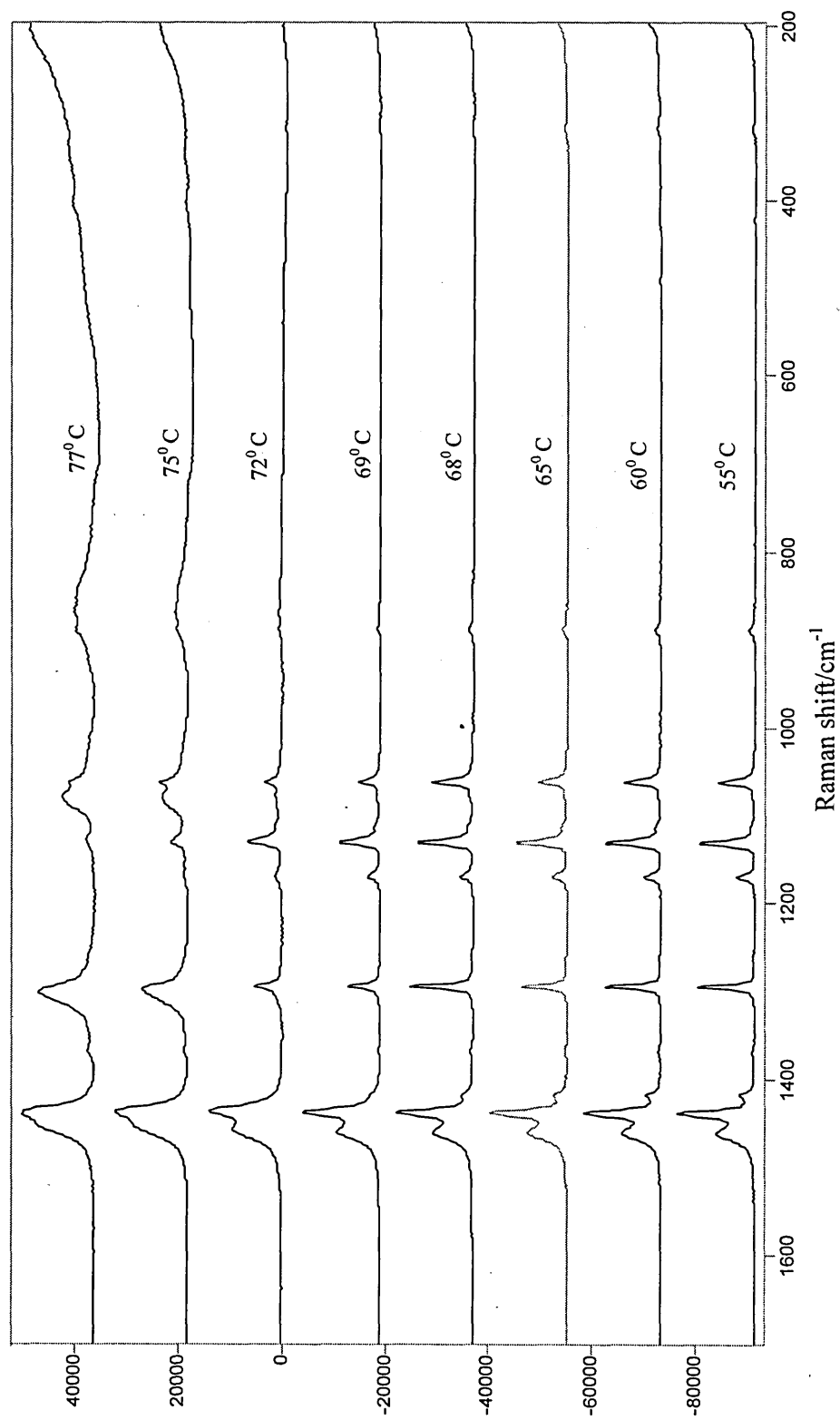


Fig 4.13 : The Raman spectra of  $C_{34}H_{70}$  at different temperatures during heating.

keep the all-*trans* conformation. However, this vibrational mode ( $\text{CH}_3$  *tt* rocking) together with the C-C crystalline bands is not sensitive to the phase transition.

#### 4.1.4 Conclusion

Our aim was to identify the phase transitions of  $\text{C}_{34}\text{H}_{70}$  by vibrational spectroscopy. We used two vibrational techniques: ATR-FTIR and Raman spectroscopy. It turned out that ATR is not very useful in this regard as the solid - solid transition was not very clearly shown by the analysis of methylene wagging modes, probably largely due to band broadening. On the other hand, Raman spectroscopy provided clear evidence of transitions. Therefore we heavily depended on Raman spectroscopy.

The changes of the various Raman bands in the region  $700 - 1700 \text{ cm}^{-1}$  were analysed. A similar analysis has been reported on polyethylene<sup>33</sup>. The key to the identification of the hexagonal phase was the disappearance of the  $1418 \text{ cm}^{-1}$  band of the bending triplet<sup>4</sup>. This is associated with changes in the band positions of bending modes, changes in  $\text{CH}_2$  twisting modes and its band width, C-C skeletal modes and  $\text{CH}_3$  rocking conformations. Our experimental observations suggest that a clear distinction can be made between the monoclinic and rotator phases using the  $1700 - 700 \text{ cm}^{-1}$  region of the spectrum. This is apparent in figure 4.13, where changes at both phase transitions are clearly seen. The monoclinic phase is characterised by the  $1418 \text{ cm}^{-1}$  band of the bending triplet and the disappearance of this band marks the rotator phase transition. All four regions discussed above clearly showed both monoclinic-rotator and rotator-melt transitions. However, we found mainly the defect bands are more sensitive to the rotator transition while the crystalline bands remains virtually constant until melting. The rotator transition was identified at  $68^\circ - 69^\circ \text{ C}$  in heating and  $70^\circ - 69^\circ \text{ C}$  in cooling. The cooling and heating figures for the transition temperatures show a  $1^\circ \text{ C}$  difference. This is somewhat surprising as they should show similar figures. This may be due to the non-uniformity of the temperature in each run.



## 4.2 Analysis of progression bands in the infrared spectrum of $C_{34}H_{70}$ and a mixture of $C_{34}H_{70}/C_{36}D_{74}$

### 4.2.1 Introduction

There are two main types of vibrational modes in the vibrational spectrum of n-alkanes. They are localised and non-localised vibrations. The localised vibrations involve motions that are localised in certain parts of the chain. Examples of them are the  $CH_2$  bending mode, *gtg*, *gg*, *gt* wagging modes and the  $CH_3$  rocking mode around  $890\text{ cm}^{-1}$  in the infrared spectrum and the  $CH_3$  rocking modes in the Raman spectrum (see Table 4.2). The frequency of these vibrations depends only on the local conformation and is independent of both chain length and the conformation of the rest of the molecule.

In contrast to the localised vibrations, the non-localised modes involve the entire chain. Such vibrations may be conformationally sensitive, for example the various progressions of bands mainly in the rocking-twisting ( $P_k$ ), C-C stretching ( $R_k$ ) and  $CH_2$  wagging ( $W_k$ ) regions in the vibrational spectrum. The most common way of labelling these modes are shown within parenthesis accompanying each mode. '*k*' in subscript is any integer which is related to the phase difference between the motions of adjacent methylene groups along the chain<sup>39</sup>(see section 4.2.2). In the infrared spectrum of an all-*trans* conformer, only *k*-odd members of the progression bands are visible in the rocking-twisting region whereas the *k*-even members are forbidden<sup>39</sup>. The chain end disorder activates the *k*-even series and they appear at the expense of the intensities of the *k*-odd modes at higher temperatures. The situation is just the opposite of this in case of Raman spectroscopy<sup>34</sup>. Table 4.4 summarises this situation.

These progression bands are useful in estimating order and disorder in alkane chains. Snyder and co-workers have extensively used these variable-frequency bands to demonstrate the high temperature rotator phase of short chain alkanes<sup>28,31</sup>. Usually the  $CH_2$  rocking-twisting mode shows a well separated series of progressive bands in the region from  $720 - 1030\text{ cm}^{-1}$  in the infrared spectrum.

Table 4.4: Selection rules and observed ir and Raman intensities of the methylene rocking modes for ordered and end-disordered chains<sup>34</sup>.

	Ordered		End-disordered	
	Allowed?	Observed intensity	Allowed?	Observed intensity
Infrared				
<i>k</i> -odd	Yes	Strong	Yes	Medium
<i>k</i> -even	No		Yes	Medium
Raman				
<i>k</i> -odd	No		Yes	Weak
<i>k</i> -even	Yes		Yes	Weak

In the crystalline phase the majority of the molecules are planar. For the planar molecule only odd *k* modes are allowed in the infrared spectrum<sup>39</sup>. In the rotator phase where some molecules are disordered, in addition to odd-*k*, even-*k* bands are also visible in the infrared spectrum. Frequency and intensity calculations have shown that these bands are associated with molecules having end-*gauche* conformations which are otherwise planar<sup>28</sup>.

The infrared and Raman spectra of Nylon, too, are characterised by a series of progression bands. They too are clearly identified and interpreted<sup>40-45</sup>. Yoshioka et al use these progression bands to identify the so - called Brill transition in Nylon<sup>46</sup>. This is very similar to the study of phase transitions of n-alkanes by Snyder et al <sup>28,31</sup>. At room temperature the methylene segments in Nylon chains are packed in a triclinic subcell. As the temperature is increased it gradually changes to a hexagonal<sup>46</sup> structure similarly to n-alkanes. It also shows a progression of bands in a similar region to alkanes (760 – 1150 cm<sup>-1</sup>). It has been observed that the intensity of some of the bands decreases and there is the appearance of new bands which are broad and weak near the transition temperature region as the temperature is raised<sup>46</sup>. This phenomenon has clearly been observed in model compounds of Nylon 10/10 <sup>47</sup>.

Mendelsohn and co-workers have used the infrared wagging band progression to estimate the conformational disorder in the chains in phospholipid bilayers<sup>48</sup>. They showed that with increasing temperature (increasing disorder), the intensities of these bands diminishes while their frequencies are nearly unaffected. Their work is based on the assumption that the progression bands represent all-*trans* chains. However, Snyder et al raised doubts about this method. They suggest that the progression bands represent not only all-*trans* chains but perhaps involve a significant concentration of conformationally disordered chains as well<sup>49</sup>. They have observed that the frequencies of the first four wagging modes ( $k = 1 - 4$ ) of the all-*trans* chain coincide or nearly coincide with the frequencies of the most intense bands in the spectrum of the liquid. All the wagging progression observed in this case must arise from disordered chains as there is little amount of all-*trans* chains present in the liquid.

Gorce and Spells used the C-C stretching/CH<sub>2</sub> twisting progressions to show the 'perfecting' of the crystal with successive annealing/cooling runs of  $n - C_{198}H_{398}$ <sup>50</sup>. They have observed that the regularity of the progression bands significantly improves with heat treatment. The fact that the thermal treatment leads to a 'perfecting' of the crystals has been proved previously by using localised CH<sub>2</sub> wagging bands of  $n - C_{198}H_{398}$  and  $n - C_{246}H_{494}$ <sup>51</sup> and the localised CD<sub>2</sub> bending mode of  $CD_3(CD_2)_{11}(CH_2)_{192}CHD(CD_2)_{10}CD_3$ <sup>52</sup>.

In addition progression bands are useful to determine the all- *trans* chain length of the alkane chain. In the study on progression bands on long chain n-alkanes by Gorce and Spells described above<sup>50</sup>, the authors use the same progression bands in order to estimate the all-*trans* chain length of the alkane by assigning each progression band with an integer. They extended the same method to show that the centre-branched long chain n-alkanes have a folded conformation and a mixture of  $n - C_{162}H_{326}$  and  $n - C_{246}H_{494}$  has a triple layer superlattice structure<sup>50</sup>.

In this study on a short chain alkane we try to identify and assign the progression bands of  $C_{34}H_{70}$  at each crystal phase and calculate the core length of the crystal of a mixture of  $C_{34}H_{70}/C_{36}D_{74}$ . We use the same method used by Gorce and Spells<sup>50</sup>. Here also we assume that the progression bands are representative of all-*trans* chains.

#### 4.2.2 Calculation of the all-*trans* chain length

For the analysis of progression bands a simple coupled oscillator model is used<sup>39</sup>. A local vibrational mode is represented by an oscillator. These oscillators are coupled together with a phase angle  $\Phi$ . The relation between  $\Phi$ , integer  $k$  and the number of carbon atoms,  $n_c$ , in the alkane chain is given below<sup>43</sup>.

$$\Phi_k = \frac{k\pi}{n_c - 1} \quad \dots\dots\dots (4.1)$$

The frequency of the each progression band was identified from the spectrum. Then the corresponding phase difference of each progression band ( $\Phi_k/\pi$ ), was read using the frequency-phase curves calculated by Snyder et al<sup>39</sup>. Our first task was to assign the  $k$  values to each progression band. An initial estimate of 34 was assigned to  $n_c$  (highest possible number of C atoms in all-*trans* conformation in C<sub>34</sub>H<sub>70</sub>). Using equation (4.1) a series of  $k$  values was calculated corresponding to each progression band. This process was then repeated using a new estimate for  $n_c$  ( usually one less than previous estimate). This process was repeated several times to get several iterations for the  $k$  values. The resulting  $k$  values were rounded off to the nearest integer. Then the iteration providing the closest correspondence of the  $k$  values with integers was chosen as the best fit. These integer  $k$  values were then substituted in equation (4.1) to obtain the  $n_c$  for each band. The average  $n_c$  was taken as the best value of all-*trans* length.

#### 4.2.3 Results and Discussion

Figures 4.14 and 4.15 show IR spectra of C<sub>34</sub>H<sub>70</sub> at room temperature. Tables 4.5 and 4.6 show several iterations obtained for  $k$  for methylene rocking and wagging progressions observed in the infrared spectrum of crystalline C<sub>34</sub>H<sub>70</sub>. Frequency-phase curves given in figures 2 and 6 of reference 39 were used for these calculations.

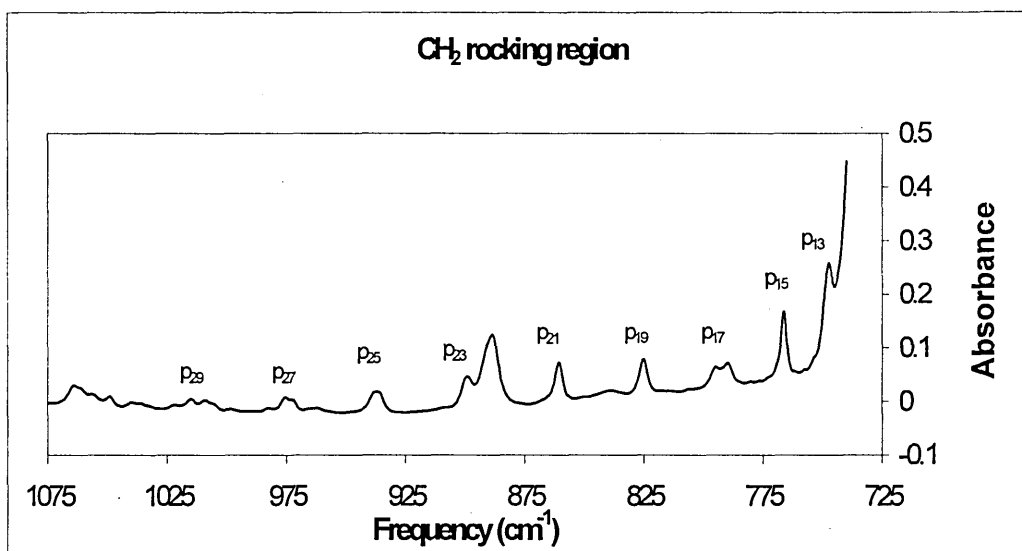


Fig 4.14: The infrared spectrum of the methylene rocking-twisting progression of  $C_{34}H_{70}$  at room temperature.

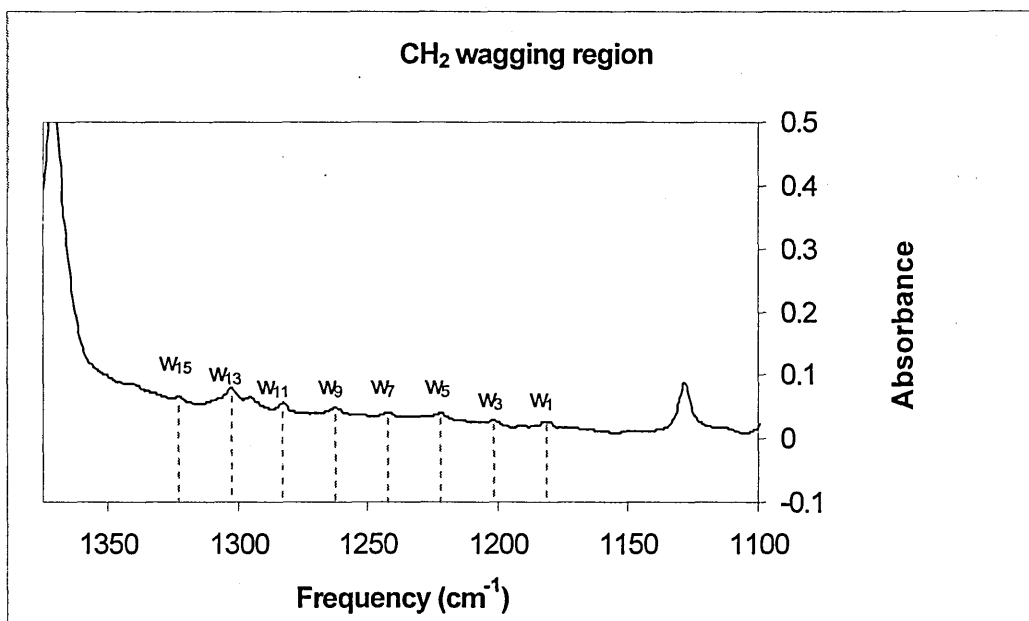


Fig 4.15: The infrared spectrum of the methylene wagging progression of  $C_{34}H_{70}$  at room temperature.

Table 4.5: Series of  $k$  values obtained for  $\text{CH}_2$  rocking progression of  $\text{C}_{34}\text{H}_{70}$  using different estimates for  $n_c$ .

Frequency ( $\text{cm}^{-1}$ )	$\Phi_k/\pi$	$k$				$n_c$
		$n_c = 34$	$n_c = 33$	$n_c = 32$	$n_c = 31$	
746.9	0.415	13.695 ~ 14	13.28 ~ 13	12.865 ~ 13	12.45 ~ 12	32.33
766	0.464	15.312 ~ 15	14.848 ~ 15	14.384 ~ 14	13.92 ~ 14	33.33
789.4	0.523	17.259 ~ 17	16.736 ~ 17	16.213 ~ 16	15.69 ~ 16	33.50
825	0.590	19.406 ~ 19	18.884 ~ 19	18.029 ~ 18	17.76 ~ 18	33.20
860.6	0.649	21.417 ~ 21	20.768 ~ 21	20.119 ~ 20	19.47 ~ 19	33.36
899.1	0.708	23.364 ~ 23	22.656 ~ 23	21.948 ~ 22	21.24 ~ 21	33.49
937.6	0.774	25.557 ~ 26	24.768 ~ 25	23.994 ~ 24	23.22 ~ 23	32.45
972.3	0.834	27.521 ~ 28	26.688 ~ 27	25.854 ~ 26	25.02 ~ 25	33.26
1014.8	0.911	29.799 ~ 30	28.896 ~ 29	27.993 ~ 28	27.09 ~ 27	33.12

Table 4.6: Series of  $k$  values obtained for  $\text{CH}_2$  wagging progression of  $\text{C}_{34}\text{H}_{70}$  using different estimates for  $n_c$ .

Frequency ( $\text{cm}^{-1}$ )	$\Phi_k/\pi$	$k$				$n_c$
		$n_c = 34$	$n_c = 33$	$n_c = 32$	$n_c = 31$	
1181.1	0.032	1.056 ~ 1	1.024 ~ 1	0.992 ~ 1	0.96 ~ 1	32.25
1201.9	0.092	3.036 ~ 3	2.994 ~ 3	2.852 ~ 3	2.76 ~ 3	33.61
1221.8	0.153	5.049 ~ 5	4.896 ~ 5	4.743 ~ 5	4.59 ~ 5	33.68
1242.3	0.217	7.161 ~ 7	6.994 ~ 7	6.727 ~ 7	6.51 ~ 7	33.26
1262.5	0.277	9.141 ~ 9	8.864 ~ 9	8.587 ~ 9	8.31 ~ 8	33.49
1283.1	0.338	11.154 ~ 11	10.816 ~ 11	10.478 ~ 10	10.14 ~ 10	33.54
1302.5	0.396	13.068 ~ 13	12.672 ~ 13	12.276 ~ 12	11.88 ~ 12	33.83
1322.8	0.456	15.048 ~ 15	14.592 ~ 15	14.136 ~ 14	13.68 ~ 14	33.89

As stated earlier only odd- $k$  values are allowed in the low temperature spectrum<sup>39</sup>. In Tables 4.5 and 4.6, only the iteration corresponding to  $n_c = 33$  shows odd- $k$  for all the progression bands whereas for the CH<sub>2</sub> wagging progression both  $n_c = 33$  and 34 show suitable iterations. All the others are mixed with even and odd values for  $k$ . Therefore the  $k$  iteration (rounded off to nearest integer) for  $n_c = 33$  was chosen as the best estimate for the CH<sub>2</sub> rocking progression to determine the all-*trans* length whereas for CH<sub>2</sub> wagging progression both  $n_c = 33$  and 34 show suitable iterations. Using each  $k$  value (rounded off to nearest integer) in equation (4.1),  $n_c$  was calculated for each progression band. The values obtained for  $n_c$  this way from the rocking and wagging progressions are shown in the last column of Tables 4.5 and 4.6. The average of all these values was taken as the all-*trans* length of C<sub>34</sub>H<sub>70</sub>. This was found to be 33.27. Figure 4.14 and 4.15 illustrate these two series in the infrared spectrum of C<sub>34</sub>H<sub>70</sub> with the assignment of  $k$  values.

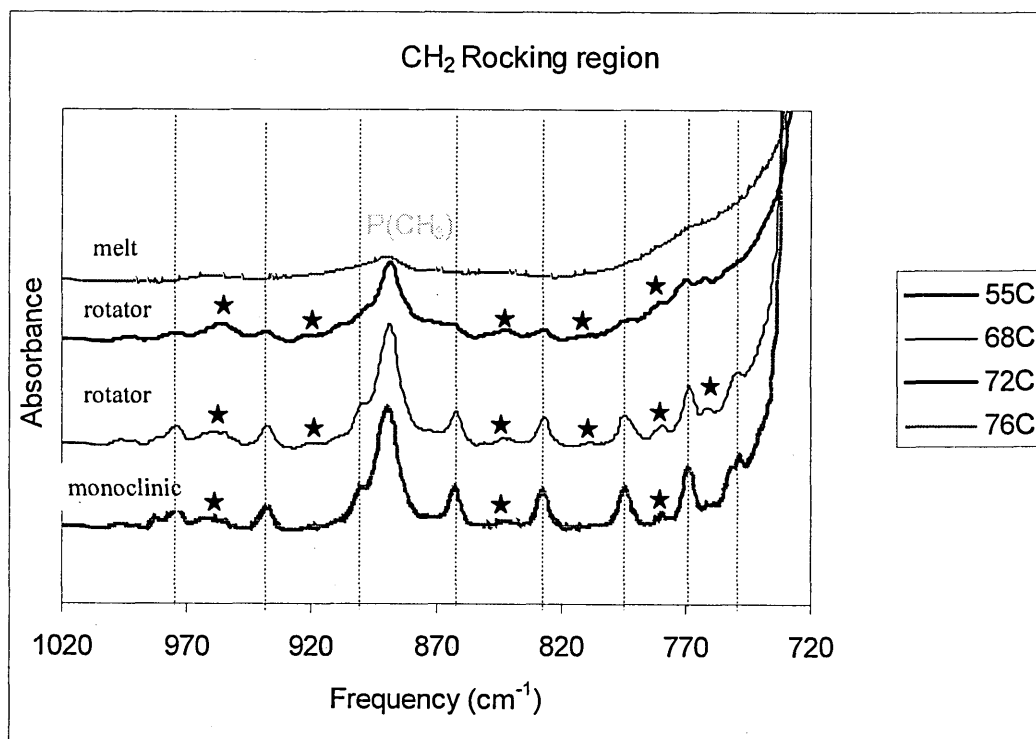


Fig 4.16: The infrared spectra of methylene rocking progression for different phases of C<sub>34</sub>H<sub>70</sub>. Dashed lines represent the  $k$ -odd bands.

Figure 4.16 shows the variation of the rocking progression of  $C_{34}H_{70}$  with increasing temperature. In the lowest temperature spectrum ( $55^{\circ}C$ )  $k$  odd bands are prominent. The rotator phase is associated mostly with end-*gauche* defects in an otherwise all-*trans* conformer. The defects activate the  $k$ -even series. We can see the rotator phase spectrum at  $68^{\circ}C$  shows both odd and even series with the odd bands showing higher intensity and the even series emerging between them. As the temperature is raised to  $72^{\circ}C$  we can see the intensity of the  $k$ -even series increases at the expense of the intensity of the  $k$ -odd series. In the liquid state the disorder is maximum. This leads to a multiplicity of bands in this region producing a broad background. Therefore in the melt spectrum we can only see a background with a broad band around  $890\text{ cm}^{-1}$ . This is the  $CH_3$  rocking mode. It is strong in all the other spectra.

According to selection rules, in the Raman spectrum,  $k$ -even bands are allowed at low temperature and the  $k$ -odd series is only observed in disordered alkanes in the methylene rocking region. However, we could not see any sign of either series in low temperature or higher temperature spectra (see figure 4.9 in section 4.1.2). Kim et al have observed a band progression in the methylene rocking region in the high temperature, phase II Raman spectrum of  $C_{21}H_{44}$ <sup>5</sup> but failed to observe the rocking progression at room temperature.

The next step was to investigate the progression bands in the infrared spectrum of a mixture of  $C_{34}H_{70}$  and  $C_{36}D_{74}$  (2:1 w/w). This mixture has been melted several times before pressing into a film in order to ensure homogeneous mixing of the chains<sup>52</sup>. For this mixture we consider the possibility that, as the deuterated chains are two carbon atoms longer than the hydrogenated chains, most of the deuterated chains will assume the end-*gauche* conformation to compensate for the chain length mismatch in the crystalline phase. The other option is to adopt a 'kink' in the middle region of the chain to shorten its straight chain length.

The infrared spectra in the rocking and wagging region of this mixture along with the infrared spectra of  $C_{34}H_{70}$  are given in figures 4.17 and 4.18. The progression bands were assigned using the same method described above. Tables 4.7 and 4.8 give a summary of the analysis.



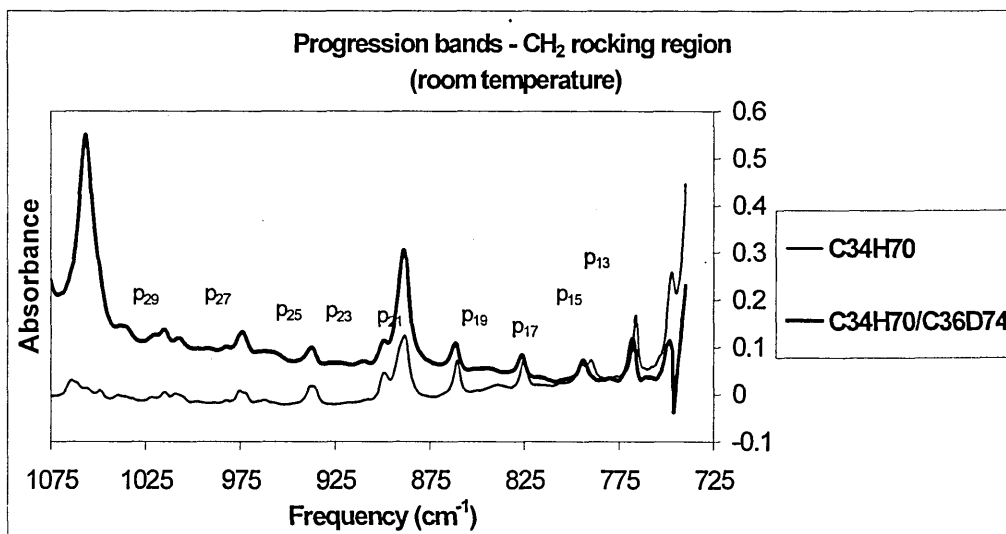


Fig 4.17: Methylene rocking progression of C<sub>34</sub>H<sub>70</sub>/C<sub>36</sub>D<sub>74</sub> mixture compared with that of C<sub>34</sub>H<sub>70</sub>.

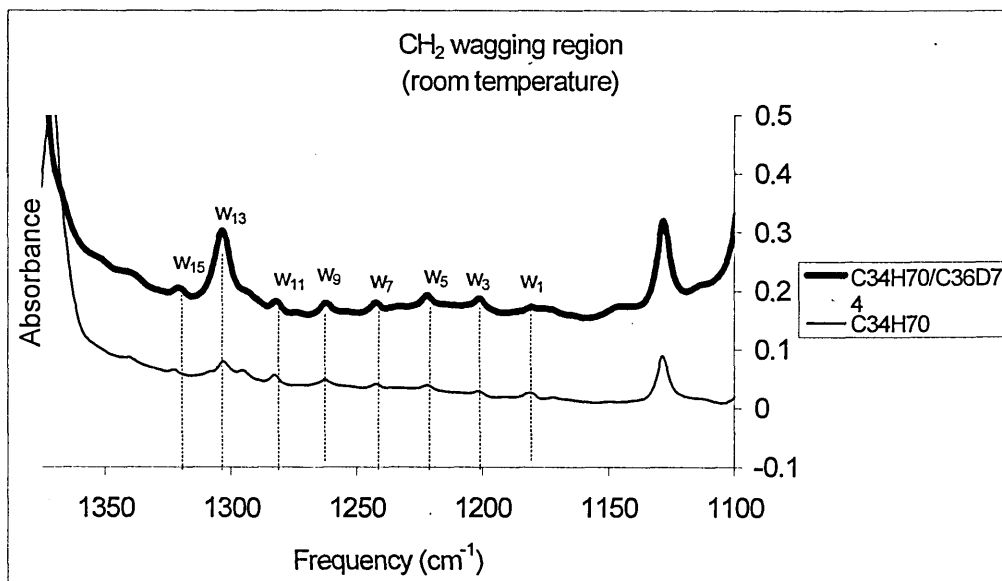


Fig 4.18: Methylene wagging progression of C<sub>34</sub>H<sub>70</sub>/C<sub>36</sub>D<sub>74</sub> mixture compared with that of C<sub>34</sub>H<sub>70</sub>.

Table 4.7: Series of  $k$  values obtained for the  $\text{CH}_2$  rocking progression of a  $\text{C}_{34}\text{H}_{70}/\text{C}_{36}\text{D}_{74}$  mixture using different estimates for  $n_c$ .

Frequency ( $\text{cm}^{-1}$ )	$\Phi_k/\pi$	$k$				$n_c$
		$n_c = 34$	$n_c = 33$	$n_c = 32$	$n_c = 31$	
748.4	0.418	13.794 ~ 14	13.794 ~ <b>13</b>	12.958 ~ 13	12.54 ~ 13	32.10
767.9	0.479	15.807 ~ 16	15.328 ~ <b>15</b>	14.849 ~ 15	14.37 ~ 14	32.32
793.6	0.533	17.589 ~ 18	17.056 ~ <b>17</b>	16.523 ~ 17	15.99 ~ 16	32.89
826.4	0.592	19.536 ~ 20	18.944 ~ <b>19</b>	18.352 ~ 18	17.76 ~ 18	33.09
861.7	0.654	21.582 ~ 22	20.928 ~ <b>21</b>	20.274 ~ 20	19.62 ~ 20	33.11
899.2	0.708	23.364 ~ 23	22.656 ~ <b>23</b>	21.948 ~ 22	21.24 ~ 21	33.49
937.8	0.774	25.542 ~ 26	24.768 ~ <b>25</b>	23.994 ~ 24	23.22 ~ 23	33.3
974.4	0.837	27.621 ~ 28	26.784 ~ <b>27</b>	25.947 ~ 26	25.11 ~ 25	33.26
1015.3	0.911	30.063 ~ 30	29.152 ~ <b>29</b>	28.241 ~ 28	27.33 ~ 27	32.83

Table 4.8: Series of  $k$  values obtained for the  $\text{CH}_2$  wagging progression of a  $\text{C}_{34}\text{H}_{70}/\text{C}_{36}\text{D}_{74}$  mixture using different estimates for  $n_c$ .

Frequency ( $\text{cm}^{-1}$ )	$\Phi_k/\pi$	$k$				$n_c$
		$n_c = 34$	$n_c = 33$	$n_c = 32$	$n_c = 31$	
1180.9	0.030	0.99 ~ 1	0.96 ~ 1	0.93 ~ 1	0.9 ~ 1	34.33
1201.7	0.090	2.97 ~ 3	2.88 ~ 3	2.79 ~ 3	2.7 ~ 3	34.33
1222.0	0.153	5.049 ~ 5	4.9 ~ <b>5</b>	4.743 ~ 5	4.59 ~ 5	33.68
1241.9	0.215	7.095 ~ 7	6.88 ~ 7	6.665 ~ 7	6.45 ~ 6	33.56
1262.2	0.273	9.009 ~ 9	8.736 ~ 9	8.463 ~ 8	8.19 ~ 8	33.97
1282.1	0.335	11.055 ~ <b>11</b>	10.72 ~ <b>11</b>	10.385 ~ 10	10.05 ~ 10	33.83
1303.8	0.400	13.2 ~ <b>13</b>	12.8 ~ <b>13</b>	12.4 ~ 12	12.0 ~ 12	33.50
1321.0	0.454	14.982 ~ <b>15</b>	14.528 ~ <b>15</b>	14.074 ~ 14	13.62 ~ 14	34.04

According to Table 4.7 the  $k$  series obtained with  $n_c = 33$  shows the best fit for the progression bands in the rocking region and in Table 4.8 both  $n_c = 33$  and 34 show the best fit for the progression bands in the wagging region. Substituting these values in equation 4.1 calculated average all-*trans* length for this mixture is 33.39. This figure further supports the above - mentioned proposed model for this mixture with most of the deuterated chain ends assuming a *gauche* conformation.

Figures 4.17 and 4.18 illustrates the infrared spectrum of these regions with their respective  $k$  values. Although we could observe a prominent series of progression bands for CH<sub>2</sub> rocking and wagging modes, no sign of progression bands was observed due to CD<sub>2</sub> vibrational modes in the infrared spectrum of this mixture. Figures 4.17 and 4.18 show the progression bands of this mixture in comparison to those of C<sub>34</sub>H<sub>70</sub>. They are located in the same position as for the C<sub>34</sub>H<sub>70</sub> series. Therefore it is clear that these bands are solely arising from CH<sub>2</sub> group vibrations and presumably they are not affected by the presence of CD<sub>2</sub> groups.

#### 4.2.4 Conclusion

Here we discussed the use of progression bands in determining the regularity of n-alkane chains within the crystal. It is a good indicator of the degree of order of each phase of the crystal: low temperature crystalline phase, high temperature rotator phase etc. We have demonstrated here the changes associated with these bands with increasing temperature. For the low temperature crystalline phase only a single series of progression bands with odd values of  $k$  are observed whereas with increasing temperature another series which corresponds to even  $k$  values emerges. This indicates the onset of disorder in an otherwise all-*trans* alkane chains.

Assignment of individual progression bands enables us to calculate the all-*trans* chain length of the alkane chain within the crystal. Both C<sub>34</sub>H<sub>70</sub> and C<sub>34</sub>H<sub>70</sub>/C<sub>36</sub>D<sub>74</sub> showed that 33 bonds are in the all-*trans* conformation in these samples. This is therefore a very useful method to obtain an estimate about the ordered chain length for hydrogenous alkanes. The other methods are SAXS and Raman LAM modes. SAXS gives the periodicity of the lamellae and the Raman LAM modes gives the straight chain length.

But neither technique shows the all-*trans* length. They are both related to the length of the whole chain, including some disorder. Therefore the value obtained from the progression band method is usually smaller than those of other methods. This infrared method has previously been used successfully to verify the structures of two branched long chain n-alkanes and a 1:1 mixture of two long chain n-alkanes<sup>50</sup>.

## References

- 1 Broadhurst MG, J. Res. Natl. Bur. Stand., **66A**, 241 (1962)
- 2 Snyder RG, J. Mol. Spectroscopy, **7**, 116 (1961)
- 3 Cutler DJ, Hendra PJ, Walker JH, Cudby MEA, Willis HA, Spectrochimica Acta, **34A**, 391 (1978)
- 4 Boerio FJ, Koenig JL, J. Chem. Phys., **52**(7), 3425, 1970
- 5 Kim Y, Strauss HL, Snyder RG, J. Phys. Chem., **93**, 485 (1989)
- 6 Naylor CC, Meier R, Kip BJ, Williams PJ, Mason SM, Conroy N, Gerrard DL, Macromolecules, **28**, 2969 (1995)
- 7 Strobl GR, Hagedorn W, J. Polym. Sci., Polym. Phys. Ed., **16**, 1181 (1978)
- 8 Tarazona A, Koglin E, Coussens B, Meier RJ, Vibrational Spectroscopy, **14**, 159 (1997).
- 9 Müller A, Proc. Roy. Soc. (London) [A], **127**, 417 (1930)
- 10 Piesczek W, Strobl GR, Malzahn K, Acta Cryst., **B30**, 1278 (1974)
- 11 Larsson K, Nature, **28**, 383 (1967)
- 12 Doucet J, Denicolo I, Craievich A, J. Chem. Phys., **75**, 1523 (1981)
- 13 Ungar G, J. Phys. Chem., **87**, 689 (1983)
- 14 Craievich A, Denicolo I, Doucet J, Phys. Rev. B, **30**, 4782 (1984)
- 15 Barnes JD, J. Chem. Phys., **58**, 5193 (1973)
- 16 Doucet J, Dianoux AJ, J. Chem. Phys., **81**, 5043 (1984)
- 17 Maroncelli M, Qi SP, Strauss HL, Snyder Rg, J. Am. Chem. Soc., **104**, 6237 (1982)
- 18 Nielsen JR, Hathaway CE, J. Mol. Spectr., **10**, 366 (1963)
- 19 Barnes JD, Fanconi BM, J. Chem. Phys., **56**, 5190 (1972)
- 20 Zerbi G, Magni R, Gussoni M, Moritz KH, Bigotto A, Dirlikov S, J. Chem. Phys., **58**, 252 (1950)
- 21 Dehl RE, J. Chem. Phys., **60**, 339 (1973)
- 22 Olf HG, Peterlin A, J. Polym. Sci. A2, **8**, 753 (1970)
- 23 Ewen B., Fischer EW, Piesczek W, Strobl G, J. Chem. Phys., **61**, 5265 (1974)
- 24 Stohrer M, Noack F, J. Chem. Phys., **20**, 541 (1952)
- 25 Chapman D, Wallach DFH, 'Biological Membranes' Vols I and II, Academic Press, London (1968 & 1973)
- 26 Ungar G, Masic N, J. Phys. Chem., **89**, 1036 (1985)
- 27 Barnes JD, Fanconi BM, J. of Chem. Phys., **56**, 5190 (1972)
- 28 Snyder RG, Maroncelli M, Qi SP, Strauss HL, Science, **214**, 188 (1981)

- 29 Maroncelli M, Strauss HL, Snyder RG, J. Phys. Chem., **89**, 5260 (1985)
- 30 Kim Y, Strauss HL, Snyder RG, J. Phys. Chem., **93**, 7520 (1989)
- 31 Maroncelli M, Qi SP, Strauss HL, Snyder RG, J. Am. Chem. Soc., **104**, 6237 (1982)
- 32 Maissara M, Devaure J, J. Raman Spectrosc., **18**, 181 (1987)
- 33 Kurelec L, Rastogi S, Meier RJ, Lemstra PJ, Macromolecules, **33**, 5593 (2000)
- 34 Kim Y, Strauss HL, Snyder RG, J. Phys. Chem., **93**, 485 (1989)
- 35 Mirabella FM, J. Polym. Sci., Polym. Phy. Ed., **22**, 1283 (1984)
- 36 Brogly M, Bistac S, Schultz J, Polymer International, **44**, 11 (1997)
- 37 Naylor CC, Meier RJ, Kip BJ, Williams KPJ, Mason SM, Conroy N, Gerrard DL, Macromolecules, **28**, 2969 (1995)
- 38 Koglin E, Meier RJ, Comput. Theor. Polym. Sci., **9**, 327 (1999)
- 39 Snyder RG, Schachtschneider, Spectrochim. Acta, **19**, 85 (1963)
- 40 Schneider B, Schmidt P, Wichterle O, Coll Czech Chem Commun, **27**, 1749 (1962)
- 41 Jakes J, Schmidt P, Schneider B, Coll Czech Chem Commun, **30**, 996 (1965)
- 42 Jakes J, J. Polym. Sci., **16**, 305 (1967)
- 43 Jakes J, Krimm S, Spectrochimica Acta, **27A**, 19 (1971)
- 44 Jakes J, Krimm S, Spectrochimica Acta, **27A**, 35 (1971)
- 45 Cooper SJ, Coogan M, Everall N, Priestnall I, Polymer **42**, 10119 (2001)
- 46 Yoshioka Y, Tashiro K, Chellaswamim R, Polymer, **44**, 6407 (2003)
- 47 Yoshioka Y, Tashiro K, Polym. Prepr. Jpn., **51**, 2057 (2002)
- 48 Chia NC, Mendelsohn R, J. Phys. Chem., **96**, 10543 (1992)
- 49 Cates DA, Strauss HL, Snyder RG, J. Phys. Chem., **98**, 4482 (1994)
- 50 Gorce J-P, Spells SJ, Polymer, **43**, 4043 (2002)

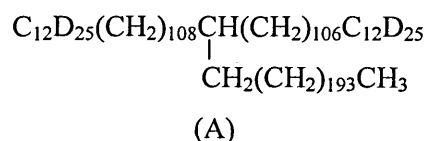
## Chapter 5

---

### Establishment of an Infrared Method to Determine the Isotopic Ratio in End-Deuterated long Chain Alkanes

#### 5.1 Introduction

Partially deuterated long chain n-alkanes are becoming increasingly popular in research work on monodisperse long chain alkanes. These alkanes with deuterium end caps enable us to study the chain end behaviour independently from the chain interior. Therefore they provide a wonderful opportunity for an interesting comparison with their undeuterated analogue. Several end deuterated long chain alkanes have been synthesised<sup>1</sup>: two straight chain alkanes  $C_{12}D_{25}-(CH_2)_{144}-CHDC_{11}H_{23}$  and  $C_{12}D_{25}-(CH_2)_{192}-CHDC_{11}H_{23}$  and a Y-shaped alkane designated 'A' below.



The basis of the Whiting's procedure to synthesise monodisperse alkanes is shown in Chapter 2 - figure 2.3. Incorporation of the deuterium end cap takes place at initial stages of the synthesis through the Grignard reagent<sup>1</sup>. The reaction of a Bromoacetal with the Grignard reagent, n- $C_{12}D_{25}MgBr$  in the presences of a catlytic amount of  $CuCN.LiCl$  replaces the Br in bromoacetal with  $C_{12}D_{25}$  - end cap. However, it turned out that the labelling process was not 100% successful during the synthesis of the deuterium-labelled Y-shaped alkane, A. Therefore here we intend to establish an infrared method to calculate the deuterium percentage in a sample of A. The basis of the method is that the absorbance of a particular vibrational mode is proportional to its weight fraction. Two binary mixtures of short chain alkanes  $C_{34}H_{70}$  and  $C_{36}D_{74}$  and a mixture of deuterated and undeuterated polyethylene are used as calibration samples. In addition, two end-deuterated monodisperse linear alkanes previously synthesised using the same procedure will be analysed as the validation of the method.

## 5.2 Experimental

### 5.2.1 Sample preparation

$C_{34}H_{70}$  was purchased from Sigma Chemical Company and 98% D,  $C_{36}D_{74}$  from Aldrich Chemical Company. The  $M_w$  of H polymer is 385000 and  $M_w$  of D polymer is 413000. Toluene used here was 99.5%, Spectrophotometric grade and purchased from Aldrich Chemical Company.

(a) Mixture 1 :  $C_{34}H_{70}$  /  $C_{36}D_{74}$  , 2.5:1 w/w

0.0751g of  $C_{34}H_{70}$  and 0.0300g of  $C_{36}D_{74}$  were dissolved in hot toluene. Two/three drops of this hot solution were pipetted on to a KBr disc to give a thin uniform film. It was allowed to crystallise under ambient conditions for 3 hrs. The rest of the solution was also allowed to crystallise in the original container.

Mixture 2 :  $C_{34}H_{70}$  /  $C_{36}D_{74}$  , 4:1 w/w

0.0600g of Mixture 1 remaining in the original container was weighed into a small container and 0.0260g of  $C_{34}H_{70}$  was further added to this mixture. It was dissolved in hot toluene and a thin sample was obtained on a KBr disc as above.

(b) Mixture 3 : HPE / DPE , 7.5:1 w/w

0.4407g of H polymer and 0.0590g of D polymer were refluxed in 50ml of Xylene. Two/three drops of the solution were pipetted onto a KBr disc and a thin film was obtained in the same way as above.

(c)  $CD_3(CD_2)_{11}(CH_2)_{144}CHD(CD_2)_{10}CD_3$  {C168D}

0.0020g of C168D was weighed on to a KBr disc. The sample was melt crystallised between two KBr discs at  $10^0\text{ C min}^{-1}$  using a Linkam hot stage.

(d)  $CD_3(CD_2)_{11}(CH_2)_{192}CHD(CD_2)_{10}CD_3$  {C216D} – Sample 1

A C216D sample left between KBr discs after a previous annealing/cooling experiment was used here. This sample had previously been heated up to melting. It was again melted and crystallised rapidly.



$\text{CD}_3(\text{CD}_2)_{11}(\text{CH}_2)_{192}\text{CHD}(\text{CD}_2)_{10}\text{CD}_3$  {C216D} – Sample 2

Sample 1 was re-melted after recording the spectrum and crystallised at  $0.2^\circ\text{C min}^{-1}$  between KBr discs using a Linkam hot stage.

e) Y – shaped molecule A

0.0050g of B was dissolved in hot toluene and a thin film was prepared on a KBr disc as stated above.

### 5.2.2 Recording the infrared spectrum

The FTIR spectra of the above samples were recorded using a Mattson Galaxy 6020 spectrometer using a Graseby-Specac 21500 cryostat. The sample space was evacuated and all the spectra were recorded at  $-173^\circ\text{C}$ . Liquid nitrogen was used to cool the samples. The spectral resolution was  $1\text{ cm}^{-1}$  and 200 scans were used for each spectrum.

## 5.3 Calculation

### 5.3.1 Calculation of weight fraction: $\text{Wt.}[\text{CH}_2] / \text{Wt.}[\text{CD}_2]$

$$\text{Wt.}[\text{CH}_2] = \frac{n[\text{CH}_2] \times 14}{\text{Mol. Wt}} \times y \quad \dots\dots\dots(5.1)$$

$$\text{Wt.}[\text{CD}_2] = \frac{n[\text{CD}_2] \times 16}{\text{Mol. Wt}} \times y \quad \dots\dots\dots(5.2)$$

where  $n[\text{CX}_2]$  = number of  $\text{CH}_2$  or  $\text{CD}_2$  groups in each sample  
 $y$  = weight of the sample

For example, the calculation of  $\text{Wt.}[\text{CH}_2] / \text{Wt.}[\text{CD}_2]$  for the mixture 1 is given below.

$$\text{Wt.}[\text{CH}_2] = \frac{32 \times 14}{478} \times 0.0751 = 0.0703\text{ g}$$

$$\text{Wt.}[\text{CD}_2] = \frac{34 \times 16}{580} \times 0.0300 = 0.0281\text{ g}$$

$$\text{Wt.}[\text{CH}_2] / \text{Wt.}[\text{CD}_2] = 2.501$$

### 5.3.2 Calculation of intensity ratio: $I[\text{CH}_2] / I[\text{CD}_2]$

The  $\text{CH}_2$  and  $\text{CD}_2$  vibrational modes of the infrared spectra were curvefitted using Gaussian and mixed Gaussian and Lorentzian profiles. The intensity ratio was calculated using the area of each mode.

### 5.3.3 Simulation of the doublet to singlet ratio of the $\text{CD}_2$ bending mode of $\text{C}_{34}\text{H}_{70}/\text{C}_{36}\text{D}_{74}$ mixtures

The infrared spectra of the above mixtures do not show a doublet splitting for the  $\text{CD}_2$  bending mode as might be expected. Normally the  $\text{CH}_2$  and  $\text{CD}_2$  bending and rocking modes of orthorhombic alkanes are split in to two due to factor group splitting<sup>2</sup>. Instead, these mixtures show a broad band around  $1087\text{ cm}^{-1}$  for the  $\text{CD}_2$  bending mode. This means a large proportion of deuterated molecules is isolated from others in these mixtures. However, the components of a doublet and a singlet could be resolved using curve fitting methods. Therefore a simulation was carried out prior to the curve fitting to estimate the doublet to singlet ratio.

In this case we used the random number generator held in the standard library of Borland C++. This supplies numbers in the range 0 up to 32767. The simulation was carried out to get a set of different arrangements of H and D molecules in a 2:1 mixture. Here, we called a random number between 0 and 1 and compared it against the weight fraction of H and D alkane. For example if the random number generated a number less than 0.667 the lattice point will be assigned a 'H'. If it is bigger than 0.667, a 'D' is assigned. For example an array of D and H generated as described above is given in figure 5.1. Then the 'D's with neighbouring 'D's were grouped together. These groups are responsible for the doublet in the infrared spectrum. The 'D's without any neighbouring 'D's result in a singlet in the infrared spectrum. Single 'D's and 'D's with neighbours were counted separately. The number of single 'D's is proportional to the singlet area and the number of 'D's with neighbouring 'D's is proportional to the doublet area of the infrared spectrum respectively. This was repeated for 11 arrays of the size [30x30] applying periodic boundary conditions.

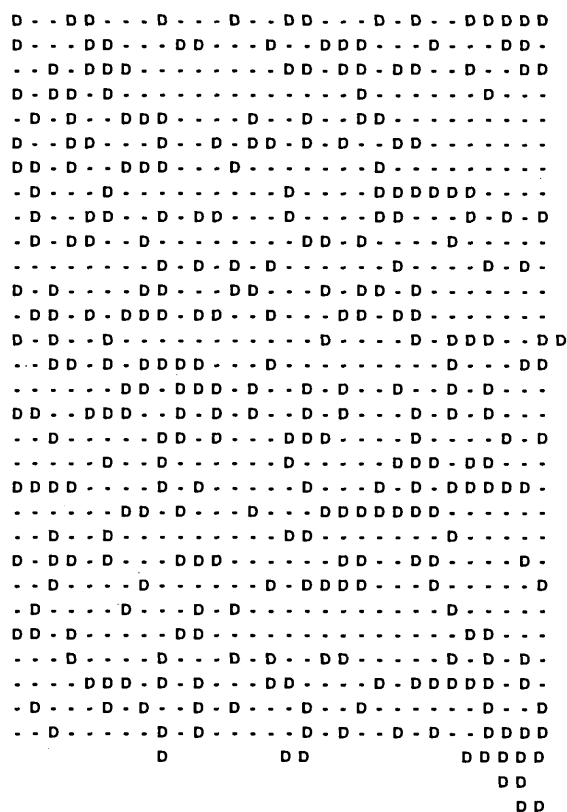


Fig 5.1: Schematic arrangement of 'D' and 'H' molecules in a 2:1  $C_{34}H_{70}/C_{36}D_{74}$  mixture. Horizontal and vertical directions in this square lattice represents  $\{110\}$  direction in the orthorhombic lattice.

The following values were obtained.

$$\sum (\text{singlet 'D'}) \text{ molecules} = 640 \pm 25$$

$$\sum (\text{doublet 'D'}) \text{ molecules} = 2800 \pm 53$$

$$\text{doublet 'D': singlet 'D'} = 4.37 \pm 0.1$$

The experimental ratio can be determined by curve fitting the  $CD_2$  bending mode for the above mixture.

## 5.4 Results and Discussion

The low temperature infrared spectra in the  $\text{CH}_2$  and  $\text{CD}_2$  bending regions for the 4:1  $\text{C}_{34}\text{H}_{70}/\text{C}_{36}\text{D}_{74}$  mixture, after background subtraction is given below. All the spectra were recorded at low temperature to obtain the maximum splitting.

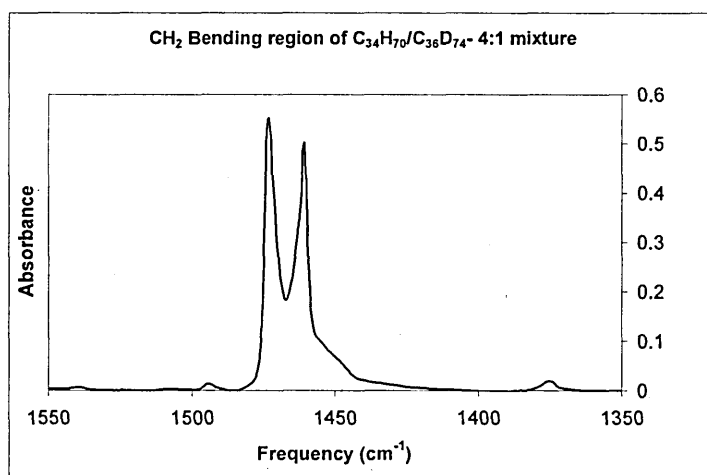


Fig 5.2: The  $\text{CH}_2$  bending region of the infrared spectrum of 4:1  $\text{C}_{34}\text{H}_{70}/\text{C}_{36}\text{D}_{74}$  mixture at  $-173^\circ\text{C}$ .

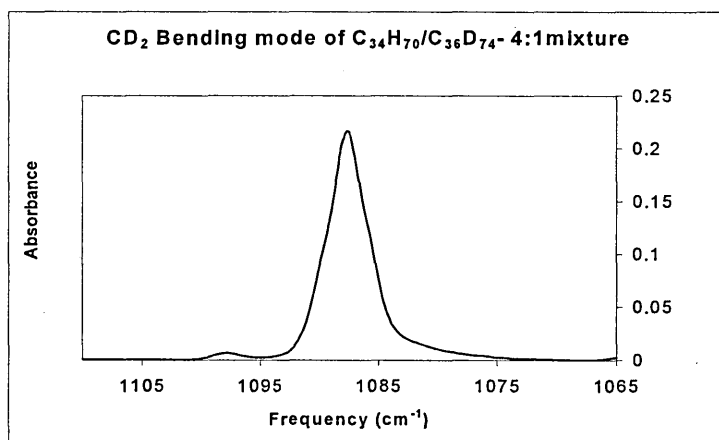


Fig 5.3: The  $\text{CD}_2$  bending region of the infrared spectrum of 4:1  $\text{C}_{34}\text{H}_{70}/\text{C}_{36}\text{D}_{74}$  mixture at  $-173^\circ\text{C}$ .

A similar spectrum was obtained for the 2.5:1  $\text{C}_{34}\text{H}_{70}/\text{C}_{36}\text{D}_{74}$  mixture. Deconvolution and curve fitting procedures were used to determine with accuracy the frequency and the

areas of the different bands present in the each spectral mode. The values are shown in Table 5.1.

According to Table 5.1, the CH<sub>2</sub> bending mode is not a simple doublet. It consists of several overlapping bands and it extends from 1474 to 1440 cm<sup>-1</sup>. It consists of weaker absorption bands of coupled methylene and methyl antisymmetric bending modes<sup>2,3</sup>. Holland and Nielsen have identified two strong bands at 1462 and 1473 cm<sup>-1</sup> as the CH<sub>2</sub> deformation 'scissoring' doublet<sup>4</sup>. Jones too has observed the CH<sub>2</sub> bending doublet in a similar area around 1467 and 1460 cm<sup>-1</sup> for liquid n-paraffins<sup>5</sup>. We identified two strong bands at 1460.9 and 1473.6 cm<sup>-1</sup> and 1461.1 and 1473.3 cm<sup>-1</sup> as the CH<sub>2</sub> bending doublet for the 4:1 and 2.5:1 mixtures respectively. According to Holland and Nielsen<sup>4</sup> the band around 1453 cm<sup>-1</sup> is the methyl out-of-plane bending mode in single crystals of n-paraffins. Jones has suggested it appears around 1458 cm<sup>-1</sup> for the liquid paraffins<sup>5</sup>. Snyder reported the methyl antisymmetric bending mode at 1465 cm<sup>-1</sup> in a range of crystalline alkanes from C<sub>20</sub>H<sub>42</sub> to C<sub>30</sub>H<sub>62</sub><sup>6</sup>. However, in a later study including even shorter alkanes, Snyder et al have proposed a spectral range between 1440 and 1468 cm<sup>-1</sup> for this mode<sup>3</sup>. Therefore in our study we tentatively omitted 1463 and 1453 cm<sup>-1</sup> bands in calculating the CH<sub>2</sub> bending area. Not all the bands resolved by deconvolution and curve fitting could be assigned to a particular vibrational mode, as no assignments were available in the literature. Some bands were necessary to improve the quality of the fit. In the CD<sub>2</sub> bending region of the spectrum the bands around 1089 and 1086 cm<sup>-1</sup> were identified as the CD<sub>2</sub> bending doublet and the 1088 cm<sup>-1</sup> as the singlet<sup>7</sup>. The rest of the bands were necessary to get a better fit. These two mixtures were used as calibration.

We also tried to extend our calculations to include the CH<sub>2</sub> rocking mode as well. Agreement of results from both regions will enhance the accuracy of the calculated weight ratios. However, we failed to get consistent results using the CH<sub>2</sub> rocking mode. Therefore our calculation was limited only to CH<sub>2</sub> bending mode.

4:1 sample						2.5:1 sample					
CH <sub>2</sub> Bending			CD <sub>2</sub> Bending			CH <sub>2</sub> Bending			CD <sub>2</sub> Bending		
G			G			G			G		
Frequency (cm <sup>-1</sup> )	Area	Frequency (cm <sup>-1</sup> )	Area	Frequency (cm <sup>-1</sup> )	Area	Frequency (cm <sup>-1</sup> )	Area	Frequency (cm <sup>-1</sup> )	Area	Frequency (cm <sup>-1</sup> )	Area
1473.6	1.536	1092.1	0.279	-	-	1473.3	1.592	1092.9	0.018	-	-
1471.0	0.976	1089.3	0.275	1089.3	0.2055	1470.8	1.254	1089.5	0.711	1089.7	0.4624
1467.1	0.895	1087.7	0.296	1087.8	0.5335	1466.9	1.256	1087.7	0.303	1087.7	0.6919
1463.5	0.820	1086.1	0.277	1086.2	0.2646	1463.5	0.921	1085.9	0.5866	1085.8	0.7045
1460.9	1.19	1083.2	0.125	1081.8	0.043	1461.1	1.367	1082.8	0.2176	1080.5	0.084
1458.4	0.373					1458.4	0.465				
1455.5	0.172					1455.2	0.224				
1453.1	0.301					1452.8	0.410				
1447.9	0.570					1447.6	0.661				

Table 5.1: Areas and band positions of each band in the CH<sub>2</sub> and CD<sub>2</sub> bending mode regions in the ir spectrum of C<sub>34</sub>/C<sub>36</sub> mixtures obtained from curve fitting and deconvolution. G=Gaussian, G+L = Gaussian + Lorentzian.

The HPE/DPE mixture was prepared in view of the long chain nature of the alkanes whose isotopic ratios are to be calculated. The  $\text{CH}_2$  bending region of this sample is less complex than those of short chain alkane mixtures. In the  $\text{CD}_2$  bending mode a doublet and a central singlet were clearly visible. The infrared spectrum in these regions of the HPE/DPE mixture is illustrated in figures 5.4 and 5.5. Deconvolution and curve fitting procedures were followed in order to determine the band positions as above. In the HPE/DPE mixture no bands were found due to  $\text{CH}_3$  deformations as the intensity of these bands is very low as only an insignificant proportion of  $\text{CH}_3$  groups is present in the mixture. The  $\text{CH}_2/\text{CD}_2$  weight ratio of this mixture was experimentally determined using short chain alkane mixtures as calibration.

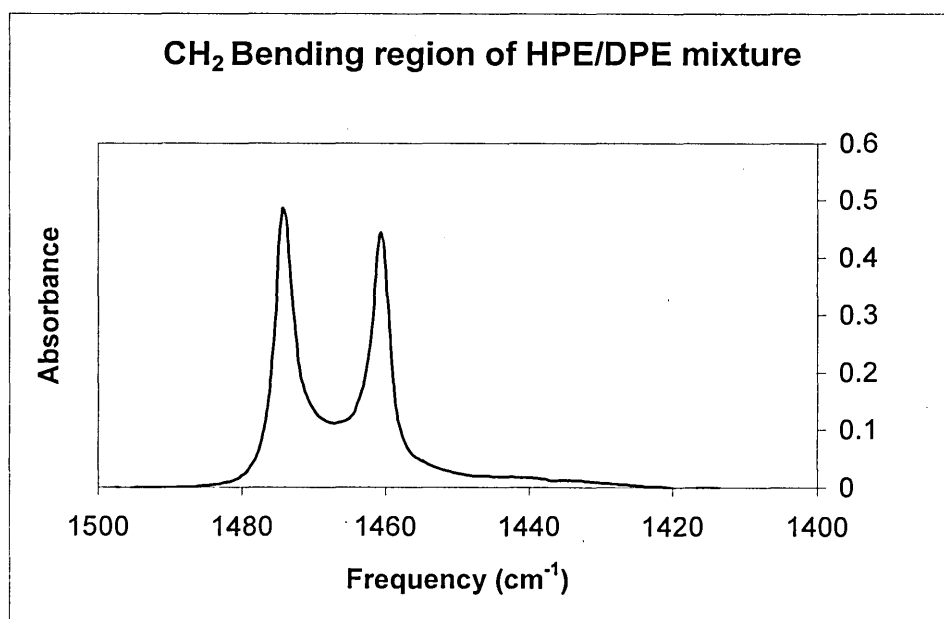


Fig 5.4: The  $\text{CH}_2$  bending region of the infrared spectrum of an HPE/DPE solution-crystallised mixture at  $-173^\circ\text{C}$ .

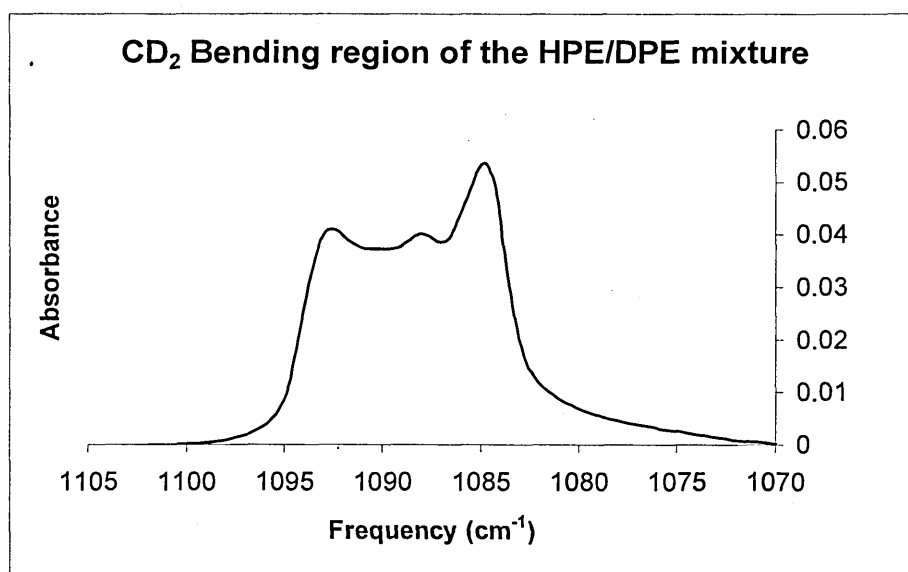


Fig 5.5: The  $CD_2$  bending region of the infrared spectrum of a HPE/DPE solution-crystallised mixture at  $-173^\circ C$ .

The basis of the calculation is:

$$\frac{W_x}{W_y} = \frac{I_x}{I_y} \quad \dots\dots\dots(5.3)$$

Where  $W_x$  =  $CH_2/CD_2$  weight ratio of sample X

$W_y$  =  $CH_2/CD_2$  weight ratio of sample Y

$I_x$  =  $CH_2/CD_2$  intensity ratios of sample X

$I_y$  =  $CH_2/CD_2$  intensity ratios of sample Y

It was assumed that all the samples have a similar absorption coefficient.

Using  $C_{34}H_{70}/C_{36}D_{74}$ , 4:1 mixture (X) to calculate the weight ratio of HPE/DPE mixture (Y);

$$W_x = 4.01 \text{ ( see section 5.3 and Table 5.2)}$$

$$I_x = \sum \text{area } CH_2 / \sum \text{area } CD_2$$

Using G+L fit for  $CD_2$ ;

$$I_x = 5.712/1.0036 \text{ ( see Table 5.1)} = 5.6915 \text{ ( see Table 5.2)}$$

$$I_y = 10.6017 \text{ ( see Table 5.2, calculated in a similar way as above)}$$



Substituting above values in equation (5.3)

$$\frac{4.01}{W_y} = \frac{5.6915}{10.6017}$$

$$W_y = 7.469$$

$W_y$  was also calculated using  $C_{34}H_{70}/C_{36}D_{74}$ , 2.5 mixture. The results are shown in Table 5.2. There is generally a good agreement between the measured weight ratios and the values calculated on the basis of ir curve fitting as shown above. Two short chain alkane mixtures and the polymer mixture were used as calibrations to determine the weight ratios of our end deuterated long chain alkanes.

Samples of C168D and C216D were analysed as a validation of the method. These samples have fully deuterated end caps. The  $CH_2$  bending areas in the infrared spectra of C168D and C216D are very similar to that of the HPE/DPE mixture. They also gave a clearly separated doublet for this mode. The  $CD_2$  bending mode of C168D and sample 2 of C216D consists of a doublet and a central singlet as expected (figures 5.6 and 5.7). However, the sample 1 of C216D shows only a single broad band centred around  $1087\text{ cm}^{-1}$  (figure 5.8). It may be due to the rapid crystallisation of the sample from the melt that it seems to be more disordered in this case.

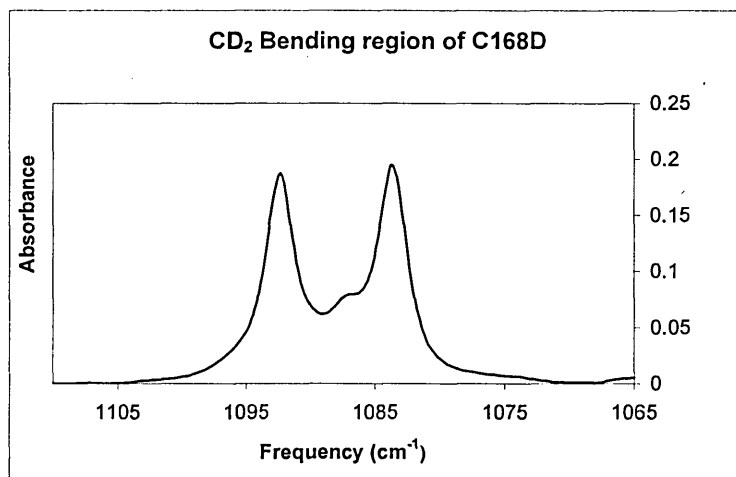


Fig 5.6: The  $CD_2$  bending region of the infrared spectrum of C168D at  $-173^{\circ}\text{C}$ .

C <sub>34</sub> H <sub>70</sub> /C <sub>36</sub> D <sub>74</sub>				HPE/DPE		C168D		C216D-melt crystallised				D-branch (A)			
4:1		2.5:1						Sample 2		Sample 1					
W	I	W	I	W	I	W	I	W	I	W	I	W	I	W	I
4.01	6.736 (G)	2.501	4.260 (G)	7.469	12.831 (G)	6.001	10.282 (G)	8.002	14.003 (G)	8.002	10.793 (G)	16.23 (100%)			
	5.6915 (G+L)		3.668 (G+L)												
calculated weight ratios using mixtures				G	G+L	G	G+L	G	G+L	G	G+L	G	G+L	G	G+L
4:1 →				7.638	7.469	6.12	5.73	8.33	7.5	6.42	3.33	20.305	18.313	34.11 (G)	25.992 (G+L)
2.5:1 →				7.532	7.228	6.03	5.54	8.22	7.3	6.34	3.3	20.025	17.722		
HPE/DPE →				-	-	5.99	5.73	8.25	7.5	6.3	3.94	19.855	18.312		

Table 5.2: Measured  $[CH_2]/[CD_2]$  weight ratios and calculated values based on observed ir band intensities.  $[CH_2]/[CD_2]$  intensity ratios observed are also listed.

Key to Table 5.2:

- ♦  $W = W[\text{CH}_2]/W[\text{CD}_2]$  from weighing out samples or calculated from ir spectra
- ♦  $I = I[\text{CH}_2]/I[\text{CD}_2]$  directly from ir spectra
- ♦  $W$  values in bold are the weight ratios obtained from weighings assuming the molecular formula is correct
- ♦ The letters in parentheses associated with  $I$  values represent the corresponding fit used for calculating intensity ratio  $I$ ; G – Gaussian and G+L – mixed Gaussian/Lorentzian
- ♦ Weight ratios calculated from ir curve fitting are given at the bottom of each  $W$  column
- ♦ Level of uncertainty of  $W$  is estimated to be  $\pm 0.5$ . This was estimated from the difference between  $W$  values calculated from ir spectra using G and G+L fits.

#### Calculation of the percentage $[\text{CH}_2]/[\text{CD}_2]$ of sample A:

Using  $\text{C}_{34}\text{H}_{70}/\text{C}_{36}\text{D}_{74}$ , 4:1 mixture (X) to calculate the weight ratio of sample A (Y);

$$W_x = 4.01$$

$$I_x = 6.736 \text{ (G)}$$

$$I_y = 34.11 \text{ (G)}$$

Substituting above values in equation (5.3)

$$\frac{4.01}{W_y} = \frac{6.736}{34.11}$$

$$W_y = 20.305$$

If sample A is 100% deuterated  $W[\text{CH}_2]/[\text{CD}_2] = 16.23 (W_y)$

$$W[\text{CD}_2]/[\text{CH}_2] = 0.0616$$

$$\text{The percentage of } W[\text{CD}_2]/[\text{CH}_2] \text{ in sample A} = \frac{100}{0.0616} \times \frac{1}{20.305}$$

$$= 79.94$$

$$\sim 80\%$$

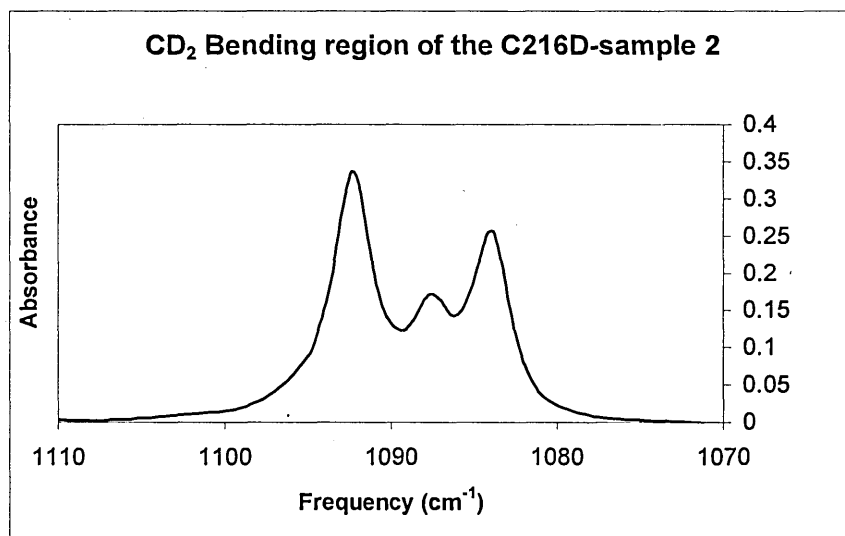


Fig 5.7: The CD<sub>2</sub> bending region of the infrared spectrum of C216D (sample 2), at  $-173^{\circ}\text{C}$ .

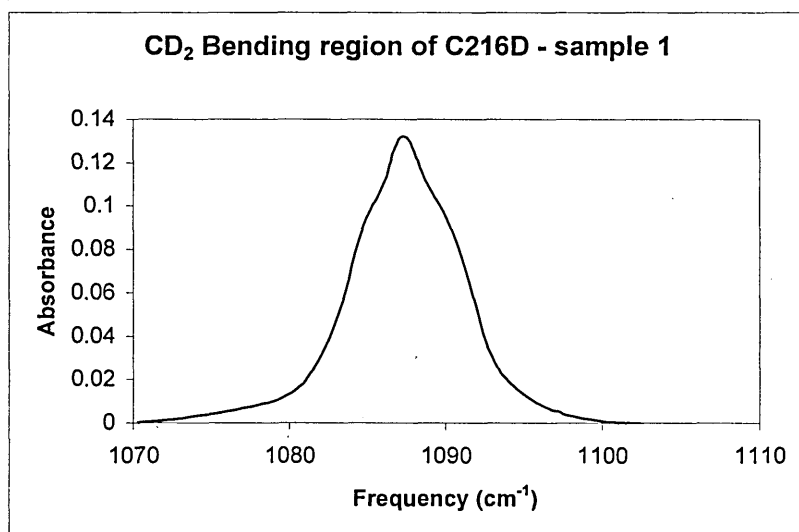


Fig 5.8: The CD<sub>2</sub> bending region of the infrared spectrum of C216D (sample 1) at  $-173^{\circ}\text{C}$ .

Deconvolution and curve fitting procedures were followed in order to determine the band positions and the area under each peak. Each sample was calibrated against the  $C_{34}H_{70}/C_{36}D_{74}$  mixtures and the HPE/DPE mixture. The results are shown in Table 5.2. According to Table 5.2 the weight ratios determined experimentally for C168D and sample 2 of C216D are in good agreement with the weight ratios calculated from ir intensities. Out of the two types of fit the Gaussian fit shows a better agreement. The mixed Gaussian/Lorentzian fit results in somewhat lower values of  $W$  than the theoretical value. However, the results of this fit are in  $\pm 0.5$  range from the directly measured weight ratio so that they are still acceptable. Surprisingly, the values for C216D - sample 1 calculated from ir intensities are significantly lower than the figure from weighings. The sample we used here had been used previously. It had undergone a heat annealing/cooling run involving temperatures up to  $130^{\circ}\text{C}$ . The melting point is around  $127^{\circ}\text{C}$ . However, we could not see any signs of oxidation (such as carbonyl or acidic groups in the ir spectrum) of the sample. This was subjected to rapid cooling from the melt in our experiment and surely this must have some impact on the regularity of the chain alignment. It failed to produce a clear doublet for the  $CD_2$  bending mode in the infrared spectrum which implies that the crystal is more disordered. Perhaps the absorptivity difference for singlet and the doublet may result in this disparity in  $W$  between the two samples of C216D.

The aim of this experiment is to calculate the true percentage of  $CD_2$  in the branched alkane, A. The  $CH_2$  and  $CD_2$  bending modes in the infrared spectrum of this sample are very similar to those of short chain alkane mixtures. These modes are illustrated in figures 5.9 and 5.10.

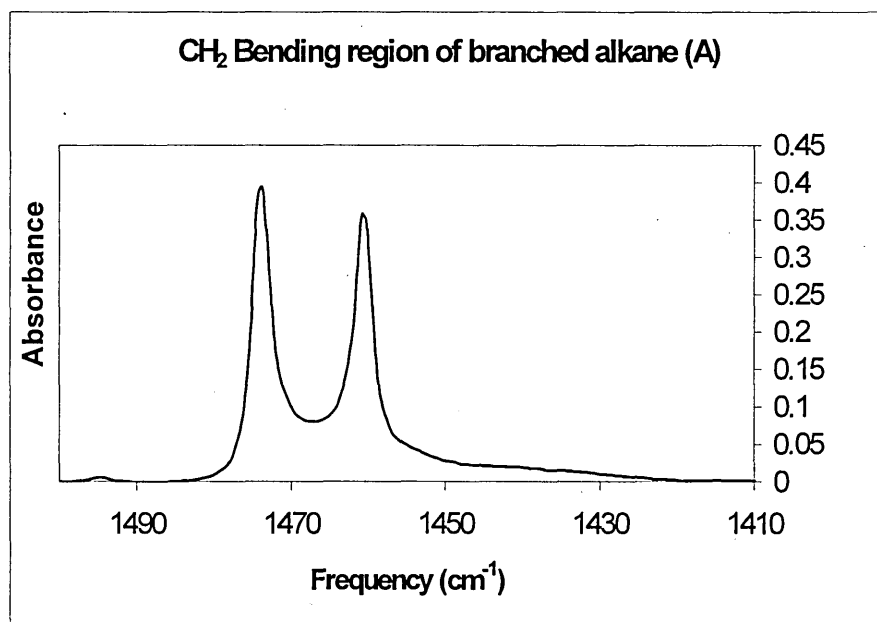


Fig 5.9: The CH<sub>2</sub> bending region of the infrared spectrum of deuterated branched alkane A at -173<sup>o</sup> C.

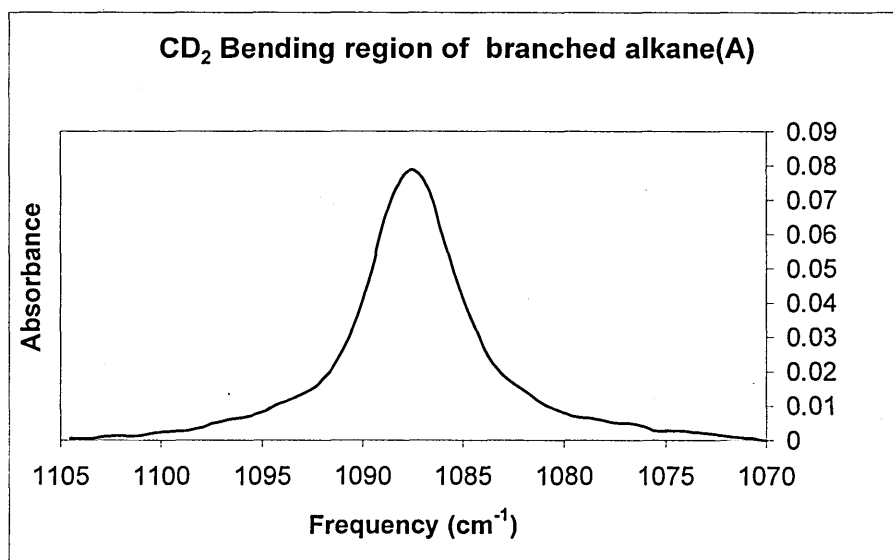


Fig 5.10: The CD<sub>2</sub> bending region of the infrared spectrum of deuterated branched alkane A at -173<sup>o</sup> C.

Deconvolution and curvefitting results of the CH<sub>2</sub> bending area show some contribution from the CH<sub>3</sub> deformation mode in this area as in the short chain alkane mixtures. According to the structure this molecule already contains an undeuterated branch which terminates with a CH<sub>3</sub> group. As we suspect that it is not fully deuterated, in some molecules either one of the two shorter branches or both can have a CH<sub>3</sub> terminating group instead of a CD<sub>3</sub> group. Therefore the presence of CH<sub>3</sub> bands in the CH<sub>2</sub> bending mode of the deuterated branched alkane is not surprising. However, the form of the CD<sub>2</sub> bending mode was unexpected. Having two end – deuterated branches out of the three branches in most of the molecules it was expected to show a doublet for this mode in the infrared spectrum. The components of a doublet were identified only from deconvolution and curve fitting. This rules out a structure with adjacent deuterated stems similar to the one proposed for C<sub>216</sub>D (see figure 6.1, Chapter 6) despite the presence of high proportion of deuterium end caps. Our calculations showed that the sample A consists only 80% of the expected deuterium content (see page 136).

We recrystallised the sample at 0.2° C min<sup>-1</sup> from the melt allowing more time to get the branches ordered with the intention of developing a doublet for the CD<sub>2</sub> bending mode in the infrared spectrum. It too failed to produce a doublet and resulted in a similar type of singlet for the CD<sub>2</sub> bending mode in the infrared spectrum. Then we did heat annealing for 30 minutes at each temperature and cooling, up to melting in order to develop a doublet for the CD<sub>2</sub> bending mode. However none of the methods was capable of developing a doublet. Therefore it is more likely that the two deuterated branches are involved in the amorphous phase with the undeuterated longer branch making the crystalline layer. The infrared spectrum was checked for the CD<sub>2</sub> wagging modes to support the above structure.

There have been several attempts to assign the CD<sub>2</sub> wagging modes in the IR spectrum. However these assignments are not in good agreement. Some very early studies state a calculated value of around 890 cm<sup>-1</sup> for the CD<sub>2</sub> defect modes in the infrared spectrum<sup>7,8,9</sup>. Cutler et al have observed a band at 892 cm<sup>-1</sup> for the CD<sub>2</sub> wagging mode of perdeuterated polyethylene<sup>10</sup>. A more recent study using a mixture of C<sub>34</sub>H<sub>70</sub> and C<sub>36</sub>D<sub>74</sub> proposes a broad band around 970 cm<sup>-1</sup> as the CD<sub>2</sub> wagging mode<sup>11</sup>. Parker and Herman's observation of a band at 977 cm<sup>-1</sup> in the infrared spectrum of perdeuteropolyethylene supports this assignment<sup>12</sup>. However, they did not make any

specific conformational assignment to it. The infrared spectra of the deuterated branched alkane were checked for CD<sub>2</sub> defect modes around the above - mentioned wavenumber regions. No signs of prominent bands were detected. No bands due to CD<sub>2</sub> wagging modes could be observed in the Raman spectrum either. (This work is described in Chapter 7). If the two end deuterated branches are in the amorphous phase it should show CD<sub>2</sub> wagging modes in the infrared and Raman spectrum. Therefore the structure of this branched alkane is not clear. However, we identified a NIF form mainly based on the Raman spectroscopic evidence from the undeuterated segment (see Chapter 7).

## 5.5 Conclusion

An infrared method to determine the isotopic ratio in partially deuterated alkanes was established. The basis of the method was the Beer Lambert Law. The theory behind this method is that the CH<sub>2</sub>/CD<sub>2</sub> weight ratio of each sample is proportional to their CH<sub>2</sub>/CD<sub>2</sub> bending absorbance ratio in the ir spectrum. The method was successful in giving consistent results for a range of samples, but showed discrepancies in C216D – sample 1 and the branched alkane (incomplete deuteration). The weight ratios obtained from the infrared method agree well with the direct weight ratios for HPE/DPE, C168D and C216D – sample 2. It was found that the sample A consists only 80% of the expected deuterium content. The CD<sub>2</sub> bending mode of the infrared spectrum of the branched alkane turned out to be a broad singlet, centred around 1087 cm<sup>-1</sup> though we anticipated a doublet with a central singlet as in C216D for this mode<sup>11</sup>. This rules out a highly ordered adjacent arrangement of deuterated end caps. This branched alkane will be further studied in Chapter 7.



## References

- 1 Brooke GM, Farren C, Harden A, Whiting MC, Polymer, **42**, 2777 (2001)
- 2 Snyder RG, J. Molec. Spec., **7**, 116 (1961)
- 3 Snyder RG, Schachtschneider, Spectrochimica Acta, **19**, 117 (1963)
- 4 Holland RF, Nielsen JR, J. Mol. Spectry., **8**, 383 (1962)
- 5 Jones RN, Spectrochim. Acta , **9**, 235 (1957)
- 6 Snyder RG, J. Mol. Spectr., **4**, 411 (1960)
- 7 Tasumi M, Shimanouchi T, J. Chem. Phys., **43**, 1245 (1965)
- 8 Piseri L, Zerbi G, J. Chem. Phys., **48**, 3561 (1968)
- 9 Tasumi M, Krimm, J. Chem. Phys., **46**, 755 (1967)
- 10 Cutler DJ, Hendra PJ, Walker JH, Spectrochimica Acta, **34A**, 391 ((1978)
- 11 De Silva DSM, PhD Thesis , University of Sheffield, February (2002)
- 12 Parker SF, Herman H, Spectrochimica Acta, Part A, **53**, 119 (1997)

### Partially (End) Deuterated Long Chain Alkanes

#### 6.1 Introduction

Direct observations of departures from crystalline regularity in polyethylene and the characterisation of the exact nature of this departure at the level of molecular conformation are needed for improved understanding of the properties of polymers. But, the vibrational spectrum of a conformationally disordered polymer is enormously complex. Deuterium substitution has been an immense help in this regard. The introduction of a low concentration of an isotopic impurity results in localised vibrations whose frequencies are dependent in a relatively simple way on conformation. Snyder and Poore made a significant step in this direction. They have used partially deuterated polymer to study the conformational structure of polyethylene<sup>1</sup>. They demonstrated that the infrared spectrum of partially deuterated polyethylene (CD<sub>2</sub> groups in low concentration) displays bands that could be associated directly with the conformational state of adjacent pairs of C-C bonds. They identified a rocking vibration at 620 cm<sup>-1</sup> for an isolated CD<sub>2</sub> group associated with a *trans-trans* bond pair and another one around 646 – 651 cm<sup>-1</sup> for an isolated CD<sub>2</sub> group associated with a *trans-gauche* bond pair. Their intensities were used to measure the relative concentrations of these bond pairs. Reneker et al have studied the *tg* band intensity as a function of temperature<sup>2</sup>. They have found an increase in the concentration of *tg* sequences in crystalline polyethylene with temperature, well below the melting temperature. This is consistent with the thermal generation of defects, which may be involved in transport of the polymer chain through the crystal. This sensitivity of the rocking mode vibration of an isolated CD<sub>2</sub> group substituted in a polymethylene chain to the conformation in the immediate vicinity of the CD<sub>2</sub> group has been the basis for the commonly used infrared method for determining site-specific conformation in polymethylene systems. Maroncelli et al have extended this CD<sub>2</sub> probe method with the use of n-alkanes<sup>3</sup>. They found that although the frequency of the CD<sub>2</sub> rocking band is determined primarily by the conformation of adjoining C-C bonds, the conformation of the next nearest C-C bonds, the position of the CD<sub>2</sub> groups in the chain and the chain length also affect the frequency of the CD<sub>2</sub>

rocking mode. Snyder and Poore's initial  $\text{CD}_2$  probe method has been expanded further to study the distribution of conformational defects in the high temperature phase II (rotator phase) of short chain alkanes<sup>4</sup>.

Recently synthesised end - deuterated n-alkanes provide important models to study the translational disorder of lamellar crystals of polyethylene. They allow independent infrared probing of molecular disorder at the deuterated surface and in the hydrogenous interior of the crystals. In addition, the infrared spectra of these end - deuterated alkanes have shown the *gtg* defect mode at  $1370\text{ cm}^{-1}$ , for the first time, without overlap from the  $1378\text{ cm}^{-1}$  symmetric methyl deformation band, due to the absence of  $\text{CH}_3$  groups<sup>5</sup>. De Silva et al have used the end deuterated n-alkane,  $\text{C}_{12}\text{D}_{25}\text{C}_{192}\text{H}_{384}\text{C}_{12}\text{HD}_{24}$ , to study both the translational and conformational disorder using infrared spectroscopy<sup>6</sup>. The  $\text{CH}_2$  and  $\text{CD}_2$  bending modes and the  $\text{CH}_2$  and  $\text{CD}_2$  wagging modes of the infrared spectrum have been used in this regard. The former give a measure of translational disorder, while the latter probe conformational disorder.

In polyethylene crystals with the orthorhombic subcell, the  $\text{CH}_2$  and  $\text{CD}_2$  bending modes show a crystal field splitting. For an infinite row of chains in a (110) plane  $\Delta v_\infty = 2\Delta v_0$ , where  $\Delta v_0$  is the splitting for an isolated pair of stems<sup>7</sup>. For an infinite stack of infinite (110) rows, i.e. an infinite crystal lamella,  $\Delta v_{\infty \times \infty} = 2\Delta v_\infty = 4\Delta v_0$ . If the domain of coupled oscillators is restricted by defects,  $\Delta v$  decreases. Hence, a deuterated alkane chain in a hydrogenous crystal matrix (\* in fig. 6.1) will decouple the oscillators and serve as a domain-limiting defect. Thus the reduction in the observed  $\text{CD}_2$  doublet splitting compared to  $\Delta v_{\infty \times \infty}$ , will give a picture of the local chain environment. Not only the positional defects, but several other types of defects such as thermal librations and conformational defects will also reduce the  $\Delta v$ . The principle of the technique in relation to the end-deuterated alkane is described below<sup>5</sup>.

If a larger number of chain ends are in perfect register along  $\langle 110 \rangle$  directions, we can observe a larger doublet splitting for the  $\text{CD}_2$  bending mode while a lesser number of chain ends in register would result in a smaller splitting. The (isotopically) isolated and amorphous chain ends will show a singlet for the  $\text{CD}_2$  bending mode in the infrared spectrum.

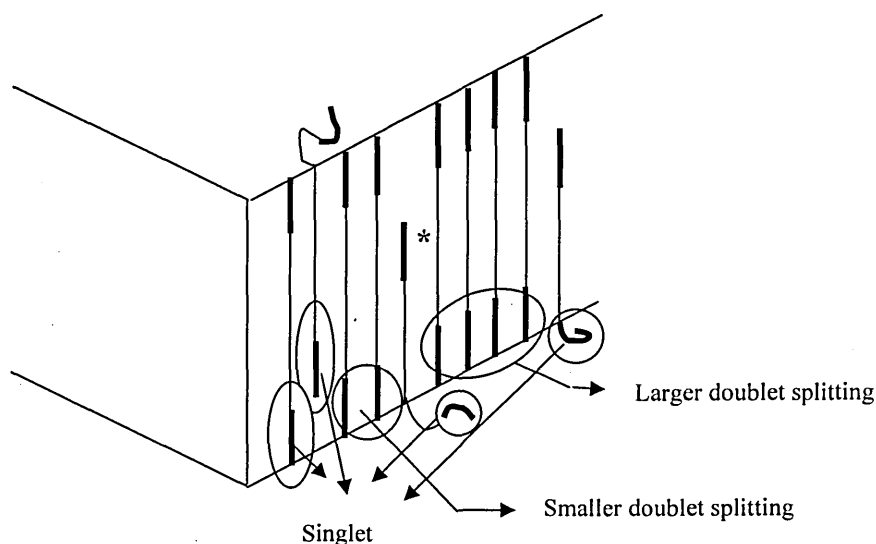


Fig 6.1: Schematic arrangement of alkane chains in an extended chain lamella, showing some crystal surface disorder. Deuterated chain ends are denoted by thicker lines.

In the case of perfectly ordered extended chain crystals of  $C_{12}D_{25}C_{192}H_{384}C_{12}HD_{24}$ , both the  $CH_2$  and  $CD_2$  bending modes should show maximum splitting as both hydrogenous and deuterated domains are surrounded by their own species. Therefore, any reduction in resulting splitting of the  $CH_2$  and  $CD_2$  bending modes serves as a probe for the hydrogenous interior and the deuterated surface respectively. De Silva et al have studied the behaviour of the  $CH_2$  and  $CD_2$  bending modes of  $C_{12}D_{25}C_{192}H_{384}C_{12}HD_{24}$  with increasing annealing temperature<sup>6</sup>. The corresponding spectra have been recorded at  $-173^\circ\text{C}$ . They have observed a full splitting of  $13.1\text{ cm}^{-1}$  for the  $CH_2$  bending mode of the as-grown crystals of  $C_{12}D_{25}C_{192}H_{384}C_{12}HD_{24}$  (which is a typical value for crystalline polyethylene and n-alkanes at this temperature<sup>7</sup>) and little change in this value with annealing. In contrast, for the corresponding  $CD_2$  mode of  $C_{12}D_{25}C_{192}H_{384}C_{12}HD_{24}$  as-grown crystals, a poorly resolved doublet and a central singlet have been observed. Using Fourier deconvolution and curve fitting techniques, it has been shown that  $\Delta\nu$  of the as-grown crystals is only  $6.8\text{ cm}^{-1}$  ( $\Delta\nu_{\infty\times\infty} = 10.1\text{ cm}^{-1}$  for perdeuterated polyethylene<sup>8</sup>). This shows that the deuterated surface of the as-grown crystals is more disordered than the hydrogenous interior. The central singlet accounts for isotopically isolated chains. Unlike the  $CH_2$  band, the  $CD_2$  deformation band changes substantially on annealing. The doublet becomes better resolved and the singlet is diminished with increasing annealing temperature up to melting for spectra recorded at  $-173^\circ\text{C}$ . The

increase in the doublet splitting was from 6.8 to 7.9  $\text{cm}^{-1}$ . This is evidence for a perfecting of the surface layer of the crystal with increasing annealing temperature, in terms of increasing the average size of ordered domains of coupled oscillators and decreasing the proportion of decoupled terminal  $\text{C}_{12}\text{D}_{25}$  end caps. The increase in the domain size corresponding to the increase in the doublet splitting will be calculated in section 6.3.1.2. The maximum splitting observed here for the  $\text{CD}_2$  bending doublet is still lower than the value for the full  $\text{CD}_2$  splitting. The question then arose as to whether the  $\text{C}_{12}\text{D}_{25}$  end cap is sufficiently long to produce the full  $\text{CD}_2$  splitting observed for deuterated polyethylenes and alkanes. Therefore we used the  $\text{C}_{13}$  deuterated alkane to investigate the maximum possible splitting given by the  $\text{C}_{12}\text{D}_{25}$  end cap (see section 6.3.1.1). In this case we could not use the corresponding  $\text{C}_{12}$  alkane due to the mismatch of the crystal structures : the crystal structure of  $\text{C}_{12}\text{D}_{25}\text{C}_{192}\text{H}_{384}\text{C}_{12}\text{HD}_{24}$  is orthorhombic<sup>6</sup>, whereas at low temperature, a triclinic phase is stable in the even paraffins below  $\text{C}_{24}$  and all the odd paraffins above  $\text{C}_9$  form a stable orthorhombic structure<sup>9</sup>.

Another use of  $\text{C}_{12}\text{D}_{25}\text{C}_{192}\text{H}_{384}\text{C}_{12}\text{HD}_{24}$  has been as a model compound, to study chain tilt, a phenomenon that is quite common in polymers<sup>6</sup>. The first experiments on such tilt, have been made on  $\text{C}_{198}\text{H}_{398}$ <sup>10</sup>. The main advantage of  $\text{C}_{12}\text{D}_{25}\text{C}_{192}\text{H}_{384}\text{C}_{12}\text{HD}_{24}$  is that it allows us to probe the crystal surface separately from the crystal interior. A series of SAXS curves have been recorded while heating the samples continuously up to melting using different heating rates in each case. All samples have shown a  $35^\circ$  maximum tilt, the tilt predicted for a theoretical angle for {201} basal plane<sup>6</sup>. An onset of tilting has been observed above  $80^\circ\text{C}$  for all the samples except for the  $\text{C}_{198}\text{H}_{398}$  extended chain form<sup>6</sup>. Here, the tilting started at a somewhat higher temperature, but the tilt angle eventually reached  $35^\circ$ . Therefore it was suspected that this delay might be due to the variation in the heating rate. Therefore  $\text{C}_{12}\text{D}_{25}\text{C}_{192}\text{H}_{384}\text{C}_{12}\text{HD}_{24}$  was further studied by SAXS using a different heating rate from the above studies (see section 6.3.2.1). In this chapter we will discuss all the infrared and SAXS work on  $\text{C}_{12}\text{D}_{25}\text{C}_{192}\text{H}_{384}\text{C}_{12}\text{HD}_{24}$  and review the findings in order to show how the chain tilt in long alkanes is related to crystal disorder.

In addition to work related to the previous study on  $\text{C}_{12}\text{D}_{25}\text{C}_{192}\text{H}_{384}\text{C}_{12}\text{HD}_{24}$ <sup>6</sup> mentioned above, this chapter includes further work on  $\text{C}_{12}\text{D}_{25}\text{C}_{192}\text{H}_{384}\text{C}_{12}\text{HD}_{24}$ . The X-ray long

spacing of  $C_{12}D_{25}C_{192}H_{384}C_{12}HD_{24}$  calculated from SAXS patterns observed in the chain tilt study shows a variation with the order of diffraction. The influence of the particle factor and lattice factor on the positions of the small angle reflections of crystalline polymer samples have been investigated by Reinhold and Fischer<sup>11</sup>. They calculated scattering curves for a lattice described by a linear paracrystalline model. The presence of defects in a crystal will give rise to broadening of the diffraction maxima. However, the broadening of diffraction maxima can also be caused by the crystals having a finite size and, since polymer crystals are normally relatively small, most of the observed broadening is usually caused by the size effect. There are several types of imperfections in crystalline polymers such as point defects and dislocations. The effect of all the many types of defects discussed above is to deform and distort the crystal lattice and produce broadening of the X-ray diffraction maxima. This type of disorder in a crystalline structure has been termed paracrystallinity. The polymer paracrystal is modelled by allowing the unit cell dimensions to vary from one cell to another and this allows the broadening of the X-ray patterns, over and above that expected from crystal size effects, to be explained. In this chapter we will evaluate the observed variation of X-ray long spacing with the diffraction order using this type of paracrystalline model.

End-deuterated  $C_{12}D_{25}C_{192}H_{384}C_{12}HD_{24}$  can also be crystallised in the once folded form. But how the folds are arranged within the lamellae is an open question. The following structures show two possible arrangements.

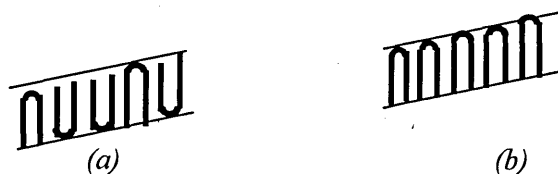


Fig 6.2: (a) Random arrangements of folds at the lamellar surfaces and (b) regular arrangement of folds on one such surface.

In figure 6.2(b) all the folds have a regular arrangement in the  $\langle 110 \rangle$  direction on one lamellar surface. In figure 6.2(a) the folds in the  $\langle 110 \rangle$  direction are arranged randomly on both lamellar surfaces. The use of the  $CD_2$  bending vibration of the infrared spectrum in determining the translational disorder of lamellar crystals was described earlier. In this study we will evaluate the use of  $CD_2$  bending vibration of the infrared spectrum to distinguish between the two structures above.

## 6.2 Experimental

### 6.2.1 FTIR studies on deuterated Tridecane

The FTIR spectrum of  $C_{13}D_{28}$  [98.9 atom% D, CDN Isotopes] was recorded using a Mattson Galaxy 6020 spectrometer. The sample was held between KBr microscope slides in a Graseby-Specac 21500 cryostat with temperature controlled by a 20120 temperature controller. The sample space was evacuated. The sample was cooled to  $-173^{\circ}C$  using liquid nitrogen. The spectrum was recorded at  $1\text{ cm}^{-1}$  resolution, using 200 scans. The crystal structure of  $C_{13}D_{28}$  at  $-173^{\circ}C$  is orthorhombic<sup>9</sup>. It is assumed here that the chain ends of  $C_{13}D_{28}$  are in perfect register within the orthorhombic structure.

### 6.2.2 SAXS on $C_{12}D_{25}C_{192}H_{384}C_{12}HD_{24}$

A small angle X-ray scattering (SAXS) experiment was done on the Regaku-Denki camera on a sample of  $C_{12}D_{25}C_{192}H_{384}C_{12}HD_{24}$  in the extended form (courtesy of Prof. G. Ungar, University of Sheffield). Several pieces of the mat were put in a capillary in such a way that their orientations were roughly the same. The capillary with the sample was held in a modified Linkam hot stage with mica windows and temperature control within  $\pm 0.2^{\circ}C$ . The sample was heated stepwise using a heating rate of  $0.2^{\circ}C\text{ min}^{-1}$  until it melted. The sample was exposed to X-rays at each temperature for more than 24 hrs. Nickel-filtered  $CuK_{\alpha}$  radiation ( $1.54178\text{ \AA}$ ) was used. The instrument was calibrated using  $C_{40}H_{82}$  in which the unit cell length is known, to determine the sample to film distance. This was found to be 274.5 mm.

#### **Sample preparation:**

The sample had been crystallised from 1.3% toluene solution for 6 hours at  $82^{\circ}C$  to obtain lamellar crystals with purely extended chains. Crystals were filtered relatively rapidly and dried in a vacuum at  $50^{\circ}C$  for 2 days. The crystals were put in a glass capillary for the X-ray measurements.

### 6.3 Results and Discussion

#### 6.3.1 Infrared work on deuterated alkanes

##### 6.3.1.1 FTIR studies on deuterated Tridecane

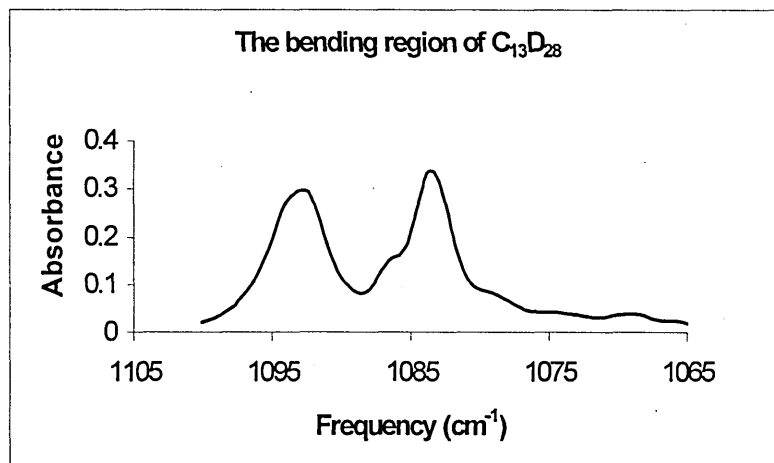


Fig 6.3: The FTIR spectrum in the bending region of  $C_{13}D_{28}$  at  $-173^{\circ}C$ .

The  $CD_2$  bending region of the infrared spectrum was of interest. We observed a doublet at  $1092.8\text{ cm}^{-1}$  and  $1083.5\text{ cm}^{-1}$  for the  $CD_2$  bending mode of  $C_{13}D_{28}$  (figure 6.3). The  $CD_2$  bending doublet splitting determined for  $C_{13}D_{28}$  is therefore  $9.3\text{ cm}^{-1}$ . For an infinite stack of infinite (110) rows,  $\Delta\nu_{\infty\infty} = 10.1\text{ cm}^{-1}$  for the  $CD_2$  bending mode<sup>8</sup>. Therefore, we can conclude that a chain length around 12 carbon atoms is not capable of producing the 'full' splitting for the bending vibration, as is observed, for example, in perdeuterated polyethylene. Thus, it is reasonable to say that the  $C_{12}D_{25}$  end cap of  $C_{12}D_{25}C_{192}H_{384}C_{12}HD_{24}$  is not long enough to allow the full splitting to develop, even when the chain ends are in perfect register. But the maximum observed splitting for the  $CD_2$  bending mode of  $C_{12}D_{25}C_{192}H_{384}C_{12}HD_{24}$  annealed crystals was  $7.9\text{ cm}^{-1}$ <sup>6</sup>. This value is  $1.4\text{ cm}^{-1}$  less than the value for  $C_{13}D_{28}$ . However,  $C_{13}D_{28}$  chains are perpendicular to the layer normal for the orthorhombic crystal structure whereas the chain stems of  $C_{12}D_{25}C_{192}H_{384}C_{12}HD_{24}$  become tilted after annealing at higher temperatures (as will be discussed further in section 6.3.2.1). This will cause further reduction in the doublet splitting of the  $CD_2$  bending mode of  $C_{12}D_{25}C_{192}H_{384}C_{12}HD_{24}$ . The doublet splitting of a particular vibration mode depends on several factors. They are:



group size, chain length, chain tilt and the chain register. Out of them, the group size is the most significant factor in determining the amount of doublet splitting. The larger the group size, the bigger is the value of the splitting. The effective size of the group depends on the chain register. In an idealized model (figure 6.1), longitudinal displacement of a chain of the order of 12 carbon atoms would create (a) a vacancy in the deuterated layer at one crystal surface, (b) substitution of a deuterated segment by a hydrogenous one at the other surface, and (c) protrusion of a deuterated chain end out of the latter surface. The effect of (a) and (b) is to limit the size of the coupled domain of  $\text{CD}_2$  oscillators and thus reduce the splitting of  $\text{CD}_2$  bending mode. The effect of (c) is the creation of a singlet in the  $\text{CD}_2$  bending mode. De Silva et al have quantified the observed reduction of the  $\text{CD}_2$  bending mode splitting of  $\text{C}_{12}\text{D}_{25}\text{C}_{192}\text{H}_{384}\text{C}_{12}\text{HD}_{24}$  as-grown crystals and the annealed crystals<sup>12</sup>. Considering the number of interactions between  $\text{CD}_2$  groups in the  $\text{C}_{12}\text{D}_{25}$  end cap, they estimated that the reduction of chain length from infinity to  $(\text{CD})_{12}$  causes a 10% reduction in  $\Delta\nu_{\infty\infty}$ . Therefore, the calculated value for the maximum  $\text{CD}_2$  bending splitting of  $\text{C}_{12}\text{D}_{25}\text{C}_{192}\text{H}_{384}\text{C}_{12}\text{HD}_{24}$  untilted crystals is  $9.1 \text{ cm}^{-1}$ .<sup>12</sup> By comparison, the splitting of  $\text{C}_{13}\text{D}_{28}$  was observed to be  $9.3 \text{ cm}^{-1}$ . After annealing  $\text{C}_{12}\text{D}_{25}\text{C}_{192}\text{H}_{384}\text{C}_{12}\text{HD}_{24}$  at higher temperature the crystal will develop a  $\{201\}$  tilt. As a consequence of that, the splitting will be further reduced. This reduction in the maximum  $\text{CD}_2$  bending splitting of  $\text{C}_{12}\text{D}_{25}\text{C}_{192}\text{H}_{384}\text{C}_{12}\text{HD}_{24}$ , was estimated to be from  $9.1$  to  $8.3 \text{ cm}^{-1}$  for the tilted crystals<sup>12</sup>. The largest observed splitting for the tilted  $\text{C}_{12}\text{D}_{25}\text{C}_{192}\text{H}_{384}\text{C}_{12}\text{HD}_{24}$  chains is  $7.9 \text{ cm}^{-1}$ .<sup>5</sup> The observed and calculated splittings of the  $\text{CD}_2$  bending mode for  $\text{C}_{12}\text{D}_{25}\text{C}_{192}\text{H}_{384}\text{C}_{12}\text{HD}_{24}$  and  $\text{C}_{13}\text{D}_{28}$  are summarised in Table 6.1.

Table 6.1: Calculated and observed values for  $\text{CD}_2$  bending mode splitting of  $\text{C}_{13}\text{D}_{28}$  and  $\text{C}_{12}\text{D}_{25}\text{C}_{192}\text{H}_{384}\text{C}_{12}\text{HD}_{24}$ .

Alkane	Chain orientation	Observed splitting ( $\text{cm}^{-1}$ )	Calculated splitting ( $\text{cm}^{-1}$ )
$\text{C}_{13}\text{D}_{28}$	perpendicular	9.3	-
$\text{C}_{12}\text{D}_{25}\text{C}_{192}\text{H}_{384}\text{C}_{12}\text{HD}_{24}$ -as grown crystals	perpendicular	6.8	9.1
$\text{C}_{12}\text{D}_{25}\text{C}_{192}\text{H}_{384}\text{C}_{12}\text{HD}_{24}$ -annealed crystals	tilted	7.9	8.3

According to Table 6.1 the experimentally observed splitting for  $C_{13}D_{28}$  and calculated splitting for  $C_{12}D_{25}C_{192}H_{384}C_{12}HD_{24}$ -as grown crystals and calculated and observed splittings for  $C_{12}D_{25}C_{192}H_{384}C_{12}HD_{24}$ -annealed crystal are within  $\pm 0.5 \text{ cm}^{-1}$ . Therefore it is reasonable to say that the reduced splitting of the  $C_{12}D_{25}$  end cap is primarily due to the shorter chain length and the chain tilt.

#### 6.3.1.2 Calculation of the domain sizes of deuterated end caps before and after annealing of $C_{12}D_{25}C_{192}H_{384}C_{12}HD_{24}$

It was seen earlier that the  $CD_2$  bending doublet splitting of  $C_{12}D_{25}C_{192}H_{384}C_{12}HD_{24}$  increased from 6.8 to 7.9  $\text{cm}^{-1}$  after heat annealing<sup>5</sup>. This suggests that annealing results in a perfecting of the surface layers of the crystal in terms of increasing the average size of ordered domains of coupled oscillators. The increase of domain size was calculated using the method suggested by Snyder et al<sup>13</sup> (described in Chapter 3.1.2). Their calibration curve used to determine domain size is shown in figure 6.4. The relationship between  $N^{1/2}$  and  $R$  for a square domain, is described by the formula;

$$R = \cos \left[ \frac{\pi}{N^{1/2} + 1} \right] \dots\dots\dots (6.1)$$

Where,  $R$  (normalised splitting) =  $\Delta\nu/\Delta\nu_0$  ( $\Delta\nu$  is the observed splitting for the bending mode of the hydrogenated or the deuterated alkane and  $\Delta\nu_0$  is the splitting for the neat n-alkane of the corresponding isotope) and  $N$  is the number of chains in the domain. Snyder has calculated the bending splittings for different shapes of domains such as square and random shaped domains<sup>13</sup>. Most polymers crystallise by chain folding into sheets of stems along a preferred fold plane. Therefore they are most likely to form square shape domains. However, in this work we used the extended crystals of  $C_{12}D_{25}C_{192}H_{384}C_{12}HD_{24}$ . These crystals do not have a preferred plane for adjacent molecules. Therefore, they are more likely to make randomly shaped domains.

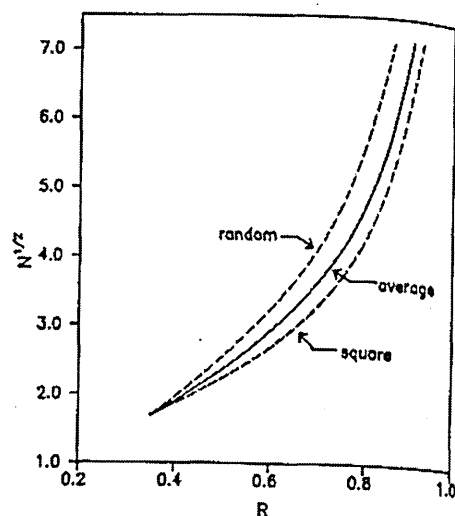


Fig 6.4: The calibration curves relating  $N^{1/2}$ , the root mean – square number of chains making up a domain, and  $R$ , the normalised splitting of the bending band<sup>13</sup>.

The curve used in this work is the average of the curves derived for the square and random – shaped cases. These latter curves are similar if  $N$  is small but diverge significantly for large  $N$ . The calibration curve was taken as the average of these because it was assumed that ‘surface tension effects’ would tend to smooth the contours of the domains and thus, on the average, nudge the random shapes toward somewhat more compact forms<sup>13</sup>.

The maximum observed  $\text{CD}_2$  bending splittings were as follows;

$\text{C}_{12}\text{D}_{25}\text{C}_{192}\text{H}_{384}\text{C}_{12}\text{HD}_{24}$ as-crystallised (perpendicular chains)	$6.8 \text{ cm}^{-1}$
$\text{C}_{12}\text{D}_{25}\text{C}_{192}\text{H}_{384}\text{C}_{12}\text{HD}_{24}$ after annealing (tilted chains)	$7.9 \text{ cm}^{-1}$

The calculated values of maximum  $\text{CD}_2$  bending splittings for infinite groups of labelled stems were as follows;<sup>12</sup>

$\text{C}_{12}\text{D}_{25}\text{C}_{192}\text{H}_{384}\text{C}_{12}\text{HD}_{24}$ as-crystallised (perpendicular chains)	$9.1 \text{ cm}^{-1}$
$\text{C}_{12}\text{D}_{25}\text{C}_{192}\text{H}_{384}\text{C}_{12}\text{HD}_{24}$ after annealing (tilted chains)	$8.3 \text{ cm}^{-1}$

We used  $\Delta\nu_0 = 9.1 \text{ cm}^{-1}$  and  $8.3 \text{ cm}^{-1}$  for the normalisation of the observed splitting for  $\text{C}_{12}\text{D}_{25}\text{C}_{192}\text{H}_{384}\text{C}_{12}\text{HD}_{24}$  as-grown crystals and annealed crystals respectively. It was estimated by means of figure 6.4 that the translationally ordered domain contains 16 chains in the as-crystallised sample, and  $> 50$  chains in the annealed sample. Therefore the increase in group size with the annealing at higher temperatures is from 16 to over

50 chains. At this stage the difference between observed and calculated splittings of  $C_{12}D_{25}C_{192}H_{384}C_{12}HD_{24}$ -annealed crystals is only  $0.4\text{ cm}^{-1}$ . This means  $C_{12}D_{25}C_{192}H_{384}C_{12}HD_{24}$  is reaching the perfectly ordered status after annealing.

### 6.3.2 X-ray work on deuterated alkanes

#### 6.3.2.1 Determination of the tilt angle of $C_{12}D_{25}C_{192}H_{384}C_{12}HD_{24}$ with increasing annealing temperature

Here, our aim was to study the chain tilt. Several SAXS studies have been done on the same sample using continuous heating<sup>6</sup> (using heating rates of  $6^{\circ}\text{C min}^{-1}$  and  $1^{\circ}\text{C min}^{-1}$ ). Here, we used stepwise heating. The main objective of this experiment was to investigate whether this heating mode and rate affect the tilt angle.

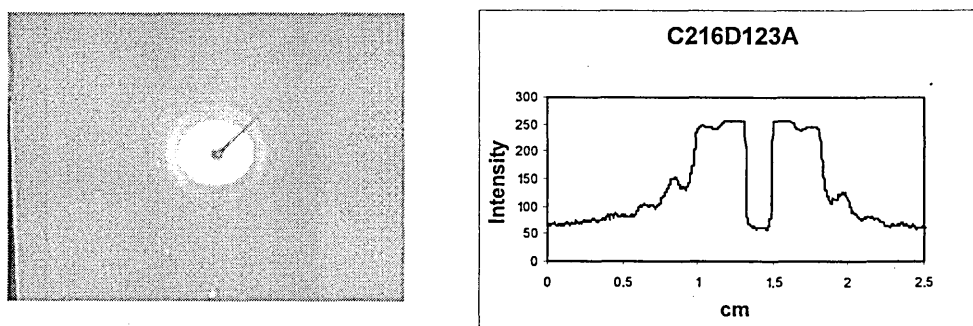


Fig. 6.5: (a) The X-ray scattering pattern obtained at  $123^{\circ}\text{C}$  (b) the radial intensity plot for this pattern.

Figure 6.5 (a) shows the X-ray scattering pattern obtained at  $123^{\circ}\text{C}$  and figure 6.5 (b) shows the radial intensity plot for this pattern. This intensity plot was obtained using the Image Pro software. It plots the intensity variation of the scattered X-rays with distance, across a diameter of the pattern. The above plot in figure 6.5(b) is a single line scan along the diameter of the scattering pattern shown in figure 6.5(a). A baseline was subtracted to remove the scattering background. The distance between two corresponding maxima of the intensity plot gives the diameter of the each ring of the scattering pattern.

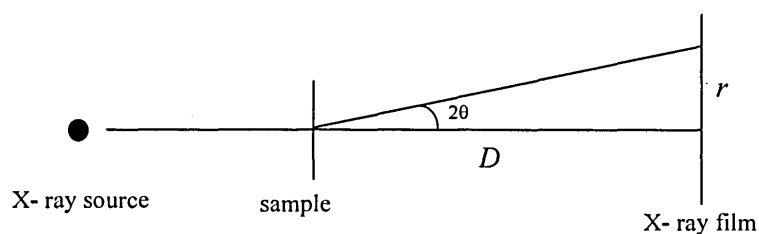


Fig 6.6: A schematic diagram of a SAXS experiment.

$r$  = radius of the diffraction pattern

$D$  = sample to film distance

The sample to film distance was calculated using  $C_{40}H_{82}$  in which the crystal thickness was known. The scattering angle,  $2\theta$ , was calculated using  $r$  and  $D$  values. Using Bragg's equation,  $n\lambda = 2d\sin\theta$ , the crystal thickness ( $d_T$ ) was calculated for each annealing temperature.

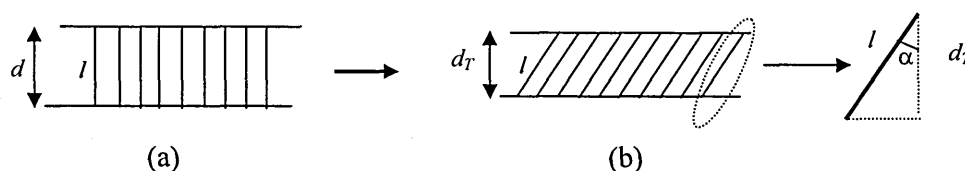


Fig 6.7: Transformation from the perpendicular extended chain structure to the tilted structure during heating. (a) perpendicular form (b) tilted form.

The length of the  $C_{216}H_{385}D_{49}$  chain,  $l$ , was calculated using the empirical formula<sup>9</sup>,  
 $l = n \cdot 1.27 + 2$ .

From figure 6.7(b):

$$\text{the tilt angle, } \alpha = \cos^{-1} \left( \frac{d_T}{l} \right) \dots\dots\dots (6.2)$$

Table 6.2: Variation of crystal thickness and tilt angle with annealing temperature

The standard deviation of the crystal thickness is 6Å.

Temperature (°C)	Crystal thickness (Å)	Tilt angle
25	267	0°
80	273	0°
100	260	20°
110	242	29°
115	240.5	29.5°
120	230	33.7°
123	228.5	34.2°
126	225	35.5°

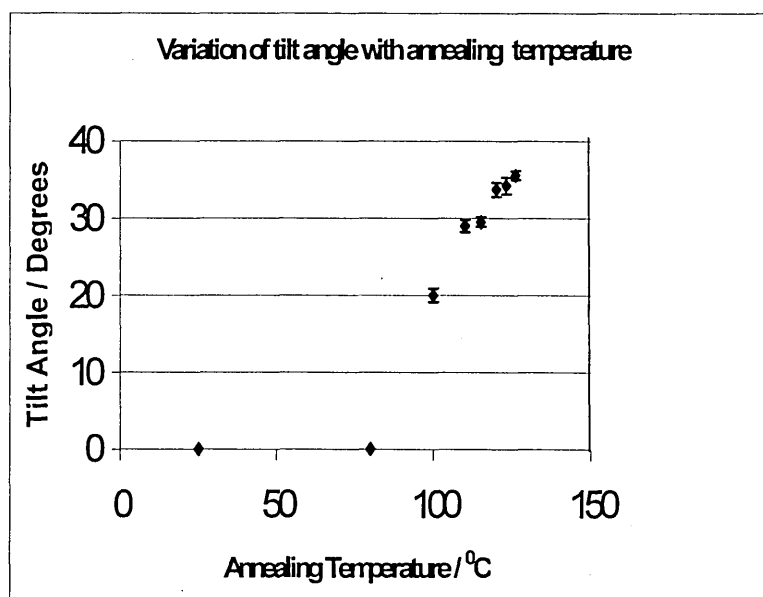


Fig 6.8: The graph of variation of tilt angle with the annealing temperature. The error represents the uncertainty in determining the positions of maxima in the radial intensity plots.

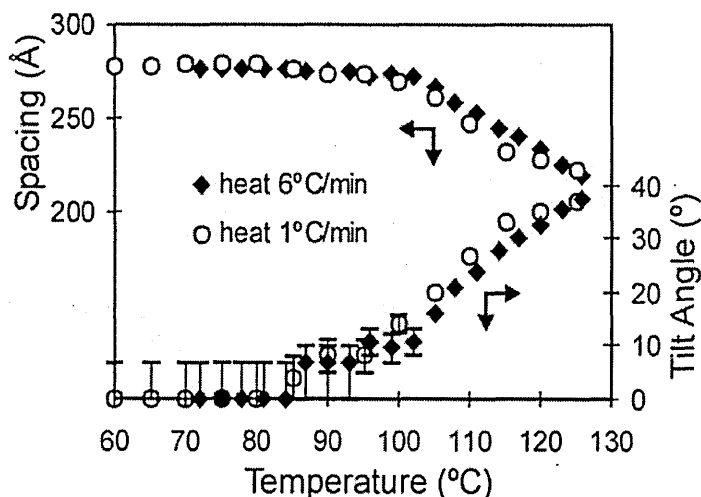


Fig 6.9: Temperature dependence of lamellar spacing  $L$  (upper half) and angle of chain tilt with respect to the lamellar normal (lower half) for extended-chain solution-grown crystals of  $C_{12}D_{25}C_{192}H_{384}C_{12}HD_{24}$  during continuous heating from  $60^{\circ}\text{C}$  to the melting point. Data for heating at  $1^{\circ}\text{Cmin}^{-1}$  (solid diamonds) and  $6^{\circ}\text{Cmin}^{-1}$  (empty circles) are shown for comparison<sup>6</sup>.

The variation of tilt angle with annealing temperature is shown in table 6.2 and figure 6.8. It was observed that tilting starts above  $80^{\circ}\text{C}$ . The maximum tilt obtained was around  $35^{\circ}$ . This also approximates to the maximum tilt angle found for polyethylene<sup>5</sup>. The results of continuous heating (using two different heating rates)<sup>6</sup> are shown in figure 6.9. This shows an onset of tilting above  $85^{\circ}\text{C}$  and a gradual increase up to melting. Since we increased the temperature from  $80^{\circ}$  to  $100^{\circ}\text{C}$  directly, a comparison of results in this temperature region from the two experiments is prevented. Both studies show a maximum tilt angle of  $35^{\circ} - 37^{\circ}$  is reached just before the melting point and the onset of tilting occurs around  $80^{\circ} - 85^{\circ}\text{C}$ . A similar study on extended chain  $C_{198}H_{398}$  using a continuous heating rate of  $2^{\circ}\text{C min}^{-1}$  has shown a similar behaviour to  $C_{12}D_{25}C_{192}H_{384}C_{12}HD_{24}$  although tilting started at a higher temperature<sup>6</sup>. A SAXS study on  $C_{198}H_{398}$  in the folded form has also shown an onset of tilting around  $85^{\circ}\text{C}$ . Around  $110^{\circ} - 114^{\circ}\text{C}$  a transformation to the extended chain form occurs, while the tilt angle continues to increase up to  $35^{\circ}$  just below the melting point of extended chain crystals<sup>6</sup>. All these experiments show an ultimate tilt angle of  $35^{\circ}$  irrespective of the heating rate and the method of heating. This is the tilt angle corresponding to the  $\{201\}$  basal plane. Similar temperature values for the onset of chain tilt and similar ultimate values for tilt-

angle lead us to the conclusion that there is no direct effect of heating rate or mode on the temperature dependence of the tilt angle.

An earlier FTIR study on  $C_{12}D_{25}C_{192}H_{384}C_{12}HD_{24}$  showed an increase in the  $CD_2$  bending doublet splitting and a significant decrease in the area of the singlet with increasing annealing temperature<sup>5</sup> (figure 6.10). All data here were collected at low temperature ( $-173^\circ C$ ). This increase in doublet splitting and the decrease in singlet area were due to the perfecting of the chain ends. Our calculations (section 6.3.1.2 above) showed that the size of the domain of labelled stems has increased from 16 to  $> 50$  chains during this perfecting process. According to figure 6.10 the most significant changes in the  $CD_2$  bending splitting and the singlet area occur above  $80^\circ C$ . Figure 6.8 and 6.9 show that tilting also starts above  $80^\circ C$ . With further increase in temperature, the tilt angle steadily increases while, according to IR evidence (figure 6.10) translational disorder steadily decreases.

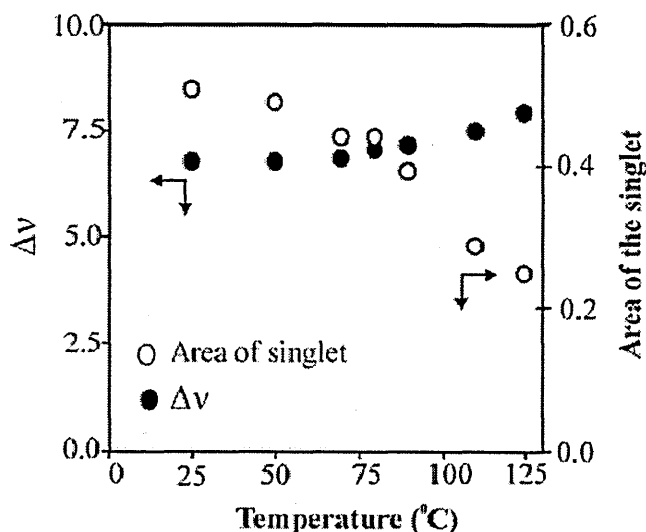


Fig 6.10: Magnitude of  $CD_2$  bending mode splitting ( $\Delta v$ , solid circles) and relative area of the central singlet component for extended-chain  $C_{216}H_{385}D_{49}$  crystals as a function of annealing temperature<sup>6</sup>.

The two phenomena – the development of chain tilt and the ordering of the chain ends – are thus seen to be related. The ordering of the chain ends causes a smoothing of the



crystal surface which induces chain tilt. However, it has been found that the chain tilting is irreversible while the surface conformational ordering is thermoreversible<sup>6</sup>.

We stated earlier that the onset of chain tilt coincides with the chain perfection in long chain alkanes. But this relationship is the exact reverse of the situation in short chain alkanes. A study on  $n\text{-C}_{33}\text{H}_{68}$  has shown that the chains are perpendicular in the highly ordered low temperature orthorhombic modification<sup>14</sup>. At higher temperatures after two first order transitions, a tilted form with a  $\{101\}$  basal plane is obtained. The latter structure is attributed to surface roughening, the tilted basal plane providing an enlarged area for the conformationally disordered chain ends. The lack of tilt in the low temperature phase of short chain alkanes is thought to be due to the absence of end group disorder. The question then arises as to why crystals with large translational disorder, such as as-grown crystals of  $\text{C}_{216}\text{H}_{385}\text{D}_{49}$ , do not require chain tilt. In such a crystal a buried chain end leaves extra space for the surrounding continuing chains to accommodate non-planar chain ends. With increasing temperature, the increase in chain mobility improves the translational order, the vacancies are eliminated and the crystal surface becomes smoother. This will cause a reduction in the free volume for chain ends, which are incorporated into the crystal with annealing. This is solved by chain tilting which will result in more space for the chain ends to accommodate.

#### 6.3.2.2 Evaluation of SAXS of $\text{C}_{12}\text{D}_{25}\text{C}_{192}\text{H}_{384}\text{C}_{12}\text{HD}_{24}$ using a paracrystalline model

The variation of the X-ray long spacing with the order of diffraction as calculated using the Bragg equation separately for each order of diffraction, is given in table 6.2 and figure 6.11. The results clearly show a significant change in the calculated periodicity with order of diffraction. Since sample crystallinity is high, for these high purity materials the long spacing approximates to the crystal thickness.

Changes in the value of lamellar periodicity obtained with order of diffraction are not surprising because the Bragg equation applies for perfect crystals. This approximation can be used for real crystals if the influence of the particle factor and of lattice disordering is small enough to be neglected. However, this neglect is not permissible in small angle scattering by polymer structures supposedly consisting of stacks of nearly

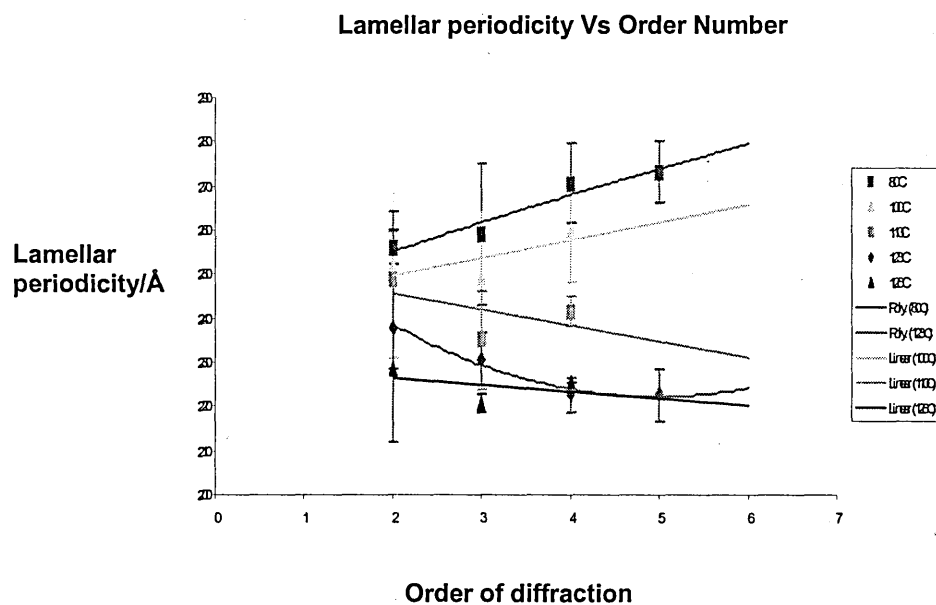


Fig 6.11: Variation of lamellar periodicity with the order of diffraction at different temperatures. Lines are drawn simply as guides for the eye.

Table 6.2: Variation of lamellar periodicity with order at each annealing temperature  
Figures in parenthesis are the estimated error in each value (in Å).

Temperature (°C)	Lamellar periodicity (Å)				
	Order number				
	2	3	4	5	6
25	-	253.6(28.0)	260.0(22.0)	264.0(18.0)	267.0(15.0)
80	256.0(4.0)	259.0(16.0)	270.6(9.0)	273.0(7.0)	
100	252.0(21.0)	249.0(15.0)	260.0(12.0)		
110	248.7(11.0)	235.0(11.0)	241.6(3.5)		
115	245.0(11.0)	235.0(9.0)	241.6(9.0)		
120	238.0(22.0)	230.6(2.0)	225.5(1.5)	225.0(3.6)	
123	238.0(26.0)	230.6(6.0)	222.6(4.0)	222.6(6.0)	
126	228.5(4.0)	220.6(2.0)	225.5(3.0)		

parallel lamella. There can be great distance fluctuations in these structures. For example, the variation in amorphous layer thickness can cause a variation in the periodicity measured. The influence of the particle factor and lattice factor on the positions of the small angle reflections of polymer crystalline samples have been investigated by Reinhold and Fischer<sup>11</sup>. They allowed some fluctuations to occur in the periodicity,  $L$ , of the structure. Calculations of scattering curves have been described for a lattice considered as a linear paracrystal to which the scattering theory of Hosemann<sup>15</sup> can be applied. The same approach is adopted here.

According to Hosemann<sup>15</sup> the scattering intensity of a linear lattice as a function of  $s = 2 \sin \theta / \lambda$  is ;

$$I(s) = N [ \langle f^2(s) \rangle - \langle f(s) \rangle^2 ] + (1/V) \langle f(s) \rangle^2 Z(s) * |S(s)|^2 \dots\dots\dots (6.3)$$

Where  $f(s)$  = scattering amplitude of a single lamella (particle amplitude)

$Z(s)$  = the paracrystalline lattice factor

$|S(s)|^2$  = the shape factor

$N$  = the number of lamellae

$V$  = the volume of the paracrystal

The first term yields a diffuse background due to the mean square fluctuation of the particle amplitude. Without such a fluctuation the intensity is given by the second term representing the crystal-like interference scattering. For an infinitely extended crystal the shape factor  $|S(s)|^2$  is a Dirac delta function. The convolution product consequently reduces to  $Z(s)$ . Hence;

$$I \sim f^2(s) Z(s) \dots\dots\dots (6.4)$$

Let us assume that a linear lattice with periodicity  $L$  consists of two phases with thicknesses  $a$  and  $L-a$ . In the direction perpendicular to the lamellar surface the electron density is a periodic step function representing the extreme case of sharp phase boundaries. The corresponding particle amplitude,  $f(s)$ , is the Fourier transform of the density difference function of one period;

$$f(s) = \int \Delta P(x) \exp(-2\pi i s x) dx \dots\dots\dots (6.5)$$

where  $\rho$  = electron density

$s$  = scattering vector

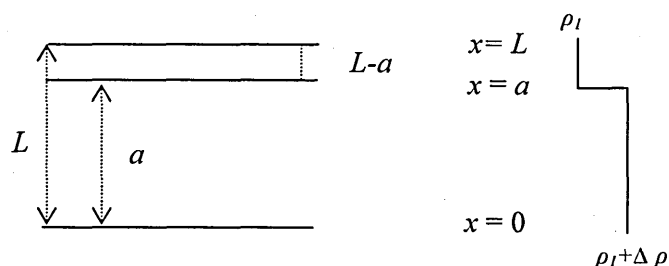


Fig 6.12: A schematic diagram of a lamella consisting of a constant crystalline thickness ( $a$ ), and a variable amorphous layer thickness ( $L-a$ ). The sketch to the right shows schematically the variation in electron density,  $\rho$ .

The particle factor,  $f^2(s)$ , consequently is ;

$$f^2(s) = (\Delta P)^2 [\sin^2 \pi s a / (\pi s)^2] \quad \dots\dots\dots (6.6)$$

Let us assume the distribution function,  $h(x)$ , for the distances of two adjacent equivalent points in the lattice is Gaussian.

$$h(x) = [1/(2\pi)^{1/2} g L] \exp[-(x-L)^2 / 2g^2 L^2] \quad \dots\dots\dots (6.7)$$

where  $L$  = average lattice distance  
 $g = \Delta L/L$ , relative distance fluctuation

The lattice factor,  $Z(s)$ , resulting from a Gaussian distance distribution is as follows;

$$Z(s) = \text{Re}[(1+H)/(1-H)] \quad \dots\dots\dots (6.8)$$

Where  $H$  is a function of  $s$  and represents the Fourier transform of the distribution  $h(x)$ .

Hence,

$$H(s) = \exp(-2\pi i s L) \exp(-2\pi^2 g^2 s^2 L^2) \quad \dots\dots\dots (6.9)$$

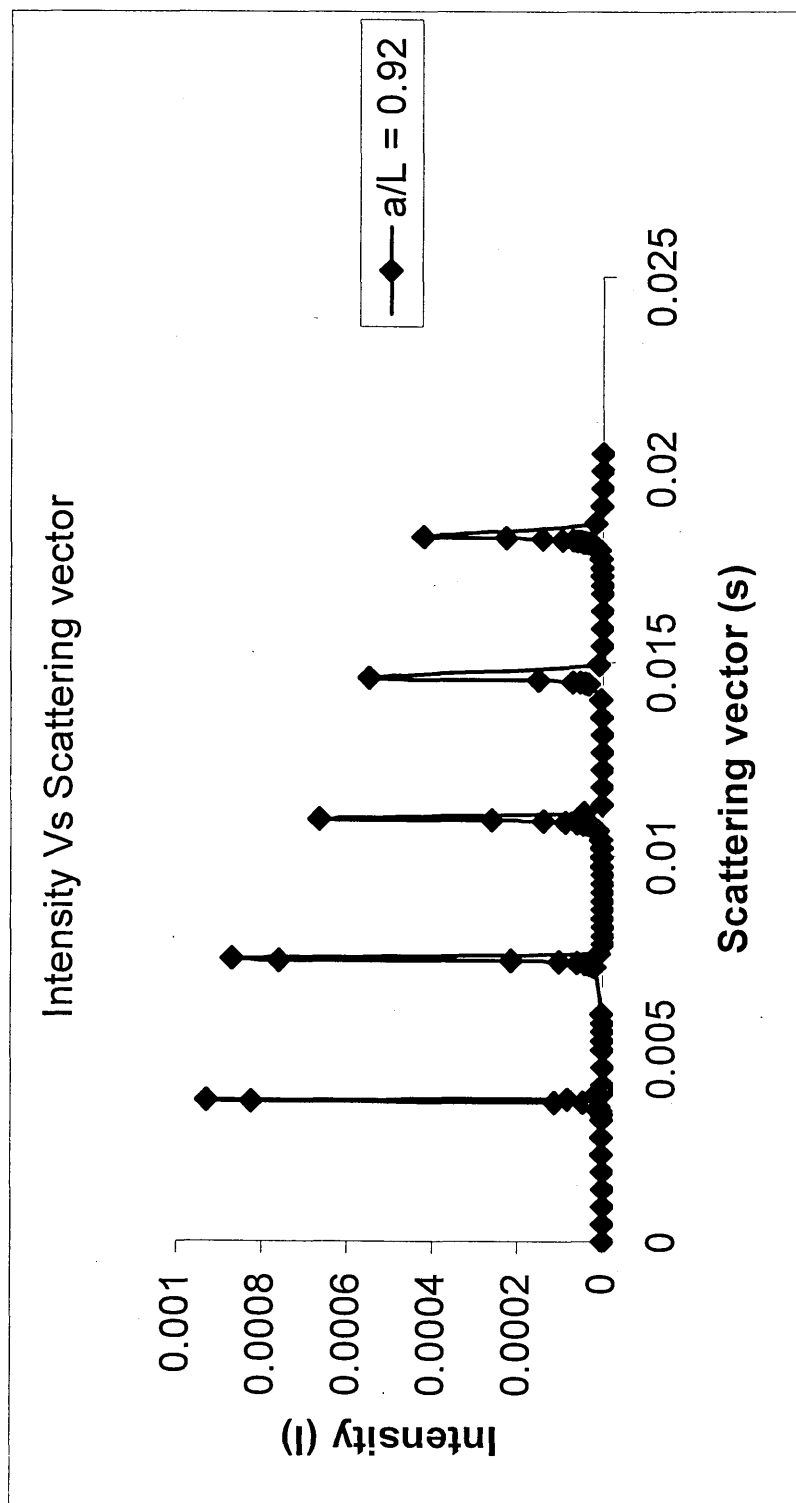
$$\text{Re}[H(s)] = |H| \cos 2\pi s L \quad \dots\dots\dots (6.10)$$

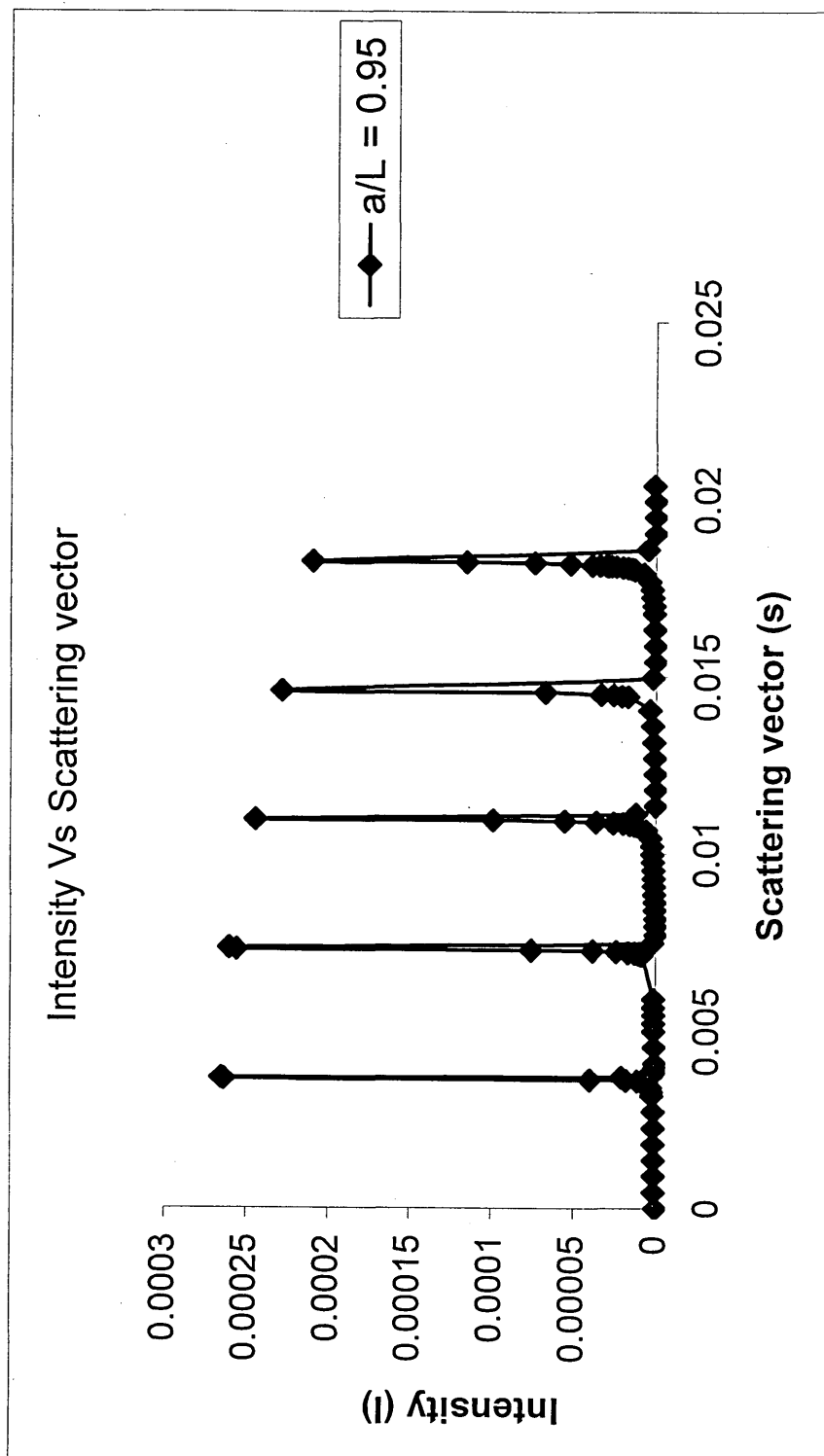
$$Z(s) = (1 + |H| \cos 2\pi s L) / (1 - |H| \cos 2\pi s L) \quad \dots\dots\dots (6.11)$$

The lattice factor  $Z(s)$ , therefore, fluctuates between the values  $Z = (1+H)/(1-H)$  for  $sL = n$  and  $Z = (1-H)/(1+H)$  for  $sL = \frac{1}{2} + n$ , with  $n$  being whole numbers.

Substituting  $L = 273 \text{ \AA}$  and  $g = 0.001$  in equation (6.9) and  $a = 260, 268$  and  $250 \text{ \AA}$  in equation (6.6) and using equation (6.4) gave the following intensity versus scattering vector plots;

(a)  $a = 250 \text{ \AA}$



(b)  $a = 260 \text{ \AA}$ 

(c)  $a = 268 \text{ \AA}$

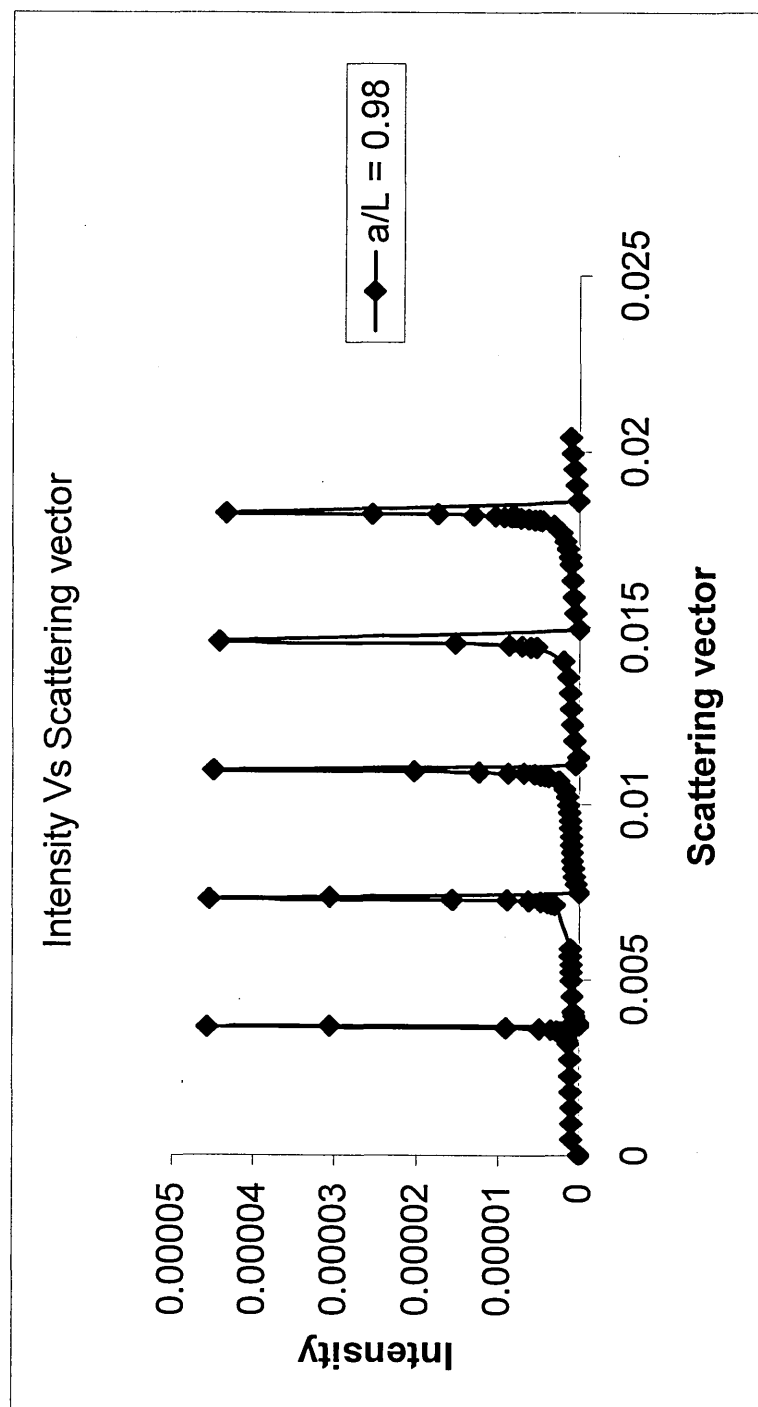


Fig 6.13: Calculated intensity versus scattering vector curves for three different thicknesses of crystalline regions.

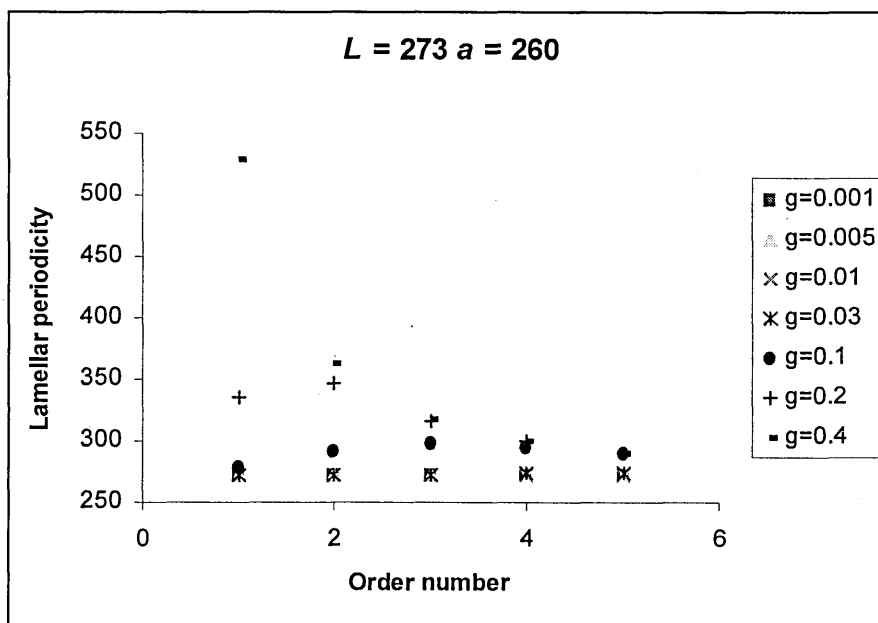
Table 6.3: The positions of the orders calculated from Intensity vs scattering vector plots.

Order number	$s (\text{\AA}^{-1})$		
	$a = 250 \text{ \AA}$	$a = 260 \text{ \AA}$	$a = 268 \text{ \AA}$
1	.0037	.0037	.0037
2	.0073	.0073	.0073
3	.0109	.0109	.0109
4	.0146	.0146	.0146
5	.0182	.0182	.0182

We can see that as  $a/L$  decreases, intensity falls more quickly with order, but the positions of the orders remain unchanged (table 6.3). They change with increasing  $g$ , the relative distance parameter.

The variation of lamellar periodicity with order calculated for different values of  $L$  and  $a$  using this linear paracrystal model is illustrated in figure 6.14.

(a)





(b)

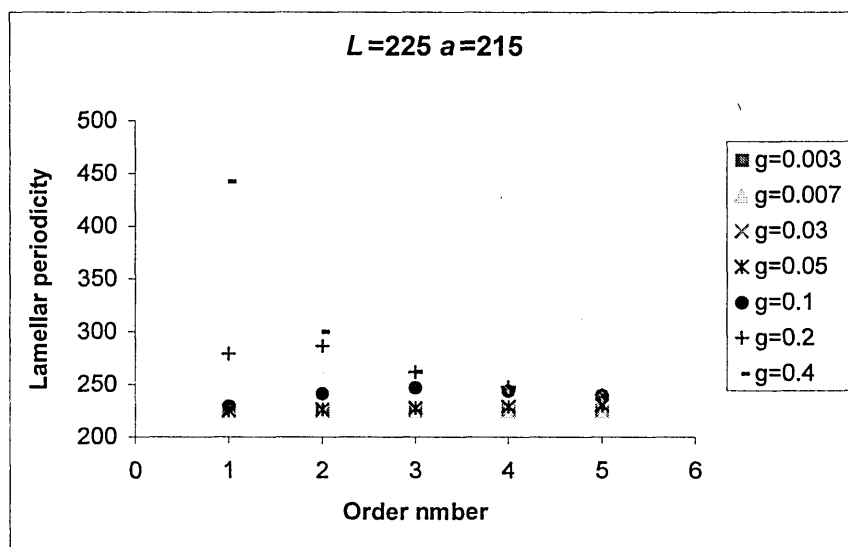


Fig 6.14: The variation of lamellar periodicity with order calculated from the maxima in  $I$  versus  $s$  plots; Relative distance function varied from  $g = 0.001$  to  $0.4$ .

According to figure 6.14, at lower  $g$  values ( $g = 0.001 - 0.03$ ), the lamellar periodicity is almost constant with order. Then the periodicity increases slightly with order with increasing  $g$  ( $g = 0.05$  and  $g = 0.07$ ). Further increase of  $g$  causes the lamellar periodicity to go through a maximum ( $g = 0.1$  and  $g = 0.2$ ). With further increase of  $g$ , the lamellar periodicity decreases with order number. The lamellar periodicities observed from the SAXS experiment (figure 6.11) have a different behaviour to that seen in figure 6.14. According to figure 6.11, at lower temperatures (more disordered), i.e. at higher  $g$  values, the lamellar periodicity increases with order. At higher temperatures (less disorder) i.e. lower  $g$  values, the lamellar periodicity decreases with order. Therefore, we cannot explain this behaviour assuming a linear paracrystalline type model for  $C_{12}D_{25}C_{192}H_{384}C_{12}HD_{24}$ . In this model we assumed a symmetric distance distribution for the crystal thickness. With the high crystallinity of these alkanes, one would expect a minimum possible disorder close to the minimum. Therefore, we cannot envisage any significantly smaller amorphous thickness than the present thickness. We can only expect the amorphous thickness to be larger than the present thickness. Therefore for these highly crystalline materials, an asymmetric distance distribution would be seen

more probable. This was not pursued because of the large number of parameters required.

### 6.3.3 Simulation of the fold arrangement and resulting $\text{CD}_2$ bending vibration in the once – folded form of $\text{C}_{12}\text{D}_{25}\text{C}_{192}\text{H}_{384}\text{C}_{12}\text{HD}_{24}$

As discussed earlier, two extreme models for the fold arrangement in crystals of long chain alkanes would be, (a) the random arrangement of folds at the lamellar surfaces and (b) the regular arrangement of folds on one such surface (figure 6.2(a) and (b)). Here we simulate the situation for the first structure. Using a random number generator held in the standard library of Borland C++, we obtained a computer-generated set of molecular conformations for the  $\text{C}_{12}\text{D}_{25}\text{C}_{192}\text{H}_{384}\text{C}_{12}\text{HD}_{24}$  once folded form. This supplies numbers in the range 0 up to 32767. But we were interested in two possible conditions, labelled 0 and 1 corresponding to a  $\text{CD}_2$  and a  $\text{CH}_2$  group respectively. Hence, we took the values supplied by the random number generator and converted it to either 0 or 1. The remainder operator, %, in C++ gives the remainder after dividing the number before the operator by the number after the operator. For example; “a % b” gives the remainder after dividing a by b. Therefore, to determine whether a site has the label 0 and 1 we did the calculation “random number % 2”. If the remainder was equal to 1, each lattice point was assigned to a  $\text{CH}_2$  group (denoted by a hyphen in figure 6.15) and if the remainder was zero, each point was assigned to a  $\text{CD}_2$  group (D in figure 6.15, where the  $\langle 110 \rangle$  directions are represented by vertical and horizontal axes). Here we assumed all the folds are adjacently re-entrant because of SAXS and Raman evidence for a sharp fold in long chain n-alkanes. Therefore, if one point is assigned with a ‘D’, an adjacent lattice point in a  $\langle 110 \rangle$  direction should also be ‘D’. Two adjacent Ds in figure 6.15 correspond to a  $\text{C}_{12}\text{D}_{25}\text{C}_{192}\text{H}_{384}\text{C}_{12}\text{HD}_{24}$  once-folded molecule in which the two deuterated ends are arranged on one lamellar surface. Two adjacent dashes represent a  $\text{C}_{12}\text{D}_{25}\text{C}_{192}\text{H}_{384}\text{C}_{12}\text{HD}_{24}$  once folded molecule in which the fold itself is arranged on this surface. In this latter case two adjacent lattice points close to the surface will both be occupied by a  $\text{CH}_2$  group. The irregular arrangements of deuterated stems produced by the program were divided into ‘groups’ in which each deuterated end cap has a similar nearest neighbour in a  $\langle 110 \rangle$  direction. To a good approximation, interactions beyond those of nearest neighbours may be neglected in calculating correlation splittings<sup>16</sup> so

that each group is effectively independent from others. Periodic boundary conditions were used to identify groups extended beyond the array. The labelled stems inside each closed contour line in figure 6.15 make one group. The group A is a closed group ( $2 \times 3$ ). Group B has a less regular arrangement, but it still includes a 'closed subgroup' ( $2 \times 2$ ). Some groups of stems form fully adjacent single sheets (C and D). However, many stems are within groups of more complex shape (E, F, G, and H). Each group was then transformed into an equivalent group (see appendix to Chapter 3).

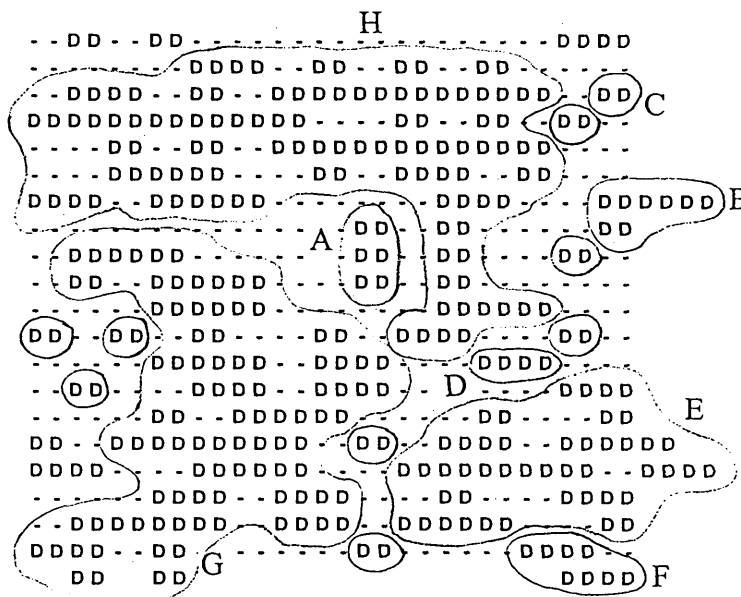


Fig 6.15: Division of a computer-generated model into groups of stems which are linked by  $\{110\}$  interactions.

Note: the  $\langle 110 \rangle$  directions are represented by vertical and horizontal axes. This is a convenient representation but the structure is somewhat distorted from the true orthorhombic one.

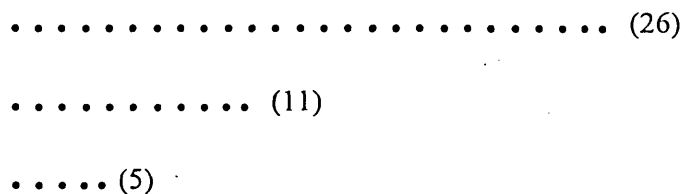


Fig 6.16: The equivalent group corresponding to the conformation of group E.

For example, figure 6.16 shows the equivalent group of group 'E' in figure 6.15. The resulting equivalent group has 26 stems in sheet 1, 11 stems in sheet 2 and 5 stems in sheet 3. This group has a distribution of nearest neighbour interactions very similar to that of group E. The number of stems with 2, 3 and 4 interactions in the equivalent group is well fitted to the distribution in group E. However, the equivalent group has only one stem with one nearest neighbour interaction. These stems have less influence on the vibrational splitting than stems with multiple interactions<sup>6</sup>. The equivalent group of E has the closed sub group,  $(5 \times 3)$ . The calculation of the doublet splitting for the equivalent group followed the procedure suggested by Spells et al<sup>17</sup>. This method uses the closed subgroup as the basis for calculating the doublet splitting for the equivalent group. Additional deuterated caps within the equivalent group, which are not included in the closed sub group, provide additional  $\{110\}$  interactions, which increase the splitting. The doublet splitting for the equivalent group in fig. 6.16 is then obtained by;

$$\begin{aligned}\Delta v_{26,11,5} &= \Delta v_{5 \times 3} + (\Delta v_{(13.5 \times 2)} - \Delta v_{(7.5 \times 2)}) + (\Delta v_{(42 \times 1)} - (\Delta v_{(27 \times 1)})) \quad \dots\dots\dots(6.12) \\ &= 8.3 + 0.2 + 0 \text{ cm}^{-1} \\ &= 8.5 \text{ cm}^{-1}\end{aligned}$$

The doublet splittings for all the equivalent groups were calculated in this way. This procedure was repeated for nine thousand hydrogen and deuterium stems. In the case of polyethylene samples with a PEH matrix, both high and low frequency components have previously been fitted to straight lines using a least squares procedure<sup>18</sup>. The results were:

$$v_{high} = 1087.4 + 0.64(\Delta v) \text{ cm}^{-1} \quad \dots\dots\dots(6.13)$$

$$v_{low} = 1087.4 - 0.36(\Delta v) \text{ cm}^{-1} \quad \dots\dots\dots(6.14)$$

where  $\Delta v$  is the doublet splitting corresponding to component at  $v_{high}$  and  $v_{low}$ .

Using the above relationships, the frequencies for the two doublet components were calculated for each and every splitting. The frequencies were grouped in  $0.5 \text{ cm}^{-1}$  class intervals (Table 6.4).

Table 6.4: Number of stems contributing to the  $CD_2$  bending vibration in various frequency intervals for the random fold direction model.

Number of stems	Frequency ( $cm^{-1}$ )
550	1083.51 – 1084.00
2448	1084.01 – 1084.50
580	1084.51 – 1085.00
348	1085.01 – 1085.50
110	1085.51 – 1086.00
322	1086.01 – 1086.50
322	1089.01 – 1089.50
36	1089.51 – 1090.00
26	1090.01 – 1090.50
162	1090.51 – 1091.00
190	1091.01 – 1091.50
288	1091.51 – 1092.00
366	1092.01 – 1092.50
514	1092.51 – 1093.00
2812	1093.01 – 1093.50
186	1093.51 – 1094.00

The histogram of number of stems versus frequency is given in figure 6.17. The measured absorbance is proportional to the number of stems. If each component in this histogram was replaced by Lorentzian peak, the spectrum would show a broadening of the dominant doublet for the  $CD_2$  bending vibration. Nevertheless, the dominant doublet splitting which can be seen from figure 6.17 is  $9.0\text{ cm}^{-1}$ .

On the other hand, for the regular fold structure of  $C_{12}D_{25}C_{192}H_{384}C_{12}HD_{24}$  we can expect infinite groups of deuterated end caps since all the folds are confined to one lamellar surface (figure 6.2(b)). Therefore we expect the spectrum to show a prominent doublet for the  $CD_2$  bending vibration with a maximum splitting close to  $10.1\text{ cm}^{-1}$  (the splitting for the perdeuterated polyethylene is  $10.1\text{ cm}^{-1}$ <sup>8</sup>).

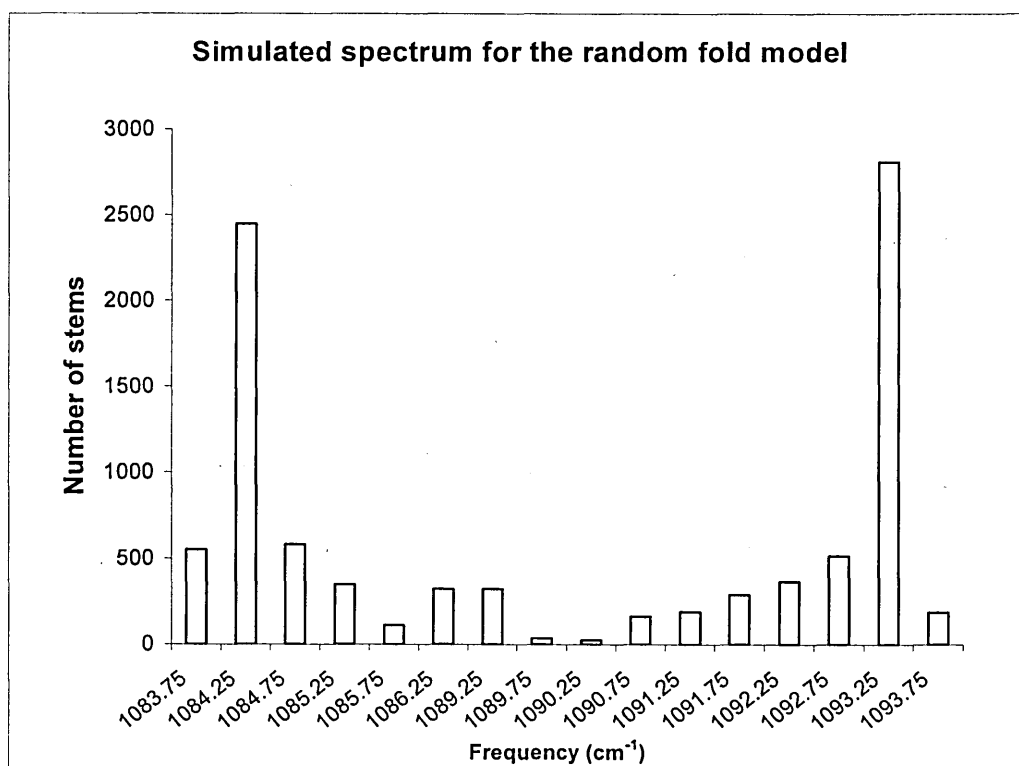


Fig 6.17: The histogram representing the simulated spectrum of the  $CD_2$  bending region of  $C_{12}D_{25}C_{192}H_{384}C_{12}HD_{24}$  random fold model.

As discussed by de Silva et al<sup>12</sup>, the reduction of chain length from infinity to  $(CD_2)_{12}$  may reduce the doublet splitting. They have calculated a 10% reduction of the full splitting i.e. from  $10.1\text{ cm}^{-1}$  to  $9.1\text{ cm}^{-1}$  due to the reduction of chain length from infinity to  $C_{12}$ . The splitting predicted here for the  $C_{12}D_{25}C_{192}H_{384}C_{12}HD_{24}$  bending mode of the random fold model is  $9.0\text{ cm}^{-1}$  ( $1084.25 - 1093.25\text{ cm}^{-1}$ ). Therefore, it is likely to be impossible to distinguish between these two models experimentally, by the difference in the value of the  $CD_2$  bending doublet splitting. Unfortunately, insufficient sample was available to test these models experimentally.

#### 6.4 Conclusion

The temperature behaviour of the chain disorder and its relation to chain tilt were studied using model alkanes. An earlier study on  $C_{198}H_{398}$  has shown that successive heat annealing causes perfecting of the chains and SAXS results indicated a simultaneous

tilting of the chains<sup>10</sup>. This was the first observation of chain tilting in relation to chain perfecting. In the present work, partially deuterated  $C_{12}D_{25}C_{192}H_{384}C_{12}HD_{24}$  served as a probe for the chain end region. It revealed that this perfection predominantly occurs at the lamellar surfaces. Combination of infrared results on chain disorder and SAXS results on chain tilting showed that these two processes are inter-related. The ordering of the chain ends causes a smoothing of the crystal surface which induces chain tilt to accommodate chain ends. These observations provide a pointer to the behaviour of polyethylene crystals: they support an early suggestion of an initially rough surface in polyethylene single crystals, with ordering and tilting occurring subsequently<sup>19</sup>. In addition, it has recently been suggested that the re-ordering of the perpendicular fold surfaces towards the preferred inclined, more ordered state is the cause of spherulite banding in polyethylene<sup>20</sup>. Continuous heating of  $C_{198}H_{398}$  extended and folded forms and continuous<sup>6</sup> and stepwise heating of  $C_{12}D_{25}C_{192}H_{384}C_{12}HD_{24}$  have shown that they all result in a similar increase in tilt angle with temperature and eventually result in a maximum tilt angle of  $35^\circ$  irrespective of the heating rate and the method of heating. Therefore, the effects of heating rate or the method of heating on the temperature dependence of the tilt angle can be excluded. Nevertheless, the exact reason for the observed delay in onset of chain tilting in the case of  $C_{198}H_{398}$  is not clear. The apparent delay may be due to a lower level of disorder in the as-grown crystals of  $C_{198}H_{398}$ .

An interesting picture of the state of order of the as-grown crystals from solution has been suggested using the  $CH_2$  and  $CD_2$  bending mode spectra of  $C_{12}D_{25}C_{192}H_{384}C_{12}HD_{24}$ <sup>5</sup>. Instead of having ordered chains, there is a high degree of translational disorder with enough  $C_{12}D_{25}$  end caps displaced outside the crystal or into the hydrogenous interior to give rise to the singlet in the  $CD_2$  bending region of the infrared spectrum. In an idealized model, a missing end-cap is either a vacancy as far as the  $CD_2$  bending band splitting is concerned or a 'guest' hydrogenous chain. Both would reduce the  $CD_2$  bending splitting. This would account for the small domain size in the as-grown crystals of  $C_{12}D_{25}C_{192}H_{384}C_{12}HD_{24}$ . With increasing annealing temperature more and more end caps are incorporated into the crystal and chain ends become in better register with each other. This is evidenced by the increase in the  $CD_2$  bending doublet splitting from  $6.75$  to  $7.9\text{ cm}^{-1}$ <sup>5</sup>. The corresponding increase in the domain size is from 16 end-deuterated chains to over 50 of them.

We tried to explain the observed shift of the X-ray long spacings of  $C_{12}D_{25}C_{192}H_{384}C_{12}HD_{24}$  away from the positions predicted by Bragg's equation by using a linear paracrystalline model. Here, we described the scattering behaviour of  $C_{12}D_{25}C_{192}H_{384}C_{12}HD_{24}$  crystals based on a periodic step function with fluctuating periods (linear paracrystal). In this model the particle factor as well as the lattice factor may shift the scattering maxima out of the positions given by the Bragg equation. We failed to find a good agreement between the lamellar periodicity obtained from SAXS results and that calculated using the paracrystalline model. The implication is that there cannot be a symmetric broadening of the amorphous layer due to their high crystallinity.

The use of the  $CD_2$  bending mode for characterising the translational disorder of long chain alkanes was reported earlier<sup>5</sup>. We used the same vibrational mode to characterise possible regular fold and the random fold structures of  $C_{12}D_{25}C_{192}H_{384}C_{12}HD_{24}$  in the once folded form. The regular fold structure forms an infinite group of deuterated stems which is capable of showing almost the maximum  $CD_2$  bending splitting ( $10.1\text{ cm}^{-1}$ ) calculated for perdeuterated polyethylene. However, due to the short chain length of  $(CD_2)_{12}$ , the maximum splitting reduces to  $9.1\text{ cm}^{-1}$ . The calculated value for the dominant  $CD_2$  splitting of the  $C_{12}D_{25}C_{192}H_{384}C_{12}HD_{24}$  random fold structure using the simulated  $CD_2$  bending vibration spectrum is  $9.0\text{ cm}^{-1}$ . Therefore, it is unlikely that the  $CD_2$  bending doublet splitting can be used to differentiate between these two models. Figure 6.17 illustrated the histogram of number of stems vs frequency of the simulated infrared spectrum of the random fold model. Development of a computer program to generate the infrared spectrum of this histogram will be very useful in similar studies in future.



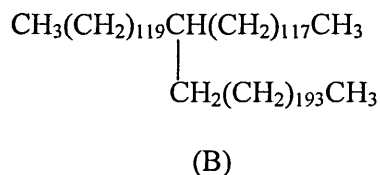
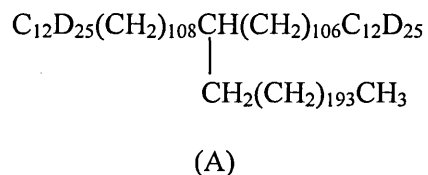
## References

- 1 Snyder RG, Poore MW, *Macromolecules*, **6**, 708 (1973)
- 2 Reneker DH, Mazur J, Colson JP, Snyder RG, *J. Appl. Phys.*, **51**(10), 5080 (1980)
- 3 Maroncelli M, Strauss HL, Snyder RG, *J. Phys. Chem.*, **89**, 4390 (1985)
- 4 Snyder RG, Maroncelli M, Strauss HL, *J. Am. Chem. Soc.*, **105**, 133 (1983),  
Maroncelli M, Strauss HL, Snyder RG, *J. Chem. Phys.*, **82**(7), 2811 (1985)
- 5 De Silva DSM, Gorce J-P, Wickramarachchi PASR, Spells SJ, *Macromol. Symp.*,  
**184**, 67 (2002)
- 6 De Silva DSM, Zeng XB, Ungar G, Spells SJ, *Macromolecules*, **35**, 7730 (2002)
- 7 Cheam TC, Krimm SJ, *Polym. Sci., Polym. Phys. Ed.*, **19**, 423 (1981)
- 8 Spells SJ in "Characterisation of Solid Polymers", ed. Spells SJ, Chapman and Hall,  
London (1994)
- 9 Broadhurst MG, *J. Res. Natl. Bur. Stand.*, **66A**, 241 (1962)
- 10 Gorce J-P, PhD Thesis, Sheffield Hallam University, June (2000)
- 11 Reinhold CHR, Fischer EW, *J. App. Phys.*, **35**, 71 (1964)
- 12 De Silva DSM, Zeng XB, Ungar G, Spells SJ, *J. of Macromol. Sci. Part B-Phys.*,  
**B42**, 915 (2003)
- 13 Snyder RG, Goh MC, Srivatsavoy VJP, Strauss HL, Dorset DL, *J. Phys. Chem.*, **96**,  
10008 (1992)
- 14 Piesczek W, Strobl GR, Malzahn K, *Acta Crystallogr. Sect., B* **30**, 1278 (1974)
- 15 Hosemann R, Bagchi SN, "Direct Analysis of Diffraction by Matter", North-Holland  
publishing Company, Amsterdam (1962)
- 16 Tasumi M, Krimm S, *J. Chem. Phys.* **46**, 755 (1967) and *J. Polym. Sci., A-2*, **6**, 995  
(1968)
- 17 Spells SJ, Keller A, Sadler DM, *Polymer*, **25**, 749 (1984)
- 18 Spells SJ, *Polymer*, **26**, 1921 (1985)
- 19 Bassett DC, Frank FC, Keller A, *Philos. Mag.*, **18**, 1753 (1963)
- 20 Abo el Maaty MI, Bassett DC, *Polymer*, **42**, 4957 (2001)

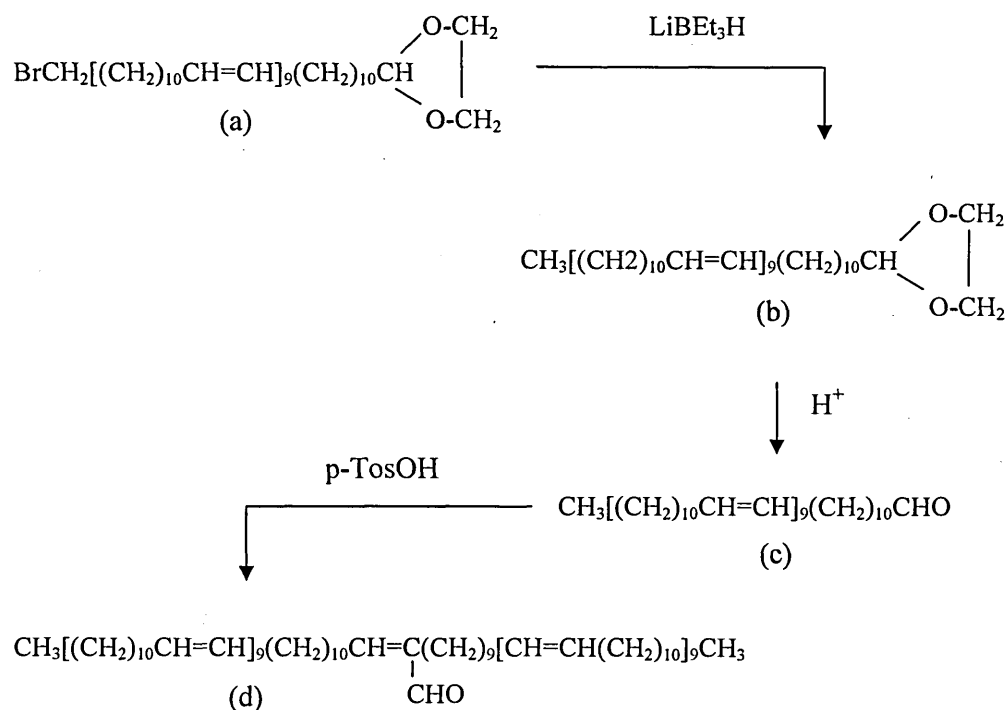
### Characterisation of Branched Alkanes

#### 7.1 Introduction

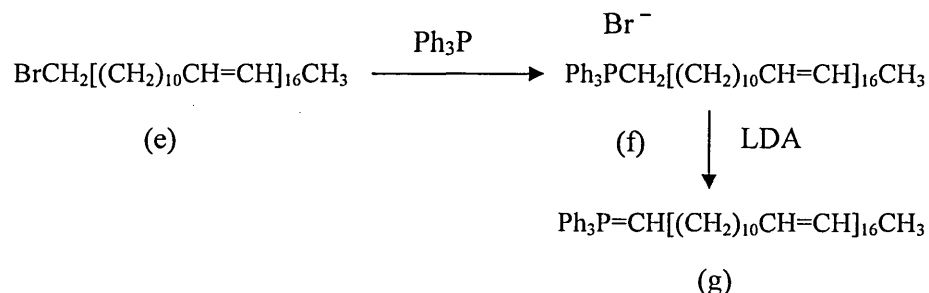
Monodisperse linear long chain alkanes (partially deuterated and undeuterated) have been successfully studied during the past two decades with a view to relate their crystallisation processes and crystal morphologies to those of linear polyethylene<sup>1</sup>. Similarly, monodisperse branched alkanes are becoming popular as model compounds for branched polyethylene. With this aim several single-branched alkanes having small ( $C_1$  and  $C_4$ ) and large ( $C_{61}$  and  $C_{195}$  : Y-shaped molecules)<sup>2</sup> branches have been chemically synthesised. The basis for the synthesis of the branched alkanes was also the same chain doubling process starting with the 12-bromododecanal ethylene acetal described in Chapter 2. The alkanes with  $C_1$  and  $C_4$  branches have already been studied by infrared spectroscopy<sup>3</sup>. Here we will study two Y-shaped alkanes (A and B) by Raman spectroscopy to identify different phases of these alkanes with the variation of temperature. The chemical formulae of A and B are given below;



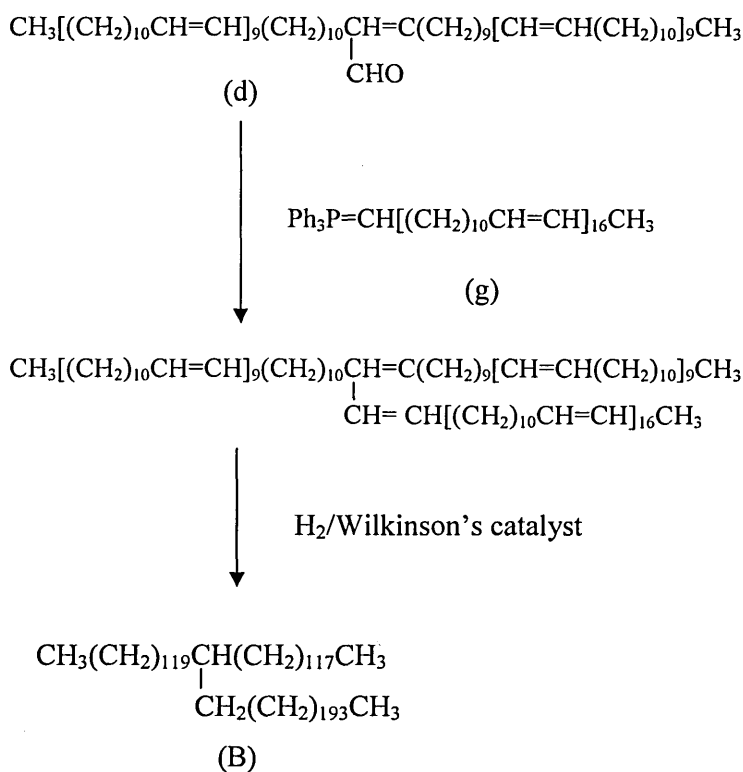
The synthetic path of the branched alkane B, is briefly described below<sup>2</sup>. The main step in the synthesis of branched alkanes was to obtain a pendant CHO group in the middle of the chain which facilitates subsequent incorporation of an alkyl branch of required length using ylides. The precursor to this material was the  $C_{120}$ -bromoacetal (a) which was prepared previously via the  $C_{96}$ -bromoaldehyde and  $C_{24}$ -ylide acetal. Replacement of Br by H followed by deprotection to the aldehyde resulted in compound (c). Aldol condensation/dehydration reaction of (c) gave the required polyalkene  $C_{120}C(CHO)C_{118}$ , with a pendent CHO group in the middle (d).



The second part is the incorporation of the branch to (d). It requires the synthesis of the  $\text{C}_{194}$  ylide unit first. Reaction of the  $\text{C}_{194}$ - bromo compound (e) with triphenyl phosphine gave the salt (f) from which the ylide (g) was prepared as illustrated below.



Reaction of (d) with (g) ultimately gave the required Y-shaped alkane (B). The reaction steps are given below.



The synthesis of Y-shaped molecule A, was described in Chapter 5. It turned out that the labelling process was not 100% successful during the synthesis of A. However, our measurements showed A is  $\sim 80\%$  deuterated (see Chapter 5).

Previous investigations on model-short branched alkanes show that they also possess different crystal structures to their linear counterparts. These structures are described in Chapter 2. A similar Y-shaped alkane to B, with a shorter branch ( $C_{61}$ ) has been prepared and investigated<sup>1</sup>. It also shows a semicrystalline form at higher temperatures (see Chapter 2 for structural details). The crystalline structures of A and B are still being investigated by SAXS\*.

However, we suspect a similar form for A and B too in the high temperature region. In this work we intend to find spectroscopic evidence of this form using Raman spectroscopy. Firstly, short chain alkane,  $C_{34}H_{70}$  was investigated by Raman spectroscopy in order to establish a suitable method for this work (see Chapter 4).

\* This work is being carried out by Prof. G. Ungar et al at the University of Sheffield, UK.

It demonstrated the changes in crystalline and amorphous bands in the region  $1700 - 200 \text{ cm}^{-1}$  with variation of temperature. Mainly four different areas were investigated in the short alkane. They were the  $\text{CH}_2$  bending region ( $1600 - 1400 \text{ cm}^{-1}$ ), the  $\text{CH}_2$  twisting band ( $\sim 1300 \text{ cm}^{-1}$ ), the C-C stretching region ( $1200 - 1000 \text{ cm}^{-1}$ ) and the  $\text{CH}_3$  rocking conformations ( $\sim 900 \text{ cm}^{-1}$ ). All four regions showed dramatic changes at the monoclinic to rotator transition in the short alkane. Here also we will investigate these four regions for evidence of a transition to a high temperature semicrystalline form. A sample of  $\text{CD}_3(\text{CD}_2)_{11}-(\text{CH}_2)_{144}-\text{CHD}(\text{CD}_2)_{10}\text{CD}_3$  [C168D] in extended form, which does not show any structural transitions between low temperature and the melting temperature, was studied first as a reference before investigating A and B.

## 7.2 Experimental

The arrangement of the sample for Raman measurements and the recording parameters for the Raman spectrum for the following samples are the same as in Chapter 4 unless stated otherwise.

### 7.2.1 C168D

A solution crystallised sample of C168D in extended form was supplied by the University of Sheffield. A few milligrams of this sample was used for Raman measurements. The sample was heated at  $1^\circ \text{ C min}^{-1}$ , with data collection at fixed temperatures, until it melted ('stepwise' heating). Three spectra, each of 50 s scan time, were collected at every two degree interval. We wanted to use a longer scan time in order to enhance the signal to noise ratio. However, due to the saturation of the detector this was not practicable. Instead, three spectra were collected at each temperature and averaged. The time lapsed between  $2^\circ \text{ C}$  intervals is  $\sim 11$  minutes (9 min. for collection of 3 spectra including data transfer time and 2 min. for the change of temperature to the next value). Therefore the effective overall heating rate is  $\sim 0.18^\circ \text{ C min}^{-1}$ .

Then the sample was slowly crystallised from the melt ( $1^\circ \text{ C min}^{-1}$ /stepwise). Two spectra of 50 s scan time were collected at every  $2^\circ \text{ C}$  interval as above while cooling. The effective cooling rate was  $\sim 0.25^\circ \text{ C min}^{-1}$ . It can be assumed that C168D crystallises in the extended form when crystallised from the melt also, as the cooling rate

is slow, and the C168D molecule is not long enough to fold. Another heating run of this melt-crystallised sample was done under the above conditions.

#### 7.2.2 End-deuterated branched alkane, A

A small amount of sample A was crystallised from melt (at  $0.2^{\circ}\text{C min}^{-1}$ ) in the sample holder to obtain a thin film. Firstly, a Raman run was done heating continuously at  $1^{\circ}\text{C min}^{-1}$  followed by a continuous cooling run at  $0.3^{\circ}\text{C min}^{-1}$ . Only one spectrum of 10 s scan time was collected at each temperature interval. This gave an unacceptable signal to noise ratio. Therefore in the later runs the total scan time was increased to 100 seconds.

Secondly, another stepwise heating/cooling run at  $1^{\circ}\text{C min}^{-1}$  between data collection was carried out collecting ten spectra of 10 s scan time at each temperature. The overall effective rate was  $\sim 0.2^{\circ}\text{C min}^{-1}$ .

#### 7.2.3 Branched alkane, B

A melt crystallised (cooling rate  $0.2^{\circ}\text{C min}^{-1}$ ) sample of B was obtained in the sample holder as above. This sample was subjected to several stepwise and continuous heating/cooling runs. The applied rates were  $1^{\circ}\text{C min}^{-1}$  (continuous heating and stepwise heating and cooling) and  $0.3^{\circ}\text{C min}^{-1}$  (continuous cooling). In the first few runs only one spectrum of 10 s scan time was collected at each interval but in subsequent runs an increased scanning time (total 100 seconds) was used.

### 7.3 Results and Discussion

#### 7.3.1 C168D

This sample was studied as a reference sample to A and B. SAXS data have shown that it crystallises in extended form<sup>1</sup>. We expect that C168D does not undergo any structural transitions prior to melting. Therefore we expect no sudden changes in crystalline and amorphous bands in the Raman spectrum with variation of temperature.

The Raman spectrum of crystalline C168D is illustrated below.

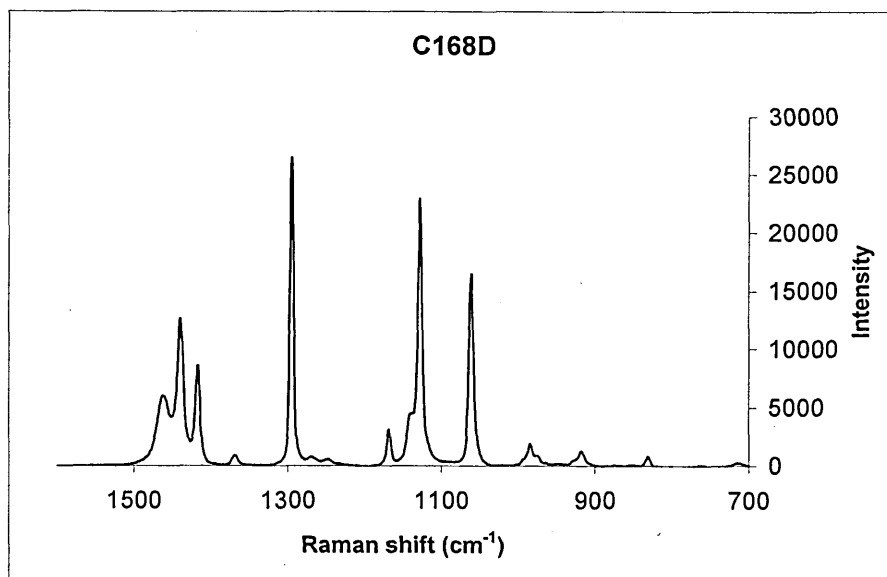


Fig 7.1 : Raman spectrum of solution crystallised C168D at 70<sup>0</sup> C.

Three main areas were identified in this spectrum. They are region 1: CH<sub>2</sub> bending, (1600 – 1400 cm<sup>-1</sup>), region 2: CH<sub>2</sub> twisting band ( 1300 cm<sup>-1</sup>) and region 3: C-C stretching region ( 1200 – 1000 cm<sup>-1</sup>). The shoulder around 1140 cm<sup>-1</sup> on the strong 1130 cm<sup>-1</sup> C-C symmetric stretching crystalline band was assigned to the C-C symmetric stretching vibration of the crystalline deuterated segments<sup>4,5</sup>. Three more bands with moderate intensity below 1000 cm<sup>-1</sup> can be observed in the above spectrum. The first of these also includes a shoulder around 975 cm<sup>-1</sup> in addition to the main band at 985 cm<sup>-1</sup>. These were assigned to CD<sub>2</sub> rocking ( 985 cm<sup>-1</sup>), CD<sub>2</sub> bending ( 975 cm<sup>-1</sup>), CD<sub>2</sub> twisting ( 917 cm<sup>-1</sup>) and C-C antisymmetric stretch ( 832 cm<sup>-1</sup>) respectively <sup>4,5</sup>. The CD<sub>2</sub> wagging mode has been assigned at 1255 cm<sup>-1</sup> <sup>4,5</sup>. However, this mode could not be observed in our Raman spectra even after melting.

The grating of the Raman spectrometer slipped sometimes while experiments were in progress. This caused significant intensity differences between spectra as well as frequency. The frequency shift was corrected by calibrating the spectrometer against a silicon band at 520 cm<sup>-1</sup>. In order to correct the intensity difference the spectra were

normalised to the integrated area of the C-C stretching region. Raw data are represented for runs where grating slippage did not occur.

The changes in regions 1, 2 and 3 were monitored. No significant change occurred in region 1 until melting. In the melt spectrum the  $\text{CH}_2$  bending triplet combined into a single broad band centred around  $1440\text{ cm}^{-1}$ .

Regions 2 and 3 are very important in monitoring the chain disorder as the disorder bands mostly occur in these regions. The behaviour of the vibrational modes in these regions with temperature is depicted in figures 7.2 and 7.3. The D band in the graphs below refers to the C-C symmetric stretch mode of the  $\text{CD}_2$  segments ( $1140\text{ cm}^{-1}$ ). The most notable difference in C168D compared with  $\text{C}_{34}\text{H}_{70}$  is the non-appearance of the  $1305\text{ cm}^{-1}$  and  $1080\text{ cm}^{-1}$  gauche bands until melting of the sample. All three  $\text{CH}_2$  crystalline bands ( $1295$ ,  $1130$  and  $1060\text{ cm}^{-1}$ ) remain more or less constant or increase slightly in intensity before melting. (This increase could be due to the lattice expansion with increasing temperature.)

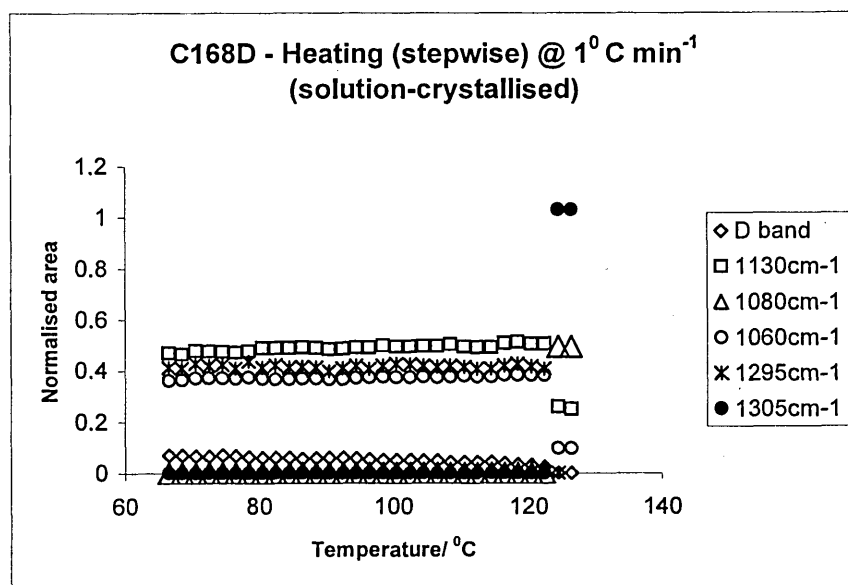


Fig 7.2: The variation of the areas of crystalline and disorder bands of regions 2 and 3 of C168D solution crystallised sample with temperature on heating. The spectra were normalised to the area of C-C stretching region.



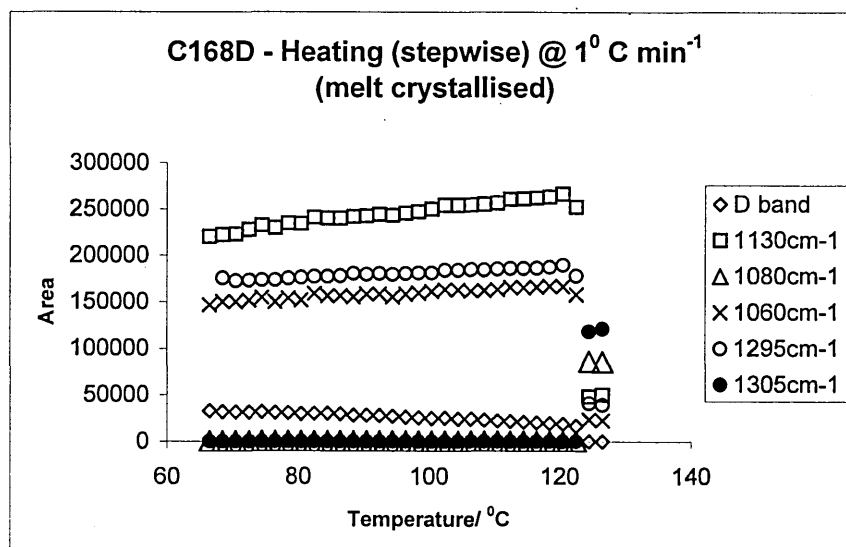


Fig 7.3: The variation of the area of crystalline and disorder bands of region 2 and 3 of C168D melt crystallised sample with temperature on heating.

This proves that the interior of the C168D crystals is highly ordered. However, the area of the CD<sub>2</sub> symmetric stretching band decreases gradually with increasing temperature. This indicates the chain end disordering of the extended chains of C168D with increasing temperature.

The variation of the area of each of these crystalline bands relative to their area at lowest recorded temperature (70°C) is given in figure 7.4 for solution-crystallised C168D. Melt crystallised sample of C168D also showed a similar behaviour to figure 7.4 in both heating and cooling runs. The area of the D-band drops to a half of the initial area just before melting while the area of the CH<sub>2</sub> bands increases by up to 20% through the temperature region up to melting (the increase in area of crystalline CH<sub>2</sub> bands could be due to the lattice expansion with increasing temperature). These figures give some idea about the extent of disorder. According to figure 7.4 this disordering of the chain ends is small until melting (at 100°C the order is reduced to 75% of its initial value) and loses 50% of its original crystallinity just above melting (122°C).

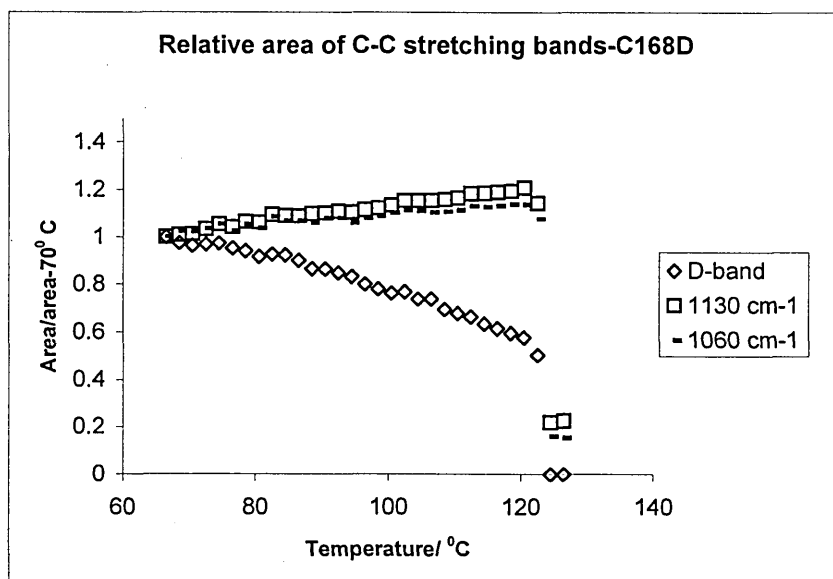


Fig 7.4: The variation of the area of the crystalline bands of C168D-solution crystallised sample in the region 3, relative to the area of each of these bands at 70°C.

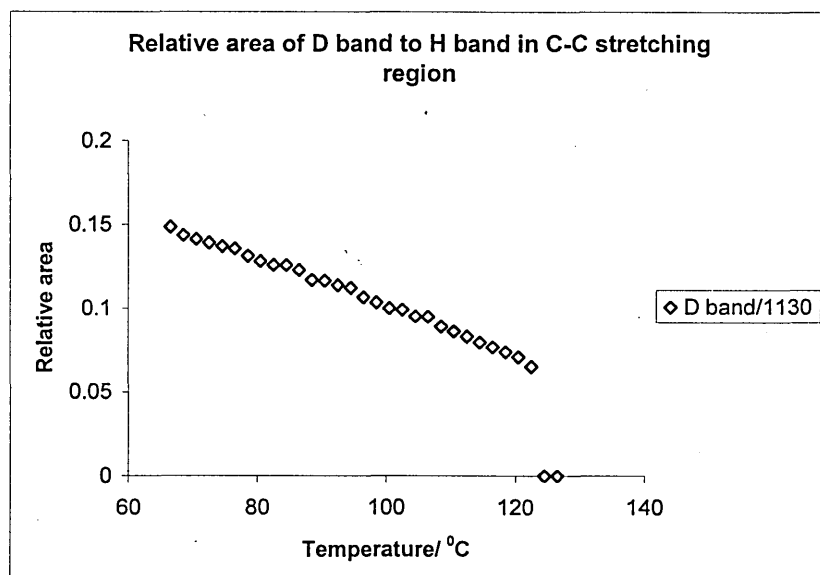


Fig 7.5: The relative area of the C-C symmetric stretching mode from CD<sub>2</sub> segments to that of CH<sub>2</sub> segments Vs temperature.

Figure 7.5 shows the variation of D band relative to its H counterpart ( $1130\text{ cm}^{-1}$ ). According to molecular formula the  $\text{CD}_2/\text{CH}_2$  ratio is 0.145. Therefore according to figure 7.5 at  $70^\circ\text{C}$ , C168D is 100% crystalline. Then it gradually becomes disordered and loses about 60% of its original crystallinity just below the melting temperature ( $122^\circ\text{C}$ ).

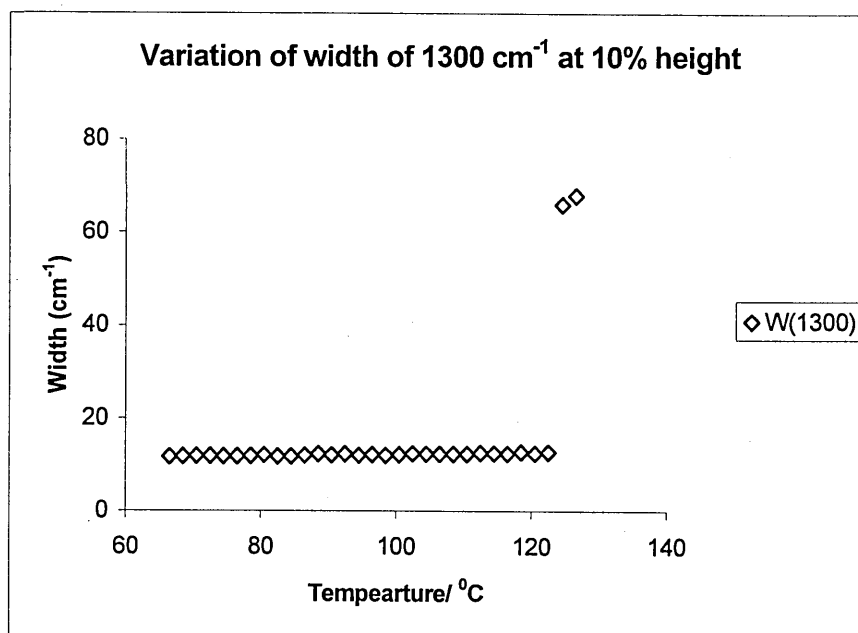


Fig 7.6: The variation of the width of the  $1300\text{ cm}^{-1}$  band of C168D melt crystallised sample with temperature.

The variation of the width of the  $\text{CH}_2$  twisting band at  $1300\text{ cm}^{-1}$  is another interesting parameter to identify the disordered structures. In short chain alkanes we could see that this band become broader with increasing disorder (see Chapter 4 - figure 4.2). The variation of the width of the  $1300\text{ cm}^{-1}$  band of C168D with temperature is shown in figure 7.6. Here, the width of this band remains constant throughout the entire temperature range until suddenly it broadens at melting. This is further evidence for high degree of crystallinity below the melting temperature, in C168D. Solution crystallised C168D also behaves in the same way.

The parameters discussed above of the Raman spectrum of C168D were very good indicators for the order/disorder of the structure. The above parameters except the area of

the D-band did not show any sudden changes in their behaviour until melting. We expected the crystalline structure of C168D to remain the same until melting and a disordering of the chain ends with increasing temperature. Therefore our Raman observations on C168D agree well with our expectations. This will provide a useful comparison with the unknown phases in branched alkanes which we will study below.

### 7.3.2 Branched alkanes: A and B

We suspect from SAXS work<sup>6</sup> A and B crystallise through at least one NIF form. This NIF form is semicrystalline. Our aim here is to identify this transition by monitoring the changes in the Raman spectrum based on the fact that the vibrational spectrum is sensitive to the crystalline structure and conformational changes.

Figure 7.7 shows the Raman spectra of A and B samples at 70<sup>0</sup> C. The main difference between them as compared with C168D is the appearance of a gauche band at 1080 cm<sup>-1</sup> (\*) even at this relatively low temperature. Although the 1305 cm<sup>-1</sup> band due to gauche conformers is hardly visible in these spectra, it is identifiable by curve fitting. In addition, the spectrum of sample B shows some signs of CH<sub>3</sub> rocking conformational bands around 900 cm<sup>-1</sup> even at low temperature. These observations suggest that these two branched alkanes are slightly disordered even at low temperature. The changes in the region 1,2,3 (A and B) and 4 (B) of the Raman spectrum were monitored to identify the transitions in samples A and B.

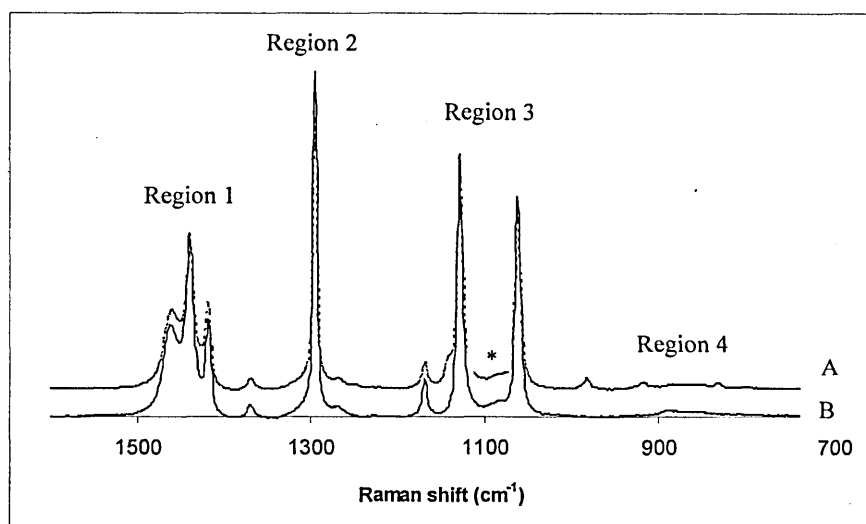


Fig 7.7: Raman spectra of branched alkanes at 70<sup>0</sup> C in the region from 1600 to 700 cm<sup>-1</sup>.

Region 1: 1600 – 1400  $\text{cm}^{-1}$

Figure 7.8 shows the variation of the band position of the  $\text{CH}_2$  bending triplet of sample A with temperature.

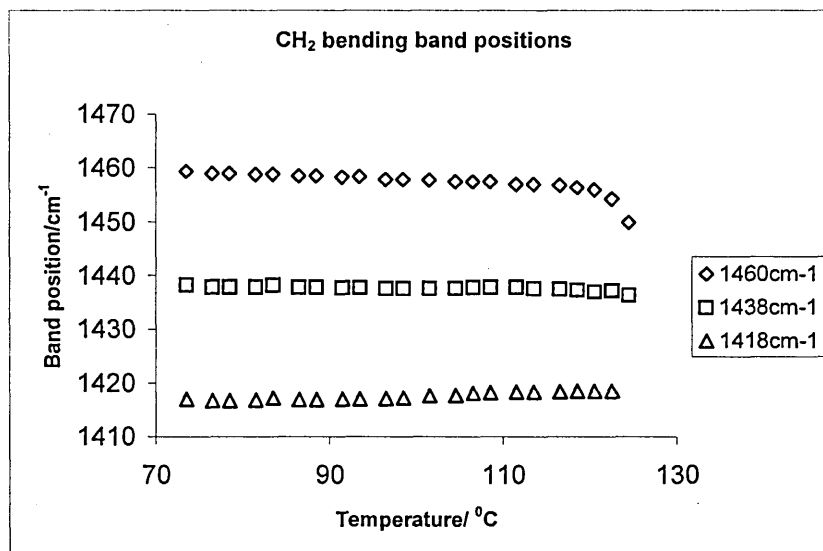


Fig 7.8: The variation of the  $\text{CH}_2$  bending band positions of sample A with temperature on cooling.

In Chapter 4,  $\text{C}_{34}\text{H}_{70}$  showed a sudden change of the position of 1460 and 1440  $\text{cm}^{-1}$  bands and the disappearance of the 1418  $\text{cm}^{-1}$  band at the rotator phase transition (see Chapter 4 - figure 4.1). However, the branched samples A and B show neither of the above changes in this region. Even the 1418  $\text{cm}^{-1}$  band, which is sensitive to lattice geometry, was visible until melting. Therefore, they may be retaining their original geometry until melting. The 1418  $\text{cm}^{-1}$  band disappears and the positions of the 1460 and 1440  $\text{cm}^{-1}$  bands slightly alter at melting. No significant changes could be identified in support of the suspected phase transition in this region of the spectrum.

Region 2: 1400 – 1200  $\text{cm}^{-1}$

This is an important area in identifying any disorder as the vibrational mode due to gauche conformations (at 1305  $\text{cm}^{-1}$ ) can be observed in this area. The changes of the gauche band and the crystalline band (1295  $\text{cm}^{-1}$ ) are described further in the next

section with those of bands in region 3. Another observation of this combined  $\text{CH}_2$  twisting band is its broadening with increasing temperature. This is illustrated in figures 7.9 and 7.10 below with their corresponding heat treatments. Sample A melts at around  $122^\circ\text{C}$  while sample B melts at around  $121^\circ\text{C}$ . However, the data at melting have been omitted from all the graphs to improve the clarity. There is usually a gradual change in width in both samples A and B, with the most rapid change identified as a transition. We can observe two such changes in these width-temperature curves. The one at the lower temperature shows one phase transition while the latter one indicates the melting/crystallisation. This change in width at the phase transition is due to the fact that the transition coincides with ordering/disordering of the structure. Both A and B show super cooling effects.

These curves are generally in good agreement. Sample A shows a maximum slope from  $82^\circ$  to  $92^\circ\text{C}$  in its heating curve while the cooling curve shows a maximum slope in the range  $70^\circ - 78^\circ\text{C}$ . The maximum slopes for sample B could be observed in the range  $84^\circ$  to  $94^\circ\text{C}$  and  $72^\circ$  to  $80^\circ\text{C}$  in its respective heating and cooling runs.

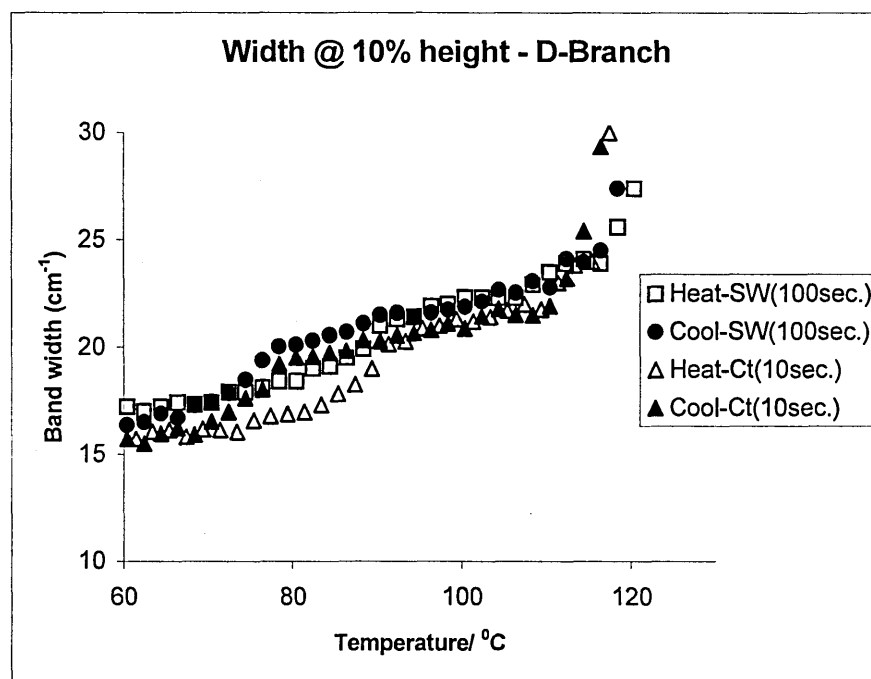


Fig 7.9: The variation with temperature of the width of the  $\text{CH}_2$  twisting band at 10% of maximum height for different heat treatments of sample A.

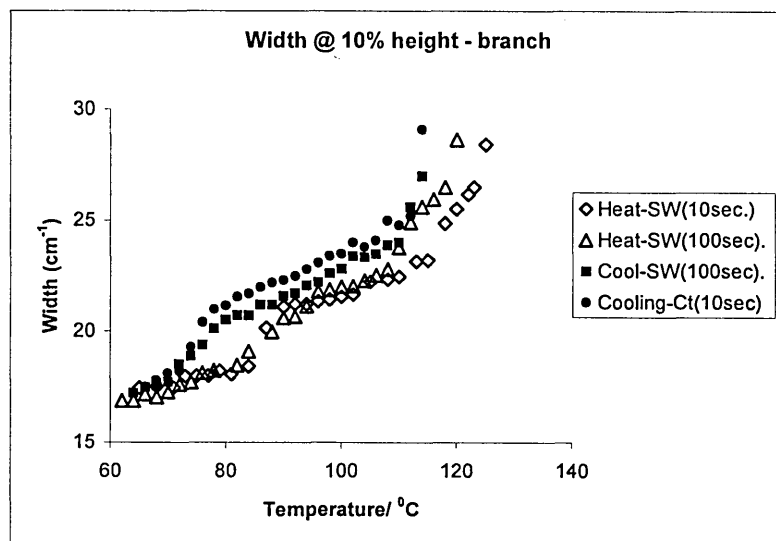


Fig 7.10: The variation with temperature of the width of the  $\text{CH}_2$  twisting band at 10% of maximum height for different heat treatments of sample B.

\*Key to graphs 7.9 and 7.10: SW – stepwise, Ct – continuous, Figures in parentheses are the total scan time at each temperature.

The estimated transition temperatures are given in Table 7.1. Although the band width of the  $\text{CH}_2$  twisting mode cannot be taken as proportional to the disorder present, as the height of the  $1295\text{ cm}^{-1}$  component is dependant on the temperature, the band width is nevertheless a useful empirical parameter.

Figure 7.11 illustrates the change of width of the  $1300\text{ cm}^{-1}$  band with temperature. Although we cannot clearly see the solid-solid transition, it clearly shows the change of the band width and shape at melting. In fact this band is a combination of two bands each representing the  $\text{CH}_2$  twisting vibration, but involving crystalline and amorphous counterparts. The melt spectrum is dominated by the vibrational mode of the amorphous counterpart.

Region 3 and 4:  $1200 - 1000\text{ cm}^{-1}$  and around  $900\text{ cm}^{-1}$

Region 3 is dominated by two strong crystalline bands due to C-C stretching of the crystalline chains. In between these two peaks lies the gauche analogue ( $\sim 1080\text{ cm}^{-1}$ ) of them. Region 4 shows the  $\text{CH}_3$  rocking conformations.

An overlaid view of the  $1080\text{ cm}^{-1}$  gauche band in the Raman spectra collected from  $60^\circ\text{C}$  to melting, during a stepwise heating run of sample B is shown in figure 7.12 below. This band was somewhat noisy so the spectra have been smoothed by 30% using the GRAMS 32AI Fourier smoothing function. From  $60^\circ$  to  $82^\circ\text{C}$  we can observe a gradual increase of the intensity of  $1080\text{ cm}^{-1}$  gauche band with increasing temperature. Then from  $82^\circ\text{C}$  to  $96^\circ\text{C}$  this increase become very rapid and slows down again from  $96^\circ\text{C}$  and above until just below melting ( $118^\circ\text{C}$ ) of the sample. When the sample starts melting it increases very rapidly and in the melt spectrum both  $1060$  and  $1130\text{ cm}^{-1}$  bands disappear and the  $1080\text{ cm}^{-1}$  band dominates. In figure 7.12 only a part of the melt spectrum can be observed. Figure 7.13 shows region 3 in full scale and we can clearly see the changes occurring in the C-C stretching bands at melting. The rapid increase of the  $1080\text{ cm}^{-1}$  band from  $82^\circ\text{C}$  to  $96^\circ\text{C}$  could be due to the phase transition occurring in this temperature range. The NIF state is more disordered and therefore the gauche content of chains would be expected to be larger.

The areas of crystalline and disorder bands in regions 2, 3 and 4 were determined by curve-fitting. The changes of each of the bands in regions 2, 3 and 4 in sample A and B are illustrated in figures 7.14 – 7.20. The most significant changes could be observed only in the disorder bands. No significant changes at the phase transition were observed in the strong crystalline bands ( $1295$ ,  $1130$  and  $1060\text{ cm}^{-1}$ ). Therefore in most of the graphs below only the disorder bands are plotted to improve the clarity. Some of the graphs include crystalline bands as well.



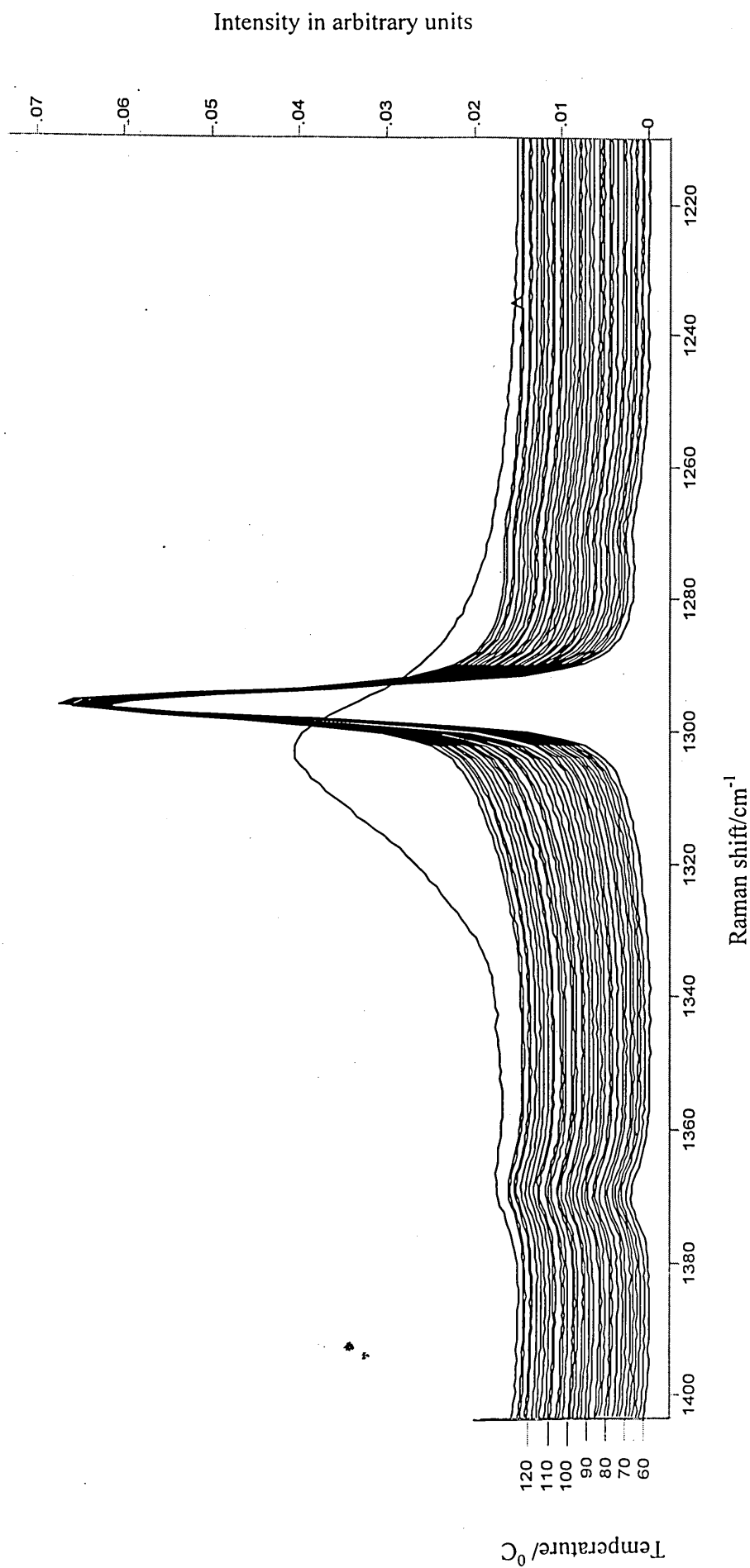


Fig 7.11: The waterfall arrangement of Raman spectra of sample B in region 2 during stepwise heating. The spectra are arranged from 60° to 128° C at 2° intervals in an upward direction.

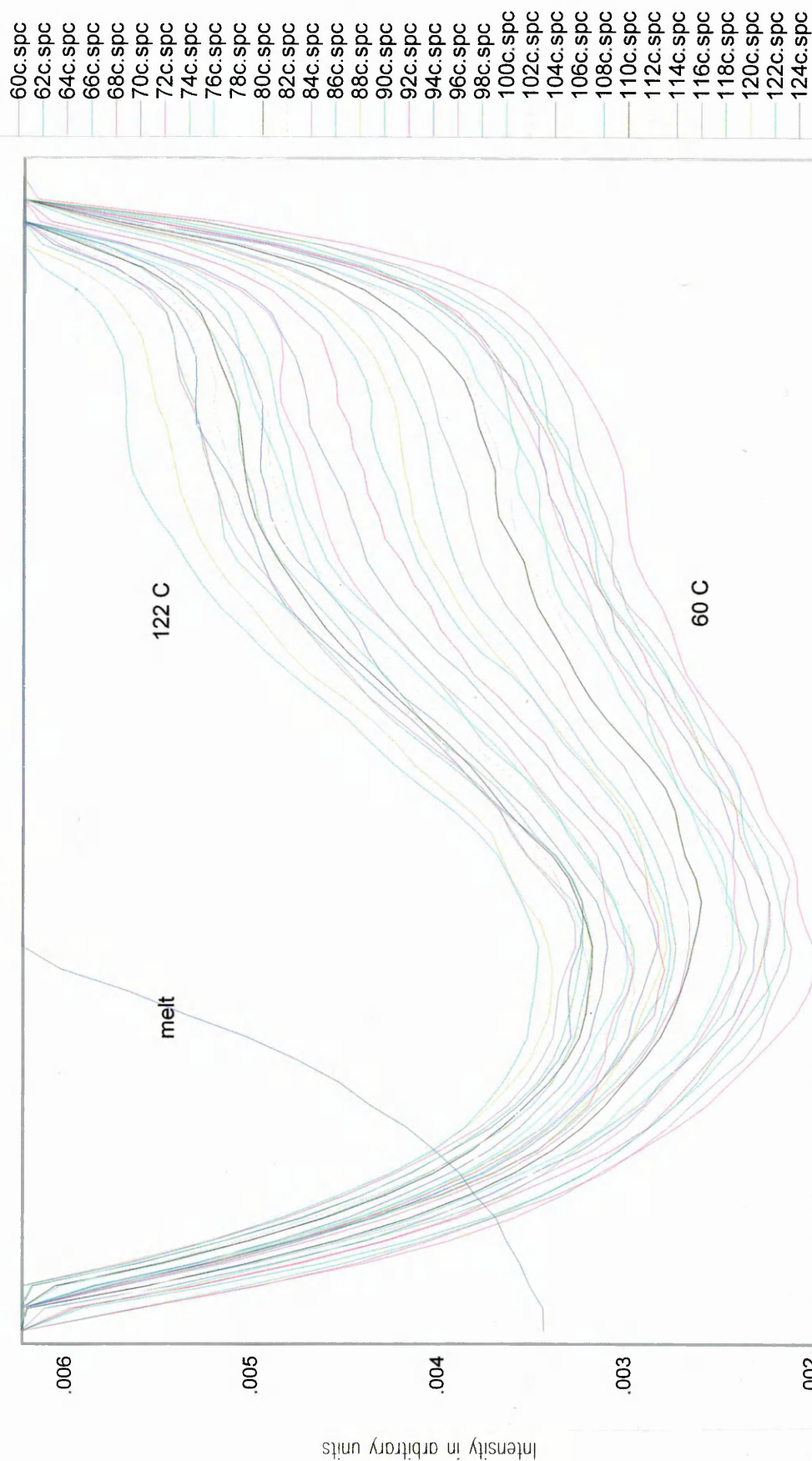


Fig 7.12: An expanded, overlaid view of the 1080  $\text{cm}^{-1}$  band from 60°C to melting at 2°C interval during a stepwise heating run of sample B.

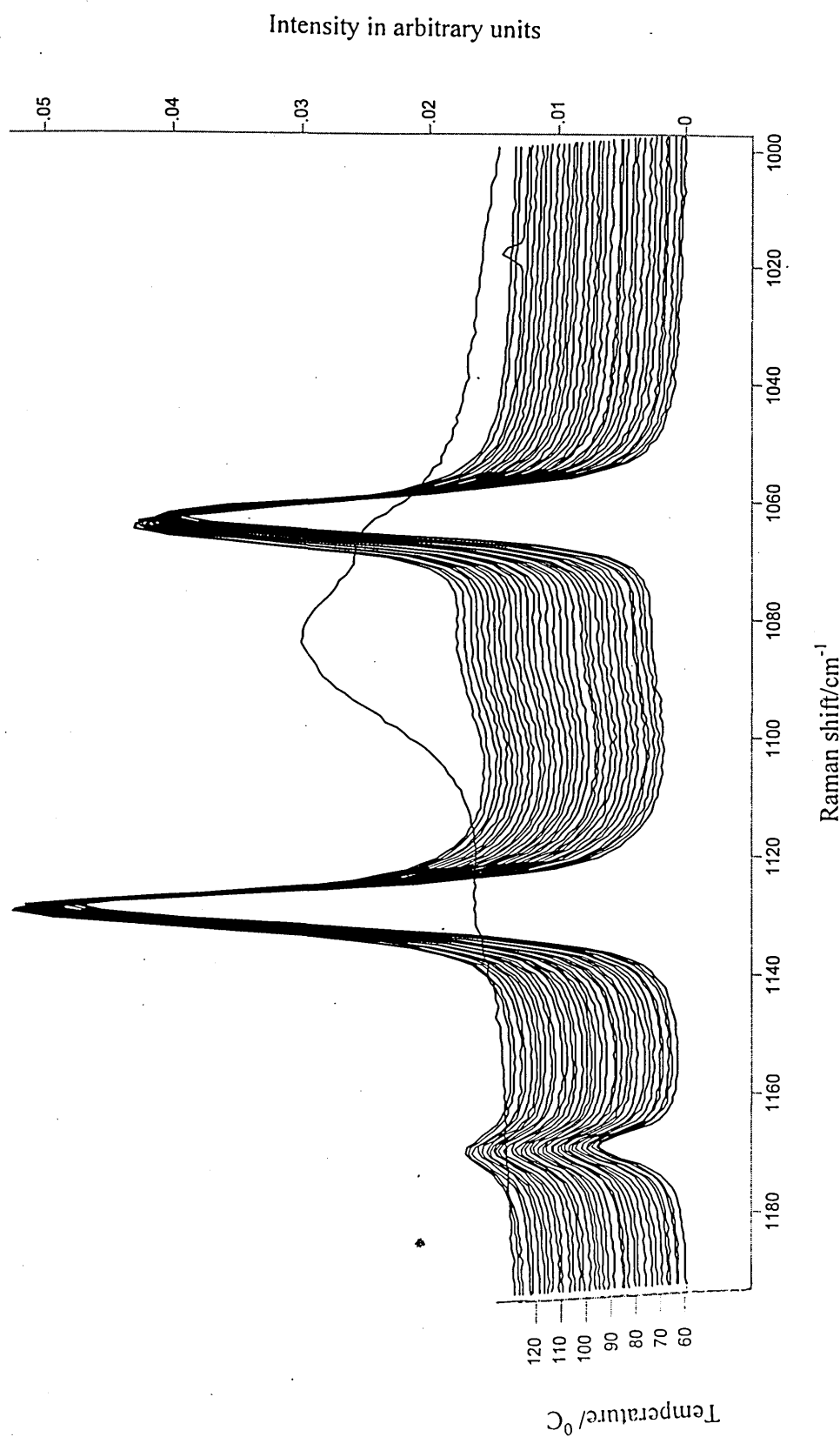


Fig 7.13: The waterfall arrangement of Raman spectra of sample B in region 3 during stepwise heating. The spectra are arranged from 60° to 128° C at 2° intervals in an upward direction.

Various heating runs of sample B are shown in figures 7.14 to 7.16. The time associated with the chart title is the total scan time of each spectrum.

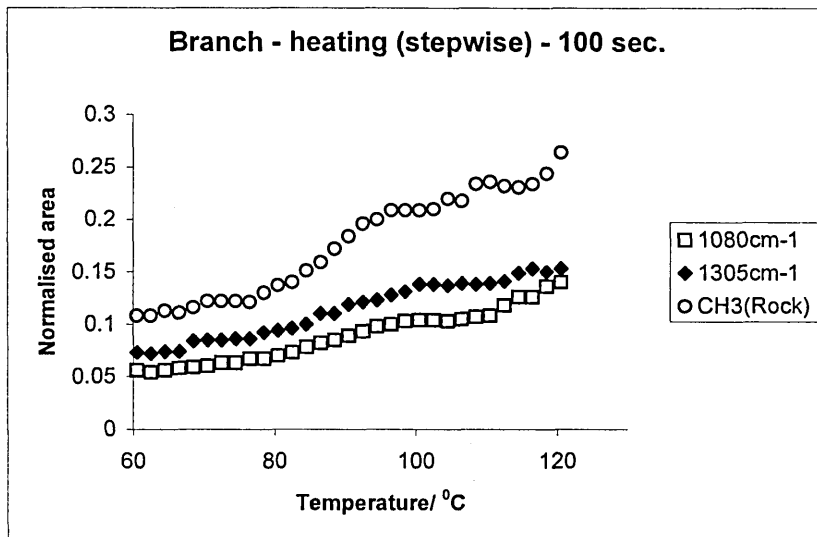


Fig 7.14: The variation of area of the bands in regions 2,3 and 4 with temperature in sample B during a stepwise heating run at  $1^{\circ} \text{C min}^{-1}$ .

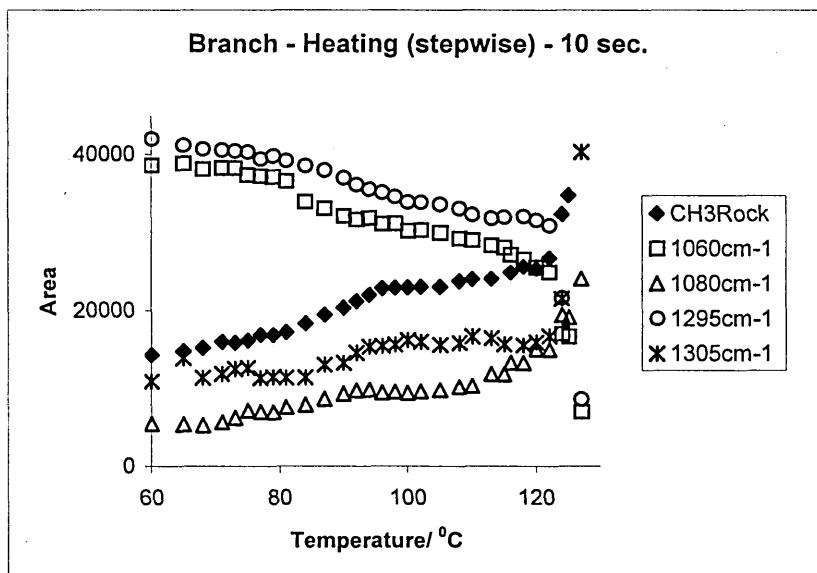


Fig 7.15: The variation of area of the bands in regions 2,3 and 4 with temperature in sample B during a stepwise heating run at  $1^{\circ} \text{C min}^{-1}$ .

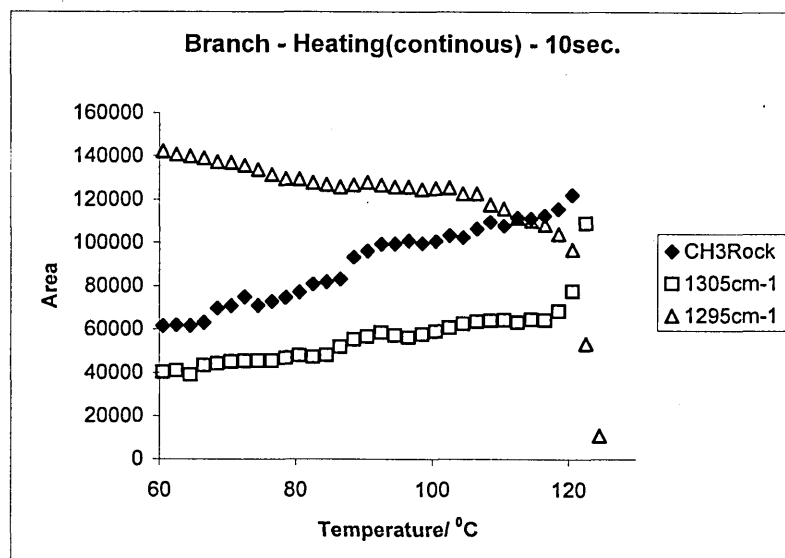


Fig 7.16: The variation of area of the bands in regions 2,3 and 4 with temperature in sample B during a continuous heating run at 1°C min<sup>-1</sup>.

All three graphs are generally in good agreement although figure 7.14 shows a broader transition range than the other two graphs (figures 7.15 and 7.16). In figure 7.14 we could observe an increased rate of change in the absorbance of the disorder bands between about 82°C and 96°C (see figure 7.12 also) and in figures 7.15 and 7.16 this was observed from 84°C to 94°C. This trend could also be observed in the width of 1300 cm<sup>-1</sup> band (see figure 7.10). The crystalline bands shown in figures 7.15 and 7.16 also show some indication of a change in their gradient at the middle of this temperature range (~90°C). This further supports the evidence of phase transition from the disorder bands.

The plots illustrated below show the changes occurring during cooling of sample B from the melt. In figures 7.10, 7.17 and 7.18 a sudden drop of the band areas could be observed at ~120°C and at ~80°C. The first one shows the onset of crystallisation whereas the later drop is an indication of the other phase transition.

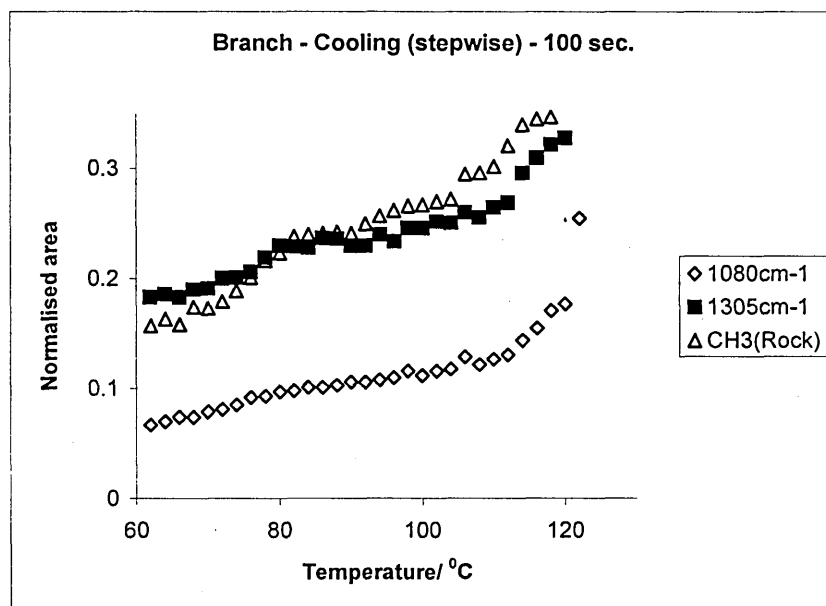


Fig 7.17: The variation of area of the bands in regions 2, 3 and 4 with temperature in sample B during a stepwise cooling run at  $1^{\circ}\text{C min}^{-1}$ . Data collection time was 100 s.

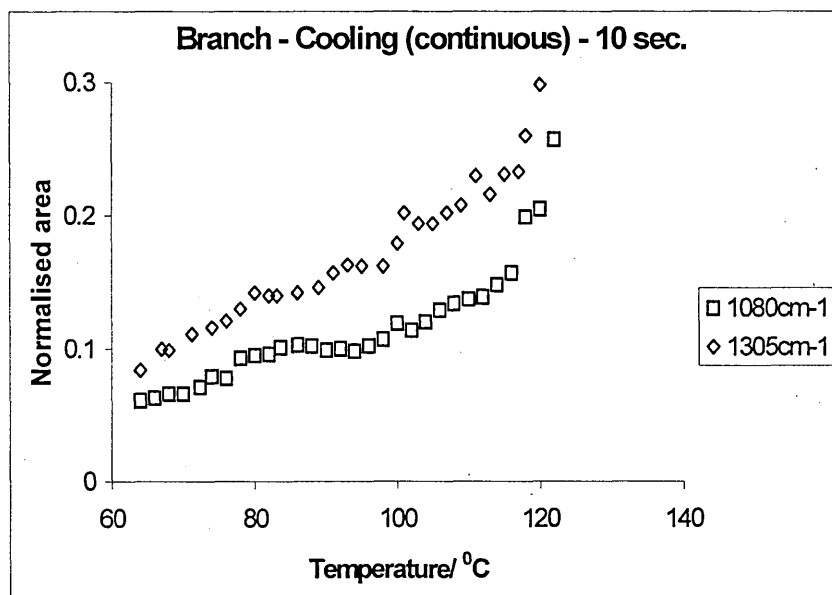


Fig 7.18: The variation of area of the bands in regions 2 and 3 with temperature in sample B during a continuous cooling run at  $0.3^{\circ}\text{C min}^{-1}$ . Data collection time was 10 s.

We were interested in the same regions of the Raman spectrum for the deuterated analogue (A) as for the undeuterated branched sample (B) except for region 4. We could not clearly observe this conformational mode ( $\text{CH}_3$  rocking) in the lower temperature spectra of sample A as the majority of the molecules of this sample have only one branch terminating with a  $\text{CH}_3$  group whereas the remaining two bands have deuterated end caps. However, in the higher temperature spectra of sample B,  $\text{CH}_3$  conformations became visible but were very noisy. Therefore we limited our investigation to regions 2 and 3 mainly.

In sample A only the region 2,  $\text{CH}_2$  twisting band showed some significant changes. They are illustrated in figures 7.9, 7.19 and 7.20. Figures 7.19 and 7.20 show a significant change of the slope in the range  $80^\circ$  to  $94^\circ$  C and around  $74^\circ$  to  $80^\circ$  C in heating and cooling runs respectively. These results further support the transition temperatures observed in figure 7.9.

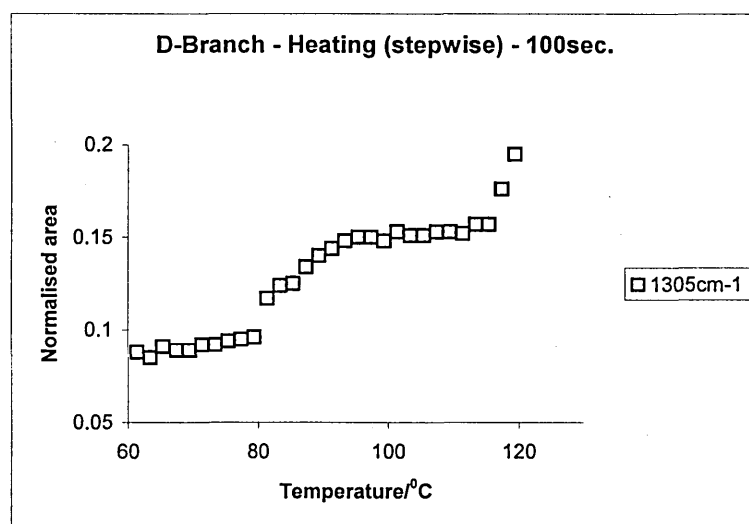


Fig 7.19: The variation of area of the bands in region 2 with temperature in sample A during a stepwise heating run at  $1^\circ \text{C min}^{-1}$ .

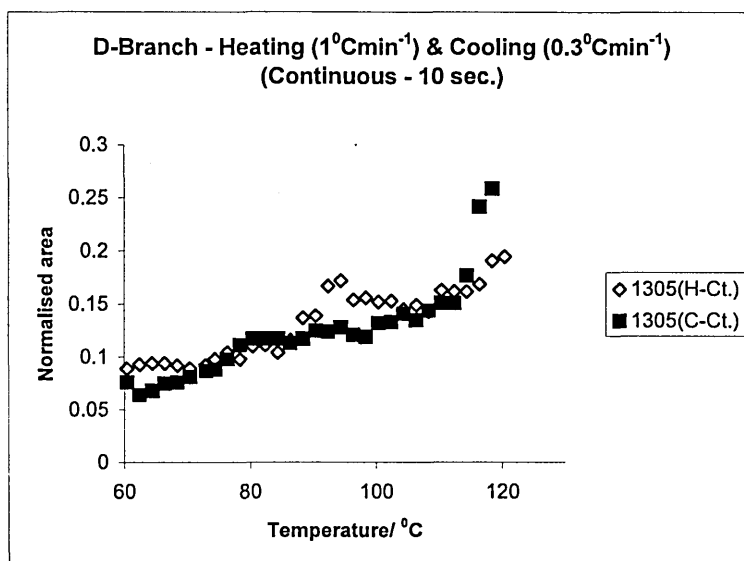


Fig 7.20: The variation of area of the  $1305\text{ cm}^{-1}$  band in region 2 with temperature in sample A during continuous heating and cooling runs.

The gauche component ( $1305\text{ cm}^{-1}$ ) of the  $\text{CH}_2$  twisting mode changes significantly at the structural transition. The area of the  $1305\text{ cm}^{-1}$  band clearly shows important changes at the above temperature ranges in the respective heating and cooling runs in figures 7.19 and 7.20.

The estimated transition temperatures are given in Table 7.1 below.

Table 7.1: Estimates for transitions temperatures of sample A and B.

Sample	Heat treatment	Temperature ( $^{\circ}\text{C}$ ) *		Best estimate of transition temperature ( $^{\circ}\text{C}$ )
		Width ( $1300\text{ cm}^{-1}$ )	Area (C-C stretch)	
A	cooling	70 - 78	74 - 80	$\sim 77 \pm 3$
	heating	82 - 92	80 - 94	$\sim 87 \pm 5$
B	cooling	72 - 80	76 - 80	$\sim 78 \pm 2$
	heating	84 - 94	84 - 94	$\sim 89 \pm 5$

\* Estimated maximum slope was used in determining these temperatures.



The SAXS work on these samples by the University of Sheffield group is still in progress. Initial SAXS results have shown a phase transition of sample A at  $\sim 90^\circ\text{C}$  and  $\sim 78^\circ\text{C}$  during slow, continuous heating and cooling runs respectively. For sample B, SAXS has shown a transition at  $\sim 90^\circ\text{C}$  in a slow heating run<sup>6</sup>.

However, the changes observed in the Raman spectrum at the phase transition of sample A were subtle. The main reason for this is because here we are mainly monitoring the changes of the  $\text{CH}_2$  segments. In most molecules of sample A two branches are deuterated at the end portion of the chain and only one branch has an undeuterated chain end. The  $\text{CH}_2$  segments in the other two branches thus correspond to the inner part of the chain. We already know it is the chain end region which is more susceptible to disorder in transitions in long n-alkanes<sup>7</sup>. Therefore the reduced sensitivity of these  $\text{CH}_2$  parameters of sample A to the phase transition is not surprising. Unfortunately we could not identify any disorder bands arising from the deuterium segments other than the crystalline C-C stretching mode due to  $\text{CD}_2$  segments at  $1140\text{ cm}^{-1}$  in the Raman spectrum of sample A.

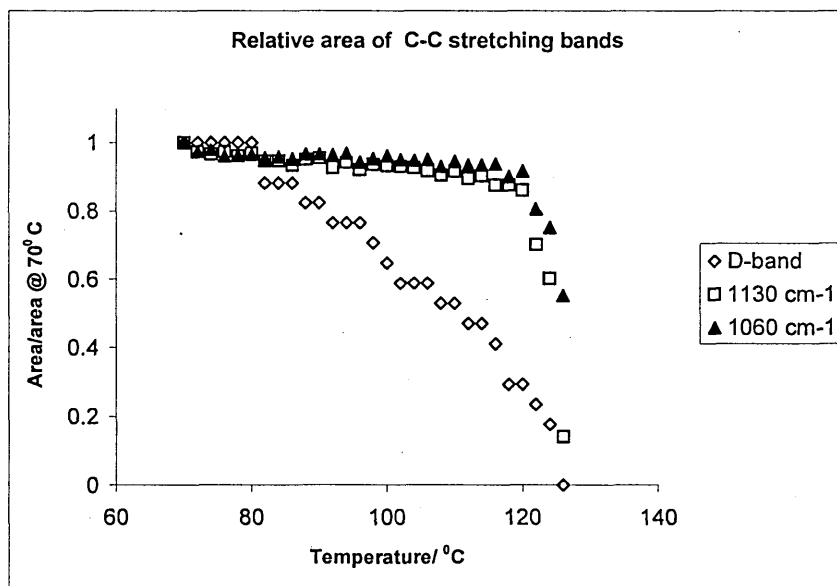


Fig 7.21: The variation of the relative area of the C-C crystalline bands of sample A in the region 3 during cooling, relative to the area of each of these bands at  $70^\circ\text{C}$ .

This mode ( $1140\text{ cm}^{-1}$ ) is very useful to understand the chain end behaviour during the heat treatment. The relative behaviour of this band compared with its undeuterated counterparts is depicted in figure 7.21. In this figure we could see the relative area of the two undeuterated bands remain more or less constant until just below melting temperature. In contrast the D-band remains constant until the transition temperature and after the transition it gradually decreases up to melting. The area of the D-band reaches 50% of its initial area about  $120^\circ\text{C}$  before the melting temperature. However, in C168D this happened just before melting of the sample (see figure 7.4). It suggests that the sample A disorders more rapidly with increasing temperature than C168D. The ratio of the area of the D band to its H analogue is illustrated in figure 7.22 below. It was calculated that the  $\text{CD}_2:\text{CH}_2$  of sample A is 0.049. According to figure 7.22 at  $70^\circ\text{C}$ , the D:H is 0.03. Therefore it suggests sample A is somewhat disordered even at that temperature. We could also see evidence of disorder in the low temperature Raman spectrum (figure 7.7).

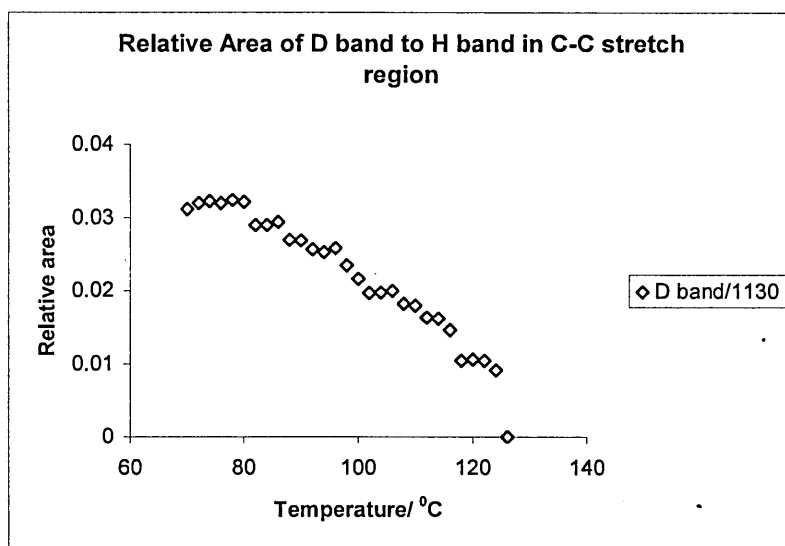


Fig 7.22: Variation with temperature of the area of the C-C symmetric stretching mode for deuterated chains relative to their H analogues.

Sample A retains this level of crystallinity until the transition temperature ( $80^\circ\text{C}$ ) and after the transition to NIF form the degree of order rapidly decreases compared to C168D. This information from the behaviour of the D-band further supports the highly disordered NIF structure which was identified above, mainly based on C-H vibrational

modes. The CD<sub>2</sub> vibrational modes show a significant change here due to the fact that the disordering is largely limited to the chain end region. Unfortunately, except for the C-C symmetric stretching mode (D-band), no other vibrational modes due to CD<sub>2</sub> groups with significant intensity were identifiable in the Raman spectrum of sample A.

#### 7.4 Conclusion

Two Y shaped long - branched samples were subjected to a vibrational analysis using Raman spectroscopy. One of them was the partially deuterated analogue of the other one. However, it was found some chain ends of sample A are not deuterated due to a fault in the synthesis. Our calculations showed it is ~ 80 % deuterated.

Regions 1, 2, 3, and 4 of the Raman spectrum were monitored. No changes could be observed in region 1 whereas the rest of the regions are sensitive to the NIF transition. We identified a single solid phase transition in A and B each from Raman data. The changes in the crystalline bands were subtle whereas the disorder bands showed the most significant changes at this transition. The high level of chain end disorder above the solid-solid transition temperature and the higher rate of disordering with increasing temperature observed in sample A compared with the linear alkane C168D, supports the assignment of a NIF phase. Our Raman results suggest the phase transition to NIF form of sample A occurs around  $\sim 87^{\circ} \pm 5^{\circ}$  C during heating and  $\sim 77^{\circ} \pm 3^{\circ}$  C during cooling. In sample B it occurs  $\sim 89^{\circ} \pm 5^{\circ}$  and  $\sim 78^{\circ} \pm 2^{\circ}$  C during heating and cooling respectively. Therefore we can conclude both sample A and B show similar transition temperatures. These figures are very close to the figures obtained from SAXS data.

Initial SAXS studies on sample A and B have also shown a NIF form at high temperature phase. However, contrary to the linear alkanes, SAXS results have shown that the NIF structure changes with temperature. We also observed that relative area of the C-C stretching mode of the CD<sub>2</sub> segments ( figures 7.21 and 7.22) shows larger changes with increasing temperature compared with the linear counterpart C168D (figures 7.4 and 7.5). This implies that the NIF form becomes more disordered with increasing temperature. This further supports the above observation from SAXS. Normally for the NIF form, we might think of a structure consisting of the two short branches in the crystalline layer and the long branch making the amorphous layer. However, the SAXS

evidence suggests that the crystalline layer not only includes shorter branches but consists of segments of the longer branch too and the rest of the longer chain emanates as cilia into the amorphous layer. Therefore the amorphous layer consists of variable length cilia, including parts of longer and shorter branches.

SAXS results on the low temperature phase, too, rules out the possibility of a simple superlattice structure unlike the linear long chain alkanes and their binary mixtures. Normally one might expect the long cilia in the amorphous layer of the NIF form to fold and make a new crystalline layer at the low temperatures. However, this structure is not possible according to SAXS results. However, at the moment the crystalline structures of these branched alkanes in both high and low temperature phases are not clear. More investigation is needed using SAXS and SANS techniques to determine these structures. This work is in progress.

## References

- 1 Ungar G, Zeng XB, Chem. Rev., **101**, 4157 (2001)
- 2 Brooke GM, Farren C, Harden A, Whiting MC, Polymer, **42**, 2777 (2001)
- 3 Gorce J-P, PhD Thesis, Sheffield Hallam University, June (2000)
- 4 Cutler DJ, Hendra PJ, Walker JH, Cudby MEA, Willis HA, Spectrochimica Acta, **34A**, 391 (1978)
- 5 Parker SF, Herman H, Spectrochimica Acta, Part A, **53**, 119 (1997)
- 6 Zeng XB and Ungar G, Unpublished work
- 7 De Silva DSM, Gorce JP, Wickramarachchi PASR, Spells SJ, Macromol. Symp., **184**, 67 (2002)

### Inelastic Neutron Scattering (INS) on Long Chain Alkanes

#### 8.1 Introduction

Vibrational spectroscopy has played a key part in the characterisation and understanding of polymers due to its sensitivity to both the crystalline structure and conformational changes. Infrared and Raman spectroscopy have been extensively used in this regard. However, optical methods are fundamentally restricted by considerations of their selection rules and other intensity factors. Use of INS circumvents the limitations of optical techniques.

Neutron scattering is based on the interaction of neutrons with atomic nuclei and thus the spectral response is independent of the electro-optic parameters and selection rules for photons. For infrared and Raman spectroscopy, the allowed modes are those at wavevector,  $k = 0$  (see Chapter 3.3). INS spectroscopy is capable of seeing all the modes at all values of  $k$ . Therefore, in INS even the unseen modes in optical methods can be observed.

The inelastic neutron scattering cross-section,  $s$ , for hydrogen is  $\sim 80$  barns whereas in all the other elements is less than 5 barns. Therefore the incoherent scattering from hydrogen dominates the spectrum and the scattering from carbon can be neglected in the INS spectrum of alkanes and polyethylenes. Therefore the modes that involve significant hydrogen displacement will dominate the spectrum. This dependence on the cross-section is why the INS spectrum is so different from infrared and Raman spectroscopy. The  $s$  of deuterium is 2.1 barns, significantly different from that of hydrogen. This simple fact has enabled vital information on structures by isotopic labelling.

Some early attempts to circumvent the limitations of optical methods by using INS have been reported<sup>1</sup>. This was followed by some work on shorter alkanes<sup>2</sup> and the LAM branch of perdeutero-polyethylene<sup>3</sup>. However, these initial attempts were only

of modest success. With the advent of better INS spectrometers, more reliable results have been obtained for a series of shorter alkanes ranging from  $C_2 - C_6$ <sup>4</sup>. The first observation of the complete INS spectrum in the region  $0 - 4000\text{ cm}^{-1}$  was reported by Parker<sup>5</sup>. This work has been performed by using the high resolution, broadband spectrometer, TFXA, at the ISIS pulsed spallation neutron source at the Rutherford Appleton laboratory, Chilton, UK. TFXA was later replaced by TOSCA<sup>6</sup>. The results obtained from TOSCA show a significant enhancement in the counting rate and the resolution (from 2-3% to 1-1.5% of the energy transfer) owing to its much larger detector area<sup>6</sup>. In addition TOSCA is capable of diffraction.

In this chapter we will discuss the potential use of INS with its enhanced resolution on our model long chain alkane compounds. SAXS, SANS and infrared methods have been successfully used in the characterisation of these novel materials. Here we will use TOSCA to study two samples of  $C_{246}H_{494}$  in folded and extended forms which were successfully studied using SAXS, Raman<sup>7</sup> and infrared<sup>8</sup> techniques previously. The objective of using INS is to obtain a more complete description than from infrared spectroscopy.

## 8.2 Experimental

The experimental work was carried out by Dr. S.J. Spells (Sheffield Hallam University) and Dr. X.B. Zeng (University of Sheffield). A once folded sample of  $C_{246}H_{494}$  was prepared by isothermal crystallisation at  $110^\circ\text{C}$ . The INS spectrum of this sample was collected over a period of 24 hours, together with background (without sample) spectra using TOSCA. Then it was recrystallised at  $124^\circ\text{C}$  to obtain the extended chain crystals. The INS spectrum of the extended form also was collected as above.

## 8.3 Results and Discussion

The  $\text{CH}_2$  wagging region of the infrared spectrum is very useful in characterising chain disorder particularly in determining the specific chain conformations. Our aim is to study the INS spectrum of these conformations with the potential for obtaining a more complete description. However, at the operational temperature of TOSCA (below 20 K),

the alkane will obtain close to 100% crystallinity. In order to circumvent this limitation, here a sample was chosen in which the departure from all-*trans* chain is structural in nature, rather than reversible on cooling. The fold itself consists of several higher energy conformers such as *gg*, *gt* and *gtg*<sup>9</sup>.  $C_{246}H_{494}$  can be crystallised both in extended and once-folded forms by suitable choice of crystallisation temperature. Subtraction of the extended spectrum from the folded spectrum will result in the spectrum of the fold itself. This method was successfully applied to obtain the infrared spectrum of the fold geometry of  $C_{198}H_{398}$ <sup>9,10</sup>.

The INS spectrum of  $C_{246}H_{494}$  folds (once-folded spectrum – extended spectrum) is shown below. Here, the  $CH_2$  wagging modes are of particular interest.

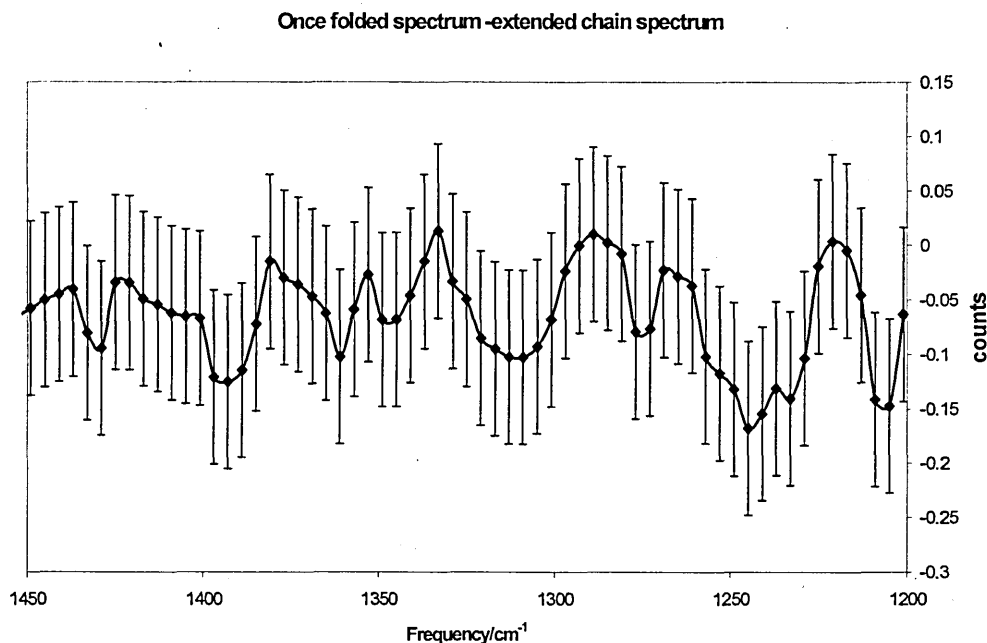


Fig 8.1: The INS spectrum of the fold geometry of  $C_{246}H_{494}$ .

Three peaks, which are in close proximity to the frequencies in the FTIR spectrum of a similar region, could be identified. The peak at  $1380\text{ cm}^{-1}$  corresponds in frequency to the  $CH_3$  “umbrella” deformation. The peak at  $1290\text{ cm}^{-1}$  and a shoulder at  $1375\text{ cm}^{-1}$  agree with ‘fold bands’. However, the general shape of the bands do not seem similar to FTIR spectrum but this is expected due to the absence of selection rules in INS. It is clear that the error bars are very large and the instrumental resolution in this region was



around  $20\text{ cm}^{-1}$ . Therefore we cannot arrive at any firm conclusions on the band assignments.

Instrumental resolution was better in the low frequency acoustic mode (LAM) region ( $\sim 5\text{ cm}^{-1}$ ). The background-subtracted folded and extended chain spectra are shown in figures 8.2 and 8.3 respectively.

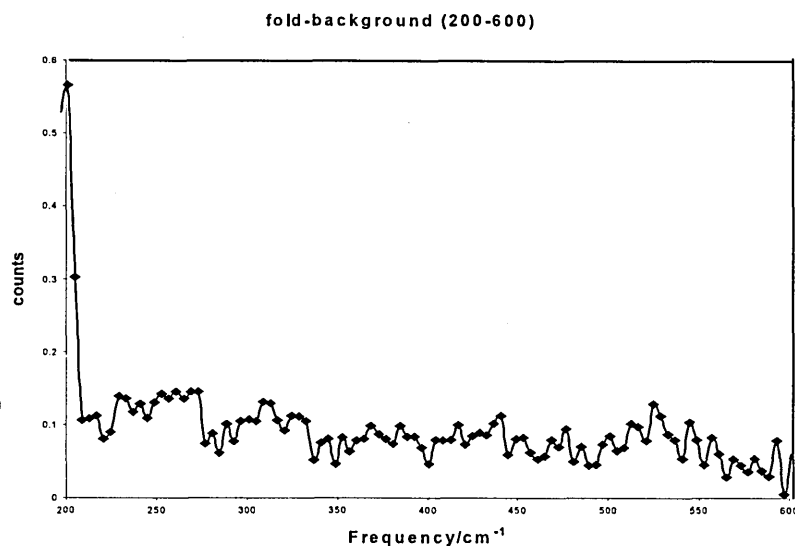


Fig 8.2: The LAM region of  $C_{246}H_{494}$  - folded form.

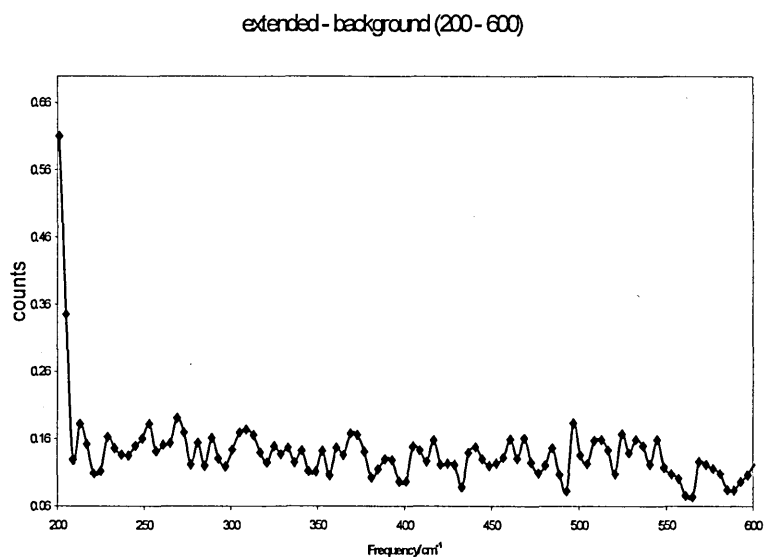


Fig 8.3: The LAM region of  $C_{246}H_{494}$  - extended form.

We could identify some skeletal modes in both these spectra. A peak around  $525\text{ cm}^{-1}$  arises due to an in-plane skeletal mode and the peak at  $200\text{ cm}^{-1}$  was assigned to the out of plane skeletal mode<sup>5</sup>. Comparison of the two spectra showed no significant difference in peak positions. This could be due to poor signal to noise ratio.

#### 8.4 Conclusion

The INS spectrum of the  $\text{C}_{246}\text{H}_{494}$  chain folds was obtained with a view to acquiring a detailed description of the  $\text{CH}_2$  wagging modes. However, the operational conditions below 20 K in TOSCA is a major constraint in seeing the disordered conformations as at low temperature the sample obtains close to 100% crystallinity. In addition, the resolution in INS was poorer than other vibrational methods. The intensity of the error bars were large due to the low sample weight available. It would require run times around eight days per sample in order to get useful information of the wagging mode region and perhaps in the LAM region too. For these reasons, it was decided not to pursue further measurements using INS.

References

- 1 Danner HR, Boutin H, Safford GJ, J Chem. Phys., **41**, 3649 (1968)
- 2 Logan KW, Danner HR, Gault JD, Kim H, J. Chem. Phys., **59**, 2305 (1973)
- 3 Feldkamp LA, Vankataraman G, King SJ, Neutron Inelastic Scattering (IAEA, Vienna, 1968) Vol **2**, p 159
- 4 Nelligan WB, LePoire DJ, Brun TO, Kleb R, J. Chem. Phys., **87**, 2447 (1987)
- 5 Parker SF, J. Chem. Soc., Faraday Trans., **92**(11), 1941 (1996)
- 6 Bowden ZA, Celli M, Cilloco F, Colognesi D, Newport RJ, Parker SF, Ricci FP, Rossi-Albertini V, Sacchetti F, Tomkinson J, Zoppi M, Physica B, **276-278**, 98 (2000)
- 7 Ungar G, Zeng XB, Spells SJ, Polymer, **41**, 8775 (2000)
- 8 Gorce JP, Spells SJ, Polymer, **45**, 3297 (2004)
- 9 Ungar G, Organ SJ, Polym. Commun., **28**, 232 (1987)
- 10 Gorce J-P, Spells SJ, Polymer, **43**, 2581 (2002)

### Conclusions and Future Work

#### 9.1 Conclusions

Monodisperse long chain alkanes have been studied over the past decade as model compounds for semicrystalline polymers in terms of their structure and crystallisation. These compounds can only be chemically synthesised under well controlled reaction conditions. Alkanes are widespread as natural products. For example, natural gas is a mixture of methane, ethane and propane and petroleum is a complex mixture of hydrocarbons. n-Alkanes are the oligomers of polyethylene. In addition we can find alkyl groups in many natural and synthetic compounds such as lipid biomembranes, carbohydrates, surfactant molecules, medicinal agents, cooking oil to name a few of them. Therefore the understanding of the structure and behaviour of the alkanes helps better understanding of these materials. With this in mind several monodisperse alkanes such as linear long chain alkanes, branched alkanes with short branches and star-shaped, partially deuterated (with deuterium end caps) linear and branched alkanes and carboxylic acids have been synthesised.

A wealth of information has been gathered so far using these n-alkanes: The mode of chain folding in polymers has been a central question for many years. This was modelled by studying monodisperse n-alkanes. Alkanes with chain lengths as short as  $C_{150}$  are capable of chain folding. The tendency for the pure alkanes to fold in integer fractions of the extended chain length is mainly due to their preference to exclude the chain ends from the crystal interior. The growth rate shows a distinct minimum when the growth temperature is near the transition between different folded forms. This was attributed to a process called 'self-poisoning'.

The crystalline structures and the crystallisation behaviour of linear long chain alkanes are fairly well understood by now. The mature crystals have distinct thicknesses which are integer fractions of the length of the underlying molecules. They form different integer forms (IF) such as extended, F2, F3, F4 etc. In addition, a non-integer form (NIF) which ultimately transforms to an integer form has been identified at higher temperature.

This NIF form is up to one-third amorphous. Different super lattice structures have been identified at low temperature in some long chain linear alkanes and their binary mixtures. Examples include folded-extended form (FE) in linear alkanes with around 200 C atoms and the triple layer super lattice structure in binary mixtures. Binary mixtures too, show a semicrystalline form at high temperature which can be related to the NIF form in pure alkanes.

Several branched alkanes have been synthesised to model branched polymers. They are  $C_{96}H_{193}CH(CH_3)C_{94}H_{189}$  and  $C_{96}H_{193}CH(C_4H_9)C_{94}H_{189}$  which contain a short branch in the centre, the asymmetrically branched alkane,  $C_{191}H_{383}CH(CH_3)C_{99}H_{199}$  and Y-shaped alkanes,  $C_{120}H_{241}CH(C_{61}H_{123})C_{119}H_{239}$ ,  $C_{120}H_{241}CH(C_{195}H_{391})C_{118}H_{237}$ , [B] and  $C_{12}D_{25}(CH_2)_{108}CH(C_{195}H_{391})(CH_2)_{106}C_{12}D_{25}$ , [A] with deuterated end caps. The crystalline structures of these materials except the last two (A and B) Y-shaped molecules have been investigated extensively. The first two with methyl and butyl branches show a rapid NIF  $\rightarrow$  F2 transition on cooling. The asymmetric methyl branched alkane shows two different semicrystalline forms depending on the crystallisation temperature followed by each transforming into a double layer (AB) and a triple layer (ABA) crystalline form respectively at low temperature. For the Y-shaped alkane with a shorter branch a semicrystalline form which is similar to a NIF has been found at high temperature and a double layer super lattice has been identified by subsequent cooling. These structures were described in Chapter 2 and for extensive review see Ungar and Zeng<sup>1</sup>. The crystalline structures of the two Y-shaped alkanes with a longer branch (A and B) are currently being investigated and will be discussed later here.

The main interests of this work were to study the chain tilting using an end-deuterated linear alkane and to identify structural changes in two Y-shaped long branched alkanes (A and B) with changing temperature. Vibrational spectroscopy has been very useful in structural studies due to its sensitivity to crystalline structure and conformational changes. A detailed study<sup>2</sup> to investigate the disorder in these highly ordered long chain linear alkanes using infrared spectroscopy has been carried out previously. Another investigation<sup>3</sup> by the same technique using an end-deuterated linear long chain alkane has revealed the behaviour of the chain ends within the crystal structure in the ordering/disordering process with heat treatments. In this study we further investigate these monodisperse long chain alkanes using vibrational spectroscopy and small angle X-ray scattering (SAXS). Some preliminary studies using short alkanes had to be done in

order to achieve the above objectives. Experimental and some associated theoretical work carried out during this work and the main findings were described in Chapters 4 to 8.

SAXS work showed that the end-deuterated alkane achieves a maximum tilt of  $35.5^{\circ}$  before melting of the sample. This is a common tilt angle in polyethylene corresponding to the {201} basal plane. A combination of SAXS work with the previous infrared work<sup>2</sup> showed that the onset of chain tilting coincides with the chain end perfecting. The chain tilt is necessary to accommodate the incoming ordered chain ends into the crystal. On the evidence of Raman data a single solid-solid transition was identified in the two Y-shaped long branched alkanes. This transition was also identified by SAXS at similar temperatures<sup>4</sup>. In addition, we found that these branched materials are generally more disordered compared with the linear alkane C168D. This suggests that the branching incorporates more disorder into the crystal structure. As evidenced from the behaviour of the D-band in the Raman spectrum of the end-deuterated Y-shaped long branched alkane (A), we found that the higher temperature form is highly disordered and the level of disorder further increases with increasing temperature. From SAXS it was found the thickness of the amorphous layer of the NIF form varies with the temperature contrary to that of linear long chain alkanes<sup>4</sup>. Therefore the above Raman observation agrees well with this SAXS finding.

The above findings suggest a semicrystalline form with a variable amorphous layer thickness at higher temperatures. This form may be similar to that of the Y-shaped short branched alkane. The crystalline thickness of this structure is determined by the short arm. Therefore we might expect a similar structure for A and B too. According to SAXS results<sup>3</sup> on A and B, it seems likely that some molecules can have both their short arms crystallised, but others have only one crystallised and some molecules have both short arms in the amorphous layer and part of the long branch crystallised. Therefore the amorphous layer consists of the longer branch (C 195), the shorter branch (C 120) and parts of the longer branch (C 75) emanating from the crystalline layer. However, the infrared spectrum of the end-deuterated long branched Y-shaped alkane (A) failed to show a doublet splitting for the CD<sub>2</sub> bending mode even at low temperatures. Even with annealing at higher temperatures, the doublet could not be developed. This rules out a significant proportion of adjacent deuterated segments in the crystal structure. Therefore having both shorter arms in the crystalline layer is highly unlikely. A structure with a mixture of one short arm in the crystalline layer and the other arm in the amorphous

layer and both short arms in the amorphous layer may be more probable. The schematic diagram of this NIF form is given in figure 9.1(a).

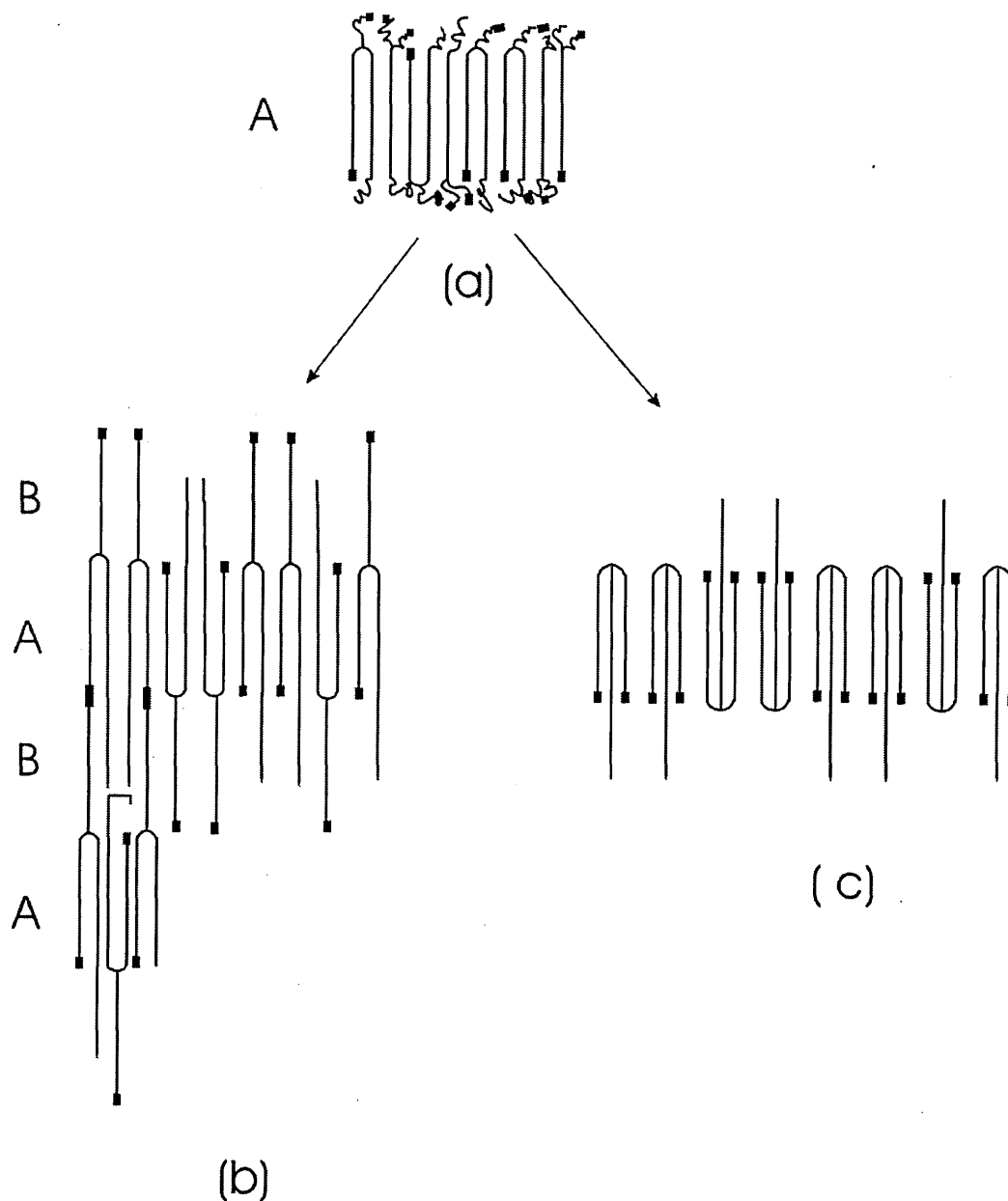


Fig 9.1: Schematic drawing of hypothetical lamellar structures in Y-shaped alkane  $C_{12}D_{25}(CH_2)_{108}CH(C_{195}H_{391})(CH_2)_{106}C_{12}D_{25}$  (a) high temperature semicrystalline form; (b) and (c) possible low temperature double layer forms. Deuterated end caps are denoted by thicker lines.

This NIF structure leads to a highly complicated structure at low temperature. SAXS data<sup>4</sup> on the low temperature phase has ruled out a simple super lattice structure, like in the short branched Y-shaped alkane or binary mixtures of linear alkanes. We can expect the longer branch and one or both of the shorter branches in the amorphous layer entering into the crystalline layer upon cooling. The remains of the longer branch and the shorter branch in the amorphous layer can crystallise to form another crystalline layer upon cooling. A schematic diagram of the suggested low temperature forms is given in figures 9.1(b) and 9.1(c). Figure 9.1(b) shows only one short arm and the long arm entering the crystal layer upon cooling whereas in 9.1(c) both short arms and the long arm enter the crystal layer. However, 9.1(c) is unlikely according to the infrared evidence of failing to show a doublet splitting for the  $\text{CD}_2$  bending mode. Therefore structure 9.1(b) is more probable leading to AB type superlattice structure. The thickness of the each layer is determined by the shorter arm ( $\text{C}_{120}$ ). Therefore the excess lengths of the  $\text{C}_{75}$  chain ends protruding from both upper and lower A layers into the middle B layer can adopt various chain end defects to fill the gaps. One such modification is shown in figure 9.1(b). However, more information is needed to confirm these structures. Nevertheless a wealth of structural data was gathered by the combination of SAXS and vibrational spectroscopy. SAXS mainly gives the dimensions of the crystal and vibrational spectroscopy indicates the pathway of an individual molecule within the crystal. This paragraph described how these evidences from the above techniques are combined to determine the crystal structure.

In addition to the above important findings made in this work, we have developed some experimental and theoretical techniques such as the use of disorder bands in Raman spectroscopy to identify phase transitions, the infrared method to calculate the isotopic ratio in deuterium labelled alkanes and the simulation of the infrared spectrum of the two possible folded arrangements of an end-deuterated alkane. Previous studies have established the use of infrared spectroscopy to study the disorder in these materials<sup>2</sup> and the perfecting of the crystal structure with heat annealing/cooling<sup>3</sup>. The latter work also showed the importance of isotopic labelling in such a study. These techniques developed here are not only limited to these long chain alkanes but can also be utilised in relevant applications in other systems containing alkyl chains.



We studied these monodisperse alkanes as model compounds for semi-crystalline polymers. The polydispersity of polymers has been a great hindrance to fundamental studies on crystallisation and crystal morphology. By studying the monodisperse compounds we can gain an insight into polymer structure and behaviour. The fact that integer folded forms found in mature crystals of long chain alkanes are formed via a transient NIF form is a good model for the technologically important process of primary and secondary nucleation of polymers. Binary mixtures of monodisperse alkanes and Y-shaped molecules introduce aspects of polydispersity and branching in polymers respectively. In this work we studied monodisperse linear and branched alkanes with extended and folded chains. Using them we observed how the order/disorder of the crystalline structure varies with temperature. Furthermore, we saw that the branching incorporates more disorder into the crystal structure.

The irreversible thickening of lamellar crystals during annealing is a general feature of polymer behaviour. Thermal annealing promotes partial unfolding of polymer chains towards the more energetically favourable extended chain conformations. Lamellar thickening has been extensively studied in many polymers as it is also an industrially important process. Polyethylene has been the most widely studied material in this respect. The thickening process has been extensively investigated using a wide variety of techniques such as X-ray diffraction, Raman LAM and TEM, DSC, NMR, WAXS etc. Extensive reviews on early work in this field can be found in Wunderlich<sup>5</sup> and Geil<sup>6</sup>. More recent work has extended these studies to real-time monitoring of changes in thickness using X-ray synchrotron radiation<sup>7</sup> and AFM<sup>8,9</sup>. In polymers the thickening process is complicated by polydispersity. Studies on the thickening process with thermal annealing benefit from the use of strictly monodisperse alkanes. Alkanes undergo reorganisation of chains within the crystal layer during high temperature annealing. The annealing behaviour of monodisperse alkanes has been monitored using both folded and extended forms<sup>3,8,9,10</sup>. Gorce and Spells have observed a 'perfecting' of the crystal of the extended and once folded forms of  $C_{198}H_{398}$  by subsequent heat annealing and cooling, by monitoring the improvement in the regularity of the progression bands<sup>10</sup>. De Silva et al observed the same phenomenon with successive annealing and cooling in extended crystals of C216D by monitoring the increase of the  $CD_2$  bending splitting in the infrared spectrum<sup>1</sup>. This annealing/cooling process leads to a 'perfecting' of the crystals. It is clear both crystal thickening in PE and 'perfecting' of the alkane chains happens by the longitudinal translation of chains. However, upon annealing the alkane crystals

undergoes a series of discrete transformations corresponding to stepwise unfolding  $F5 - F4 - F3 - F2 - E^8$ , whereas in polyethylene chain unfolding is generally a continuous and slower process. In some exceptional cases integer doubling of crystal thickness has been observed, particularly in single crystal mats of polyethylene<sup>7</sup>.

Chain tilting is another interesting observation in lamellar polymers. In some polymers chains are always tilted while in others tilt develops on high temperature crystallisation or by annealing. In polyethylene the chain tilt is believed to be responsible for the 'hollow pyramid' shape of solution-grown crystals<sup>5,11</sup>. Furthermore this leads to the lamellar twist in melt crystallised spherulites<sup>12</sup>. In solution grown crystals of long chain alkanes both folded and extended forms are perpendicular while those grown from the melt are tilted<sup>13</sup>. In both polyethylene and long chain alkanes this difference is associated with the crystallisation temperature,  $T_c$ . Low  $T_c$  results in the perpendicular form while high  $T_c$  gives the tilted morphology. Absence of chain tilt in lamellar crystals of polyethylene<sup>12</sup> and alkanes<sup>14</sup> is due to frozen-in surface roughness and not due to high surface order. In this work and in previous studies<sup>14</sup>, this chain tilting was monitored using the monodisperse alkanes. It was shown that annealing at increasing temperatures causes perfecting of the crystal structure which induces chain tilting. It has been proposed recently that in melt crystallised polyethylene below  $T_c \sim 127^\circ \text{C}$  chains may be initially perpendicular, with fold ordering and chain tilting occurring subsequently<sup>12</sup>. Monodisperse n-alkanes show a maximum tilt angle of  $35^\circ$  which is also the most common tilt angle for polyethylene.

Although monodisperse n-alkanes are very good models for polyethylene, there are limitations to their applicability to all polymers. For example they are not good models for nylons. Nylon chains are rigid due to intermolecular hydrogen bonding whereas alkane chains are flexible. Therefore they may not show similar behaviour. In this regard, research work is being carried out on monodisperse nylon oligomers as model compounds to nylon polymers. Another interesting piece of work has been carried out on monodisperse hydroxy butyrate oligomers (HB) as models for the biopolymer poly (hydroxy butyrate) (PHB) which is mainly found in cell walls.

## 9.2 Future work

By now the crystal structures, structural changes with varying temperature and the crystallisation kinetics of linear long chain alkanes and their binary mixtures are fairly well understood. However, the work on star-shaped alkanes (Y-shaped molecules) is still at an early stage. In this work we developed a Raman spectroscopic method to identify the solid phase transitions in two Y-shaped alkanes (A and B). A SAXS analysis has also been carried out on them<sup>4</sup>. On the evidence of SAXS, Raman and low temperature infrared results the hypothetical structures shown in figure 9.1 were proposed. However, more investigation is needed to confirm the above structures probably using other techniques such as infrared and SANS. Heating and cooling runs using infrared spectroscopy similar to these reported here using Raman spectroscopy would be expected to further support the change of the level of crystallinity and disorder already found by Raman spectroscopy. Evidence from the CH<sub>2</sub> and CD<sub>2</sub> wagging modes of the infrared spectrum will be very useful in this regard. Infrared spectroscopy is also sensitive to molecular folds. Specific folds bands such as 1298, 1340, 1347 and 1369 cm<sup>-1</sup> indicate regular, adjacent (110) folds in the methylene wagging region of the infrared spectrum. Therefore using infrared spectroscopy we can identify folds if there are any. This would be advantageous in confirming the hypothetical models.

A real time SANS study parallel to SAXS will supplement the information obtained by SAXS. The possibility of doing real time SANS has been demonstrated using long chain alkanes<sup>15</sup>. SANS is able to provide information on the location of the deuterated segments. In this regard use of a new sample with 100% deuterated end caps would be more useful as the deuteration of the sample A turned out to be incomplete. Combination of long periods from SAXS and SANS and information from electron density profiles and scattering length profiles constructed from SAXS and SANS intensities, with infrared and Raman spectroscopic evidence will be able to provide a clear picture of crystal structures of the above Y-shaped alkanes, A and B. SANS has been successfully applied to confirm the high temperature semi-crystalline form and low temperature superlattice structures in linear long chain alkanes and their binary mixtures using partially deuterated monodisperse long chain alkanes previously<sup>15,16,17</sup>. Parallel studies on another Y-shaped alkane with the deuterated end cap on the longer branch would help to map the pathway of the long branch in the crystal structure. Also studies on a symmetric molecule (3 arms of equal lengths) may be able to provide guidance on the

crystal structures of A and B molecules. However, there is little likelihood of these monodisperse compounds being synthesised in the near future.

These Y-shaped alkanes were of interest as models for branched polymers. However, they have only limited ability to demonstrate the aspect of branching in polymers as the branching in polymers may be very irregular. Therefore use of alkanes with more irregular branches e.g. 3 branches with different lengths, at a later stage of this study would enable a more complete picture to be formed.

Binary mixtures of long chain alkanes introduce the concept of polydispersity to these samples in controlled levels. So far only the binary mixtures of linear long chain alkanes have been studied. Mixtures of branched alkanes will be more interesting models for polymers in this regard.

So far, studies on monodisperse alkanes have been limited to SAXS, SANS, infrared, Raman and NMR techniques. Fold surfaces of integer folded forms devoid of an amorphous layer will be amenable to study by different surface techniques. Microscopy will be useful to obtain information on different morphologies of these alkanes with different crystallisation conditions. We can also obtain information on transitions between different forms as the crystal shape is varied with these changes.

In addition, there are some technical features used in this study which can be further improved. The main barrier to use of infrared transmission spectroscopy in our heating/cooling runs is the vertical arrangement of the sample in the cryostat. This generally results in the leakage of the sample and a loss of the intensity of the spectral peaks after melting of the sample, thus denying us information on the melt state of the sample. Therefore use of a device which can seal the sample, for example in liquid cells, is worth trying out.

For our Raman studies we used a DSC pan-lid covered with an Al foil with a hole in the middle, as the sample holder. The purpose of covering the sample is to obtain a uniform temperature within the sample. However, sometimes we failed to get good temperature control in our experiments. Therefore it will be better to use a lid made of a material which is non-absorbing (eg. KBr) in the region of interest.

Also there are some areas in data analysis of this work which can be further improved. We could see in our Raman experiments (Chapter 7) the signal to noise ratio was better

for 100 second scans in total, than in 10 second scans. Therefore further increase of total scan time would be beneficial as most of the disorder bands in the Raman spectrum are very low in intensity.

References

- 1 Ungar G, Zeng XB, Chem. Rev., **101**, 4157 (2001)
- 2 Gorce J-P, PhD Thesis, Sheffield Hallam University, June (2000)
- 3 De Silva DSM, PhD Thesis, University of Sheffield, February (2002)
- 4 Ungar G, Zeng XB, Unpublished data
- 5 Wunderlich B, Macromolecular physics, Crystal nucleation, growth, annealing, **2**, Academic Press, New York (1976)
- 6 Geil PH, Polymer single crystals, Polymer reviews, New York: Wiley (1963)
- 7 Rastogi AB, Spoelstra JGP, Goossens PJ, Lemstra, Macromolecules, **30**(25), 7880 (1997)
- 8 Magonov SN, Yerina NA, Ungar G, Reneker DH, Ivanov D, Macromolecules, **36**, 5637 (2003)
- 9 Winkel AK, Hobbs JK, Miles MJ, Polymer, **41**, 8791 (2000)
- 10 Gorce J-P, Spells SJ, Polymer, **43**, 4043 (2002)
- 11 Wunderlich B, Macromolecular physics, Crystal structure, morphology, defects, **1**, Academic Press, New York (1976)
- 12 Abbo el Maaty MI, Bassett DC, Polymer, **42**, 4957 (2001)
- 13 Ungar G, Stejny J, Keller A, Bidd I, Whiting MC, Science, **229**, 386 (1985)
- 14 Ungar G, Zeng XB, Chem. Rev., **101**, 4157 (2001)
- 15 Zeng XB, Ungar G, Spells SJ, King SM, Macromolecules, **38**, 7201 (2005)
- 16 Zeng XB, Ungar G, Spells SJ, Brooke GM, Farren C, Harden A, Phys. Rev. Lett., **90**, 155508 (2003)
- 17 Zeng XB, Ungar G, Macromolecules, **36**, 4686 (2003)